Theoretical Study of Single-Molecule Spectroscopy and Vibrational Spectroscopy in Condensed Phases

by

Shilong Yang

B.S., Univ. of Sci. & Tech. of China, China (1998)
M.S., University of California, Los Angeles (1999)

Submitted to the Department of Chemistry
in partial fulfillment of the requirements for the degree of

Doctor of Philosophy

at the

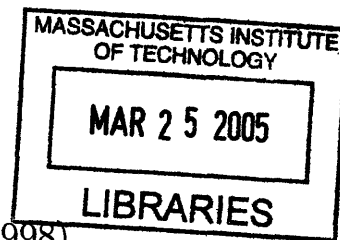## MASSACHUSETTS INSTITUTE OF TECHNOLOGY

February 2005

Author . . . .
Department of Chemistry
November 16, 2004
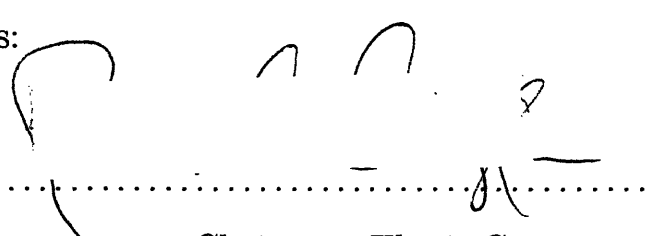
Certified by . . . .
Jianshu Cao
Associate Professor of Chemistry
Thesis Supervisor

Accepted by . . . .
Robert W. Field
Chairman, Department Committee on Graduate Students
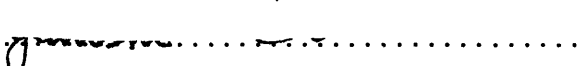
This doctoral thesis has been examined by a Committee of the Department of Chemistry as follows:

Professor Robert G. Griffin ....

Chairman, Thesis Committee

Professor of Chemistry

Professor Jianshu Cao ....

Thesis Supervisor

Associate Professor of Chemisty

Professor Robert J. Silbey ....

Class of 1942 Professor of Chemistry

2

Theoretical Study of Single-Molecule Spectroscopy and Vibrational Spectroscopy in Condensed Phases

by

Shilong Yang

Submitted to the Department of Chemistry
on November 16, 2004, in partial fulfillment of the
requirements for the degree of
Doctor of Philosophy

Abstract

In this thesis, theoretical models and computer simulations are employed to study several problems of single-molecule spectroscopy and vibrational spectroscopy in condensed phases. The first part of the thesis concentrates on studying dynamic disorders probed by single molecule fluorescence spectroscopy. Event statistics and correlations of single-molecule fluorescence sequences of modulated reactions are evaluated for multi-channel model, diffusion-controlled reaction model, and stochastic rate model. Several event-related measurements, such as the on-time correlation and the two-event number density, are proposed to map out the memory function, which characterizes the correlation in the conformational fluctuations. A semiflexible Gaussian chain model is used to determine the statistics and correlations of single-molecule fluorescence resonant energy transfer (FRET) experiments on biological polymers. The distribution functions of the fluorescence lifetime and the FRET efficiency provide direct measures of the chain stiffness and their correlation functions probe the intrachain dynamics at the single-molecule level. The fluorescence lifetime distribution is decomposed into high order memory functions that can be measured in single-molecule experiments. The scaling of the average fluorescence lifetime on the contour length is predicted with the semi-flexible Gaussian chain model and agrees favorably with recent experiments and computer simulations. To interpret the fluorescence measurements of the mechanical properties of double-stranded DNA, a worm-like chain model is used as a first-principle model to study double-stranded DNA under hydrodynamic flows. The second part of the thesis concentrates on nonperturbative vibrational energy relaxation (VER) effects of vibrational line shapes. In general, nonperturbative and non-Markovian VER effects are demonstrated more strongly on nonlinear vibrational line shapes than on linear absorption.

Thesis Supervisor: Jianshu Cao
Title: Associate Professor of Chemistry

Acknowledgments

Upon the completion of my PhD study in the Department of Chemistry, I am indebted to a number of people. First of all, I would like to express my sincere thanks to my advisor, Prof. Jianshu Cao. Without his valuable guidance, motivation, and generous support, I would not have reached this point. He has always listened to my questions and explanations of ideas, and provided important suggestions and comments. It has been a great experience to work with him.

I am truly grateful to Prof. Robert Silbey for helpful suggestions and useful discussions as well as many favors. Prof. Robert Griffin is greatly acknowledged for valuable comments while chairing the thesis committee. Also I thank Prof. Robert Field and Prof. Andrei Tokmakoff for useful discussions.

During my graduate study at MIT, I have benefitted from fruitful discussions with Seogjoo Jang, Jaeyoung Sung, Younjoon Jung, James. B. Witkoskie, Lorin Gutman, Yuan-Chung Cheng, and Jianlan Wu. It is my great pleasure to include collaborations with James B. Witkoskie as chapters of this thesis.

Last, but not the least, I would like to express my sincere gratitude to my wife, Bin Hu, for her love and support over these years. She is the most important part of my life. I also thank my parents, Shaoyin Yang and Guihua Yao, for their love and support. This thesis is dedicated to them.

Contents

List of Figures

14

15

16

17

21

23

List of Tables

Chapter 1

Introduction

1.1 Motivation

The issue of multiple time-scales is a recurring theme in physical chemistry and has been explored from various perspectives.[1] Traditional chemical kinetics assumes a clear separation of time-scales; that is, the rate process in a reactive system occurs on the slowest time-scale so that all other motions can be averaged on the reaction time-scale to yield dissipation and random noise. Under these assumptions, the depletion from the reactant to the product is a Poisson process and the average population disturbance decays exponentially. However, in proteins and glassy systems chemical reactions are usually modulated by geometric constraints, slow structural relaxation, and hydrogen bonding network in aqueous systems. In the presence of such slow environmental fluctuations the competition between the reaction process and the conformational dynamics leads to non-exponential kinetics and memory effects.[2, 3, 4, 5, 6, 7, 8] Yet, such conformational modulation can not be completely described by phenomenological kinetics and is often not resolved in bulk measurements. In comparison, single molecule trajectories consist of a chain of correlated reaction events of various durations and thus provide a unique probe to conformational fluctuations.

Advances in optical spectroscopy and microscopy have made it possible to directly measure the optical spectrum along single molecular trajectories and monitor the molecular dynamics and chemical kinetics of individual reactive systems.[9, 10, 11,

12, 13, 14, 15, 16, 17] Early experiments pioneered by Moerner and co-workers have investigated the single molecule emission process in low temperature glasses, which has since been analyzed by Skinner, Silbey, and other groups within the framework of the standard two-level model.[18, 19, 20, 21, 22] Recent progress has expanded the regime of single molecule spectroscopy from low temperatures to room temperatures, and from glassy systems to reactive chemical systems and biomolecules. As reviewed by Xie and Trautman,[23] new developments in room temperature single molecule experiments include observations of spectral fluctuations, translational and rotational diffusion motions, conformational dynamics, fluorescence resonant energy transfer, exciton dynamics, and enzyme reactivity. These new experiments contain rich information that needs theoretical interpretations and models. Of particular relevance are recent studies of non-exponential reaction dynamics in single molecule kinetics. For example, Hochstrasser and Rigler measured the fluorescence decay associated with single DNA and tRNA.[13, 14] Geva and Skinner applied a stochastic two-state model to interpret bi-exponential relaxation in these experiments.[24, 25] Xie and coworkers demonstrated slow fluctuations in the turn-over rate of cholesterol oxidation and the dependence of enzymatic turnovers on previous history.[15] This experiment has inspired several theoretical studies of memory effects in single molecule kinetics.[26, 27, 28] Weiss and coworkers developed fluorescence resonance energy transfer as a means to explore conformational dynamics.[16] Theoretically, a well-studied reactive system is ligand-binding proteins, which exemplify the concept of potential landscapes in protein environments.[3, 29, 30] Wang and Wolynes explored single molecule reaction dynamics in fluctuating environments and showed theoretically that the statistics of single reaction events exhibits intermittency and does not follow the Poisson law.[31] Onuchic, Wang, and Wolynes explored the possibility of using replica correlation functions along single molecule trajectories to analyze complex energy landscapes.[32] Mukamel and coworkers calculated stochastic trajectories of solvent-controlled electron transfer and demonstrated non-Poisson kinetics in the waiting time distribution function.[33] Metiu and his coworkers devised a four-state kinetic scheme to model room-temperature fluorescence of single dye molecules

adsorbed on a glass surface.[34] Agmon introduced a diffusion model for the conformational cycle of a single working enzyme.[28] Though much progress has been made, it remains a challenge to quantify dynamic disorder in single molecule kinetics.

It is well appreciated that single molecule spectroscopy detects spatial disorder without the usual ensemble averaging in conventional spectroscopy. An equally important advantage of single molecule techniques is the direct observation of slow variations in reaction kinetics, which are often limited by spectral resolution in conventional bulk experiments. In single molecule experiments, the traced molecular system inter-converts between the dark and bright states so that the observed fluorescence turns on and off intermittently. Such blinking phenomena have been observed in a variety of systems, including low-temperature glasses, quantum dots, molecular aggregates, and biological molecules. The waiting time of each on-off event corresponds to the duration of a single molecule reaction event, and the statistics of on-off events of various durations records the real-time trajectory of the single reactive system. In a sense, the on-off sequence can be viewed as a *binary code*, which contains the essential information about reaction mechanisms. The key to decipher this code is the statistical analysis of on-off blinking trajectories. The use of single molecule spectroscopy for detecting dynamic disorder has been demonstrated through the measurements of the fluorescence correlation function, the waiting time distribution function, and the two-event joint distribution function. Though a clear evidence of non-Markovian and non-Poisson kinetics, these single molecule measurements and related analyses are qualitative and descriptive.

Various types of single fluorescence probes have been developed, among which fluorescence resonant energy transfer is a widely used technique with high accuracy. In these experiments, donor and acceptor dye molecules are attached to polymers at different points. Upon excitation, the donor molecule is pumped to its excited state and a nonradiative energy transfer from the donor to the acceptor may occur. This probe replies on the distance-dependent energy transfer between a donor fluorophore and acceptor fluorophore and is capable of measuring distances on the 2 to 8 nm scale.[35] More importantly, this technique can report on dynamical changes

in the distance or orientation between the two fluorophores for both intramolecular and intermolecular FRET. Another important probe is intramolecular fluorescence quenching. The strong dependence of quenching rate on the fluorophore-quencher distance makes the fluorescence quenching a sensitive probe of loop formation dynamics in polypeptides and proteins, which is a fundamental step in protein folding. Both techniques have been used widely to study ligand binding reactions, to probe equilibrium protein structure fluctuations, and enzyme-substrate interactions during catalysis.[14, 16, 36] Biopolymers are normally stiff on a wide range of length scales from 5nm to 50 nm.[37, 38] To interpret single-molecule FRET measurements on a biopolymers, we need to study the dynamics of a semi-flexible polymer chain. This semi-flexible chain model needs to capture the stiffness of a biopolymer and provide a straightforward way to explore the dynamics of semi-flexible chains. Furthermore, hydrodynamic interactions between different polymer segments can be incorporated. In light of these considerations, we propose a semi-flexible chain model which includes the persistence length into the Rouse model in analogous to the Ornstein-Uhlenbeck process.

With the techniques of fluorescence resonant energy transfer and intramolecular fluorescence quenching, the reaction dynamics in solution can be probed directly by fluorescence spectroscopy. Biopolymer reactions are often coupled to the internal relaxation processes. The experimentally observed fluorescence lifetime is a result of the convolution of the reaction time scale and the conformation relaxation time scale. Due to the competition between reaction process and internal relaxation process, different kinetic regimes can be observed. In the homogeneous limit where internal relaxation is extremely fast, the system remains at equilibrium configuration, the reaction process is a homogeneous average over the equilibrium configuration. In the inhomogeneous limit where the internal relaxation is extremely slow, the system remains at its initial configuration, hence the reaction process is a static average over the initial configuration. Hence, it is of great importance to understand different kinetic regimes of the fluorescence lifetime distribution function. Normally the fluorescence in experiments is monitored over a finite time window. This experimental time scale

provides another dimension to the reaction kinetics. For a short experimental time scale, transient configurations are probed close to their initial configurations; While for a long experimental scale, the system is dominated by the relaxation process. Therefore, we can explore different kinetics regimes by varying the length of the time window.

When the fluorophore-quencher pair are attached to both ends of polypeptides chain, a fluorescence quenching event indicate the formation of a loop.[39, 40, 41, 42] The relaxation of the end-to-end distance is generally non-Markovian. The theory by Szabo, Schulten and Schulten[43] only considers the effective diffusion of the end-to-end distance and completely neglected the non-Markovian nature of the end-to-end motion. Hence it does not correctly describe the contour length dependence of the fluorescence lifetime over the full kinetic range. On the other hand, the Wilemski-Fixman approximation,[44, 45, 46] which is derived for diffusion-controlled reactions, can be readily generalized for non-Markovian relaxation processes. This theory has been validated recently by experiments and simulations.[42, 47] However, the criterion to apply the Wilemski-Fixman approximation is still not yet available. The dependencies of this criterion on the contour length, the solvent viscosity, and characteristics of fluorophore-quencher pair are to be explored.

Another important application of fluorescence-labeled molecules is to study the mechanical properties of biopolymers with fluorescence video spectroscopy. It is a unique technique to visualize the stretching of single DNA molecules in real time, offering a lot of freedom to probe previously inaccessible regime of polymer dynamics. The accuracy of these methods has been sufficiently improved so that quantitative studies can be explored extensively on mechanical properties of DNAs, proteins and other biopolymers. Macroscopic properties of polymer solutions result from the deformation of polymers when they are stretched by hydrodynamic or external forces. The fluorescence video spectroscopy offers a novel way to understand the microscopic origin of the macroscopic properties at the single molecule level. In a series of experiments, Chu and his co-workers[48, 49, 50, 51, 52, 53, 54] observe the steady state extension of DNA molecules subject to constant plug, elongational, and shear

flows. Although many Brownian dynamics simulations are used to model these experiments and predict the mechanical properties of polymers, yet these calculations are phenomenological and computationally intensive. We employ the path integral formulation of equilibrium statistical mechanics to formulate hydrodynamic flows as an effective potential. With this first-principle model, we propose a less intensive Monte Carlo algorithm to evaluate the time averaged ensemble properties.

Vibrational energy relaxation (VER) in liquids is a central component of chemical and biological processes. The ability of molecules to redistribute energy into other degrees of freedom is the key in product stabilization. Modern femtosecond laser techniques can probe the intermolecular and intramolecular vibrations directly. Vibrational line shapes from nonlinear optical spectroscopy such as pump-probe, photon echo, and Fourier transformed infrared spectroscopy provides rich information about the dynamics in condensed phases. Previous theoretical treatments of the vibrational energy relaxation effects were based on a perturbative approach, which is limited to weak couplings between vibrational degree of freedom and the bath fluctuations. Furthermore, most optical line shape theories consider pure dephasing only or approximate VER as a simple relaxation rate. These approximations break down at large anharmonicities or slow bath relaxation. In general, the non-perturbative contributions have strong effects on nonlinear spectroscopy. Therefore, it is crucial to establish a reliable method that can incorporate the non-perturbative VER effects, which becomes the main focus of the second part of this thesis.

1.2   Overview

This thesis consists of two parts. The first part uses statistical models and computer simulations to study the single molecule spectroscopy. The second part concentrates on a path integral approach of the non-perturbative vibrational energy relaxation effects on vibrational line shapes.

In Chapter 2, the existence of fluctuations in the rate of activation step in enzymatic dynamics is observed in recent single-molecule measurements. The recurrence

behavior in the same-time difference function of two events is found for both discrete multi-channel model and continuous diffusive reaction model. Further calculations clearly demonstrate the conformational dynamics dependence of the recurrence behavior, which is believed as a means to quantify the conformational fluctuations. A generic model, the stochastic rate model is proposed to explain the on-off sequences of single molecule measurements induced by fluctuations on rate process. Based on cumulant expansion of the rate constant, the stochastic rate model is shown to be able to approximately incorporate other models on conformational dynamics.

In Chapter 3, statistics and correlations of single molecule reaction events are formulated with the modulated reaction model and explicitly evaluated via the stochastic rate representation. The memory function, introduced through the second order cumulant truncation of the stochastic rate expression, characterizes the correlation in single molecule measurements, reveals the long-time behavior of conformational fluctuations, and interprets the experimental observation of stretched exponential and power-law decay. Within this formalism, the on-time correlation function and the sequence density are shown to be equivalent to the memory function of the fluctuating rate. Though both are obtained under the small variance condition, the on-time correlation function, measured at the discretized number of events, maps out the memory function at discretized effective time separations, whereas the sequence density maps out the memory function over the continuous time. Confirmed by numerical calculations of the three-conformational-channel model, these relations quantify conformational dynamics and hence are useful for analyzing single molecule kinetics.

In Chapter 4, a semi-flexible Gaussian chain model is used to determine the statistics and correlations of single-molecule fluorescence resonant energy transfer (FRET) experiments on biological polymers. The model incorporates a persistence length in a Rouse chain and describes single-chain dynamics with normal modes. The hydrodynamic interaction is included in the dynamics of the semi-flexible Gaussian chain on the pre-averaging level. The distribution functions of the fluorescence lifetime and the FRET efficiency provide direct measures of the chain stiffness, and their correlation functions probe the intra-chain dynamics at the single-molecule level. When mea-

sured with finite time resolution, the instantaneous diffusion coefficient for FRET is much smaller in the collapsed structure than in the coiled structure, and the variation has a quadratic dependence on the donor-acceptor distance. In the fast reaction limit, single-molecule FRET lifetime measurements can be used to map out the equilibrium distribution function of inter-fluorophore distance. As an example of microrheology, the intrinsic viscoelasticity can be extracted from single-molecule tracking of the Brownian dynamics of polymers in solution.

In Chapter 5, the configuration-controlled regime and the diffusion-controlled regime of conformation-modulated fluorescence emission are systematically studied for Markovian and non-Markovian dynamics of the reaction coordinate. A path integral simulation is used to model fluorescence quenching processes on a semi-flexible chain. First order inhomogeneous cumulant expansion in the configuration-controlled regime defines a lower bound for the survival probability, while the Wilemski-Fixman approximation in the diffusion-controlled regime defines an upper bound. Inclusion of the experimental time window of the fluorescence measurement adds another dimension to the two kinetic regimes and provides a unified perspective for theoretical analysis and experimental investigation. We derive a rigorous generalization of the Wilemski-Fixman approximation [44] and recover the $1/D$ expansion of the average lifetime derived by Weiss.[46]

In Chapter 6, fluorescence lifetime measurements in a polymer chain are modeled using a memory function expansion, computer simulations, and simple scaling arguments. Unless the quenching rate is localized and infinitely fast, the fluorescence lifetime is generally not equivalent to the first passage time. The fluorescence lifetime distribution is decomposed into memory functions that can be measured separately in single-molecule experiments. The leading order of the expansion gives the Wilemski-Fixman approximation, and the convergence of higher order terms determines its validity. Simulations of the fluorescence quenching on a Rouse chain verify the accuracy of the WF approximation at small contact radii, short contour lengths and small quenching rates. Detailed investigation of the average fluorescence lifetime reveals two competing mechanisms: the independent motion of end-to-end

34

vector, which dominates at small contact radius, and the slowest relaxation of polymer, which dominates at large contact radius. The Wilemski-Fixman rate is used in combination with scaling arguments to predict the dependence of fluorescence lifetime on the contour length. Our predictions for the scaling of the average lifetime with the contour length are in good agreement with both simulations and recent experiments by Eaton and his group.[40]

In Chapter 7, we use the worm-like chain as a first-principles model to study single molecule experiments of double stranded DNA subject to constant plug, elongational, and shear flows. The steady state configurations of the polymer correspond to a locally defined potential and result in a path integral description of the canonical partition function. The parameters of this model are consistent with previous theory and experimental measurements. The time averaged mean extension reproduces experimental results and compares well with computationally more expensive Brownian dynamics simulations of reduced models.

In the second part of the thesis, we discuss non-perturbative vibrational energy relaxation (VER) effects on vibrational line shapes. In Chapter 8, a general formulation of non-perturbative quantum dynamics of solutes in a condensed phase is proposed to calculate linear and nonlinear vibrational line shapes. In the weak solute-solvent interaction limit, the temporal absorption profile can be approximately factorized into the population relaxation profile from the off-diagonal coupling and the pure dephasing profile from the diagonal coupling. The strength of dissipation and the anharmonicity induced dephasing rate are derived. The vibrational energy relaxation (VER) rate is negligible for slow solvent fluctuations, yet it does not justify the Markovian treatment of off-diagonal contributions to vibrational line shapes. Non-Markovian VER effects are manifested as asymmetric envelops in the temporal absorption profile, or equivalently as side bands in the frequency domain absorption spectrum. The side bands are solvent-induced multiple-photon effects which are absent in the Markovian VER treatment. Exact path integral calculations yield non-Lorentzian central peaks in absorption spectrum resulting from couplings between population relaxations of different vibrational states. These predictions cannot be reproduced by the pertur-

bative or the Markovian approximations. For anharmonic potentials, the absorption spectrum shows asymmetric central peaks and the asymmetry increases with anharmonicity. At large anharmonicities, all the approximation schemes break down and a full non-perturbative path integral calculation that explicitly accounts for the exact VER effects is needed. A numerical analysis of the O-H stretch of HOD in D_2O solvent reveals that the non-Markovian VER effects generate a small recurrence of the echo peak shift around 200 fs, which can not be reproduced with a Markovian VER rate. In general, the non-perturbative and non-Markovian VER contributions have a stronger effect on nonlinear vibrational line shapes than on linear absorption.

Chapter 2

Two-event Echo in Single-Molecule Kinetics

2.1 Introduction

Recently, theoretical tools have been developed to calculate measured single molecule statistics.[27] That paper clearly demonstrated the essential difference between ensemble-averaged bulk measurements associated with the population dynamics of full-reactions and event-averaged single molecule measurements associated with a sequence of half-reactions. In particular, the prediction of the focal time in the single-event distribution function and of the recurrent behavior in the two-event distribution function reveals the nature of conformational landscapes. Similar to the photon echo phenomenon, the recurrence can be understood as the echo signal due to the inhomogeneous distribution of environments. Analogous to motion narrowing, in the fast modulation limit, the echo signal vanishes, and the single exponential law is recovered. The height of the echo signal and its position vary with the modulation rate and hence can be a sensitive probe of the dynamics disorder resulting from conformational fluctuations.

Since conformational fluctuations are not directly accessible experimentally, dynamic disorder is a *hidden* mechanism that requires quantitative analysis of single molecule measurements. The prediction of the two-event echo signal in Ref. [27] holds

the promise of characterizing dynamic disorder in single molecule kinetics. However, questions remain with regards to the generality of the recurrence and the quantitative relationship between the echo and conformational dynamics. This chapter presents quantitative analysis of conformational dynamics as revealed by the two-event echo in single molecule kinetics. The following issues will be addressed in this chapter: General features of modulated reactions are reviewed and examined in Sec. 2.2. Phenomenological kinetics, the fluctuation-dissipation relation, and the detailed balance conditions are formulated and clarified on the basis of event-averaged single molecule quantities. Then, the two-event echo signal is calculated in Sec. 2.3 to Sec. 2.6, respectively, for the two-channel model, for the three-channel model, for the diffusion model, and for the Gaussian stochastic model. These calculations show that the distribution and the relaxation rate of conformational fluctuations can be estimated from the echo time and the echo amplitude. Of the four models calculated, the stochastic Gaussian model in Sec. 2.6 provides a general description of rate fluctuations in a similar way as Kubo's stochastic line-shape theory and allows other models to be compared and calibrated.[55, 56] We conclude with a summary in Sec. 2.7.

2.2 General considerations of modulated reactions

Modulated reaction models have been used for analyzing the fluctuating environment and its effects on chemical kinetics. Early examples include a series of papers by Hynes[57, 58] on the influence of solvent relaxation on the reaction rate constant and the Agmon-Hopfield model for ligand binding to myoglobin.[3] A recent application is the analysis of Xie's single enzyme turnover experiment.[15, 27, 28]

A generic modulated reaction model is the N-conformational-channel reactive system, illustrated in Fig. 2-1a. A special case of the generic model is the two-channel model system illustrated in Fig. 2-1b. To be specific, the conformational distribution of the reaction is represented by N discretized conformational channels, each associated with a reversible reaction between the dark and bright states, with forward rate $k_{a,i}$ and backward rate $k_{b,i}$. The conformational dynamics is represented by the
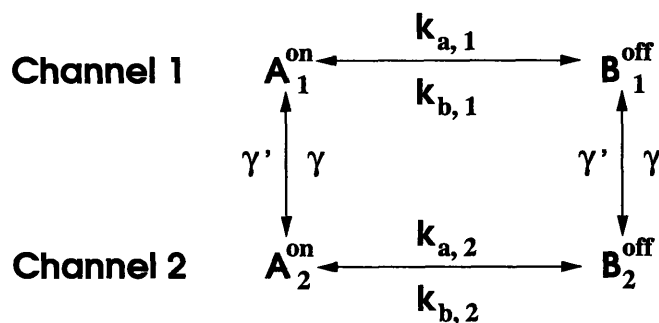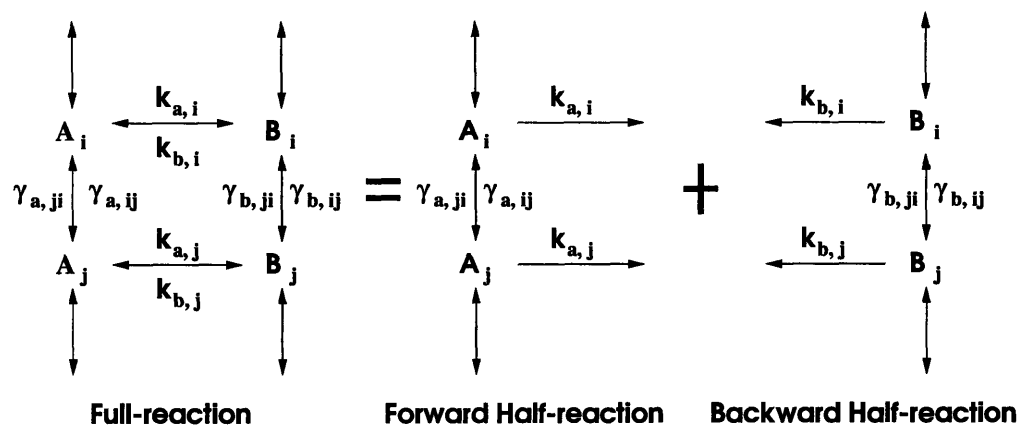
Figure 2-1: (a) The decomposition of the N conformational-channel reaction model into forward and backward half-reactions. (b) The reaction diagram of the discrete two-channel model. The forward rates are k_{a1} and k_{a2}, the backward rates are k_{b1} and k_{b2}, γ is the conversion rate from channel 1 to channel 2, and γ' is the inter-conversion rate from channel 2 to channel 1.

inter-conversion rate $\gamma_{a,ij}$ from the j-th state to the i-th state when the system is in the bright state A (i.e., the on-state), and the inter-conversion rate $\gamma_{b,ij}$ from the j-th state to the i-th state when the system is in the dark state B (i.e., the off-state). The different conformational sub-states are not directly detectable since only the bright state is monitored by fluorescence emission. In single molecule experiments, the on/off time measures the duration that a single molecule spends in the bright/dark state, and a trajectory of on-off events records the dynamics of the single reactive system.

The two-channel model in Sec. 2.3 and the three-channel model in Sec. 2.4 are examples of the N-channel model, the diffusion-modulated reaction in Sec. 2.5 is a continuous version of the N-channel model, and the stochastic Gaussian model in Sec. 2.6 can be understood as the small variance approximation of the N-channel model. In the fast modulation limit, the N-channel reaction model reduces to a single-channel reaction with an effective rate constant, whereas, in the slow modulation limit, it reduces to an inhomogeneous average of the N channels. In the latter limit, the single molecule system remains ergodic, but the rate variation within a single reaction event can be ignored. We briefly review the N-channel reaction model as formulated in Sec.II of Ref. [27] and then examine general features of the model within the context of single molecule measurements.

2.2.1 Event-averaged measurements in single molecule kinetics

As formulated in Ref. [27], a reaction process can be decomposed into a forward half-reaction, which turns the bright state to the dark state, and a backward half-reaction, which turns the dark state to the bright state. The master equation for the forward half-reaction of the N-conformational sub-states is written as

$$\dot{P}_a(t) = -(\Gamma_a + K_a)P_a(t), \qquad (2.1)$$

where the vector $P_{a,i}$ is the survival probability of being in the i-th conformational sub-state, the matrix $\Gamma_{a,ij} = \delta_{ij}\gamma_{a,ii} - \gamma_{a,ij}$, with $\gamma_{a,ii} = \sum_j \gamma_{a,ji}$, describes the con-

formational kinetics in the bright state, and the matrix $K_{a,ij} = \delta_{ij} k_{a,i}$ describes the reaction process from the dark state to the bright state. Eq. (2.1) can be formally solved by the Green's function,

$$G_a(t) = \exp[-t(\Gamma_a + K_a)] \tag{2.2}$$

which is a N-dimensional matrix. The Green's function for the backward half-reaction, $G_b(t)$, is defined in a similar fashion. The two half-reactions are related through the forward rate constant matrix K_a and the backward rate constant matrix K_b, yielding the master equation for the full reaction,

$$\begin{pmatrix} \dot{\rho}_a(t) \\ \dot{\rho}_b(t) \end{pmatrix} = \begin{pmatrix} -\Gamma_a - K_a & K_b \\ K_a & -\Gamma_b - K_b \end{pmatrix} \begin{pmatrix} \rho_a(t) \\ \rho_b(t) \end{pmatrix}, \tag{2.3}$$

where $[\rho_a(t), \rho_b(t)]$ are the population distribution in the dark and bright states, respectively. The time-independent solution to Eq. (2.3) defines the equilibrium distribution,

$$(\Gamma_a + K_a)\rho_a = K_b \rho_b, \tag{2.4}$$

$$(\Gamma_b + K_b)\rho_b = K_a \rho_a, \tag{2.5}$$

which relate ρ_a to ρ_b and vice versa. It is shown in Ref. [27] that population evolution measured in bulk experiments is equivalent to the summation of all the possible reaction events along single molecule trajectories, and the equilibrium ensemble-averaged quantities in the bulk state can be realized by time-averaging single molecule trajectories over long durations. To explicitly evaluate single molecule quantities, we introduce the probability density

$$\begin{pmatrix} F_a \\ F_b \end{pmatrix} = \mathcal{N} \begin{pmatrix} K_b \rho_b \\ K_a \rho_a \end{pmatrix}, \tag{2.6}$$

where F_a is the normalized stationary flux from the bright state to the dark state, and F_b is the normalized stationary flux from the dark state to the bright state. It follows from Eqs. (2.4) and (2.5) that $\sum K_a \rho_a = \sum K_b \rho_b = \mathcal{N}^{-1}$, implying that the total flux is a conserved quantity. Given the stationary fluxes, we can define the distribution function of single on-time events

$$f_a(t) = \sum K_a G_a(t) F_a = \sum_{i,j} k_{a,i} G_{a,ij}(t) F_{a,j} \tag{2.7}$$

and the joint distribution function of on-off events

$$f_{ab}(t_2, t_1) = \sum K_b G_b(t_2) K_a G_a(t_1) F_a, \tag{2.8}$$

which will be evaluated explicitly for several different models in the following sections. These event-averaged quantities can not be obtained directly in bulk experiments and must be collected along a sequence of reaction events of single reactive systems.

2.2.2 Phenomenological chemical kinetics

The rate constant used in the phenomenological kinetic description can be interpreted as the average time that the single molecular system spends in a macroscopic state. To be specific, the average on-time is evaluated from the single event distribution function as $\langle t_a \rangle = \int_0^t t f_a(t) dt = \sum K_a (K_a + \Gamma_a)^{-2} F_a$, where F_a is the flux from the bright state to the dark state. Using the properties of the equilibrium distribution, $K_b \rho_b = (K_a + \Gamma_a) \rho_a$ and $\sum \Gamma_a = 0$, we have

$$\langle t_a \rangle = \int_0^t t f_a(t) dt = \sum (K_a + \Gamma_a)(\frac{1}{K_a + \Gamma_a})^2 (K_a + \Gamma_a) \rho_a \mathcal{N} = \frac{\sum \rho_a}{\sum K_a \rho_a}. \tag{2.9}$$

The same result can be easily obtained from the average survival time in the bright state, i.e., $\langle t_a \rangle = \int G_a(t) F_a dt$. The average forward rate constant follows as

$$\langle k_a \rangle = \frac{\sum K_a \rho_a}{\sum \rho_a}, \tag{2.10}$$

42

which is an inhomogeneous average of forward rate constants and is independent of conformational dynamics. A similar definition can be derived for the backward reaction, $\langle k_b \rangle = \sum K_b \rho_b / \sum \rho_b$. The ratio of the average forward and backward reaction rate constants satisfies the phenomenological detailed balance relation

$$\langle k_a \rangle n_a = \langle k_b \rangle n_b, \tag{2.11}$$

where $n_a = \sum \rho_a$ and $n_b = \sum \rho_b$ are, respectively, the equilibrium populations of the bright state and of the dark state. Consequently, phenomenological chemical kinetics is simply an inhomogeneous average of the microscopic reaction rate constants and therefore does not contain any information about dynamic disorder.

It should be pointed out that relaxation experiments in the bulk state measure the total rate constant $\langle k \rangle = \langle k_a \rangle + \langle k_b \rangle$, and the forward and backward rate constants are obtained through the detailed balance condition in Eq. (2.11). In contrast, single molecule experiments separate the forward and backward half-reactions, and uniquely determine the two rate constants. Furthermore, in the context of single molecules, the detailed balance relation in Eq (2.11) is self-evident as long-time averaging along single molecule trajectories leads to the equilibrium population, which according to Eq. (2.9) defines the average rate constant.

High order moments of the on-time distribution function can also be calculated from $\langle t^n \rangle = \int_0^\infty f(t) t^n dt$. Generally, higher order moments do not satisfy $\langle t^n \rangle \neq \langle t \rangle^n$ and the decay process is not a Poisson process. Though ensemble-averaged experiments can also measure the waiting-time distribution and high-order moments, such measurements may suffer from spatial disorder and require special initial preparation in order to apply the fluctuation-dissipation theorem (see the next subsection). Even if the waiting-time distribution can be obtained, interpreting memory effects and extracting the modulation rate constant can be difficult. Therefore, single molecule measurements are more reliable and robust, and the information about dynamic disorder can be inferred from the statistics and correlation of half-reaction events.

2.2.3 Fluctuation-dissipation relation

A central result of the fluctuation-dissipation theorem is Onsager's regression hypothesis, which relates the relaxation of macroscopic non-equilibrium disturbances to the correlation of spontaneous microscopic fluctuations in an equilibrium system.[59] Application of this theorem to chemical kinetics leads to

$$\frac{\Delta c_a(t)}{\Delta c_a(0)} = \frac{C(t)}{C(0)} = \frac{G_{aa}(t) - n_a}{1 - n_a} \tag{2.12}$$

where $\Delta c_a(t) = c_a(t) - c_a(\infty)$ describes the concentration relaxation after a disturbance, measured in ensemble-averaged experiments, and $C(t) = \langle n_a(t)n_a(0) \rangle - n_a^2$ describes the occupation correlation function of the equilibrated reaction system, measured in single molecule experiments.

We now generalize Eq. (2.12) to multi-channel reactions. Consider the fluorescent correlation function measured along a single molecule trajectory, starting from an arbitrary initial time on the trajectory. The probability of starting from a bright state is n_a, and the initial on-time is then averaged over the on-time distribution function, giving

$$\langle n_a(t)n_a(0) \rangle = \frac{\int_0^\infty G_{aa}(t)G(t_0)F_a dt_0}{\int_0^\infty G(t_0)F_a dt_0} n_a = \sum G_{aa}(t)\rho_a, \tag{2.13}$$

where the propagation matrix $G_{aa}(t)$ is the diagonal component of the Green's function solution for the master equation in Eq. (2.3). It is shown in Ref. [27] that $G_{aa}(t)$ can be expanded in an infinite series of terms in the sequence of single molecule events

$$G_{aa}(t) = G_a(t) + \int_0^t \int_0^{t_1} G_a(t - t_1)K_b G_b(t_1 - t_2)K_b G_a(t_2)dt_1 dt_2 + \cdots, \tag{2.14}$$

where the first term represents staying in the bright state without reaction, the second term represents one sojourn to the dark state, and so on. To measure the macroscopic relaxation, the concentration disturbance $c_a(0)$ in the bright state is introduced ac-

cording to the equilibrium conformational distribution, i.e.,

$$\rho_{a,i}(0) = \frac{\rho_{a,i}}{\sum \rho_{a,i}} c_a(0). \tag{2.15}$$

Then, the concentration relaxation follows

$$\Delta c_a(t) = \frac{\sum G_{aa}(t)\rho_{a,t}}{n_a} c_a(0) - n_a c_a(0), \tag{2.16}$$

where $c_a(\infty) = n_a c(0)$ is the equilibrium concentration of the bright state. Comparing Eq. (2.13) and Eq. (2.16), we have

$$\frac{\Delta c_a(t)}{\Delta c_a(0)} = \frac{C(t)}{C(0)} = \frac{\sum G_{aa}(t)\rho_a - n_a^2}{n_a - n_a^2}, \tag{2.17}$$

which is the multi-channel version of Eq. (2.12). Therefore, the fluctuation-dissipation relation is obeyed under the condition that the initial population disturbance is distributed according to the equilibrium ratio of conformational channels. However, in the relevant scenario discussed in Sec. 2.1, the conformational modulation rate is slower than or comparable to the reaction rate. Then, the initially prepared disturbance will not have enough time to relax in the conformational sub-states before the concentration starts to decay, thus violating the initial condition in Eq. (2.15) necessary for the fluctuation-dissipation relation in Eq. (2.17). Consequently, the initial preparation of relaxation experiments in the bulk state must be taken into consideration in interpreting conformational distribution and dynamics.

Finally, we simplify Eq. (2.17) be noting that the asymptotic limit of $G_{aa}(t)$ is the equilibrium distribution ρ_a. Thus, the propagator $G_{aa}(t)$ can be decomposed as $G_{aa}(t) = \rho_a + G'_{aa}(t)$, which allows us to rewrite the fluorescence correlation function as

$$\frac{C(t)}{C(0)} = \frac{\sum G'_{aa}(t)\rho_a}{n_a n_b}, \tag{2.18}$$

where $G'_{aa}(t)$ is the time-dependent part of the Green's function.

2.2.4 Detailed balance conditions

The conservation of the population flux requires an overall balance relation between the bright state and the dark state, as explicitly given in Eq. (2.11). While this condition conserves the total flux, it does not exclude the possibility of a net current between different conformational channels. To exclude this possibility, the forward flux and backward flux must be equal,

$$K_a \rho_a = K_b \rho_b, \tag{2.19}$$

which is a more stringent balance relation than Eq. (2.11). It follows from Eqs. (2.4) and (2.5) that

$$\Gamma_a \rho_a = \Gamma_b \rho_b = 0, \tag{2.20}$$

which are the detailed balance conditions for the equilibrium conformational distributions in the dark state and the bright state, respectively. Furthermore, it is reasonable to assume that the conformational dynamics are the same for the bright state and for the dark state, i.e., $\Gamma_a = \Gamma_b$. Then, we have $\rho_a \propto \rho_b$ and

$$K_b \propto K_a, \tag{2.21}$$

which means that the ratio between the forward reaction rate constant and backward rate constant is the same for all the conformational channels. Without loss of generality, this chapter analyzes on-off events based on symmetric reactions with $K_a = K_b$. As shown in Fig. 3 of Ref. [27], the nature of the two-event distribution function does not change with the backward reaction; therefore, the echo from the on-off correlation for symmetric reactions is similar to the echo from the on-on correlation for asymmetric reactions.

2.3 Two-channel model

The two channel model, the simplest scheme of multi-channel reactions, has been used to analyze event-averaged quantities and to show that the two-event echo has a strong dependence on the conformational distribution and dynamics.[27] The following derivation generalizes the results in Sec. 3 of Ref. [27] in that the downward rate γ and the upward rate γ' are different. The master equation for the forward half-reaction is given in Eq. (2.1) with P_a, K_a and Γ defined as

$$P_a(t) = \begin{pmatrix} P_{a1}(t) \\ P_{a2}(t) \end{pmatrix}, \quad K_a = \begin{pmatrix} k_{a1} & 0 \\ 0 & k_{a2} \end{pmatrix}, \quad \Gamma = \Gamma_a = \Gamma_b = \begin{pmatrix} \gamma & -\gamma' \\ -\gamma & \gamma' \end{pmatrix}. \quad (2.22)$$

The Green's function is given by

$$
\begin{aligned}
G_a(t) &= e^{-(K_a+\Gamma)t} \\
&= \frac{1}{\Delta_a} \begin{pmatrix} \Delta_a F_a(t) + (k_{ad} + \gamma_d)E_a(t) & \gamma' E_a(t) \\ \gamma E_a(t) & \Delta_a F_a(t) - (k_{ad} + \gamma_d)E_a(t) \end{pmatrix}, (2.23)
\end{aligned}
$$

where $\Delta_a = \sqrt{\gamma_s^2 + k_{ad}^2 + 2k_{ad}\gamma_d}$, $k_{ad} = (k_{a2} - k_{a1})/2$, $k_{as} = (k_{a2} + k_{a1})/2$, $\gamma_s = (\gamma + \gamma')/2$, $\gamma_d = (\gamma' - \gamma)/2$, $z_{a\pm} = k_{as} + \gamma_s \pm \Delta_a$, $F_a(t) = (e^{-z_{a-}t} + e^{-z_{a+}t})/2$, and $E_a(t) = (e^{-z_{a-}t} - e^{-z_{a+}t})/2$. These expressions reduce to Eq. (14) in Ref. [27] when $\gamma = \gamma'$. The backward Green's function can be obtained in the same fashion. The master equation of the full reaction, given in Eq. (2.3), has a stationary solution

$$
\begin{pmatrix} \rho_{a1} \\ \rho_{a2} \\ \rho_{b1} \\ \rho_{b2} \end{pmatrix} = C \begin{pmatrix} \gamma'[\gamma k_{b2} + \gamma' k_{b1} + k_{b1}(k_{a2} + k_{b2})] \\ \gamma[\gamma k_{b2} + \gamma' k_{b1} + k_{b2}(k_{a1} + k_{b1})] \\ \gamma'[\gamma k_{a2} + \gamma' k_{a1} + k_{a1}(k_{a2} + k_{b2})] \\ \gamma[\gamma k_{a2} + \gamma' k_{a1} + k_{a2}(k_{a1} + k_{b1})] \end{pmatrix}, \quad (2.24)
$$

where $C^{-1} = (\gamma + \gamma')[\gamma(k_{a2} + k_{b2}) + \gamma'(k_{a1} + k_{b1}) + (k_{a1} + k_{b1})(k_{a2} + k_{b2})]$. The equilibrium flux from the bright state to the dark state is $F_b = \mathcal{N}K_a\rho_a$, and that from the dark state to the bright state is $F_a = \mathcal{N}K_b\rho_b$. The normalization factor is

47

$$\mathcal{N}^{-1} = \sum K_b \rho_b = \sum K_a \rho_a = \gamma^2 k_{a2} k_{b2} + \gamma'^2 k_{a1} k_{b1} + \gamma\gamma'(k_{a2} k_{b1} + k_{a1} k_{b2}) + \gamma(k_{a1} + k_{b1}) k_{a2} k_{b2} + \gamma'(k_{a2} + k_{b2}) k_{a1} k_{b1}.$$ Thus, the distribution function of on-time events is

$$f_a(t) = \sum K_a G_a(t) F_a = \frac{\langle K_a e^{-(K_a+\Gamma)t} K_b \rangle}{\langle K_b \rangle}, \tag{2.25}$$

where $\langle \cdots \rangle$ denotes an average over the equilibrium population distribution in the dark state. The distribution function of off-time events is defined in the same fashion. The joint distribution function of on-off events is defined as

$$f_{ab}(t_1, t_2) = \sum K_b G_b(t_2) K_a G_a(t_1) F_a = \frac{\langle K_b e^{-(K_b+\Gamma)t_2} K_a e^{-(K_a+\Gamma)t_1} K_b \rangle}{\langle K_b \rangle}, \tag{2.26}$$

which can be used to analyze memory effects. In particular, the difference function $\delta(t_1, t_2) = f_{ab}(t_1, t_2) - f_a(t_1) f_b(t_2)$ is given explicitly as,

$$\delta(t_1, t_2) = \delta(0) \frac{[\Delta_a F_a(t_1) - (k_{a,s} + \gamma_s) E_a(t_1)][\Delta_b F_b(t_2) - (k_{b,s} + \gamma_s) E_b(t_2)]}{\Delta_a \Delta_b}, \tag{2.27}$$

where the initial value $\delta(0)$ is a complicated function of the reaction rate constants and the inter-conversion rates.

For simplicity, we consider symmetric reactions with $K_a = K_b = K$. In this case, the forward and backward propagators become the same,

$$G(t) = e^{-(K+\Gamma)t} = \frac{1}{\Delta} \begin{pmatrix} \Delta F(t) + (k_d + \gamma_d) E(t) & \gamma' E(t) \\ \gamma E(t) & \Delta F(t) - (k_d + \gamma_d) E(t) \end{pmatrix}, \tag{2.28}$$

where $\Delta_a = \Delta_b = \Delta$, $E_a(t) = E_b(t) = E(t)$ and $F_a(t) = F_b(t) = F(t)$. The equilibrium populations are $\rho_{a1} = \rho_{b1} = \gamma'/[2(\gamma + \gamma')]$ and $\rho_{a2} = \rho_{b2} = \gamma/[2(\gamma + \gamma')]$, which depend only on the inter-conversion rates. The difference function $\delta(t_1, t_2)$ is simplified to

$$\delta(t_1, t_2) = \delta(0) \frac{[\Delta F(t_1) - (k_s + \gamma_s) E(t_1)][\Delta F(t_2) - (k_s + \gamma_s) E(t_2)]}{\Delta^2}, \tag{2.29}$$

48

where the initial value is

$$\delta(0) = \frac{k_d^2(k_s^2 - k_d^2)(\gamma_s^2 - \gamma_d^2)}{(k_d\gamma_d - k_s\gamma_s)^2} \tag{2.30}$$

with $k_d = (k_2 - k_1)/2$ and $k_s = (k_2 + k_1)/2$. The same-time difference function follows Eq. (2.29) as $\delta(t) = \delta(t, t)$. From $d\delta(t)/dt = 0$, the focal time of the same-time difference function is found as

$$t_f = \frac{1}{2\Delta} \ln \frac{z_+}{z_-} = \frac{1}{2\Delta} \ln \frac{k_s + \gamma_s + \Delta}{k_s + \gamma_s - \Delta}, \tag{2.31}$$

where the difference function is zero, $\delta(t_f) = 0$, and the echo time is found to be related to the focal time via

$$t_e = 2t_f, \tag{2.32}$$

where the amplitude of the echo is

$$\delta(t_e) = \delta(0)(\frac{\eta - 1}{\eta + 1})^{2\eta} \tag{2.33}$$

with $\eta = (k_s + \gamma_s)/\Delta$. From Eq. (2.29), we find a minimum along the t_1 axis or the t_2 axis at the echo time, respectively.

The same-time difference function $\delta(t)$ is a complicated function of reaction rate constants and conformational inter-conversion rates. To facilitate our analysis, we consider several special cases.

1. Fig. 2-2 is a two dimensional contour plot of the difference distribution function, $\delta(t_1, t_2)$, for $k_1 = 2$, $k_2 = 4$ and $\gamma = \gamma' = 0.5$. As predicted by Eq. (2.29), the contour clearly shows a minimum at $t_f = 0.287$ and a maximum at $t_e = 0.575$ along the diagonal axis, as well as a minimum at the focal time t_e along the t_1 and t_2 axis.

49
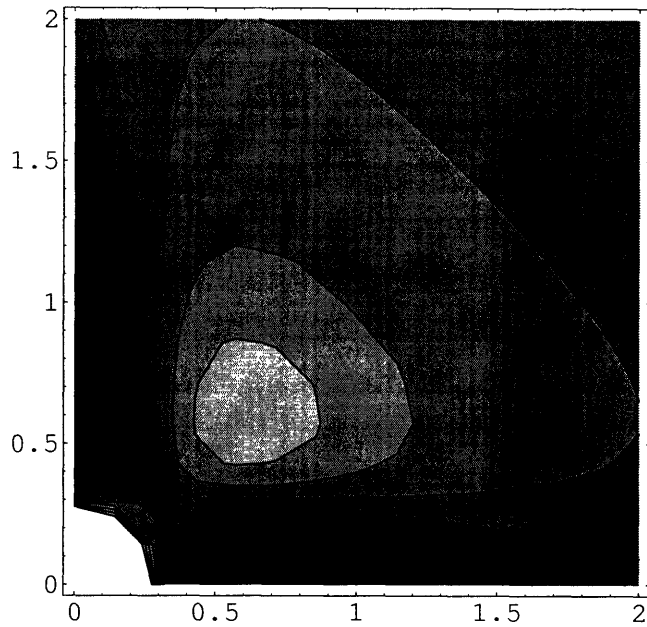
Figure 2-2: A two-dimensional contour plot of the difference function of two events $\delta(t_1, t_2) = f(t_1, t_2) - f(t_1)f(t_2)$ for the two-channel model with $k_1 = 2$, $k_2 = 4$, and $\gamma = \gamma' = 0.5$. At $t = t_e$, $\delta(t_1, t_2)$ reaches its maximum along the diagonal and its minimum along each time axis.

2. When the reactive time-scale is relatively fast, i.e., $k_d, \gamma \ll k_s$, we have

$$t_e = \frac{1}{\Delta} \ln\left[\frac{k_s + \gamma_s + \Delta}{k_s + \gamma_s - \Delta}\right] \approx \frac{2}{k_s + \gamma_s}, \tag{2.34}$$

where the approximate relation directly measures the average modulation rate for a given rate constant. In Table 2.1, for $k_s = 3.0$ and $k_d = 0.5$, the echo time predicted from Eq. (2.34), $t_{e,pred}$, is compared with the echo time measured from the same-time distribution function, $t_{e,meas}$. For a wide range of modulation rates, these two sets of echo times agree within an error less than 10%.

3. Eq. (2.33) gives the amplitude of the echo, which, under the condition of $k_d < \gamma < k_s$, can be shown to be proportional to the variance k_d^2, i.e.,

$$\delta(t_e) \propto k_d^2. \tag{2.35}$$

50

Table 2.1: The echo time in two-channel model.

γ	0	0.5	1.0	1.5	2.0	2.5
$t_{e,pred}$	0.667	0.571	0.500	0.444	0.400	0.364
$t_{e,meas}$	0.645	0.555	0.485	0.440	0.390	0.375
Error	3.4%	2.9%	3.1%	0.9%	2.6%	3.7%

$k_1 = 2.5$ and $k_2 = 3.5$. $t_{e,pred}$ is evaluated from $t_{e,pred} = 2/(\langle k \rangle + \gamma)$ and $t_{e,meas}$ is obtained from the numerical calculation of $\delta(t)$. $\gamma = \gamma'$ is the inter-conversion rate. The error is defined as $|t_{e,pred} - t_{e,meas}|/t_{e,meas} \times 100\%$.
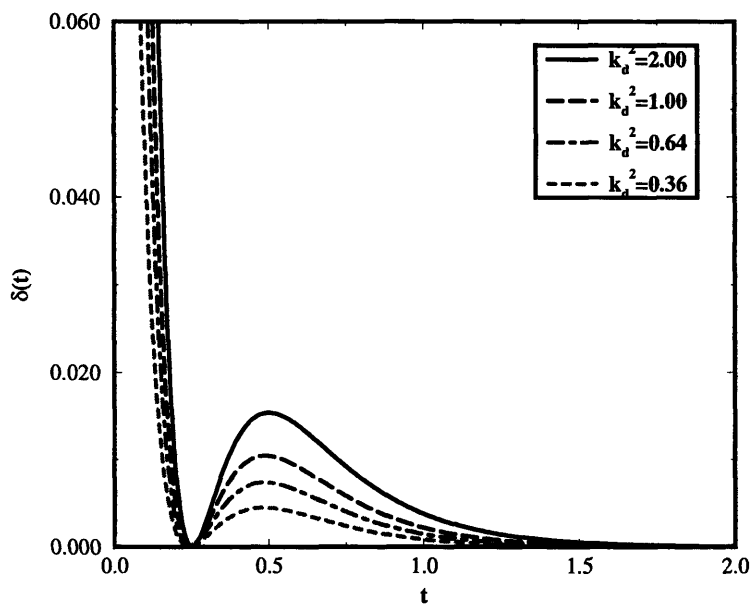
Figure 2-3: The same-time difference function in the two-channel model where $\gamma = \gamma' = 2.0$ and $k_s = 2.5$. The echo time predicted by $t_e = 2t_f \approx 2/(\langle k \rangle + \gamma)$ is confirmed with small error at large k_d where $k_d \ll k_s$ is not strictly followed. The amplitude of the echo approximately proportional to the variance in the rate constant.
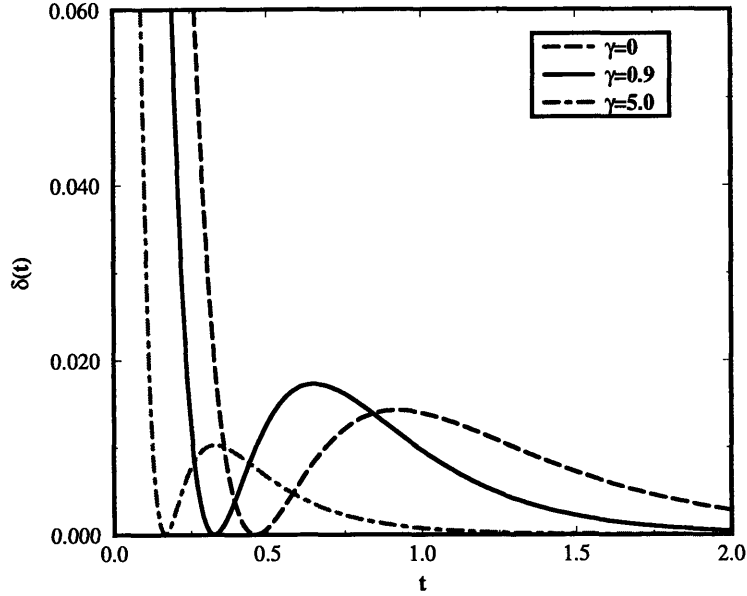
Figure 2-4: The same-time difference function in the two-channel model when $\gamma = \gamma'$, $k_1 = 1$, and $k_2 = 4$. The maximal echo is reached when $\gamma = k_d^2/k_s$. As predicted by $t_e = 2t_f \approx 2/(\langle k \rangle + \gamma)$, the echo time decreases as the modulation rate γ increases.

In Fig. 2-3, the same-time difference distribution function $\delta(t)$ is plotted for $k_s = 2.5$ and $\gamma = \gamma' = 2.0$. As seen from the plot, the echo amplitude increases proportionally with k_d^2, even for relatively large k_d^2. The plot also confirms that the focal time is half the echo time and both times are invariant to k_d^2.

4. In the case of equal inter-conversion rates, $\gamma' = \gamma$, Eq. (2.33) still applies with $\delta(0) = k_d^2(k_s^2 - k_d^2)/k_s^2$ and $\eta = (k_s + \gamma)/\sqrt{k_d^2 + \gamma^2}$. It can be shown that the amplitude of the echo $\delta(t_e)$ reaches its maximum at $\eta_{max} = \sqrt{k_s^2 + k_d^2}/k_d$ when

$$\gamma = \frac{k_d^2}{k_s} = \frac{\langle (\delta k)^2 \rangle}{\langle k \rangle}, \qquad (2.36)$$

which is the critical conformational inter-conversion rate for the maximal echo. Fig. 2-4 is a plot of the same-time difference distribution function for $k_1 = 1$, $k_2 = 4$, and several values of γ. The maximal echo occurs at $\gamma = 0.9$, which
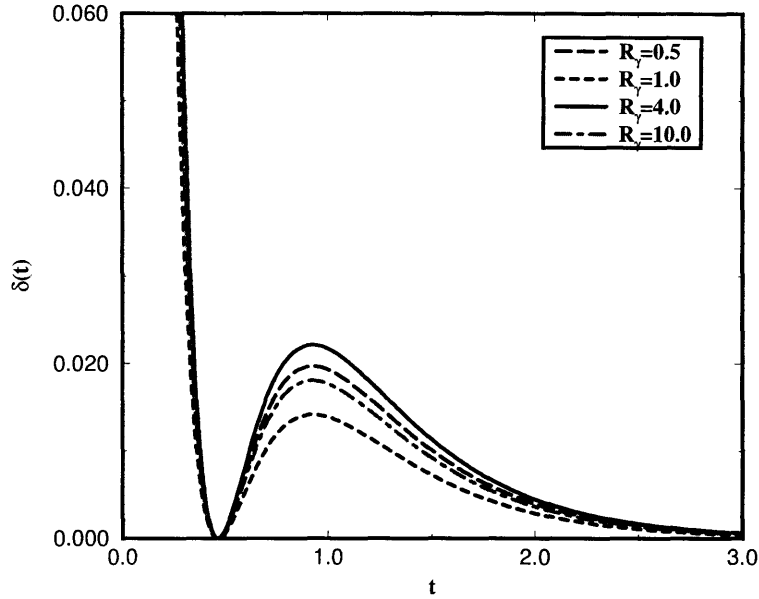
Figure 2-5: The conformational conversion rate dependence of the two-event echo in the two-channel model with $k_1 = 1$ and $k_2 = 4$. In this slow modulation limit, γ and γ' are the downward and upward inter-conversion rates, respectively, and $\gamma, \gamma' \ll k_{1,2}$. R_γ is the ratio of the two inter-conversion rates, $R_\gamma = \gamma'/\gamma$.

follows the critical condition in Eq. (2.36). It can also be noticed in Fig. 2-4 that the focal time and the echo time decrease as γ increases, as predicted by Eq. (2.34).

5. In the slow modulation limit, $\gamma, \gamma' \ll k_{1,2}$, which is a possible scenario for sluggish environments, Eq. (2.29) is simplified to

$$\delta(t_e) = \frac{(k_2 - k_1)^2}{4} \frac{R_k R_\gamma}{(R_k + R_\gamma)^2} \left(\frac{R_k - 1}{R_k + 1}\right)^{2R_k}, \tag{2.37}$$

where $R_k = k_2/k_1$ and $R_\gamma = \gamma'/\gamma$. With k_1 and k_2 fixed, the maximal echo occurs at

$$R_\gamma = R_k \quad or \quad \frac{k_2}{k_1} = \frac{\gamma'}{\gamma} = \frac{\rho_1}{\rho_2}, \tag{2.38}$$

53
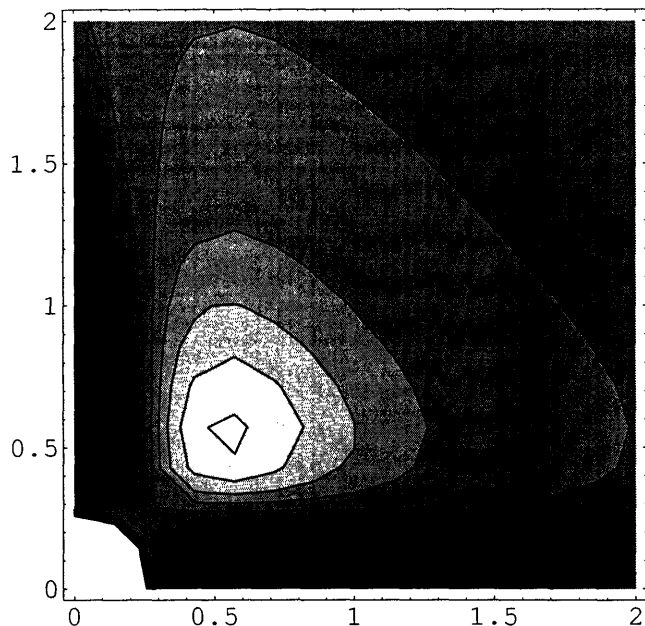
Figure 2-6: A two-dimensional contour plot of $\delta(t_1, t_2)$ for the three-channel model with $k_1 = 2.5$, $k_2 = 3$, $k_3 = 3.5$, $\gamma = \gamma' = 0.5$. It is clearly shown that $t_e = 2t_f \approx 2/(\langle k \rangle + \gamma)$ and that both $\delta(0, t)$ and $\delta(t, 0)$ reach their minima at $t = t_e$.

which implies a detailed balance relationship between the two channels, $k_1 \rho_1 = k_2 \rho_2$. As shown in Fig. 2-5, in the slow modulation limit, t_f and t_e are fixed at $\ln[k_2/k_1]/(k_2 - k_1)$ and $2\ln[k_2/k_1]/(k_2 - k_1)$, respectively. The maximal echo is achieved when the ratio in Eq. (2.38) is satisfied at $R_\gamma = 4$. It can be argued from this example that memory effects of conformational modulation can be measured by the variation of the reaction rate constants $\langle (\delta k)^2 \rangle$ and the variance of the flux $\langle (\delta k \rho)^2 \rangle$. To have the maximal echo, $\langle (\delta k)^2 \rangle$ should be maximized while $\langle (\delta k \rho)^2 \rangle$ should be minimized.

Table 2.2: The echo time in three-channel model.

γ	0	0.5	1.0	1.5	2.0	2.5
$t_{e,pred}$	0.667	0.571	0.500	0.444	0.400	0.364
$t_{e,meas}$	0.665	0.550	0.465	0.410	0.370	0.335
Error	0.3%	3.8%	7.5%	8.3%	8.1%	8.7%

k_1, k_2 and k_3 are 2.5, 3.0 and 3.5, respectively. $t_{e,pred}$ is evaluated from $t_{e,pred} = 2/(\langle k \rangle + \gamma)$ and $t_{e,meas}$ is obtained from the numerical calculation of $\delta(t)$. The error is defined as $|t_{e,pred} - t_{e,meas}|/t_{e,meas} \times 100\%$.
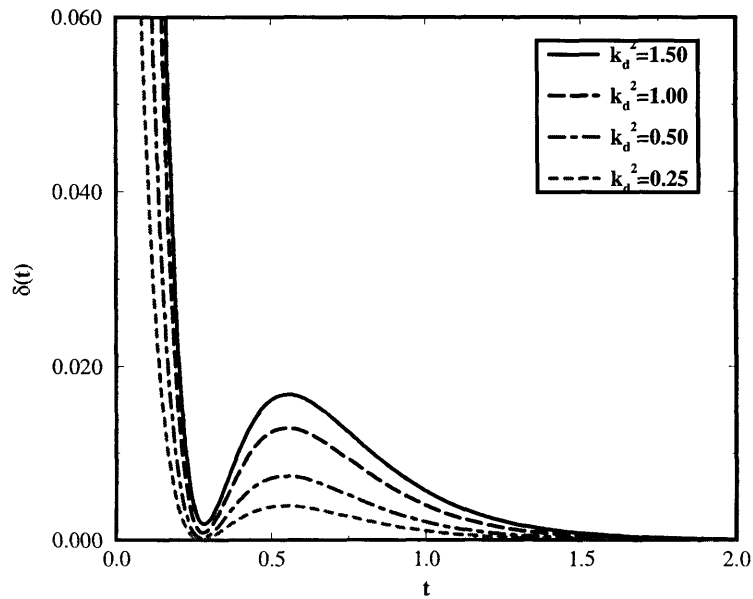
Figure 2-7: The same-time difference function $\delta(t)$ in the three-channel model with $\langle k \rangle = 3.0$ and $\gamma = 0.5$. It is clearly shown that the two-event echo increases as k_d^2 increases.

55
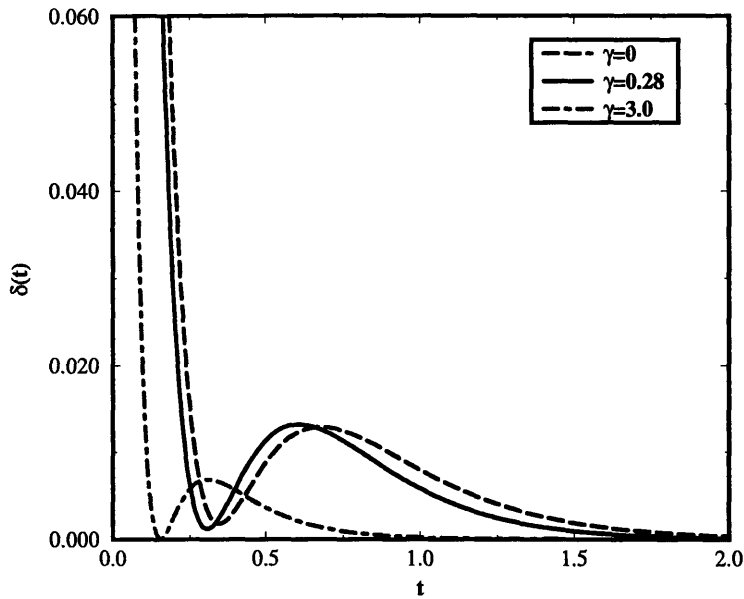
Figure 2-8: The same-time difference function $\delta(t)$ in the three-channel model with $\langle k \rangle = 3.0$ and $k_d^2 = 1.0$. It is clearly shown that the echo time decreases as γ increases. The maximum echo occurs at $\gamma \approx k_d^2/\langle k \rangle \approx 0.3$, as predicted in Eq. (2.36).

2.4 Three-Channel Model

To explore the generality of the recurrent behavior of the two-event distribution function, we study a cyclic three-channel model with

$$\Gamma = \begin{pmatrix} 2\gamma & -\gamma & -\gamma \\ -\gamma & 2\gamma & \gamma \\ -\gamma & -\gamma & 2\gamma \end{pmatrix}, \quad K_a = K_b = \begin{pmatrix} k_1 & 0 & 0 \\ 0 & k_2 & 0 \\ 0 & 0 & k_3 \end{pmatrix}. \quad (2.39)$$

Numerical calculations clearly demonstrate the basic features consistent with our observations in the two-channel model:

1. Fig. 2-6 is a contour of the difference function $\delta(t_1, t_2)$ calculated for the three-channel model with the modulation rate $\gamma = 0.5$, and the three reaction rates $k_1 = 2.5$, $k_2 = 3.0$ and $k_3 = 3.5$, respectively. As seen from the two dimensional

56

contour, the diagonal distribution has a minimum at the focal time t_f and a maximum at the echo time $t_e = 2t_f$, whereas both $\delta(t,0)$ and $\delta(0,t)$ have a minimum at the echo time t_e.

2. In Table 2.2, $t_{e,pred}$ calculated from $t_e \approx 2/(\langle k \rangle + \gamma)$ agrees well with $t_{e,meas}$ measured by numerical calculations, for the three-channel model with $k_1 = 2.5$, $k_2 = 3.0$ and $k_3 = 3.5$. The error is within 10% over a range of γ.

3. Fig. 2-7 shows the linear dependence of the amplitude of the two-event echo on $\langle (\delta k)^2 \rangle$ for the three-channel model described earlier. Again, the echo time and the focal time are invariant to $\langle (\delta k)^2 \rangle$ and follows the estimation $t_e = 2/(\langle k \rangle + \gamma)$.

4. Fig. 2-8 shows the same-time difference function for several values of γ. As predicted, the maximal echo occurs at $\gamma \approx k_d^2/\langle k \rangle$, and the focal time is half the echo time and decreases as γ increases.

We also calculated other three-channel and four-channel models with various parameters and geometries and found essentially the same behavior. Thus, we believe that these features are universal for discretized multiple channel models. In the next section, we will investigate the diffusion reaction model.

2.5 Diffusion model

The diffusion-modulated reaction was first introduced by Agmon and Hopfield to describe the ligand binding in myoglobin, and was analyzed by Zwanzig and elaborated by Wang and Wolynes[3, 29, 31, 60] Similar models have been applied for studying solvent-controlled electron transfer.[61, 62, 63, 64, 65] The diffusion reaction model describes a reactive system modulated by a diffusive coordinate, which represents collective environmental motions. The diffusion coordinate is described by the Smoluchowski operator

$$\hat{L}_D = \lambda \theta \frac{\partial}{\partial x} \left(\frac{\partial}{\partial x} + \frac{x}{\theta} \right), \tag{2.40}$$

where λ characterizes the relaxation time scale of the diffusive solvent, θ is the variance of the equilibrium distribution of the diffusion coordinate, and $\lambda\theta = D$ is the diffusion constant. The relaxation rate λ in the diffusion model is equivalent to the inter-conversion rate γ in the two-channel model. The reaction rate $k(x)$ is related to the diffusion coordinate x by $k(x) = \kappa x^2$, with κ the proportionality coefficient, so that the survival probability satisfies

$$\frac{\partial}{\partial t} P(x, t) = -k(x) P(x, t) + \hat{L}_D P(x, t). \qquad (2.41)$$

The corresponding Green's function is derived in Appendix 2-A, giving

$$G(x, y, t) = e^{-\frac{\lambda(s-1)t}{2}} \left[\frac{s}{2\pi\theta(1 - e^{-2\lambda st})} \right]^{\frac{1}{2}} \exp\left[-\frac{s(x - ye^{-\lambda st})^2}{2\theta(1 - e^{-2\lambda st})} + \frac{(s-1)(x^2 - y^2)}{4\theta} \right] \qquad (2.42)$$

where $s = \sqrt{1 + 4\kappa\theta/\lambda}$ represents the coupling of the two time scales associated with diffusion and rate processes. The equilibrium population obtained from $\hat{L}_D \rho_{eq}(x) = 0$ is a Gaussian function, $\rho_{eq}(x) = e^{-x^2/(2\theta)}/\sqrt{2\pi\theta}$; hence, we have $\langle k \rangle = \kappa\theta$ and $\langle (\delta k)^2 \rangle = 2\kappa^2\theta^2$.

To study the master equation for the full reaction, we consider the symmetric case, where the bright and dark states, labeled as a and b, respectively, have the same relative rate,

$$\begin{pmatrix} \dot{\rho}_a(x, t) \\ \dot{\rho}_b(x, t) \end{pmatrix} = \begin{pmatrix} -k(x) - \hat{L}_D & k(x) \\ k(x) & -k(x) - \hat{L}_D \end{pmatrix} \begin{pmatrix} \rho_a(x, t) \\ \rho_b(x, t) \end{pmatrix}. \qquad (2.43)$$

With the Green's function in Eq. (2.42), we obtain the distribution function of on-time events

$$f(t) = \frac{\langle \int_{-\infty}^{\infty} \int_{-\infty}^{\infty} dx dy k(x) G(x, y, t) k(y) \rangle}{\langle k(y) \rangle} = \frac{\sqrt{s}\kappa\theta[2s^2 + \varphi(t)^2]}{[\varphi(t/2)\psi(t/2)]^{5/2}} \exp[\frac{\lambda t}{2}], \qquad (2.44)$$

and the joint distribution function of on-off events

$$f(t,t) = \frac{\langle \int_{-\infty}^{\infty} \int_{-\infty}^{\infty} \int_{-\infty}^{\infty} dx\,dy\,dz\,k(x)G(x,y,t)k(y)G(y,z,t)k(z)\rangle}{\langle k(z)\rangle}$$

$$= \frac{\kappa^2\theta^2[(\varphi(2t)+2s)^2+6s^2]}{\sqrt{s}\varphi(t)^{3/2}\psi(t)^{7/2}}\exp[\lambda t], \qquad (2.45)$$

where $\varphi(t) = [(s+1)e^{\lambda st} + (s-1)e^{-\lambda st}]/2$ and $\psi(t) = [(s+1)e^{\lambda st} - (s-1)e^{-\lambda st}]/2$. The same-time difference function $\delta(t) = f(t,t) - f(t)^2$ is given by

$$\delta(t) = \kappa^2\theta^2\left[\frac{(\varphi(2t)+2s)^2+6s^2}{\sqrt{s}\varphi(t)^{3/2}\psi(t)^{7/2}} - \frac{s(\varphi(t)^2+2s^2)^2}{\varphi(t/2)^5\psi(t/2)^5}\right]\exp[\lambda t], \qquad (2.46)$$

with the initial value $\delta(0) = 6\kappa^2\theta^2$.

These single molecule quantities are complicated functions of $\kappa\theta/\lambda$. We examine their behavior in several limiting cases.

1. In the fast modulation limit, $\lambda \to \infty$, the distribution functions become

$$f(t) \longrightarrow \kappa\theta\exp[-\kappa\theta t], \qquad (2.47)$$

$$f(t,t) \longrightarrow \kappa^2\theta^2\exp[-2\kappa\theta t], \qquad (2.48)$$

$$\delta(t) \approx 0, \qquad (2.49)$$

thus resulting in single exponential kinetics with an effective rate constant $k_{eff} = \kappa\theta$.

2. In the slow modulation limit, $\lambda \to 0$, the Green's function simplifies to

$$G(x,y,t) = \delta(x-y)\exp[-\kappa x^2 t]. \qquad (2.50)$$

Then, the event averaged distribution functions decay by power law,

$$f(t) \longrightarrow \frac{3\kappa\theta}{(1 + 2\kappa\theta t)^{5/2}}, \tag{2.51}$$

$$f(t, t) \longrightarrow \frac{15\kappa^2\theta^2}{(1 + 4\kappa\theta t)^{7/2}}, \tag{2.52}$$

$$\delta(t) \approx 15\kappa^2\theta^2/(1 + 4\kappa\theta t)^{7/2} - 9\kappa^2\theta^2/(1 + 2\kappa\theta t)^5, \tag{2.53}$$

which are a result of inhomogeneous averaging of the rate distribution. Because the flux $k(x)\rho_{eq}(x)$ is distributed around $x = 0$, the diffusion model in the slow modulation limit effectively reduces to a single channel, and therefore no echo is observed in this limit. However, if a sufficiently large bias is introduced into the rate constant, $k(x) = \kappa(x - x_b)^2$, the diffusion model maps to a two-channel model and the echo can be observed in the inhomogeneous limit.

3. In the long time regime, $f(t)$ and $f(t, t)$, both decay exponentially as

$$f(t) \longrightarrow \frac{8\sqrt{s}\kappa\theta}{(s + 1)^3} \exp[-\frac{\lambda}{2}(s - 1)t], \tag{2.54}$$

$$f(t, t) \longrightarrow \frac{8\kappa^2\theta^2}{\sqrt{s}(s + 1)^3} \exp[-\lambda(s - 1)t], \tag{2.55}$$

$$\delta(t) \propto \exp[-\lambda(s - 1)t], \tag{2.56}$$

with the effective rate constant $k_{eff} = \lambda(s - 1)/2$.

4. In the short time regime, we expand the distribution functions to first order in t,

$$f(t) \longrightarrow 3\kappa\theta(1 - \frac{4}{3}\lambda t - 5\kappa\theta t + O[t^2]), \tag{2.57}$$

$$f(t, t) \longrightarrow 15\kappa^2\theta^2(1 - \frac{16}{5}\lambda t - 14\kappa\theta t + O[t^2]), \tag{2.58}$$

$$\delta(t) \approx 6\kappa^2\theta^2(1 - \frac{20}{3}\lambda t - 30\kappa\theta t + O[t^2]), \tag{2.59}$$

which predict the initial decay due to the reaction and diffusion processes.

To facilitate calculations, we use $1/\kappa\theta$ as the unit time and normalize function

Table 2.3: The echo time in the diffusion model.

λ	2.0	2.5	3.0	3.5	4.0
$t_{e,pred}$	0.667	0.571	0.500	0.444	0.400
$t_{e,meas}$	0.615	0.560	0.520	0.485	0.455
Error	8.5%	2.0%	3.8%	8.5%	12%

$\kappa\theta = 1.0$. $t_{e,pred}$ is calculated by $t_{e,pred} = 2/(\langle k \rangle + \lambda)$ and $t_{e,meas}$ is obtained from numerical calculation of $\tilde{\delta}(\tilde{t})$ in Eq. (2.60). The error is defined as $|t_{e,pred} - t_{e,meas}|/t_{e,meas} \times 100\%$.
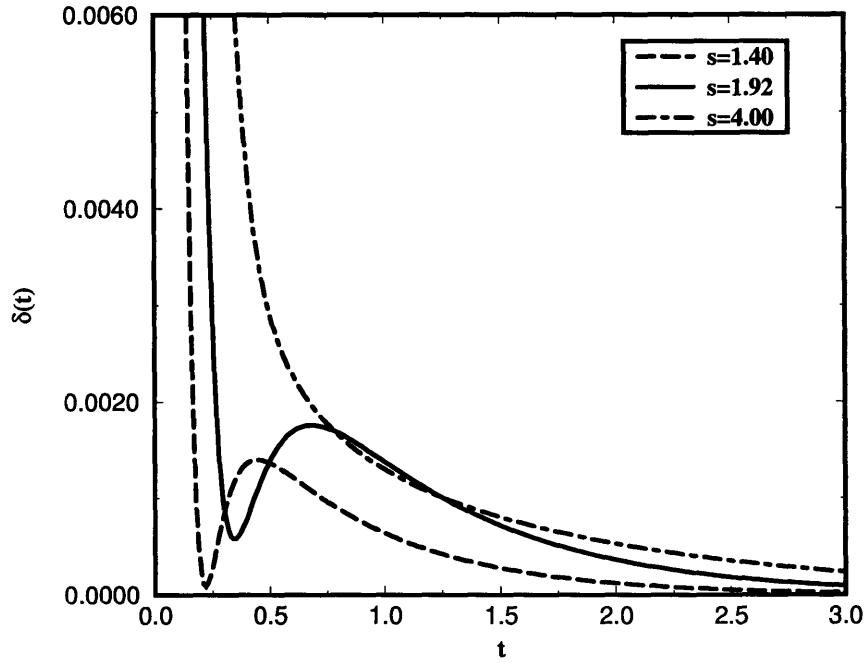
Figure 2-9: The s dependence of the same-time difference function $\delta(t)$ in the continuous diffusion model. $s = \sqrt{1 + 4\kappa\theta/\lambda}$, reflects the competition between the time scales of the diffusion and the rate process. $\delta(t)$ is normalized by $\delta(0)$ and the time variable is scaled by $1/(\kappa\theta)$.

$\delta(t)$ by $\delta(0)$. Thus, the reduced same-time difference function reads

$$\tilde{\delta}(\tilde{t}) = \frac{\delta(t)}{\delta(0)} = \frac{e^{\frac{4\tilde{t}}{s^2-1}}}{6} \left[\frac{(\tilde{\varphi}(2\tilde{t}) + 2s)^2 + 6s^2}{\sqrt{s}\tilde{\varphi}(\tilde{t})^{3/2}\tilde{\psi}(\tilde{t})^{7/2}} - \frac{s(\tilde{\varphi}(\tilde{t})^2 + 2s^2)^2}{\tilde{\varphi}(\tilde{t}/2)^5\tilde{\psi}(\tilde{t}/2)^5} \right], \qquad (2.60)$$

where $\tilde{t} = t\kappa\theta$, $\tilde{\varphi}(\tilde{t}) = [(s + 1)e^{4s\tilde{t}/(s^2-1)} + (s - 1)e^{-4s\tilde{t}/(s^2-1)}]/2$ and $\tilde{\psi}(\tilde{t}) = [(s + 1)e^{4s\tilde{t}/(s^2-1)} - (s - 1)e^{-4s\tilde{t}/(s^2-1)}]/2$. As shown in Fig. 2-9, the same-time distribution function $\delta(t)$ has an echo in the region $1 < s < 2.81$ and reaches its maximum amplitude at $s = 1.92$. In the slow modulation limit, where s is large, $\tilde{\delta}(\tilde{t})$ reduces to power law decay and no recurrence is found. In the fast modulation limit, where s approaches 1, reaction kinetic becomes single exponential and $\tilde{\delta}(\tilde{t})$ vanishes. It can also be observed in Fig. 2-9 that the relation between the focal time and the echo time, $t_e = 2t_f$, remains valid, and that the maximal echo occurs at $\lambda \approx \langle(\delta k)^2\rangle/\langle k\rangle$ as predicted by Eq. (2.36). The echo time, listed in Table 2.3, confirms the prediction of $t_e = 2/(\langle k\rangle + \gamma)$. The two-dimensional contour $\delta(t_1, t_2)$ (not included here) shows the same features as for the multiple channel model. Thus, the conformational fluctuation rate in the diffusion model has a strong influence on the two-event echo signal in the same-time difference function. However, because of its single channel nature in the inhomogeneous limit, the diffusion model predicts weaker echo signals than the multiple channel model.

2.6 Stochastic Rate Model

The analysis of on-off sequences is usually based on specific kinetic schemes and assumed functional forms. Different versions of the discretized multiple channel model include the two-channel two-state scheme, two-channel three-state scheme, and three-channel two-state scheme. In the continuous limit, a diffusion coordinate is introduced to modulate the rate constant: the exponential dependence was used to describe diffusion-controlled ligand-binding and more recently enzymatic reactions,[28] the localized population sink was used for solvent-controlled electron transfer, the quadratic dependence was used to describe stochastic gating.[31] To analyze and

compare single molecule quantities predicted by various reaction schemes in a unified framework, we adopt a general approach based on the stochastic rate model and the cumulant expansion.[66, 67] In this model, environmental fluctuations introduce time-dependence in the rate constant, which is treated as a stochastic variable. Each realization of the time-dependent rate constant defines a rate process, and single molecular measurements can be obtained after taking the stochastic average of rate fluctuations. This approach is inspired by Kubo's stochastic line-shape theory as the rate constant in the rate model and the frequency in the Kubo's model are both treated as stochastic variable.[55] In principle, the stochastic properties of the rate are completely described by all the multiple time cumulants. In practice, we truncate the cumulant expansion to second order in time variables, thus yielding a *Gaussian stochastic rate model*. The analysis of single molecule quantities in the Gaussian approximation is similar to the study of spectral diffusion at cryogenic temperatures by Silbey and Skinner.[68, 69] Then, various reaction schemes can be mapped to the Gaussian stochastic rate model characterized by average rate constants and rate correlation functions, and all single molecule quantities can be evaluated accordingly.

2.6.1 Cumulant expansion of the stochastic rate model

The rate constant, modulated by slow environmental fluctuations, can be treated as a stochastic variable. For the forward half-reaction,

$$on \xrightarrow{k(\tau)} off, \tag{2.61}$$
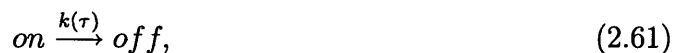
the survival probability distribution function is given by

$$P(t) = \langle e^{-\int_0^t k(\tau)d\tau} \rangle, \tag{2.62}$$

where $k(\tau)$ is the stochastic rate variable. Cumulant expansion of Eq. (2.62) leads to

$$P(t) = \exp[\sum_{n=1}^{\infty} \frac{(-1)^n}{n!} \int_0^t d\tau_1 \cdots \int_0^t d\tau_n \chi_n(\tau_1, \ldots, \tau_n)], \tag{2.63}$$

where $\chi_n(\tau_1, \ldots, \tau_n)$ is the n-th order correlation function defined as

$$
\begin{aligned}
\chi_1(t) &= \langle k(t) \rangle, \\
\chi_2(t_1, t_2) &= \langle k(t_1)k(t_2) \rangle - \langle k(t_1) \rangle \langle k(t_2) \rangle, \\
\chi_3(t_1, t_2, t_3) &= \langle k(t_1)k(t_2)k(t_3) \rangle - \langle k(t_1) \rangle \langle k(t_2)k(t_3) \rangle - \langle k(t_2) \rangle \langle k(t_1)k(t_3) \rangle \\
&\quad - \langle k(t_3) \rangle \langle k(t_1)k(t_2) \rangle + 2\langle k(t_1) \rangle \langle k(t_2) \rangle \langle k(t_3) \rangle, \\
&\cdots
\end{aligned}
\tag{2.64}
$$

These cumulant functions contain all the information necessary to describe the dynamics of modulated rate processes; thus, all the single molecule quantities can be expressed in cumulants with different weights. Some examples are given in Appendices 2-B and 2-C.

For a stationary Gaussian process, $\chi_k(t_1, \ldots, t_k) \overset{k \geq 2}{=} 0$ and $\chi_2(t_1, t_2) = \chi(t_1 - t_2)$, the survival probability is simplified to

$$
P(t) = \exp[-\langle k \rangle t + M(t)],
\tag{2.65}
$$

where $M(t) = \int_0^t (t-\tau)\chi(\tau)d\tau$ is the second order cumulant. The distribution function of single on-time events is related to the survival probability by

$$
\mathcal{F}(t) = -\frac{dP(t)}{dt},
\tag{2.66}
$$

which, for the stationary Gaussian case, becomes

$$
\mathcal{F}(t) = \left(\langle k \rangle - \int_0^t \chi(\tau)d\tau \right) \exp[-\langle k \rangle t + M(t)].
\tag{2.67}
$$

Since the single-event distribution function is always finite, $\langle k \rangle \geq \int_0^t (1 - \tau/t)\chi(\tau)d\tau$ has to be satisfied at any time t. Especially, when t approaches infinity, $\langle k \rangle \geq \int_0^\infty \chi(\tau)d\tau$, i.e., there exists a finite time scale for conformational fluctuations. Given the finite time scale for conformational fluctuations, τ_c, the condition for the second order cumulant expansion can be established as $\langle k \rangle \geq \chi(0)\tau_c$, implying a small

variance of reaction rates and a short correlation time for conformational fluctuations.

The stochastic rate model is flexible in describing single molecule measurements. With a proper choice of $\chi(t)$, the model can reproduce power-law and other non-exponential time-dependence. The second cumulant expansion of the model, however, is only accurate for describing Gaussian processes. The deviation of real measurements from the second cumulant expansion is an indication of the non-Gaussian behavior.

2.6.2 Two-event echos in the Gaussian approximation

To simplify our calculations, we consider symmetric reactions with $k_f(t) = k_b(t) = k(t)$. In this case, the single-event and two-event distribution functions can be expressed as,

$$f(t) = \frac{\langle k(t)e^{-\int_0^t k(\tau)d\tau}k(0)\rangle}{\langle k\rangle}, \tag{2.68}$$

$$f(t_1, t_2) = \frac{\langle k(t_1 + t_2)e^{-\int_{t_1}^{t_1+t_2} k(\tau)d\tau}k(t_1)e^{-\int_0^{t_1} k(\tau)d\tau}k(0)\rangle}{\langle k\rangle}. \tag{2.69}$$

For further simplification, we truncate the cumulant expansion to second order, giving

$$f(t) = \frac{[\langle k\rangle - L(t)]^2 + \chi(t)}{\langle k\rangle}\exp[-\langle k\rangle t + M(t)], \tag{2.70}$$

$$\begin{aligned}
f(t_1, t_2) = {} & \{\langle k\rangle^2 - \langle k\rangle[2L(t_1 + t_2) + L(t_1) + L(t_2)] \\
& + \chi(t_1) + \chi(t_2) + \chi(t_1 + t_2) + 2L(t_1 + t_2)[L(t_1) + I(t_2)] + L(t_1 + L_2)^2 \\
& - \frac{1}{\langle k\rangle}[\chi(t_1)L(t_1 + t_2) + \chi(t_2)L(t_1 + t_2) + \chi(t_1 + t_2)L(t_1) \\
& + \chi(t_1 + t_2)L(t_2) + L(t_1 + t_2)L(t_1) + L(t_1 + t_2)L(t_2)]\} \\
& \exp[-\langle k\rangle(t_1 + t_2) + M(t_1 + t_2)], \tag{2.71}
\end{aligned}$$

where $L(t) = \dot{M}(t) = \int_0^t \chi(\tau)d\tau$. The detailed derivation of Eqs. (2.70) and (2.71) can be found in Appendix 2-B. Other related single molecule quantities are defined in Appendix 2-C.
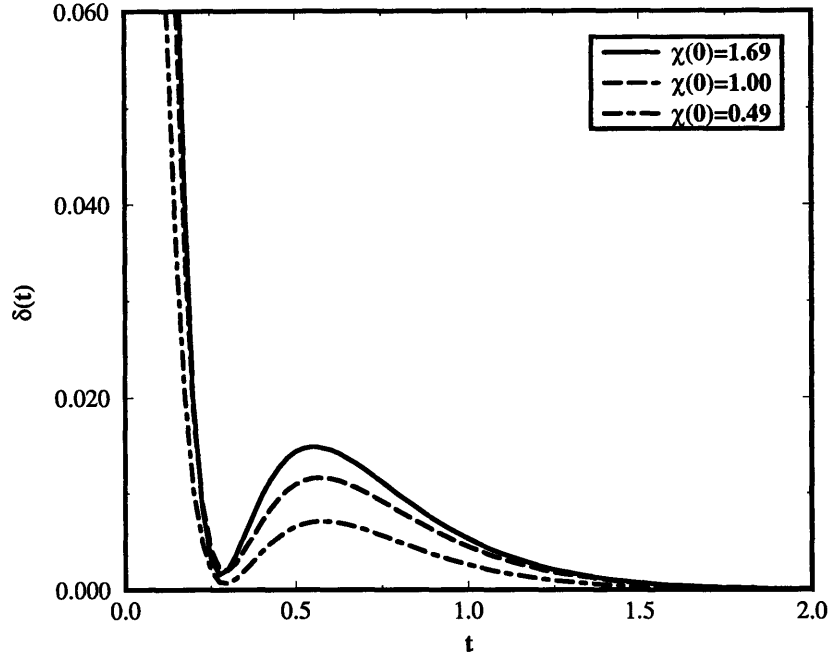
Figure 2-10: The two-event echo in the stochastic rate model with $\langle k \rangle = 3.0$, $\gamma = 0.5$, and $\chi(t) = \chi(0)e^{-2\gamma t}$. The echo time $t_e \approx 2/(\langle k \rangle + \gamma)$ is approximately fixed when varying $\chi(0)$, and the echo increases with $\chi(0)$.

In the short time limit, when $L(t) \ll \chi(t)/\langle k \rangle$, we have

$$\frac{f(t_1, t_2) - f(t_1)f(t_2)}{f(t_1)f(t_2)} \approx \frac{\chi(t_1 + t_2) - \frac{\chi(t_1)\chi(t_2)}{\langle k \rangle^2}}{(\langle k \rangle + \frac{\chi(t_1)}{\langle k \rangle})(\langle k \rangle + \frac{\chi(t_2)}{\langle k \rangle})} \overset{t \to 0}{\approx} \frac{\chi(t_1 + t_2)}{\langle k \rangle^2}, \qquad (2.72)$$

which indicates that $\chi(t)$ is a direct measure of memory effects in the initial decay regime.

The focal time and the echo time in the same-time difference function can be derived from the Taylor expansion of Eqs. (2.70) and (2.71). We assume the exponential decay form of $\chi(t) = \chi(0)e^{-2\gamma t}$ for simplicity, and the small variance condition of $\chi(0) \ll \langle k \rangle^2$ i.e., $k_d \ll k_s$, so that $L(t) = \chi(0)(1 - e^{-2\gamma t})/(2\gamma)$, $M(t) = \chi(0)(e^{-2\gamma t} - 1 + 2\gamma t)/(4\gamma^2)$. Then, to first order in the small parameter $\chi(0)/\langle k \rangle^2$,

66
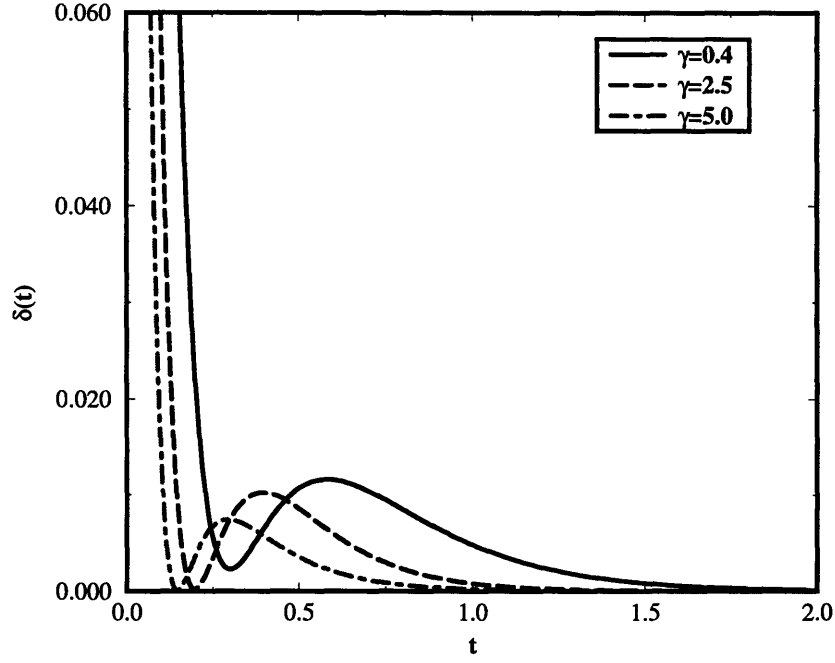
Figure 2-11: The two-event echo in the stochastic rate model with $\langle k \rangle = 3.0$, $\chi(0) = 1.0$, and $\chi(t) = \chi(0)e^{-2\gamma t}$. The echo time $t_e \approx 2/(\langle k \rangle + \gamma)$ decrease as γ increases. The maximum amplitude of the echo is flat within an interval of γ. The position of the maximal echo is approximately the medium of this interval, $\gamma \approx 0.4$.

we have

$$f(t) \approx \langle k \rangle e^{-\langle k \rangle t} \left\{ 1 + \frac{\chi(0)}{\langle k \rangle^2}[e^{-2\gamma t} - \frac{\langle k \rangle}{\gamma}(1 - e^{-2\gamma t}) + \frac{\langle k \rangle^2}{4\gamma^2}(e^{-2\gamma t} + 2\gamma t - 1)] \right\}, \quad (2.73)$$

$$f(t,t) \approx \langle k \rangle^2 \{ 1 - \frac{\chi(0)}{\langle k \rangle^2}[e^{-4\gamma t} + 2e^{-2\gamma t} + \frac{\langle k \rangle}{\gamma}(e^{-4\gamma t} + e^{-2\gamma t} - 2)$$

$$+ \frac{\langle k \rangle^2}{4\gamma^2}(e^{-4\gamma t} + 4\gamma t - 1)] \} \exp(-2\langle k \rangle t), \quad (2.74)$$

and the same-time difference function

$$\delta(t) \approx \chi(0)(\frac{\langle k \rangle + 2\gamma - \langle k \rangle e^{2\gamma t}}{2\gamma})^2 \exp(-2\langle k \rangle t). \quad (2.75)$$

The minimum of $\delta(t)$ can be found at

67

Table 2.4: The echo time in the stochastic rate model.

γ	0	0.5	1.0	1.5	2.0	2.5
$t_{e,pred}$	0.667	0.571	0.500	0.444	0.400	0.364
$t_{e,meas}$	0.665	0.575	0.515	0.465	0.425	0.395
Error	0.3%	0.7%	2.9%	4.5%	5.9%	7.8%

$\langle k \rangle = 3.0$ and $\chi(0) = 0.25$. $t_{e,pred}$ is calculated with $t_{e,pred} = 2/(\langle k \rangle + \gamma)$ and $t_{e,meas}$ is obtained from numerical calculation of the stochastic rate model with $\chi(t) = \chi(0)e^{-2\gamma t}$. The error is defined as $|t_{e,pred} - t_{e,meas}|/t_{e,meas} \times 100\%$.

$$t_f = \frac{1}{2\gamma} \ln[\frac{\langle k \rangle + 2\gamma}{\langle k \rangle}] \approx \frac{1}{\langle k \rangle + \gamma}, \qquad (2.76)$$

and the maximum at

$$t_e = \frac{1}{\gamma} \ln[\frac{\langle k \rangle + 2\gamma}{\langle k \rangle}] \approx \frac{2}{\langle k \rangle + \gamma}. \qquad (2.77)$$

The amplitude of the echo proportional to the variance of the rate constant, $\delta(t_e) \propto \chi(0)$. Thus, we obtain the same expressions for t_e and t_f as derived for the two-channel model in Sec. 2.3. In Table 2.4, the echo time predicted from Eq. (2.71), $t_{e,pred}$, is compared with the echo time calculated from the same-time distribution function, $t_{e,meas}$. Good agreement is found over a wide range of modulation rates γ between these two sets of echo times.

In Fig. 2-10, the same-time difference function $\delta(t)$ calculated from Eqs. (2.70) and (2.71) is plotted for $k_s = \langle k \rangle = 3.0$ and $\gamma = 0.5$. For several values of $\chi(0) = k_d^2 = \langle \delta k^2 \rangle$, the focal time and the echo time remain constant, but the amplitude of the echo increases proportionally with $\chi(0)$. In Fig. 2-11, the echo time is shown to be twice the focal time and decreases with the modulation rate γ according $t_e = 2t_f = 2/(\langle k \rangle + \gamma)$. The maximal echo is found around $\gamma = \chi(0)/\langle k \rangle$. These features are consistent with our observations in the multiple channel kinetic model.
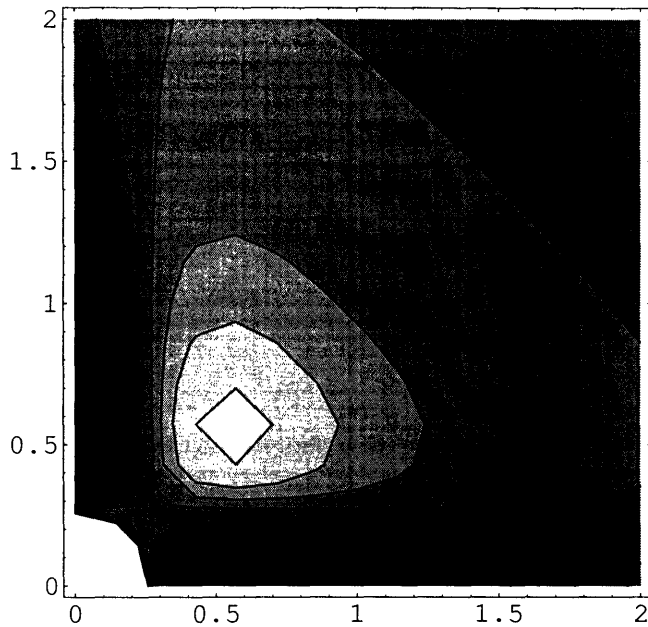
Figure 2-12: A two-dimensional contour plot of the difference function of two events $\delta(t_1, t_2) = f(t_1, t_2) - f(t_1)f(t_2)$ in the stochastic rate model with $k_1 = 2$, $k_2 = 4$ and $\gamma = \gamma_1 = \gamma_2 = 0.5$. $f(t)$ and $f(t_1, t_2)$ are calculated by Eq. (2.70) and (2.71), respectively, with $\chi(t)$ in Eq. (2.78) obtained from matching the survival probability.

2.6.3 Mapping to the Gaussian stochastic rate model

We now map the discrete two-channel model to the Gaussian stochastic rate model. For simplicity, we consider a two-channel model with symmetric half-reactions, $K_a = K_b$, and with equal conformational states, $\gamma = \gamma'$. In this model, the survival probability function is $P(t) = [(\Delta + \gamma)e^{-Z_- t} + (\Delta - \gamma)e^{-Z_+ t}]/(2\Delta).[27]$ Matching the survival probability function with Eq. (2.65), we have, in the second cumulant approximation scheme, $\langle k \rangle = k_s$ and

$$\chi(t) = \frac{\Delta^2 k_d^2}{[\gamma \sinh(\Delta t) + \Delta \cosh(\Delta t)]^2}, \tag{2.78}$$

which gives the variance $\chi(0) = k_d^2$ and the long-time correlation Fig. 2-12 is a two-dimensional plot of $\delta(t_1, t_2)$ for the stochastic Gaussian model corresponding to a two channel model with $k_1 = 2$, $k_2 = 4$, and $\gamma = 0.5$. In comparison with Fig. 2-13,
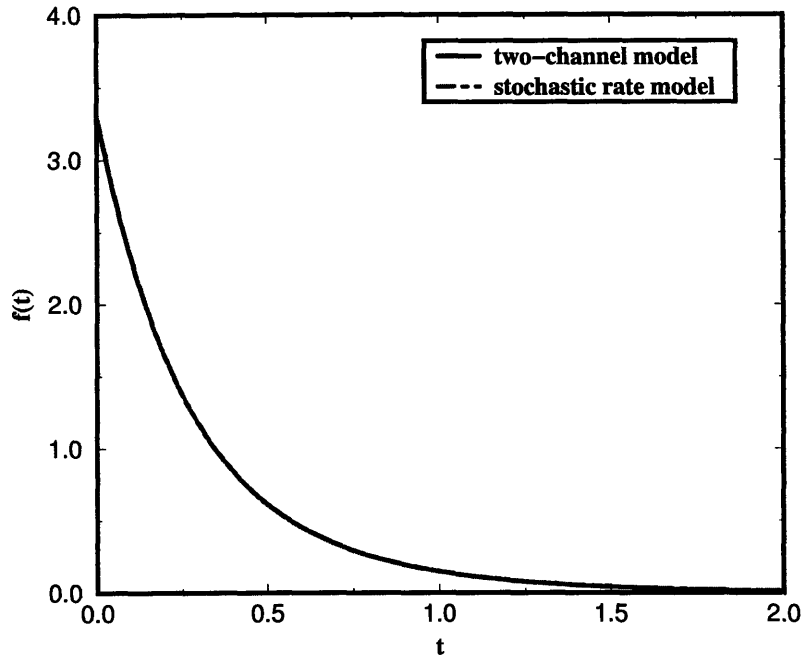
Figure 2-13: Comparison of the single-event distribution functions in the two-channel model and in the corresponding stochastic rate model with $k_1 = 2$, $k_2 = 4$ and $\gamma = 0.5$. The single-event distribution function $f(t)$ in stochastic rate model is calculated by Eq. (2.70) with $\chi(t)$ given in Eq. (2.78).

the stochastic Gaussian model reproduces all the essential features of the difference function for the corresponding two channel model. $\chi(t) \propto \exp(-2\Delta t)$. To be quantitative, the distribution functions of single events in Fig. 2-13 agree very well by matching the survival probability. The same-time distribution functions calculated from the two models are compared in Fig. 2-14, where the stochastic rate model is shown to give reasonable approximations to the position of the echo, the amplitude of the echo, and the shape of the same time difference function. The slight deviations are believed to be the approximate nature of the second order cumulant expansion, i.e., non-Gaussian effects.
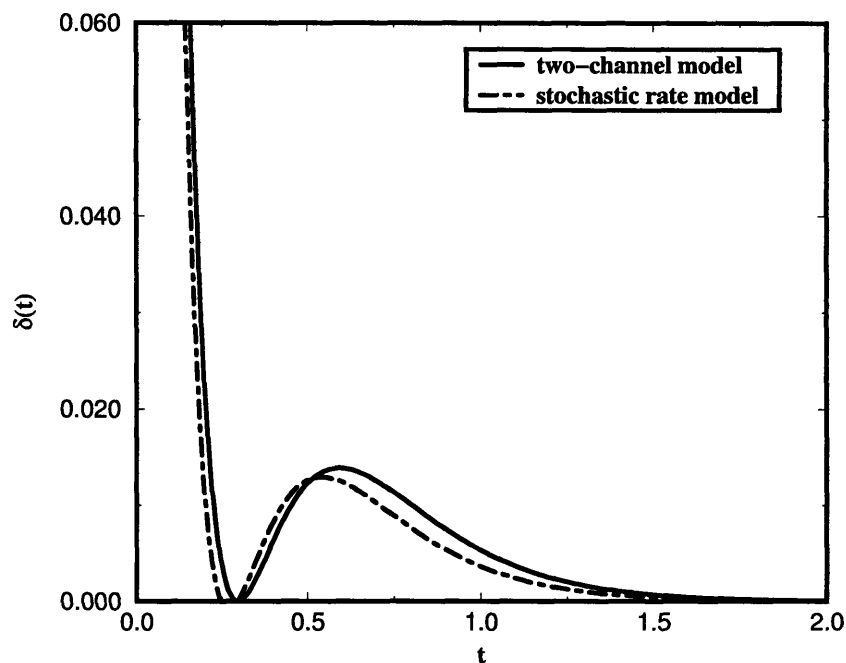
Figure 2-14: Comparison of the same-time difference function $\delta(t)$ in the two-channel model and in the corresponding stochastic rate model with $k_1 = 2$, $k_2 = 4$ and $\gamma = 0.5$. The stochastic rate model gives good approximations to the echo time, the echo height, and the shape of $\delta(t)$.

2.7 summary

The aim of this chapter is to establish quantitative relation between the two-event echo and conformational fluctuations. The primary findings of our analysis can be summarized as follows:

1. The N-channel kinetic scheme provides a generic model for understanding the influence of conformational fluctuations on reaction dynamics. Based on this model, ensemble-averaged measurements can be formulated as a long-time average along single molecule trajectories. As a result, phenomenological chemical kinetics is shown to be an inhomogeneous average of reaction rate constants and thus does not contain any information about dynamic disorder. It is also

shown that the fluctuation-dissipation relation is obeyed on the single molecule level only if the initial non-equilibrium disturbance is prepared according to conformational equilibrium. This condition imposes a difficult condition on the use of ensemble-averaged measurements to probe conformational fluctuations. In addition, a more stringent detailed balance condition can be established to exclude the possibility of microscopic current between different conformational channels.

2. Calculations of four different models (the two-channel kinetic model, the three-channel kinetic model, the diffusion reaction model, and the stochastic rate model) confirm the universal features of the two-event joint distribution function and its quantitative relationship to conformational dynamics. In the two-dimensional plane of $\delta(t_1, t_2)$, there is a local minimum at the focal time, t_f, and a local maximum at the echo time, t_e, along the diagonal cross-section $\delta(t, t)$, and there is a minimum at the echo time along both the t_1 axis and the t_2 axis. The echo time is twice the focal time, $t_e = 2t_f$, and can be approximated, within 10% error, by $t_e = 2/(\langle k \rangle + \langle \gamma \rangle)$. This approximate relation is independent of the backward reaction, the distribution of the reaction rate constant, and other variables, thus resulting in a direct estimation of the average relaxation rate of conformational fluctuations, for a given ensemble-averaged reaction rate constant.

3. The correlation between the amplitude of the echo and the distribution of reaction rate constants provides useful information about conformational landscapes. The amplitude of the echo is shown to be proportional to the variance of the reaction rate constant, $\delta(t_e) \propto \langle \delta k^2 \rangle$. For a given set of reaction rate constants, the maximum echo occurs at approximately $\gamma \approx \langle (\delta k)^2 \rangle / \langle k \rangle$, which is proportional to the variance of the reaction rate constant. In the slow modulation limit, the existence of the two-event echo can be related to the individuality and distinctiveness of conformational landscapes. The maximum echo occurs when the difference between rate constants associated with different conforma-

tional channels is maximized whereas the difference between reactive fluxes is minimized.

4. The stochastic rate model provides a complete and unified description of the stochastic nature of the fluctuating rate constant. Its second order cumulant expansion, based on the small variance assumption, leads to the Gaussian stochastic rate model that serves as a first-order model for analyzing single molecule trajectories. Similar to Kubo's stochastic line-shape theory, the stochastic Gaussian model describes the fluctuating rate process with an average rate constant $k = \langle k \rangle$ and a rate correlation function $\chi(t) = \langle [k(t) - k_s][k(0) - k_s] \rangle$. The resulting formalism reproduces the recurrent behavior in the two-event joint distribution function. Through the mapping to the Gaussian stochastic rate model, various modulated reaction schemes can be compared and characterized in a unified framework.

These results provide a quantitative tool to interpret and analyze event-averaged single molecule quantities. Though a single time-scale for conformational fluctuations is assumed for the simplicity of calculations, applications of current analysis to power-law decay and other non-exponential relaxation processes can also be formulated. Furthermore, conformational relaxation is reflected not only in modulated reactions but also in other dynamic processes, including diffusion and quantum dissipation. Theoretical analysis of possible single molecule measurements of these processes is an interesting topic for future studies.[70, 71, 72, 73]

2.8 Appendix 2-A: The Green's Function in the diffusion model

Eq. (2.42) satisfies the Smoluchowski equation with a quadratic sink,

$$\frac{\partial}{\partial t}G(x,y,t) = -\kappa x^2 G(x,y,t) + \lambda\theta\frac{\partial}{\partial x}(\frac{\partial}{\partial x} + \frac{x}{\theta})G(x,y,t), \qquad (2.79)$$

with the initial condition

$$G(x, y, 0) = \delta(x - y). \tag{2.80}$$

Applying the transformation

$$G(x, y, t) = g(x, y, t)e^{\alpha(x^2 - y^2)} \tag{2.81}$$

where $\alpha = (s - 1)/(4\theta)$, $s = \sqrt{1 + 4\kappa\theta/\lambda}$, we find that $g(x, y, t)$ satisfies the Fokker-Planck equation for the Ornstein-Uhlenbeck process with a constant potential sink,

$$\frac{\partial}{\partial t}g(x, y, t) = [\lambda s\frac{\partial}{\partial x}(x\frac{\partial}{\partial x}) + \lambda\theta\frac{\partial^2}{\partial x^2}]g(x, y, t) - \frac{\lambda}{2}(s - 1)g(x, y, t), \tag{2.82}$$

with the initial condition

$$g(x, y, t) = \delta(x - y). \tag{2.83}$$

Further, we rewrite $g(x, y, t)$ as

$$g(x, y, t) = g_1(x, y, t)e^{-\frac{\lambda}{2}(s-1)t}, \tag{2.84}$$

where $g_1(x, y, t)$ is the Green's function for the standard Ornstein-Uhlenbeck process.

$$\frac{\partial P}{\partial t} = \gamma\frac{\partial}{\partial x}(xP) + D\frac{\partial^2 P}{\partial x^2}, \tag{2.85}$$

with $\gamma = \lambda s$ and $D = \lambda\theta$. The standard solution to Eq. (2.85) is given in Ref. [74] as

$$g_1(x, y, t) = \sqrt{\frac{\gamma}{2\pi D(1 - e^{-2\gamma t})}} \exp[-\frac{\gamma(x - ye^{-\gamma t})^2}{2D(1 - e^{-2\gamma t})}]. \tag{2.86}$$

Therefore, the Green's function for the Ornstein-Uhlenbeck process in a constant potential sink is

$$g(x, y, t) = e^{-\frac{\lambda(s-1)t}{2}} \left[\frac{s}{2\pi\theta(1 - e^{-2\lambda st})} \right]^{\frac{1}{2}} \exp\left[-\frac{s(x - ye^{-\lambda st})^2}{2\theta(1 - e^{-2\lambda st})} \right], \qquad (2.87)$$

which, after the transformation in Eq. (2.81), leads to $G(x, y, t)$ in Eq. (2.42). The same result was obtained by G. H. Weiss.[46] The equivalence can be confirmed by replacing D, β, and α in his derivation with $\lambda\theta$, $1/\theta$, and κ in our notation.

2.9   Appendix 2-B: Single-event and two-event distribution functions in the Gaussian stochastic rate model

We first define a two-time survival probability function as

$$P(t_0, t_1) = \langle \exp[- \int_{t_0}^{t_1} k(\tau) d\tau] \rangle_s, \qquad (2.88)$$

where the $\langle \cdots \rangle_s$ represents a stochastic average. Then, the single-event distribution function $f(t)$ defined in Eq. (2.69) can be related to $P(t_0, t_1)$ by

$$f(t) = -\frac{1}{\langle k \rangle} \frac{\partial^2 P(t_0, t_1)}{\partial t_0 \partial t_1} |_{t_0 = 0, \ t_1 = t} = \frac{\langle k(t) e^{-\int_0^t k(\tau) d\tau} k(0) \rangle}{\langle k \rangle}. \qquad (2.89)$$

The second cumulant expansion truncated at second order gives $P(t_0, t_1)$ explicitly as

$$P(t_0, t_1) = \exp[-\langle k \rangle(t_1 - t_0) + M(t_1 - t_0)], \qquad (2.90)$$

75

where $M(t) = \int_0^t (t - \tau)\chi(\tau)d\tau$. Substitution of Eq. (2.90) into Eq. (2.89) leads to $f(t)$ in Eq. (2.70). Similarly, a four-time survival probability function is defined as

$$P(t_0, t_1, t_1', t_2') = \langle \exp[-(\int_{t_0}^{t_1} + \int_{t_1'}^{t_2'})k(\tau)d\tau]\rangle_s. \tag{2.91}$$

The two-event distribution function $f(t_1, t_2)$ defined in Eq. (2.69) is related to $P(t_0, t_1, t_1', t_2')$ by

$$
\begin{aligned}
f(t_1, t_2) &= \frac{1}{\langle k \rangle}\frac{\partial^3 P(t_0, t_1, t_1', t_2')}{\partial t_0 \partial t_1 \partial t_2'}\Big|_{t_0=0,\ t_1'=t_1,\ t_2'=t_1+t_2} \\
&= \frac{\langle k(t_1 + t_2)e^{-\int_{t_1}^{t_1+t_2} k(\tau)d\tau}k(t_1)e^{-\int_0^{t_1} k(\tau)d\tau}k(0)\rangle}{\langle k \rangle}.
\end{aligned}
\tag{2.92}
$$

The four-time survival probability function $P(t_0, t_1, t_1', t_2')$ is obtained in the second cumulant approximation as

$$
\begin{aligned}
P(t_0, t_1, t_1', t_2') = \ \exp[\ &-\langle k\rangle(t_1 + t_2' - t_1' - t_0) + M(t_1 - t_0) + M(t_2' - t_1') + M(t_2' - t_0) \\
&-M(t_1' - t_0) - M(t_2' - t_1) + M(t_1' - t_1)],
\end{aligned}
\tag{2.93}
$$

which in combination with Eq. (2.92) leads to Eq. (2.71).

2.10 Appendix 2-C: Other single molecule quantities in the Gaussian stochastic model

In the forward half-reaction of the stochastic rate model, the normalized correlation function of two on-time events of durations t_1 and t_2 separated by time τ is expressed as

$$C_{on}(t_1, \tau, t_2) = \frac{\langle e^{-\int_0^{t_1} k_f(t')dt'}e^{-\int_{t_1+\tau}^{t_1+\tau+t_2} k_f(t')dt'}\rangle}{\langle e^{-\int_0^{t_1} k_f(t')dt'}\rangle\langle e^{-\int_{t_1+\tau}^{t_1+\tau+t_2} k_f(t')dt'}\rangle}. \tag{2.94}$$

The second order truncation of Eq. (2.94) leads to

$$C_{on}(t_1, \tau, t_2) = \exp\left\{ M(t_1 + t_2 + \tau) + M(\tau) - M(t_1 + \tau) - M(t_2 + \tau) \right\}, \quad (2.95)$$

where $M(t) = \int_0^t (t-\tau)\chi_{on}(\tau)d\tau$. In the small time limit, the above expression reduces

$$\lim_{t_1,t_2 \to 0} \frac{C_{on}(t_1, \tau, t_2) - 1}{t_1 t_2} = \chi_{on}(\tau), \quad (2.96)$$

which provides a direct measure of the rate correlation function $\chi_{on}(t)$.

Another function to illustrate memory effects is the on-off population correlation function

$$C(t) = \frac{\langle \delta\rho_{off}(t)\delta\rho_{on}(0)\rangle}{\langle \delta\rho_{off}(0)\delta\rho_{on}(0)\rangle}, \quad (2.97)$$

where $\rho_{on}(t)$ and $\rho_{off}(t)$ satisfy the master equation for the full reaction

$$\begin{pmatrix} \dot{\rho}_{on}(t) \\ \dot{\rho}_{off}(t) \end{pmatrix} = \begin{pmatrix} -k_f(t) & k_b(t) \\ k_f(t) & -k_b(t) \end{pmatrix} \begin{pmatrix} \rho_{on}(t) \\ \rho_{off}(t) \end{pmatrix}. \quad (2.98)$$

Using the second cumulant expansion, the on-off population correlation function can be derived as

$$C(t) = \exp[-2\langle k\rangle t + 4M(t)], \quad (2.99)$$

where the forward and the backward reactions are assumed to be equivalent.

77

Chapter 3

Direct measurements of memory effects

3.1 Introduction

Advances in single molecule spectroscopy allow us to observe real-time single molecule trajectories, which consist of a chain of correlated reaction events of various lifetimes and contain rich information about microscopic mechanisms.[9, 10, 13, 14, 16, 17, 23] An advantage of single molecule techniques is the direct observation of slow variations in reaction kinetics, which are often limited by the spectral resolution in conventional bulk experiments.[20, 21, 24, 32, 33, 34, 75, 76] In single molecule experiments, the traced molecular system inter-converts between the dark and bright states so that the observed fluorescence turns on and off intermittently. The on/off waiting time corresponds to the duration that a single molecule spends in the bright/dark state, and a trajectory of on-off events records the history of the single reactive system. For example, the single molecule enzymatic turnover experiment by Xie and coworkers clearly demonstrates slow fluctuations in the turn-over rate of cholesterol oxidation and the dependence of the enzymatic turnovers on previous history.[15] Since only the bright state is monitored by fluorescence emission, conformational dynamics is not directly accessible, and the dynamic disorder is a *hidden* mechanism that requires statistical analysis of single molecule reaction events.[26, 27, 28, 77]

A (bright state)   B (dark state)   A (bright state)   B (dark state)

$$\Gamma_a \quad \overset{K_a}{\underset{K_b}{\rightleftharpoons}} \quad \Gamma_b \qquad\qquad A \quad \overset{k_a(t)}{\underset{k_b(t)}{\rightsquigarrow}} \quad B$$

(a) modulated reaction scheme   (b) stochastic rate model
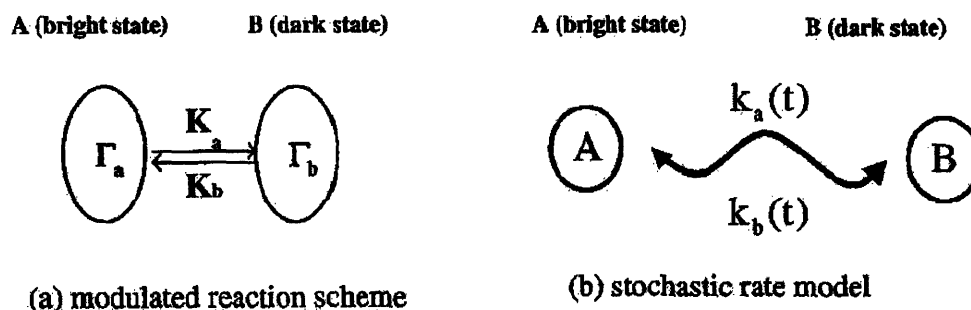
Figure 3-1: An illustration of (a) the modulated reaction scheme and (b) the stochastic rate model.

In a recent calculation of the two-conformational-channel model, we observed the focal time in the single-event distribution function and the recurrent behavior (i.e., the echo) in the two-event distribution function.[27] Questions remain regarding to the generality of the two-event echo, the quantitative description of conformational fluctuations in single molecule kinetics, and the plausibility of direct measurements of memory effects from on-off sequences. In this chapter, we use the stochastic rate model to derive explicit expressions for the reported event-averaged quantities and introduce two quantitative measurements of the memory effects due to conformational fluctuations.

3.2   Stochastic rate model

As demonstrated in Ref. [78], given a specific model, the single molecule quantities can be computed and the features such as the focal time and the echo time can be identified. In this chapter, we will show the generality of these features by virtue of the stochastic rate model. The environmental fluctuations introduces a time-dependence on the rate constant, which can now be treated as a stochastic variable. Similar to Kubo's stochastic line-shape theory,[55, 56] each realization of the stochastic rate defines a rate process, and single molecular measurements can be obtained by taking a stochastic average of rate fluctuations. The modulated reaction model is analogous to the Schrödinger picture in quantum mechanics, as the occupancy in each confor-

mational channel changes with time but the rate constant for each channel remains constant. The stochastic reaction rate model is analogous to the Heisenberg picture in quantum mechanics, as the rate evolves with time. As illustrated in Fig. 3-1, though in different pictures, these two models are equivalent.

To begin, we write the kinetics of the generic modulated reaction model in a compact form

$$\dot{\rho}(t) = -(\Gamma + K)\rho(t) \tag{3.1}$$

where Γ characterizes the conformational dynamics and K characterizes the reaction kinetics. In general, Γ can be any dynamic operator (e.g., $\Gamma = -\lambda\theta\partial_x(\partial_x + x/\theta)$ is the Fokker-Planck operator for normal diffusion in a harmonic potential), and K can be any form of kinetic processes, including discretized multi-channel rate and coordinate-dependent rate. We introduce the stochastic representation for modulated reactions by rewriting the Green's function solution to Eq. (3.1) in the interaction picture as

$$G(t) = e^{-(\Gamma + K)t} = e^{-\Gamma t}e^{-\int_0^t K(\tau)d\tau}. \tag{3.2}$$

The time-dependent rate is defined through a unitary transformation

$$K(t) = e^{\Gamma t}Ke^{-\Gamma t} = \begin{pmatrix} e^{\Gamma_a t}K_a e^{-\Gamma_a t} & -e^{\Gamma_a t}K_b e^{\Gamma_b t} \\ -e^{\Gamma_b t}K_a e^{\Gamma_a t} & e^{\Gamma_b t}k_b e^{\Gamma_b t} \end{pmatrix}, \tag{3.3}$$

so that conformational modulation is incorporated into the time-dependence of the rate.

With the time-dependence rate, all single molecule quantities can be evaluated explicitly in the stochastic rate model. For example, using the identity $\sum \Gamma_a = 0$, the average survival probability in the bright state can be written as

$$S(t) = \langle G_a(t)\rangle = \langle e^{-\int_0^t K_a(\tau)d\tau}\rangle, \tag{3.4}$$

where the average is taken with respect to the equilibrium conformational distribution

81

$\langle A \rangle = \sum A\rho_a / \sum \rho_a$. Cumulant expansion of S(t) leads to

$$S(t) = \exp[\sum_{n=1}^{\infty} \frac{(-1)^n}{n!} \int_0^t d\tau_1 \cdots \int_0^t d\tau_n \chi_n(\tau_1, \ldots, \tau_n)], \tag{3.5}$$

where $\chi_n(\tau_1, \ldots, \tau_n)$ is the n-th order cumulant function. As a result of the detailed balance condition, $\Gamma_a \rho_a = 0$, the average rate and correlation functions are stationary. Thus, we have

$$\chi_1(t) = \langle K_a(t) \rangle = \langle K_a \rangle = k_a, \tag{3.6}$$

which is the phenomenological rate constant, and

$$\chi_2(t_1, t_2) = \langle \delta K_a(t_1) \delta K_a(t_2) \rangle = \langle \delta K_a e^{-\Gamma_a(t_1-t_2)} \delta K_a \rangle = \chi_{aa}(t_1 - t_2), \tag{3.7}$$

which rigorously defines the memory function for the stochastic rate. The initial value of the memory function gives the variance of the reactive rate $\chi(0) = \langle \delta k^2 \rangle = k_d^2$. By truncating the expansion in Eq. (3.5) to second order, we obtain the Gaussian stochastic rate model

$$S(t) = \exp[-k_a t + M_{aa}(t)] \tag{3.8}$$

with $M_{aa}(t) = \int_0^t (t - \tau) \chi_{aa}(\tau) d\tau$. Similar expressions can be obtained for the backward half-reaction as well as for the reversible full-reaction. Since the survival probability decreases with time, $k_a \gg \int_0^t (1 - \tau/t) \chi_{aa}(\tau) d\tau$ has to be satisfied, which implies a small variance of reaction rates and a finite correlation time for conformational fluctuations. We emphasize that the stochastic model and the memory function are completely general whereas the Gaussian stochastic rate model is approximate.

The introduction of the memory function allows us to quantify memory effects in single molecule kinetics and to evaluate single molecule measurements in explicit and general forms. In other words, the memory kernel is the key quantity we extract from single molecule sequences and use to characterize modulated reactions. As an

example, in Appendix 3-A, we derive the expression for the two-event distribution function within the framework of the Gaussian stochastic rate approximation.

Our definition of the memory function provide a possible interpretation of the recent finding of stretched exponential relaxation in single molecule experiments.[79] In a general situation where the rate constant is coupled to a set of conformational degrees of freedom with the coordinate-dependence $k(x)$, the memory function becomes

$$\chi(t) \quad = \quad \frac{1}{(2\pi)^2} \int d\eta_1 d\eta_2 \tilde{k}(\eta_1)\tilde{k}(\eta_2)[\langle e^{i\eta_1 x(0)+i\eta_2 x(t)}\rangle - \langle e^{i\eta_1 x(0)}\rangle\langle e^{i\eta_2 x(0)}\rangle] \quad (3.9)$$

where $\tilde{k}(\eta) = \int k(y)\exp(iy\eta)dy$ is the Fourier transform of the rate function $k(x)$ and the stochastic average is carried out with respect to the conformational dynamics of $y(t)$. Assuming a Gaussian stochastic process for the conformational coordinate Eq. (3.9) can be evaluated with the second order cumulant expansion. This expression incorporates a large class of modulated rate processes and leads to a stretched exponential with a proper choice of the coordinate-dependence in the rate function.

We note that the memory function measures modulating effects of environments on two-state kinetics, but does not directly probe environmental fluctuations. Nevertheless, the asymptotic behavior of the memory function reveals the nature of the long-time relaxation of environmental fluctuations. To demonstrate this, we expand conformational fluctuations as $G(t) = |\varphi_n\rangle E_n(t)\langle \varphi_n|$ where the eigenstates satisfy $\langle \varphi_n|\varphi_m\rangle = \delta_{nm}$, and $E_n(t)$ is the characteristic function for the n-th eigenstate. In order words, $\varphi_n(x)$ are the normal modes of conformational fluctuations. In this basis set, we expand the rate constant as $k(x) = \sum c_n \varphi_n(x)$ so that

$$\langle k(x)\rangle = c_0$$
$$\chi(t) = \sum_{n=0}^{\infty} c_n^2 E_n(t). \quad (3.10)$$

The smallest non-zero eigenvalue has the slowest decay and thus dominates the asymp-

totic behavior, i.e.,

$$\lim_{t\to\infty} \chi(t) \propto E_1(t) \qquad (3.11)$$

which directly probes the fundamental mode of conformational fluctuations. As an important example, we demonstrate this aspect of the memory kernel using the example of sub-diffusive environments.

Memory function for sub-diffusive environments

To illustrate the generality of memory effects, we hereby consider a single-molecule experiment in a disordered medium where the conformational dynamics is modeled by sub-diffusive motion in a harmonic potential. Sub-diffusive transport is widely observed in diverse fields, including charge transport in amorphous semiconductors, NMR diffusometry in disordered materials, and bead dynamics in polymer networks. Metzler, Barkai and Klafter proposed a generalized fractional Fokker-Planck equation for anomalous diffusion, and later justified the approach from a continuous time random walk model.[80] Unlike linear Brownian motion in the diffusive regime, the mean square displacement in the free sub-diffusive space follows

$$\langle (\Delta x)^2 \rangle = \frac{2K_\gamma}{\Gamma(1+\gamma)} t^\gamma \ \ with \ 0 < \gamma < 1, \qquad (3.12)$$

where K_γ is the generalized diffusion coefficient, and the Stokes-Einstein relation is generalized as

$$K_\gamma = \frac{k_B T}{m\eta_\gamma}, \qquad (3.13)$$

where η_γ is the generalized friction coefficient. The sub-diffusive motion in a potential is described by the corresponding Fokker-Planck operator $-\mathcal{L}_{FP} = \partial_x[V'(x)/m\eta_\gamma] + K_\gamma \partial_x^2$. In a harmonic potential, $V(x) = m\omega^2 x^2/2$, the Green's function for the sub-

diffusive motion is

$$G(x, x', t) = \sqrt{\frac{m\omega^2}{2\pi k_B T}} \sum_{n=0}^{\infty} \frac{1}{2^n n!} E_\gamma(-n\tilde{t}^\gamma) H_n(\frac{\tilde{x}'}{\sqrt{2}}) H_n(\frac{\tilde{x}}{\sqrt{2}}) \exp[-\frac{\tilde{x}^2}{2}], \qquad (3.14)$$

where the characteristic time unit τ is defined by $\tau^{-\gamma} = \omega^2/\eta_\gamma$, $\tilde{t} = t/\tau$ and $\tilde{x} = x\sqrt{m\omega^2/k_B T}$ are temporal and spatial coordinates in reduced units,

$$H_n(x) = (-1)^n \exp[x^2]\partial_x^n \exp[-x^2] \qquad (3.15)$$

is the Hermite polynomial, and

$$E_\gamma(z) = \sum_{m=0}^{\infty} \frac{z^m}{\Gamma(1+\gamma m)} \qquad (3.16)$$

is the Mittag-Leffler function. For $\gamma = 1$, the Mittag-Leffler function becomes the exponential function, $E_1(z) = \exp(z)$. The equilibrium distribution is deduced from the long time limit of the Green's function, $\rho(x) = \sqrt{m\omega^2/2\pi k_B T} \exp[-\tilde{x}^2/2]$.

In general, a coordinate-dependent rate function can be expanded as

$$k(x) = \sum_{n=0}^{\infty} c_n H_n(\tilde{x}/\sqrt{2}) \qquad (3.17)$$

so that the average stochastic rate and the correlation function of the stochastic rate become

$$\langle k(x) \rangle = c_0, \qquad (3.18)$$

$$\chi(t) = \langle \delta k(x) G(x, x', t) \delta k(x') \rangle = \sum_{n=1}^{\infty} c_n^2 2^n n! E_\gamma(-n\tilde{t}^\gamma). \qquad (3.19)$$

In the long time limit, the memory function of the fluctuating rate $\chi(t)$ follows a power law decay according to the properties of the Mittag-Leffler function.

As a special case, we assume a quadratic form of the coordinate-dependence, i.e.,

$k(x) = \kappa x^2$, so that the correlation function of the stochastic rate is given by

$$\chi(t) = \chi(0) E_\gamma(-2\tilde{t}^\gamma). \tag{3.20}$$

In the short time regime, when $t \ll \tau$,

$$E_\gamma(-2\tilde{t}^\gamma) \sim 1 - 2\tilde{t}^\gamma/\Gamma(1+\gamma) \sim \exp[-2\tilde{t}^\gamma/\Gamma(1+\gamma)] \tag{3.21}$$

is a stretched exponential; while in the long time regime, $t \gg \tau$,

$$E_\gamma(-2\tilde{t}^\gamma) \sim \frac{\tilde{t}^{-\gamma}}{2\Gamma(1-\gamma)} - \frac{\tilde{t}^{-2\gamma}}{4\Gamma(1-2\gamma)} \tag{3.22}$$

is a power law decay. Numerical calculations of $E_\gamma(-2\tilde{t}^\gamma)$ are shown in Fig. 3-2 for different values of γ. As γ approaches 1, the Mittag-Leffler function becomes close to a single exponential function; while for small γ, it clearly deviates from exponential decay and shows the power-law behavior in the long time regime.

3.3   On-time correlation function

One direct measure of the memory function is the on-time correlation function, which was first used in Xie's experiment and was believed to be a measure of memory effects. With the introduction of the stochastic rate model and memory function, we are now able to explicitly show the relation between memory and the on-time correlation function. Here, this relationship is proved within the slow modulation limit and the small variance limit. Though both are derived for the small variance limit, the first proof invokes the second cumulant approximation but does not require the slow modulation assumption; and the second proof does not involve any assumptions about the convergence of the memory function but requires the slow modulation assumption.
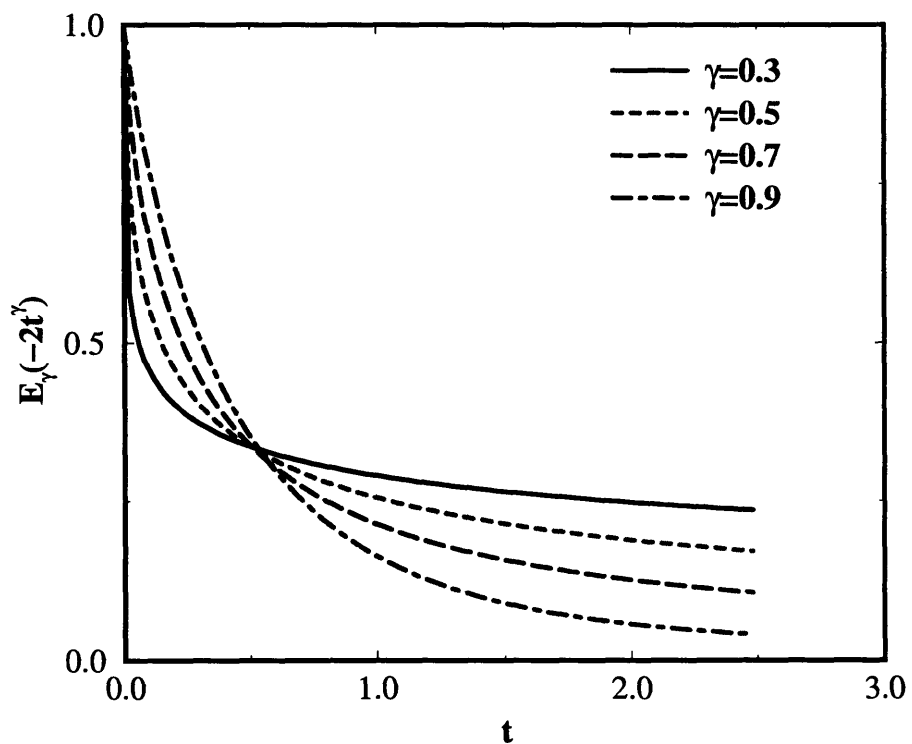
Figure 3-2: Numerical calculation of $E_\gamma(-2t^\gamma)$. For γ close to 1, $E_\gamma(-2t^\gamma)$ is similar to exponential decay; while for small γ, it clearly deviates from exponential decay and exhibits stretched exponential in the short time regime and power-law behavior in the long time regime.
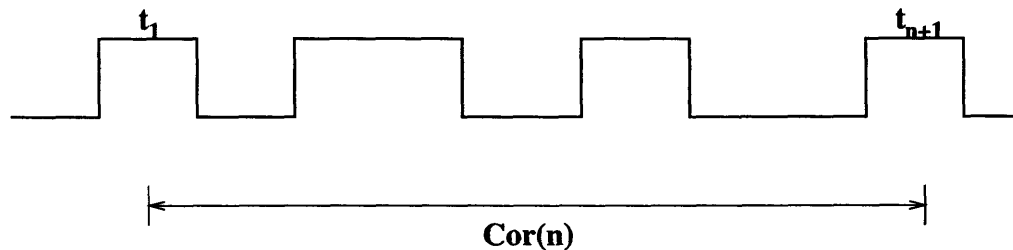
Figure 3-3: Two on-time events separated by n off-events along a typical single molecule trajectory

3.3.1 Second cumulant expansion

The on-time correlation function is defined as

$$Cor(n) = \frac{\overline{t_1 t_{n+1}} - \bar{t}^2}{\overline{t^2} - \bar{t}^2},\tag{3.23}$$

which is the cross-correlation function of two on-time events separated by n off-events. From Eq (5) of Ref. [27], the joint probability distribution is given as

$$f(t_1, t_{n+1}) = \sum K_a G_a(t_{n+1}) K_b \tilde{G}_b [K_a \tilde{G}_a K_b \tilde{G}_b]^{n-1} K_a G_a(t_1) F_a,\tag{3.24}$$

so that

$$\overline{t_1 t_{n+1}} = \int dt_1 \int dt_{n+1} f(t_1, t_{n+1}) t_1 t_{n+1} = \langle [\tilde{G}_a K_a \tilde{G}_b K_a]^n \tilde{G}_a \rangle / k_a\tag{3.25}$$

with $\tilde{G} = \int_0^\infty G(t)dt$. Here, the stochastic average is defined as $\langle A \rangle = \sum A \rho_a / \sum \rho_a$. To evaluate the on-time correlation function, we introduce a generating function $H(x) = \sum_{n=0}^\infty \overline{t_1 t_{n+1}} x^n$, where the $n = 0$ term is included for convenience and $x \leq 1$ is assumed for convergence. Thus, we have

$$k_a H(x) = \sum_{n=0} x^n \langle [\tilde{G}_a K_b \tilde{G}_b K_a]^n \tilde{G}_a \rangle = \langle \tilde{G}_{aa}(x) \rangle = \int_0^\infty \langle G_{aa}(t, x) \rangle dt.\tag{3.26}$$

As illustrated in Fig. 3-4, the Green's function $G_{aa}(t, x)$ corresponds to the following kinetics

$$\begin{pmatrix} \dot{\rho}_a(t) \\ \dot{\rho}_b(t) \end{pmatrix} = - \begin{pmatrix} \Gamma_a + K_a & -K_b \\ -x K_a & \Gamma_b + K_b \end{pmatrix} \begin{pmatrix} \rho_a(t) \\ \rho_b(t) \end{pmatrix},\tag{3.27}$$

which describes the forward reaction with rate $x K_a$, the backward reaction with rate K_b, the population depletion at the bright state with rate $(1 - x)K_a$. For symmetric reactions with $K_a = K_b = K$, Eq. (3.27) is solved explicitly for a stochastic rate

88

process $K(t)$, giving

$$kH(x) = \int_0^\infty dt \frac{1}{2} \langle e^{-(1-\sqrt{x})\int_0^t K(\tau)d\tau} + e^{-(1+\sqrt{x})\int_0^t K(\tau)d\tau} \rangle$$

$$\approx \frac{1}{2} \int_0^\infty dt \{\exp[-(1-\sqrt{x})kt + (1-\sqrt{x})^2 M(t)]$$

$$+ \exp[-(1+\sqrt{x})kt + (1+\sqrt{x})^2 M(t)]\} \qquad (3.28)$$

where the second cumulant truncation is applied. Under the small variance condition, Eq. (3.28) is expanded to the leading order of $M(t)$, giving

$$kH(x) = \int_0^\infty \left\{ [1 + M(t) + xM(t)] \cosh(kt\sqrt{x}) - 2\sqrt{x}M(t)\sinh(kt\sqrt{x}) \right\} e^{-kt} dt. \quad (3.29)$$

This closed-form expression is then used to generate the moment in order of x^n, leading to

$$k^2 H(x) = \sum x^n [1 + I_{2n} + I_{2n-2} - 2I_{2n-1}] \qquad (3.30)$$

where $I_m = \int_0^\infty d\tau M(\tau)(k\tau)^m e^{-kt}/m!$. Assuming that the memory function of the rate varies much slower than the rate process, the integral of $M(\tau)$ can be approximated by the value of the first moment $t_m = (m+1)/k$, that is $I_m \approx M(t_m)$. Then, the difference function in Eq (3.30) becomes

$$I_{2n} + I_{2n-2} - 2I_{2n-1} \approx M(\frac{2n+1}{k}) + M(\frac{2n-1}{k}) - 2M(\frac{2n}{k}) \approx \frac{1}{k^2}\chi(\frac{2n}{k}), \quad (3.31)$$

where the continuous limit is taken under the slow relaxation assumption. Combining Eqs. (3.23)-(3.31), we finally arrive at an approximate expression

$$Cor(n) = \frac{\chi(2n/k)}{\chi(0)} = \frac{\chi(t_{eff})}{\chi(0)}, \qquad (3.32)$$

indicating that the on-time correlation function is proportional to the memory function of the rate at the discrete time separation. The number of off-events in $Cor(n)$ is translated into the average time separation between the two events in $\chi(t)$. For
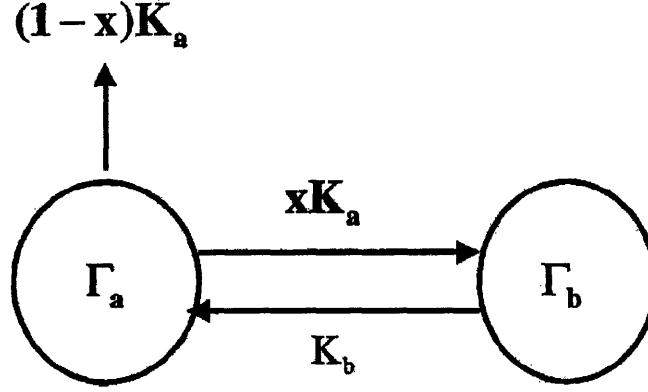
Figure 3-4: An illustration of the reaction scheme for the evaluation of the generating function $H(x)$.

asymmetric reactions, Eq. (3.32) can be generalized to $Cor(n) = \chi(n/k_f + n/k_b)/\chi(0)$, with the effective time separation $t_{eff} = n/k_f + n/k_b$. Although the final result in Eq. (3.32) is obtained approximately under the slow modulation limit, Eq. (3.31) is derived without this approximation and is therefore more general.

The generating function in Eq. (3.26) can be evaluated explicitly for the symmetric two-channel model illustrated in Fig. 2-1b, giving

$$H(x) = \frac{8\gamma\langle k\rangle^2 + (1-x)(\langle k\rangle^2 - k_d^2)\langle k\rangle - 2\gamma k_d^2(1+x)}{(1-x)\langle k\rangle[(2\gamma\langle k\rangle + \langle k\rangle^2 - k_d^2)^2 - x(\langle k\rangle^2 - k_d^2)^2]} \tag{3.33}$$

where $\langle k\rangle = (k_1 + k_2)/2$ and $k_d = (k_1 - k_2)/2$. Expansion of the above expression in terms of x results in

$$Cor(n) = \left(\frac{\langle k\rangle^2 - k_d^2}{k^2 - k_d^2 + 2k\gamma}\right)^{2n} \approx \left(\frac{\langle k\rangle}{\langle k\rangle + 2\gamma}\right)^{2n} \tag{3.34}$$

where the approximation is introduced for $k_d \ll \langle k\rangle$. In the slow relaxation limit, Eq. (3.34) reduces to $Cor(n) \approx \exp(-4\gamma/\langle k\rangle) = \exp(-2\gamma t_{eff})$, which agrees with the memory function for the two-channel model $\chi(t) = \chi(0)\exp(-2\gamma t)$.

90
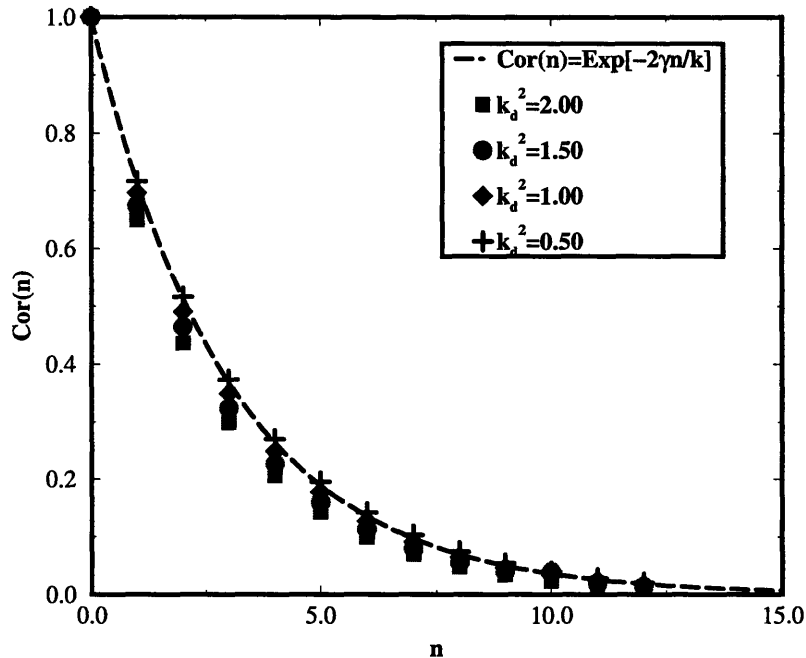
Figure 3-5: A comparison of the on-time correlation function $Cor(n)$ with the normalized memory function for the linear three-channel model, $\exp(-2\gamma n/k)$, for several values of rate variance $\chi(0) = k_d^2$. The three-channel model is defined in Eq. (3.41) with $k = 3.0$ and $\eta = 1.0$, and $\gamma = 1.0$.

3.3.2 Slow modulation limit

When conformational kinetics is much slower than reaction kinetics, each event can be approximated by a Poisson process with a probability to jump from one channel to another. Since the on-time duration measures the rate constant for one event within this approximation, the on-time correlation function directly measures the correlation of the reaction rate. This simple reasoning leads to the following derivation.

For Eq. (7) in Ref. [78], the on-time correlation function $\overline{t_1 t_{n+1}}$ is given by

$$\overline{t_1 t_{n+1}} = \frac{1}{k_a} \langle [\frac{1}{K_a + \Gamma_a} K_b \frac{1}{K_b + \Gamma_b} K_a]^n \frac{1}{K_a + \Gamma_a} \rangle, \tag{3.35}$$

where t_1 and t_{n+1} are the time durations for the two on-time events separated by n

91

off-time events. For simplicity, we consider the case when $\Gamma_a = \Gamma_b = \Gamma$ such that the equilibrium distribution satisfies $\Gamma \rho_a = \Gamma \rho_b = 0$. Under this condition, two rate matrices K_a and K_b are proportional to each other [78] and we have

$$\frac{1}{k_a + \Gamma} \rho_a = \frac{1}{k_a} \rho_a. \tag{3.36}$$

Second-order expansion in terms of $\delta K_a = K_a - k_a$ leads to

$$\begin{aligned}
\frac{1}{K_a + \Gamma} &= \frac{1}{k_a + \Gamma + \delta K_a} \\
&\approx \frac{1}{k_a + \Gamma}(1 - \delta K_a \frac{1}{k_a + \Gamma} + \delta K_a \frac{1}{k_a + \Gamma} \delta K_a \frac{1}{k_a + \Gamma}) \tag{3.37} \\
K_a \frac{1}{K_a + \Gamma} &= 1 - \Gamma \frac{1}{K_a + \Gamma} \\
&\approx 1 - \Gamma \frac{1}{k_a + \Gamma}(1 - \delta K_a \frac{1}{k_a + \Gamma} + \delta K_a \frac{1}{k_a + \Gamma} \delta K_a \frac{1}{k_a + \Gamma}) \tag{3.38}
\end{aligned}$$

In the slow modulation limit, when the eigenvalues of Γ are much smaller than k_a, Eq. (3.35) can be evaluated approximately to give

$$\begin{aligned}
\overline{t_1 t_{n+1}} &\approx \frac{1}{k_a^2}[1 + \langle \frac{\delta K_a}{k_a} \frac{k_a}{k_a + \Gamma} \frac{\delta K_a}{k_a} \rangle \\
&\quad - \langle \frac{\delta K_a}{k_a} \frac{k_a}{k_a + \Gamma} \sum_{m=0}^{n-1}(\frac{k_b}{k_b + \Gamma} \frac{k_a}{k_a + \Gamma})^m (1 - \frac{k_b}{k_b + \Gamma} \frac{k_a}{k_a + \Gamma}) \frac{\delta K_a}{k_a} \rangle] \\
&\approx \frac{1}{k_a^2} + \frac{1}{k_a^2} \langle \frac{\delta K_a}{k_a} \exp[\Gamma(\frac{n}{k_a} + \frac{n}{k_b})] \frac{\delta K_a}{k_a} \rangle \\
&= \frac{1}{k_a^2} + \frac{1}{k_a^2} \langle \frac{\delta K_a}{k_a} G(\frac{n}{k_a} + \frac{n}{k_b}) \frac{\delta K_a}{k_a} \rangle, \tag{3.39}
\end{aligned}$$

where $\chi(t) = \langle \delta K_a G(t) \delta K_a \rangle$ is the memory function for rate fluctuations, and only the leading order correlation of δK is retained approximately. Thus, the cross-correlation function of two on-time events separated by n off-time events is related to $\chi(t)$ as

$$Cor(n) = \frac{\overline{t_1 t_{n+1}} - \bar{t}^2}{\overline{t^2} - \bar{t}^2} = \frac{\chi(t_{eff})}{\chi(0)}. \tag{3.40}$$

with $t_{eff} = n/k_a + n/k_b$. In conclusion, in the slow modulation limit, the on-time
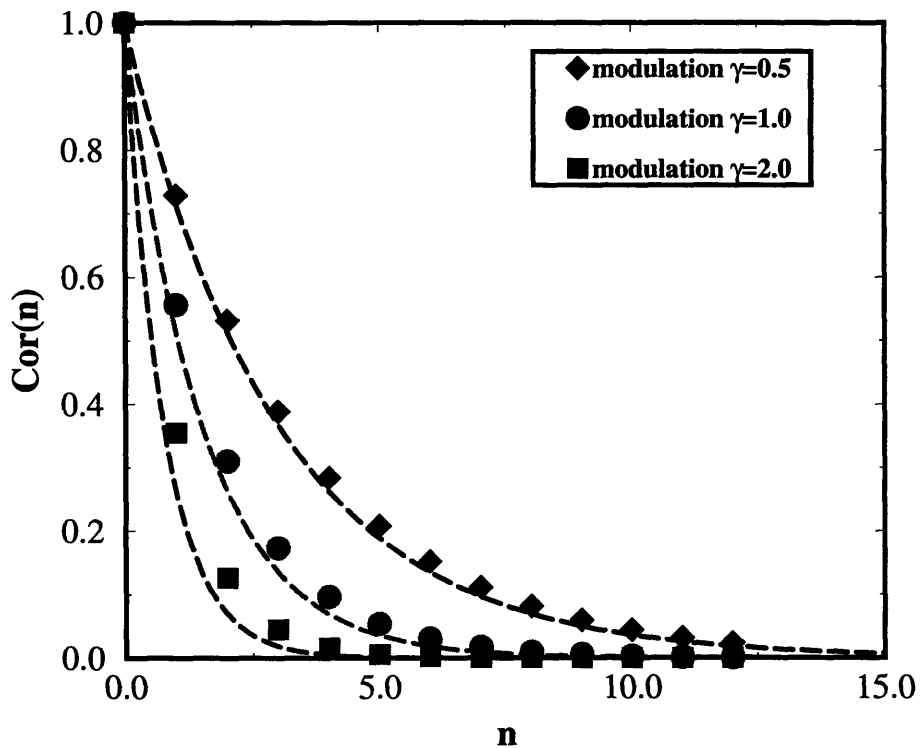
Figure 3-6: A plot of the on-time correlation function $Cor(n)$ for the same model as in Fig. 3-5 for several values of γ, along with the normalized memory function $\exp(-2\gamma n/k)$.

correlation function is proportional to the memory function of rate fluctuations due to conformational dynamics.

3.3.3 Examples

As a numerical example, we study the linear three-channel model illustrated in Fig. 3-1a with

$$\Gamma_a = \Gamma_b = \begin{pmatrix} \gamma & -\gamma & 0 \\ -\gamma & 2\gamma & -\gamma \\ 0 & -\gamma & \gamma \end{pmatrix}, \quad K_a = \eta K_b = \begin{pmatrix} k + \sqrt{3/2}k_d & 0 & 0 \\ 0 & k & 0 \\ 0 & 0 & k - \sqrt{3/2}k_d \end{pmatrix}, \quad (3.41)$$

93
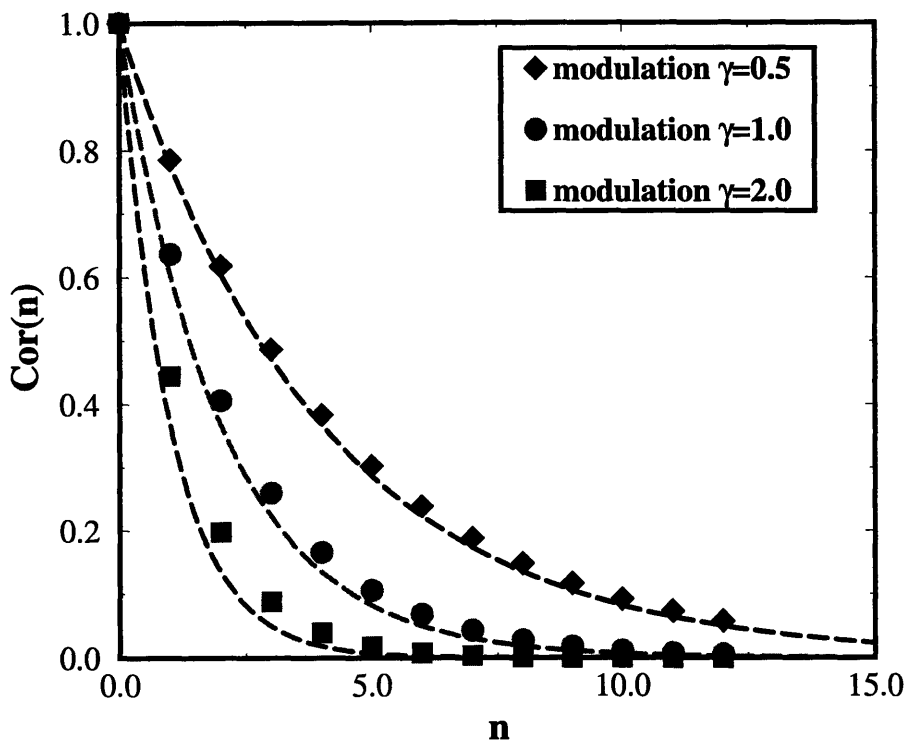
Figure 3-7: A comparison of the on-time correlation function $Cor(n)$ with the effective memory function for an asymmetric reaction. The three-channel model is defined in Eq. (3.41) with the forward rates $k_a = 3.0$, the variance $k_d = 1/\sqrt{6.0}$, and the equilibrium ratio $\eta = 2.0$. The modulation kinetics is the same for both the bright and dark states.

which has a memory function $\chi(t) = k_d^2 \exp(-\gamma t)$. The conformational dynamics are the same for the two states, and the equilibrium coefficient η is the ratio between the backward and forward rate constants. We first consider a symmetric reaction with $\eta = 1.0$. In Fig. 3-5, $Cor(n)$ is plotted for the three-conformational-channel model defined in Eq. (3.5) with several values of k_d but with fixed k and γ. Evidently, the equivalence relation is approximately obeyed and the deviation from the theoretical prediction increases with the variance. In Fig. 3-6, the on-time correlation function is plotted for the same values of k and k_d but for three different values of γ. The agreement between the discrete $Cor(n)$ and the memory function $\exp(-2\gamma n/k)$ is
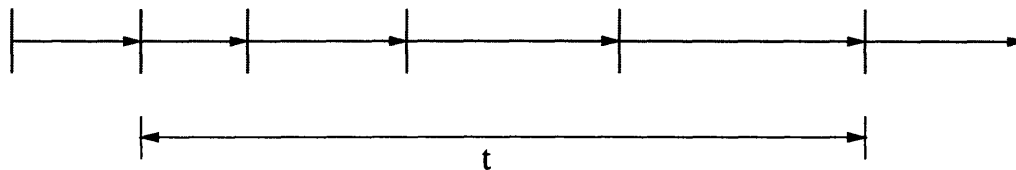
Figure 3-8: A sequence of bright events interrupted by instantaneous dark events for the case where the system is constantly pumped back to the bright state.

reasonably accurate and improves as γ decreases. As an example of the asymmetric reaction, we take the ratio between the forward and backward rate constants as $\eta = 2.0$. The on-time correlation function of the asymmetric linear three-channel model is plotted in Fig. 3-7 and is compared favorably with the memory function.

3.4   Sequence counting in Single Molecule Spectroscopy

Time trajectories in single molecule experiments provide detailed records of single-molecule events; therefore, statistical analysis of single molecule trajectories can provide rich information of conformational dynamics. In addition to the on-time correlation function, we introduce here a new single molecule measurement: the number density of single molecule sequences. In a special experimental setup,[79] short laser pulses are constantly shined on the enzyme at a very high frequency so that the single enzyme is quickly pumped back to the bright state once oxidized to the dark state. As a result, a trajectory of on events are collected with instantaneous interruptions of dark events. Fig. 3-8 illustrates a typical trajectory with a sequence of length t. Here, a sequence begins from a on-time event and ends with the same or another on-time event. The sequence density of on-time events is the probability distribution function of sequences as a function of the sequence time duration t regardless of the number of events included. The sequence density thus defined will be shown to be proportional to the memory function of the stochastic rate.

The reaction from the bright state to the dark state is denoted by the rate operator
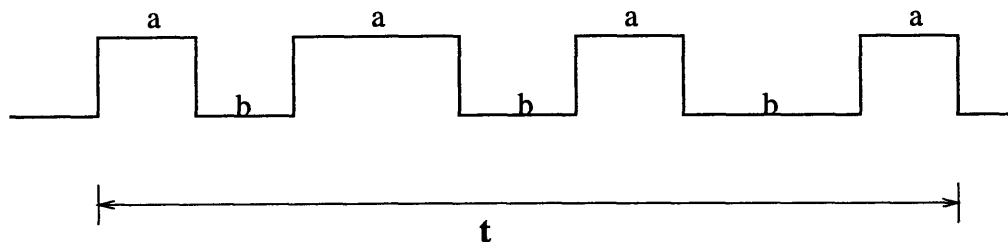
Figure 3-9: A sequence of on-off events with length t that starts and ends with on-time events along a typical single molecule trajectory.

K, the conformational dynamics is governed by the operator Γ, and the stationary population distribution satisfies $\Gamma\rho = 0$. The number density $N(t)$ with the time duration t is formulated in Laplace space as

$$
\begin{aligned}
\tilde{N}(u) &= \langle K\frac{1}{u+K+\Gamma}[1-K\frac{1}{u+K+\Gamma}]^{-1}K\rangle/k \\
&= \langle K\frac{1}{u+\Gamma}K\rangle/k \\
&= k[\frac{1}{u}+\frac{1}{k^2}\langle \delta K\frac{1}{u+\Gamma}\delta K\rangle],
\end{aligned}
\tag{3.42}
$$

where $k = \langle K\rangle$ is the average rate and $\delta K = K - k$ gives the fluctuation of the rate. Thus, in the time domain, we have

$$
N(t) = k[1 + \frac{1}{k^2}\chi(t)],
\tag{3.43}
$$

where $\chi(t) = \langle \delta K \exp[-\Gamma t]\delta K\rangle$ is the memory function of the stochastic rate. It is important to note that the above relation is obtained without any approximation and thus provides an exact relation between the sequence density $N(t)$ and the memory function $\chi(t)$ under this experimental setup.

Similar quantities are defined in single molecule experiments with both on and off times, as illustrated in Fig. 3-9. For simplicity, we consider the case with the same conformational dynamics for both bright and dark states, and assume detailed balance condition $\Gamma\rho_a = \Gamma\rho_b = 0$. Under this condition, K_a and K_b must be proportional to each other in order to exclude non-stationary effects or net current among different

conformational channels. Then, $N_{aa}(t)$ in Laplace space is

$$\tilde{N}_{aa}(u) = \langle K_a \frac{1}{u + K_a + \Gamma} [1 - K_b \frac{1}{u + K_b + \Gamma} K_a \frac{1}{u + K_a + \Gamma}]^{-1} K_a \rangle / k_a, \quad (3.44)$$

where $k_a = \langle K_a \rangle$ and $k_b = \langle K_b \rangle$ are the average forward and backward rates. In the slow modulation limit, when the characteristic time in Γ is much greater than $1/k_a$ and $1/k_b$, we have

$$[u + K_a + K_b + \Gamma]^{-1}(u + K_b + \Gamma) \approx \begin{cases} k_b/(k_a + k_b), & u \ll k_a, k_b, \\ (u + K_a + K_b)^{-1}(u + K_b), & u \geq k_a, k_b, \end{cases} \quad (3.45)$$

where $K_a \propto K_b$ is applied and Γ is ignored due to the separation of conformational and reaction time scales. Combining the above two equations, we have

$$\begin{aligned} \tilde{N}_{aa}(u) &= \langle K_a (u + K_a + K_b + \Gamma)^{-1} (u + K_b + \Gamma)(u + \Gamma)^{-1} K_a \rangle / k_a \\ &\approx \begin{cases} k_b \langle K_a (u + \Gamma)^{-1} K_a \rangle / [k_a(k_a + k_b)], & u \ll k_a, k_b, \\ \langle K_a [k_b u^{-1} + k_a(u + K_a + K_b)^{-1}] K_a \rangle / [k_a(k_a + k_b)], & u \geq k_a, k_b; \end{cases} \end{aligned} \quad (3.46)$$

or, in the time domain,

$$N_{aa}(t) \approx \begin{cases} \frac{k_a k_b}{k_a + k_b} [1 + \frac{1}{k_a^2} \chi_{aa}(t)], & k_a t, k_b t \gg 1; \\ \frac{k_b}{k_a(k_a + k_b)} \langle K_a K_a \rangle + \frac{1}{k_a + k_b} \langle K_a \exp[-(K_a + K_b)t] K_a \rangle, & k_a t, k_b t \leq 1. \end{cases} \quad (3.47)$$

where $\chi_{aa}(t) = \langle \delta K_a \exp[-\Gamma t] \delta K_a \rangle$ is the correlation function of the stochastic rate.

The central result of this section, Eq. (3.44) and Eq. (3.47), leads to several observations:

1. In Poisson processes, there is no memory, i. e., $\chi(t) = 0$ and $\delta K_a = \delta K_b = 0$, the sequence density $N_{aa}(t)$ is given by the Eq. (3.47) as,

$$N_{aa}(t) = \frac{k_a k_b}{k_a + k_b} + \frac{k_a^2}{k_a + k_b} \exp[-(k_a + k_b)t], \quad (3.48)$$

which decays to the constant sequence density $k_a k_b/(k_a + k_b)$ in the long time

limit.

2. With a separation of time-scales implied by the slow modulation condition, the initial fast decay of the sequence density is followed by the slow decay. The plateau value of the slow-decay in the sequence density is the constant for the Poisson process: $\lim_{t \to \infty} N_{aa}(t) = k_a k_b / (k_a + k_b)$. Hence, the slow decay to this constant allows us to map out the memory function

$$\frac{N_{aa}(t) - N_{aa}(\infty)}{N_{aa}(\infty)} \approx \frac{\chi_{aa}(t)}{k_a^2}, \tag{3.49}$$

which is more accurate than the on-time correlation function.

3. In the short time limit, the rate fluctuates on a time scale much greater than the measurement time t under the slow modulation condition so that each reaction channel evolves independently. As a result, the short-time limit in Eq. (3.47) is equivalent to the inhomogeneous average of the sequence density associated with each reaction channel.

4. In the limit of $k_b \to \infty$, $N_{aa}(t) \to k_a[1 + \chi_{aa}(t)/k_a^2]$ recovers exactly the previous result in Eq. (3.43) when laser pulses constantly pump the single molecule from the dark state back to the bright state.

Following the same derivation, $N_{bb}(t)$, $N_{ba}(t)$, and $N_{ab}(t)$ can be obtained as

$$N_{bb}(t) \approx \begin{cases} \frac{k_a k_b}{k_a + k_b}[1 + \frac{1}{k_a^2}\chi_{bb}(t)], & k_a t, k_b t \gg 1 \\ \frac{k_a}{k_b(k_a + k_b)}(\langle K_b K_b \rangle + \langle K_b \exp[-(K_a + K_b)t]K_b \rangle), & k_a t, k_b t \leq 1; \end{cases} \tag{3.50}$$

$$N_{ab}(t) \approx \begin{cases} \frac{k_a k_b}{k_a + k_b}[1 + \frac{1}{k_a k_b}\chi_{ab}(t)], & k_a t, k_b t \gg 1, \\ \frac{1}{k_a + k_b}(\langle K_a K_b \rangle - \langle K_a \exp[-(K_a + K_b)t]K_b \rangle), & k_a t, k_b t \leq 1; \end{cases} \tag{3.51}$$

$$N_{ba}(t) \approx \begin{cases} \frac{k_a k_b}{k_a + k_b}[1 + \frac{1}{k_b k_a}\chi_{ba}(t)], & k_a t, k_b t \gg 1, \\ \frac{1}{k_a + k_b}(\langle K_b K_a \rangle - \langle K_b \exp[-(K_a + K_b)t]K_a \rangle), & k_a t, k_b t \leq 1. \end{cases} \tag{3.52}$$

Note that $N_{ab}(t) = N_{ba}(t)$ reflects the time reversal symmetry in sequences counting. From Eq. (3.52), the short time limit of $N_{ab}(t)$ equals zero, which is due to the zero
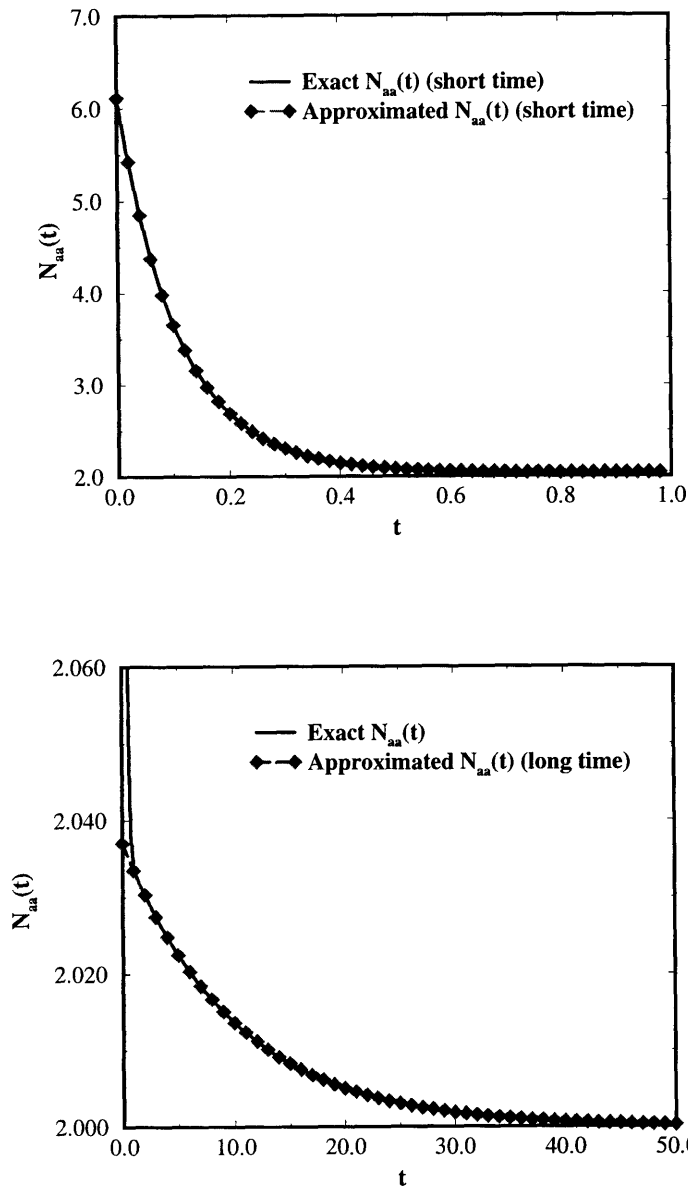
Figure 3-10: Comparison between $N_{aa}(t)$ from Eqs. (3.44) and (3.47) for a linear three-channel reaction with $k = 3.0$, $k_d = 1/\sqrt{6}$, $\gamma = 0.1$ and $\eta = 0.5$. (a) The short-time approximation $N_{aa}(t)$ given in Eq. (3.47) agrees well with the result calculated from Eq. (3.44) in the short time regime. (b) The long-time approximation $N_{aa}(t)$ given in Eq. (3.47) agrees with the result from Eq. (3.44) over a wide range of time-scales except for the short time period.

probability for finding a zero length sequence starting with an on-time event and ending with an off-time event.

As a numerical example, we calculate the quantities $N_{aa}(t)$ and $\chi_{aa}(t)$ for the linear three-channel model as we used for $Cor(n)$ with $K_b = \eta K_a$. Under these parameters, the memory function $\chi_{bb}(t)/k_b^2 = k_d^2 \exp(-\gamma t)/k^2$, and $k_a k_b/(k_a + k_b) = \eta k/(\eta + 1)$. The approximate expression in Eq. (3.47) and the exact expression in Eq. (3.44) are calculated and compared in Fig. 3-10a for the short time regime and in Fig. 3-10b for the long time regime, respectively. As shown in the figures, $N_{aa}(t)$ calculated with Eq. (3.44) decays sharply with a short time scale. The initial value of $N_{aa}(t)$ can be deduced from Eq. (3.47) in the limit $t \to 0$, giving $N_{aa}(t \to 0) = \langle K_b K_b \rangle / k_b = \eta k(1 + k_d^2/k^2)$, which agrees well with the calculated value. The predictions from Eq. (3.47) fit the curve of the $N_{aa}(t)$ from Eq. (3.44) over a wide range of timescales. Similar observation can be made for $N_{ab}(t)$ in Fig. 3-11, which has a zero initial value. The only difference is that the initial value of N_{ab} is zero, because the on-off sequence involves at least one on event and one off event.

3.5 Concluding remarks

In summary, the stochastic rate approach is rigorously established in the interaction representation of the modulated reaction model. To second-order, the cross-correlation of the stochastic rate, i.e., the memory function, completely characterizes the rate process. The memory function can be decomposed into the normal modes of conformational fluctuations and directly probes the fundamental mode of environments in the long time limit.

Within this formalism, we propose two direct single molecule measurements of the memory function of the fluctuating rate. The correlation of two on-time events separated by a given number of off-events is shown to be proportional to the memory function evaluated at the discretized average time separation between the two on-time events. The approach to the asymptotic value of the sequence density is shown to be proportional to the memory function, thus allowing us to obtain the memory function
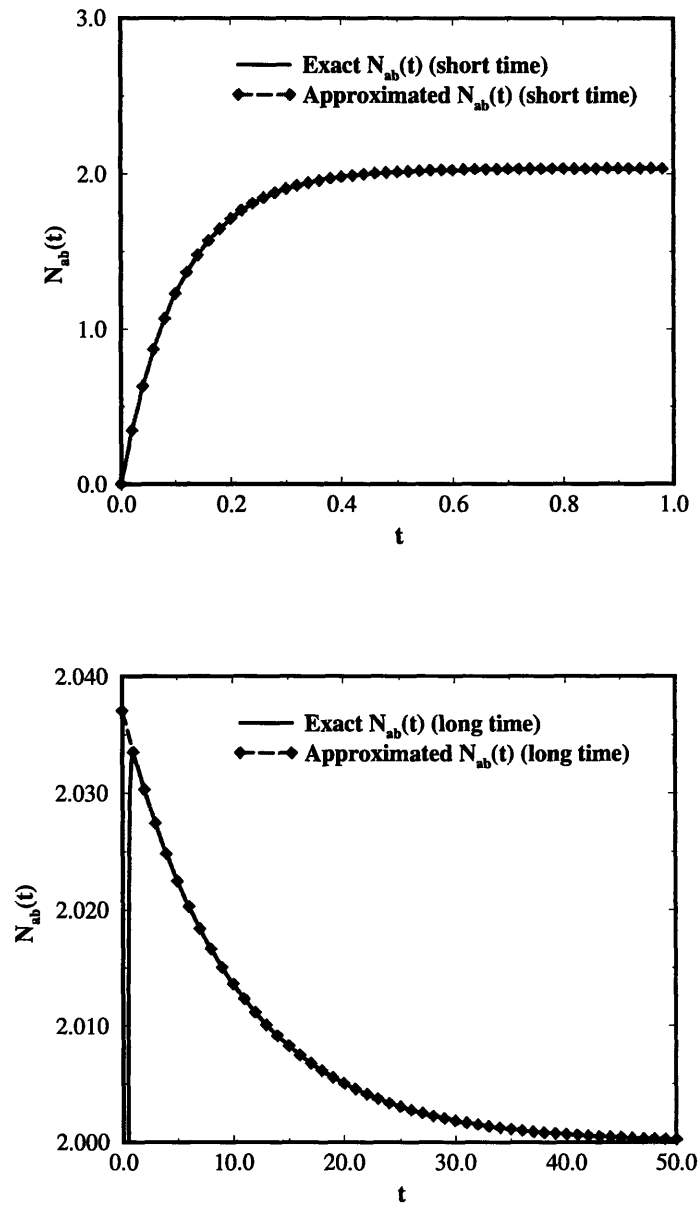
Figure 3-11: Density probability distribution function of on-off sequence $N_{ab}(t)$ for the same model used in Fig. 3-10. (a) The short-time approximation $N_{ab}(t)$ given in Eq. (3.52) agrees well with the result in the short time regime. (b) The long-time approximation $N_{ab}(t)$ given in Eq. (3.52) agrees with the exact result over a wide range of time-scales except for the short time period.

over the whole time domain except for the initial time. The same formalism also leads to the explicit derivation of the echo in the two-event joint probability distribution function (see Appendix 3-B). The three complementary measurements (two-event echo, on-time correlation, and the sequence density) are experimentally feasible and will help to quantify conformational dynamics in single molecule experiments.

3.6 Appendix 3-A: Two-event joint probability distribution function

Two event echo was explored extensively in a recent publication, where an expression for the echo is obtained through the Gaussian approximation.[78] However, the Gaussian rate model is determined by mapping the survival probability computed from the modulated reaction model. The rigorous definition of the stochastic rate in Sec. 3.2 quantifies the mapping and allows us to establish the two-event echo phenomena in a broad context.

Without loss of generality, our analysis is carried out for symmetric reactions with $\Gamma_a = \Gamma_b = \Gamma$ and $K_a = K_b = K$. Numerical calculations of the asymmetric reaction in Sec. 3.3 suggest that the conclusions drawn for symmetric reactions hold for asymmetric reactions. The symmetric reaction can be understood as the limiting case of fast backward rate processes. Applying the Gaussian stochastic approximation to symmetric reactions, we obtain the single-event distribution function

$$\langle k \rangle f(t) = \langle K \exp(-Kt - \Gamma t) K \rangle \approx \{[\langle k \rangle - L(t)]^2 + \chi(t)\} \exp[-\langle k \rangle t + M(t)] \quad (3.53)$$

and the joint distribution function for adjacent on-off events

$$
\begin{aligned}
\langle k \rangle f(t_1, t_2) &= \langle K \exp[-(K + \Gamma)t_1] K \exp[-(K + \Gamma)t_2] K \rangle \\
&\approx \exp[-\langle k \rangle (t_1 + t_2) + M(t_1 + t_2)]\{[\chi(t_1) + \chi(t_2)][\langle k \rangle - L(t_1 + t_2)] \\
&+ [\langle k \rangle - L(t_1) - L(t_2)]\chi(t_1 + t_2) \\
&+ [\langle k \rangle - L(t_1 + t_2)]^2[\langle k \rangle - L(t_1) - L(t_2)]\} \quad (3.54)
\end{aligned}
$$

102

where $L(t) = \int_0^t \chi(\tau)d\tau$. Under the small variance condition, the difference function $\delta(t_1, t_2) = f(t_1, t_2) - f(t_1)f(t_2)$ is approximated by

$$
\begin{aligned}
\delta(t_1, t_2) \approx \; & \chi(0) \exp[-\langle k \rangle (t_1 + t_2)]\{\chi(t_1 + t_2) + \langle k \rangle [L(t_1) + L(t_2) - 2L(t_1 + t_2)] \\
& - \langle k \rangle^2 [M(t_1) + M(t_2) - M(t_1 + t_2)]\},
\end{aligned} \tag{3.55}
$$

which is in the linear order of $\chi(0)$. For further analysis, we assume a single exponential decay form, $\chi(t) = \chi(0) \exp(-\lambda t)$, so that

$$
\delta(t_1, t_2) \approx \chi(0) \frac{\exp[-(\langle k \rangle + \lambda)(t_1 + t_2)]}{\lambda^2} (\langle k \rangle + \lambda - \langle k \rangle e^{2\lambda t_1})(\langle k \rangle + \lambda - \langle k \rangle e^{2\lambda t_2}) \tag{3.56}
$$

Then, the difference function has a maximum at the echo time

$$
t_e = \frac{2}{\lambda} \ln \frac{\langle k \rangle + \lambda}{\langle k \rangle}, \tag{3.57}
$$

and a minimum at the focal time, which is half the echo time, $2t_f = t_e$. The difference function also has a minimum along the t_1 axis and the t_2 axis at the focal time t_e. The small variance expansion implies that the echo amplitude is proportional to the variance of the reaction rate. These features have been confirmed in Ref. [78] with an extensive calculation of multiple channel models and the continuous diffusion controlled reaction model. The prediction of the focal time in the single-event distribution function and of the recurrent behavior in the two-event distribution function helps reveal the nature of conformational landscapes. Similar to the photon echo phenomenon, the recurrence can be understood as the echo signal due to the inhomogeneous distribution of environments, and the conformational modulation can be understood as dephasing.[78] Analogous to motional narrowing, in the fast modulation limit, the echo signal vanishes, and the single exponential law is recovered. The height of the echo signal and its position vary with the modulation rate and can be a sensitive probe of the dynamics disorder resulting from conformational fluctuations.

3.7 Appendix 3-B: On-time correlation function related to sequence counting

The moments of on-time events associated with sequence counting also provide a direct measure of the correlation function of the stochastic rate. As an example, we consider the experimental setup where laser pumping from dark states is constantly applied. In the ensemble of sequences with length t, as shown in Fig. 3-8, the joint distribution function of the first and last on-time events can be expressed as

$$f(t_1, t, t_2) = [k_s N(t)]^{-1} \ \langle \sum_{n=0}^{\infty} KG(t_2) \int dt_1 \cdots \int dt_n KG(t - t_1 - \cdots - t_n)$$

$$KG(t_1) \cdots KG(t_n) KG(t_1) K \rangle, \qquad (3.58)$$

where $G(t) = \exp[-(K + \Gamma)t]$ denotes the evolution of a single on-time event and $N(t)$ is the number density of such sequences. In this ensemble of these sequences, the average on-time of the first event is given as

$$\overline{t_2}(t) = \int_0^\infty dt_1 \int_0^\infty t_2 dt_2 f(t_1, t, t_2)$$

$$\approx \frac{1}{N(t)} + O(\frac{|\Gamma|}{k_s}) \frac{\chi(t)}{k_s^2}, \qquad (3.59)$$

where $1/|\Gamma|$ is defined as the slowest time scale of the conformation dynamics and the small variance of rate fluctuations is assumed in the calculation. So $\overline{t_2}(t)$ is approximately $1/N(t)$ to the zeroth order of the slow modulation limit when $|\Gamma| \ll k_s$, and $\overline{t_1}(t)$ can be shown as the same. The cross moment of these two on-time events is

$$\overline{t_1 t_2}(t) = \int_0^\infty t_1 dt_1 \int_0^\infty t_2 dt_2 f(t_1, t, t_2)$$

$$\approx \frac{1}{k_s N(t)} + O(\frac{|\Gamma|}{k_s})^2 \frac{\chi(t)}{k_s^2}. \qquad (3.60)$$

so that $\overline{t_1 t_2}(t) \approx 1/k_s N(t)$ to the zeroth order of $|\Gamma|/k_s$. Applying the expression of the number density of such sequences $N(t)$ in Eq. (3.43), the correlation between

these two on-time events $Cor(t)$ is

$$
\begin{aligned}
Cor(t) &= \frac{\overline{t_1 t_2}(t) - \overline{t_1}(t)\overline{t_2}(t)}{\overline{t_1 t_2}(0) - \overline{t_1}(0)\overline{t_2}(0)} \\
&= \frac{1/[k_s N(t)] - [1/N(t)]^2}{1/[k_s N(0)] - [1/N(0)]^2} \\
&\approx \chi(t)/k_s^4,
\end{aligned}
\tag{3.61}
$$

which provides another way to measure the memory function of the stochastic rate. The correlation function $Cor(t)$ defined here is different from the $Cor(n)$ discussed in Sec. 3.3. First, $Cor(n)$ is a disrectized function of the number of events while $Cor(t)$ is a continuous function of time. Second, $Cor(n)$ is an event-averaged quantity, which is averaged over all time separations with a given number of intermediate events. Evidently, $Cor(t)$ and $N(t)$ are mixed average of events and time, whereas the average of $Cor(t)$ is performed over all the sequences with length t.

Chapter 4

Single molecule dynamics of semi-flexible Gaussian chains

4.1 Introduction

Single molecule techniques provide a powerful method to measure the conformational structure and dynamics of synthetic and biological polymers. Examples include recent progress in studying the response of single DNA molecules under twisting and stretching and probing the relaxation dynamics of polymers on short time and length scales. One promising candidate for studying these time and length scales in polymers is fluorescence resonant energy transfer spectroscopy (FRET). In these experiments donor and acceptor dye molecules are attached to the polymer at two different points. A laser is used to pump the donor dye to an excited state. Depending on the distance between the donor and acceptor molecule, non-radiative energy transfer from the excited donor dye to the acceptor dye may occur, which results in the fluorescence of the acceptor dye molecule. The light intensity at the fluorescence frequency of the acceptor molecule is strongly dependent on the distance between the two molecules and can be used as a measurement of this distance. With current synthetic techniques, the position of the donor and acceptor dyes on a polymer like DNA can be controlled, which allows us to explore the polymer dynamics on any length scale.[9, 13, 14, 16, 23, 24, 25, 31, 35, 37, 38, 81, 82, 83] This technique has

been used to investigate the denaturation of chymotrypsin inhibitor, the dynamics and folding of single peptides, the fluorescence lifetime distribution of single TMR molecules, etc. [83, 84] A similar technique based on the distance dependence of the electron transfer rate has recently been developed by the Xie group. [23] Using a different set of single molecule techniques, Chu and his coworkers observed the single polymer dynamics in steady shear flow, the relaxation of a single DNA molecule, the response of a flexible polymer to a sudden elongation flow, etc. [52, 53, 54] In comparison with bulk experiments, these single molecule experiments have several advantages, such as the removal of inhomogeneous averaging, the direct observation of intra-molecular dynamics without the subtraction of the solvent background as is done in bulk measurements, and site-specific measurement of a polymer chain. [35] Motivated by the experimental progress, we analyze the information revealed by single molecule measurements and calculate their single molecule quantities based on the Brownian dynamics of semi-flexible ideal Gaussian chains.

An ideal polymer assumes random coil configurations and follows Gaussian chain statistics. Without the explicit consideration of the excluded volume effect and the geometrical constraints, the simple Rouse model treats the connectivity between next neighbor pairs by harmonic bonds. But biological polymers are stiff on the length scale ranging from 5nm for microtubes, 17nm for actin, and up to 50nm for DNA. [37, 38] Most single molecule experiments are performed on length scales where the polymer exhibits some rigidity so that the Rouse Gaussian chain model will have to be extended. In Sec. 4.2, we modify the Gaussian chain model by introducing the persistence length that prevents the polymer from being flexible on all length scales. Similar models for semi-flexible chain have been studied by Kratky and Porod, Harris and Hearse, Freed, Fixman and Kovac, Ha and Thirumalai, and others. [85, 86, 87, 88, 89, 90, 91, 92, 93] Interest in these semi-flexible chain models is revived by the effort to model single molecule force measurements of proteins and DNAs. Our emphasis here is to formulate the semi-flexible model using the analogue to the Ornstein-Uhlenbeck random walk process and thus incorporate the persistence length into the Rouse model in a natural and rigorous way.

In order to interpret single molecule experiments and extract the desired information on polymers, we need to calculate the dynamics of semi-flexible chains. In Sec. 4.3, we solve the Brownian dynamics by performing a normal mode decomposition of the Langevin equation of a polymer chain. This normal mode decomposition is similar to the standard decomposition performed in the Rouse and Zimm models, with a modification to account for the short length scales that this chapter considers. The model calculation can be elaborated by including excluded volume and hydrodynamic effects under a similar approximation made in the Zimm model. [94, 95] Using the normal mode approach, we calculate distance-distance correlation functions that are relevant for single molecule measurements.

In FRET experiments, people can measure the separation of two dye molecules attached to the polymer chain. The fluorescence energy transfer reaction usually occurs on a nano-second time scale while the intra-chain relaxation takes milli-second or even longer. [16, 82, 83] Hence the FRET lifetime as well as the FRET efficiency is a "snap-shot" of the transient configuration. The correlations of the FRET lifetime and the FRET efficiency reveal the slow intra-chain relaxation process that modifies the donor-acceptor distance. In Sec. 4.4.1, the distribution of E is derived to show different features to distinguish collapsed and coiled conformations. In Sec. 4.4.1 and Sec. 4.4.2, the FRET efficiency and the lifetime correlation functions are formulated for the semi-flexible chain model introduced in Sec. 4.2. These two correlation functions are directly related to the distance correlation function characterizing the intra-chain motion, and thus provide experimentally reliable measures to probe the conformational dynamics. Furthermore, each measurement of the donor-acceptor distance in real experiments corresponds to a large number of polymer configurations. To differentiate them, the instantaneous diffusion coefficient is calculated in Sec. 4.4.3 to probe the variation of the donor-acceptor distance with time, and yielding information about the mean square distance as well as instantaneous distance between the dye molecules.

To model FRET experiments, we treat the reaction dynamics as a convolution of the polymer motions and the actual energy transfer event which depends on the

separation between probes. Without the intra-chain motion, each fluorescence lifetime τ corresponds to a specific donor-acceptor distance R_{nm}. And the fluorescence lifetime distribution function directly reflects the equilibrium distribution of intra-fluorophore distance. [83] However, the slow intra-chain slightly modifies this correspondence and brings another configuration-dependent weighting factor. In Sec. 4.5, the FRET lifetime in the fast reaction limit is discussed to incorporate the intra-chain motion during the energy transfer reaction. Inhomogeneous cumulant expansion of τ leads to a weighted inhomogeneous reaction time, which serves as a perturbative correction to the static lifetime $\tau = K^{-1}$. Thus through single-molecule lifetime measurements one can map out the distance distribution function even with intra-chain relaxation.

The single molecule spectroscopy and imaging directly track the Brownian dynamics of polymers in solution, which determines the viscoelasticity property from the correlation function of single molecules. The single molecule approach has become known as microrheology in analogy to rheology which studies the viscoelasticity behavior through the response of the bulk material to applied mechanical perturbation. [96, 97] Evidently, rheology and microrheology measurements are related to each other, and this relationship will be explained in Sec. 4.6 through the example of the intrinsic viscosity. The theoretical calculation of polymer viscosity has a long history, ranging from Kirkwood's classical treatment, to the formulation by Fixman, Bixon and Zwanzig, etc. [98, 99, 100, 101] In Sec. 4.6, we relate the correlation function of intra-chain dynamics on the single polymer to intrinsic viscosity and evaluate the viscosity explicitly with the consideration of the persistence length. Our expression for the intrinsic viscosity is related to the correlation function formula discussed by Felderhof, Deutch, and Titulaer, [102] but is further simplified for the application to single molecule measurements of Gaussian chain dynamics.

4.2   Semi-flexible Gaussian chains

Before calculating the dynamics, we first develop the Gaussian model with a persistence length. Consider a discretized version of a continuous polymer chain without

explicit account of the excluded volume effects. The nth unit of the polymer is at a position denoted $\mathbf{r}_n$. The bond vector $\mathbf{u}_n = \mathbf{r}_n - \mathbf{r}_{n-1}$ separates two neighboring units of the polymer chain. It should be noted that the bond vector does not correspond to an actual chemical bond nor do the sub-units correspond to a single monomer.

Although the focus of this chapter will be on single polymer dynamics, we start by examining the equilibrium distribution of the polymer chain. Averaging $\mathbf{u}$ and $\mathbf{u}^2$ over all possible orientations gives $\langle \mathbf{u}_n \rangle = 0$ and $\langle \mathbf{u}_n^2 \rangle = a_0^2$ with a_0 the bond length. To describe the rigidity of the polymer chain, we define the correlation between two bonds as $\langle \mathbf{u}_n \mathbf{u}_m \rangle = a_0^2 b^{|n-m|}$ with $0 < b < 1$. If $b = 1$, every $\mathbf{u}_n$ must point in the same direction resulting in a rigid rod. If $b = 0$, there is no correlation between two bond vectors and the chain is an ideal Gaussian chain on all length-scales. The total length of the polymer is the sum of all the individual bond vectors, $\mathbf{R} = \sum_{n=1}^{N-1} \mathbf{u}_n$, where $N - 1$ is the number of bond vectors. Using the relations between bond vectors we have $\langle \mathbf{R} \rangle = 0$ and

$$\langle \mathbf{R}^2 \rangle = \sum_{nm} \langle \mathbf{u}_n \mathbf{u}_m \rangle = \left[\frac{(1+b)}{(1-b)}(N-1) - 2b\frac{(1-b^{N-1})}{(1-b)^2} \right] a_0^2. \tag{4.1}$$

In most applications to polymers the second term would be neglected because of the large N limit, which gives us the expected result $\langle \mathbf{R}^2 \rangle = L_k(N-1)a_0^2$ where $L_k = (1+b)/(1-b)$ is the Kuhn length. The persistence length is related to the Kuhn length by $L_p = L_k/2$. Taking the continuous limit of the discretized model we have $b = \exp(-1/L_p)$ and $\langle \mathbf{u}(s)\mathbf{u}(s') \rangle = a_0^2 \exp(-|s - s'|/L_p)$. where the variables s and s' are the continuous analogue of the index for the sub-units and allow us to trace the positions of the sub-units on the polymer. In the continuous limit, the expression for $\langle \mathbf{R}^2 \rangle$ becomes

$$
\begin{aligned}
\langle \mathbf{R}^2 \rangle &= \int_0^{N-1} \int_0^{N-1} ds\,ds' \exp(-|s - s'|/L_p) \\
&= 2a_0^2 L_p(N-1) - 2a_0^2 L_p^2 [1 - e^{-(N-1)/L_p}]
\end{aligned}
\tag{4.2}
$$

For the long chain length limit we get the expected scaling relation for a random

Gaussian chain $\langle \mathbf{R}^2 \rangle = 2(N-1)L_p a_0^2$. In the short chain length limit, we also have the expected relationship for a rigid rod $\langle \mathbf{R}^2 \rangle = (N-1)^2 a_0^2$.

It is known that the Gaussian process with exponential-decay correlation defines the Ornstein-Uhlenbeck process. The three-dimensional equilibrium distribution function is denoted as $P_{eq}(\mathbf{u}) \propto \exp[-\beta U]$ with the exponential functional given by

$$\beta U(\mathbf{u}) = \frac{3}{2a_0^2(1-b^2)} \sum_{n=1}^{N-2} (\mathbf{u}_{n+1} - b\mathbf{u}_n)^2 + \frac{3\mathbf{u}_1^2}{2a_0^2}. \tag{4.3}$$

where U is understood as the potential energy of the Gaussian chain. For the purpose of further calculations, the potential function can be cast into

$$
\begin{aligned}
\beta U &= \frac{3}{2a_0^2(1-b^2)} \sum_{n=1}^{N-2} [(\frac{1+b}{2})^2 (\mathbf{u}_{n+1} - \mathbf{u}_n)^2 + (1-b)^2 (\frac{\mathbf{u}_{n+1} + \mathbf{u}_n}{2})^2] \\
&\quad + \frac{3}{4a_0^2}(\mathbf{u}_{N-1}^2 + \mathbf{u}_1^2) \\
&= \frac{3}{4a_0^2} \sum_{n=1}^{N-2} [L_p(\mathbf{u}_{n+1} - \mathbf{u}_n)^2 + \frac{1}{L_p}(\frac{\mathbf{u}_{n+1} + \mathbf{u}_n}{2})^2] + \frac{3}{4a_0^2}(\mathbf{u}_{N-1}^2 + \mathbf{u}_1^2) \quad (4.4)
\end{aligned}
$$

where L_p is the persistence length defined earlier. Note the extra terms for the initial and final vectors $\mathbf{u}_1$ and $\mathbf{u}_{N-1}$ in Eq. (4.4) are necessary for satisfying the chain homogeneity, i.e., the length of each bond is constant on average. The Boltzmann distribution generated from this potential function rigorously reproduces the Gaussian statistics as introduced in Eq. (4.1). For a long Gaussian chain, we take the continuous limit as

$$\beta U[\mathbf{u}(s)] = \frac{3}{4a_0^2} [\int_0^{N-1} ds L_p (\frac{\partial \mathbf{u}}{\partial s})^2 + \frac{1}{L_p}\mathbf{u}^2] + \frac{3}{4a_0^2}(\mathbf{u}_{N-1}^2 + \mathbf{u}_1^2), \tag{4.5}$$

where the bond index is treated as a continuous variable. Clearly, from Eq. (4.5), the semi-flexible model exhibits the same long chain asymptotic behavior as the original Rouse modes as well as the proper behavior for a stiff rod on shorter length scales.

Similar results have also been obtained by Winkler, Reineker, and Harnau [103] using the maximum entropy method and by Ha and Thirumalai [93] using a mean-field

approach. As noted by Lagowski, Noolandi, and Nickel, [104] the Gaussian chain thus generated is homogeneous and has an exponential decay correlation, which are the properties of the Ornstein-Uhlenbeck process. Earlier adaptations of the process to stiff chains treat the boundaries differently and do not lead to the chain homogeneity implied in the Gaussian statistics.

4.3 Brownian dynamics of semi-flexible chains

Single molecule experiments measure trajectories of intra-chain motions of polymers, and the interpretation of such measurements is helped by model calculations of polymer dynamics. The Brownian motion of a polymer chain is governed by the Langevin equation for each bead,

$$\zeta \dot{\mathbf{r}}_n = -\nabla_n U + \mathbf{f}_n \tag{4.6}$$

where $\mathbf{f}_n$ is the random force with local Gaussian distribution, $\langle \mathbf{f}_n(t) \rangle = 0$, and $\langle f_{n\alpha}(t) f_{m\beta}(t') \rangle = 2\zeta k_B T \delta_{mn} \delta_{\alpha\beta} \delta(t-t')$. Although the equations of motion are straightforward, the solutions to these equations are not trivial. To make the problem more tractable, we define normal modes so that the dynamics of each mode are independent and the equations of motion for these modes are simplified. For the flexible Gaussian polymer chain, one usually defines the Rouse normal modes, which have a Fourier decomposition into functions of the form $\cos(\pi p n/N)$, where n is the bead index, N is the total number of beads, and p is an integer denoting the normal modes. The $\sin(\pi p n/N)$ components are zero by the requirement that the derivative be zero at the end points of the polymer chain. Because the applications that we are examining are for semi-flexible chains, it is advantageous to modify the Rouse mode to treat the end units more rigorously. The normal modes are defined as

$$\mathbf{r}_n = \mathbf{x}_0 + 2 \sum_{p=1}^{N-1} \mathbf{x}_p \cos[(n - \frac{1}{2})\frac{p\pi}{N}] \tag{4.7}$$

113

where p is an integer denoting the modes. This definition removes the artificial constraint on the end point derivatives previously imposed in the Rouse normal mode decomposition. For the semi-flexible Gaussian chain, the normal modes defined in Eq. (4.7) approximately diagonalize the potential and simplify the dynamics of the polymer chain (see Appendix 4-A). The equation of motion for the pth mode becomes

$$\zeta_p \frac{\partial \mathbf{x}_p}{\partial t} = -\lambda_p \mathbf{x}_p + \mathbf{f}_p \tag{4.8}$$

where

$$\lambda_p = \frac{24Nk_BT}{a_0^2} \sin^2 \frac{p\pi}{2N}(2L_p \sin^2 \frac{p\pi}{2N} + \frac{1}{2L_p}\cos^2 \frac{p\pi}{2N}), \tag{4.9}$$

$$\zeta_p = 2N\zeta - \delta_{0,p}N\zeta, \tag{4.10}$$

$$\langle f_{p\alpha}(t)f_{q\beta}(t')\rangle = 2\delta_{pq}\delta_{\alpha\beta}\zeta_p k_B T\delta(t - t'). \tag{4.11}$$

Evidently, the random force acts on each mode independently and satisfies the fluctuation-dissipation relation.

The concept of normal modes in polymer dynamics has been directly applied to the interpretation of single molecule experiments. For example, Winkler has calculated the normal mode relaxation dynamics of stretched flexible chain molecules,[105] which agrees with Chu's experimental data. [52] In the limit $L_p \to 1/2$, the normal modes given above recover the Rouse model discussed in standard textbooks.[95] For a rigid-rod like polymer, $L_p \to \infty$, all the normal modes will be suppressed, keeping only the center of mass motion. Exact numerical solution of the original equation of motion in Eq. (4.6) will keep both the translational and rotational motion of the rigid rod.

Through the Brownian dynamics of the semi-flexible chain, one can relate single molecule FRET measurements to the correlations between the sites on the polymer chain where two dye molecules are attached. We define the distance between the two beads on the polymer chain $\mathbf{R}_{nm} = \mathbf{r}_n - \mathbf{r}_m$, where m and n correspond to the index of the two points on the polymer chain. In terms of normal modes we can express

114
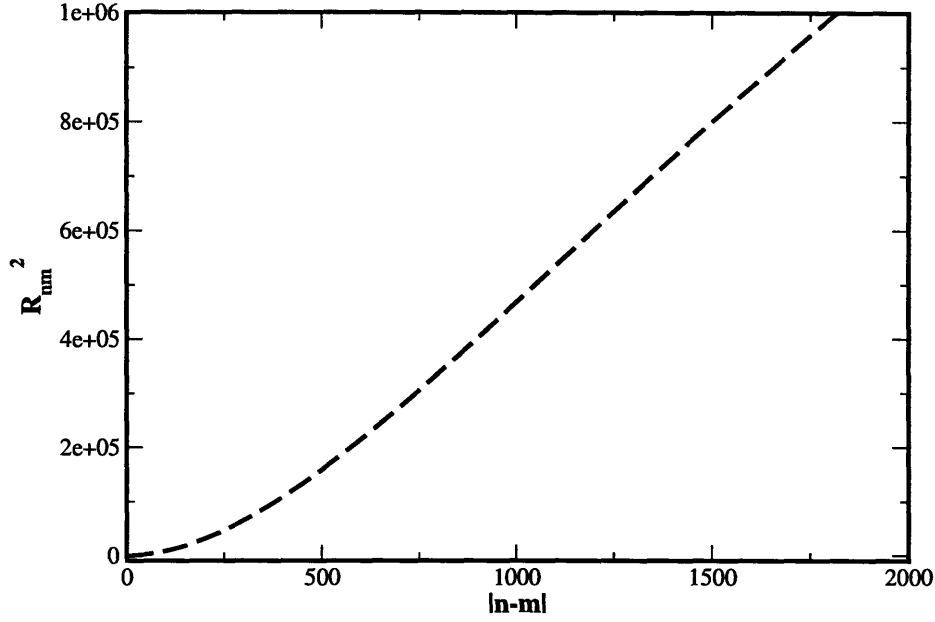
Figure 4-1: The mean square distance between the nth and the mth beads given in Eq. (4.61) for a polymer chain with 5000 beads. Here a_0 is taken as the unit length and the persistence length L_p is taken as 500. As shown in Eq. (4.71), R^2_{nm} has a quadratic dependence on $|n - m|$ for $|n - m| \ll L_p$, and is proportional to $|n - m|$ for $|n - m| \gg L_p$.

this quantity as

$$\mathbf{R}_{nm} = \sum_{p=1}^{N-1} c^p_{nm} \mathbf{x}_p \quad with \quad c^p_{nm} = -4 \sin \frac{p\pi}{2N}(n - m) \sin \frac{p\pi}{2N}(n + m - 1). \quad (4.12)$$

The propagation of the normal modes follows the Smoluchowski equation in a quadratic potential (see Appendix 4-A). The correlation between $\mathbf{R}_{nm}(0)$ and $\mathbf{R}_{nm}(t)$ is

$$\langle \mathbf{R}_{nm}(t) \cdot \mathbf{R}_{nm}(0) \rangle = \sum_{p=1}^{N-1} (c^p_{nm})^2 \frac{3k_B T}{\lambda_p} \exp[-\frac{\lambda_p}{\zeta_p} t]. \quad (4.13)$$

At $t = 0$, the above expression gives the mean square distance between the nth and the mth beads along the chain, R^2_{nm}, as is given in Eq. (4.61). Direct evaluation of the sum in the equation is plotted in Fig. 4-1, where R^2_{nm} shows a quadratic dependence on $|n - m|$ for small $|n - m|$ and a linear dependence on $|n - m|$ for large $|n - m|$.

115

1. In the short time region, summation over the first-order Taylor expansion of each exponential function leads to

$$\langle \mathbf{R}_{nm}(t) \cdot \mathbf{R}_{nm}(0) \rangle = \langle \mathbf{R}_{nm}^2 \rangle - 6Dt, \ \ with \ D = \frac{k_B T}{\zeta}, \tag{4.14}$$

so each bead undergoes instantaneous diffusive motion in three-dimensional space without feeling the interaction of the polymer chain. This short time behavior does not depend on the persistence length and exists in the ideal Rouse chain as well.

2. In the intermediate time region, each normal mode decays with various rates, and contributes jointly to the correlation function $\langle \mathbf{R}_{nm}(t) \cdot \mathbf{R}_{nm}(0) \rangle$. For different degrees of stiffness, the correlation function has different time scales. In the large N limit, the summation over p can be approximated by an integral from 1 to infinity, resulting in

$$\langle \mathbf{R}_{nm}(t) \cdot \mathbf{R}_{nm}(0) \rangle = \begin{cases} \frac{2a_0^2}{\pi} L_p^{3/2}(n-m)^2 \ t^{*\,-1/2}\Gamma(\frac{1}{2}, \frac{\pi^2 t^*}{4N^2 L_p}), & L_p \ll N; \\ \frac{a_0^2}{2\sqrt{2\pi}} L_p^{-3/4}(n-m)^2 \ t^{*\,1/4}\Gamma(-\frac{1}{4}, \frac{\pi^4 L_p t^*}{4N^4}), & L_p \geq N, \end{cases} \tag{4.15}$$

where $t^* = 6Dt/(a_0^2)$ is the reduced time, and $\Gamma(\alpha, z) = \int_z^\infty x^{\alpha-1}\exp(-x)dx$ is the incomplete Gamma function. As shown in Fig. 4-2, the normalized distance correlation function $\phi(t) = \langle \mathbf{R}_{nm}(t) \cdot \mathbf{R}_{nm}(0) \rangle / \langle \mathbf{R}_{nm}^2 \rangle$ decays non-exponentially for both flexible and stiff chains. The decay time increases with the persistence length.

3. In the long time region, only the slowest mode survives, and the correlation function becomes

$$\langle \mathbf{R}_{nm}(t) \cdot \mathbf{R}_{nm}(0) \rangle = (c_{mn}^1)^2 \frac{3k_B T}{\lambda_1} \exp[-\frac{\zeta_1}{\lambda_1}t], \tag{4.16}$$

which represents the fundamental relaxation mode of the polymer chain.

At this point, the model that we have constructed is similar to the Rouse model,
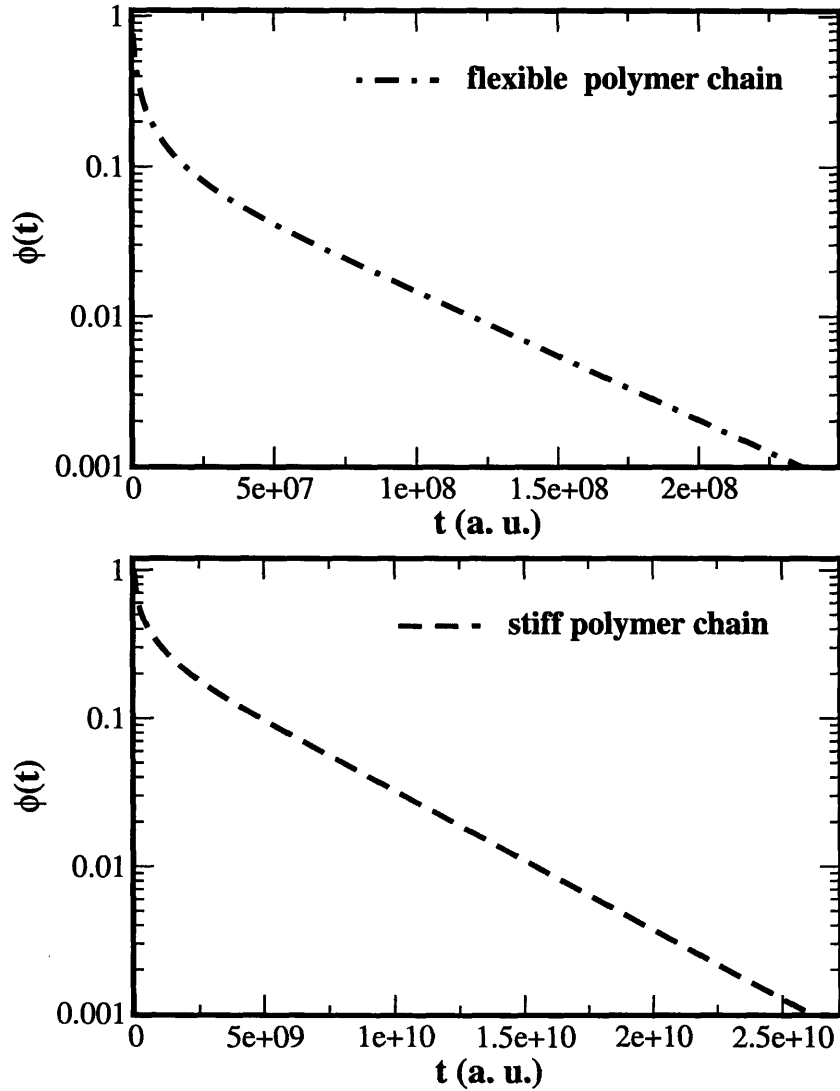
Figure 4-2: Log-plot of the normalized distance correlation function $\phi(t)$ for a polymer chain with 5000 beads. $L_p = 5$ for the flexible chain and $L_p = 500$ for the stiff chain. $\zeta a_0^2/6k_B T$ is taken as the time unit. $\phi(t)$ decays non-exponentially with time. Obviously $\phi(t)$ decays on a much longer time scale for the stiff chain than for the flexible chain.

where the only interactions are those dictated by the connectivity of the polymer. It is known that the Rouse model does not reproduce experimental results because spatial interactions between two monomers separated by large distances along the polymer backbone are important. To develop a more realistic polymer model, we should include real polymer interactions like hydrodynamic and excluded volume effects. These effects can be included by similar approximations introduced in the Zimm model. We discuss hydrodynamic interactions briefly in Appendix 4-D.

From the analysis above, it is apparent to note that the inter-fluorophore distance $\mathbf{R}_{nm}$ follows an effective diffusion process, with the Green's function in Eq. (4.65) characterizing a Gaussian process with non-exponential correlation. $\int_0^\infty \phi(t)dt$ provides a time scale for the effective diffusion, the effective diffusion coefficient in the potential of mean force can be formulated as $6D_{eff}\int_0^\infty \phi(t)dt = \langle \mathbf{R}_{nm}^2 \rangle$, which is generally different from the diffusion coefficient $2D$ used in Pastor, Zwanzig and Szabo's work,[47] where $D = k_B T/\zeta$ is the diffusion coefficient for each polymer bead. As discussed later in Sec. 4.4.3, the diffusion coefficient $2D$ only reflects the diffusive motion of each polymer bead independently and contains no information about the collective motion of the polymer chain.

4.4 Single Molecule FRET of semi-flexible chains

Single molecule fluorescence resonant energy transfer (FRET) allows us to measure the separation of donor and acceptor dye pairs on a single polymer chain. In a simple experimental set-up, the donor and acceptor are located on specific sites on the polymer chain. According to Förster theory, resonant energy transfer is mediated by the dipole-dipole interaction, and the transfer rate depends on the donor-acceptor separation as $K(R) \propto 1/R^6$. The inverse sixth-power law leads to a sensitive probe of intra-chain dynamics, which has been exploited extensively in recent single molecule experiments. To interpret the FRET experiments and extract the desired information, we calculate single molecule quantities for the intra-polymer energy transfer process, which is controlled by the polymer conformations.

4.4.1 Distribution and correlation function of FRET efficiency

With the help of two photon-counting detection channels, one can track the real-time evolution of intra-molecular and inter-molecular distances of a freely diffusing individual macromolecule.[35] The instantaneous FRET efficiency $E(t)$ is calculated from the donor and acceptor emission intensities I_d and I_a, using the formula $E = [1 + \gamma I_d/I_a]^{-1}$, where γ is a correction factor. According to the Förster theory, the efficiency E has a strong dependence on the inter-fluorophore distance, $E = [1 + (R/R_F)^6]^{-1}$, where R_F is the Förster radius. The Förster energy transfer occurs on nano-second scale, whereas conformational changes of polymers usually occur on milli-second scale or even longer. Therefore the donor and acceptor fluorophores quickly reach kinetic equilibrium under a laser pump, and hence the efficiency E provides "snap-shots" of the polymer configurations over time. The correlation of the FRET efficiency, defined as,

$$C_{nm}(t) = \frac{\langle E(t)E(0)\rangle - \langle E\rangle^2}{\langle E^2\rangle - \langle E\rangle^2},$$ (4.17)

provides additional information on conformational dynamics on a large time scale that is difficult, and sometimes impossible, to obtain by conventional techniques.[16]

For the semi-flexible Gaussian chain introduced in Sec. 4.2, we evaluate the correlation function explicitly. Assuming that the donor and acceptor dye molecules are attached to the nth and the mth beads of a single semi-flexible polymer chain, the FRET efficiency E is related to the inter-fluorophore distance R_{nm} by

$$E(R_{nm}) = \frac{1}{1 + (R_{nm}/R_F)^6}.$$ (4.18)

The inter-fluorophore distance R_{nm} is governed by the Brownian motion of the poly-

mer chain. The equilibrium distribution and evolution derived in Appendix 4-B are

$$P_{eq}(\mathbf{R}_{nm}) = [\frac{2\pi}{3}\langle\mathbf{R}_{nm}^2\rangle]^{-3/2}\exp\left\{-\frac{3\mathbf{R}_{nm}^2}{2\langle\mathbf{R}_{nm}^2\rangle}\right\}, \qquad (4.19)$$

$$G(\mathbf{R}_{nm}(t),t|\mathbf{R}_{nm}(0)) = \left[\frac{2\pi}{3}\langle\mathbf{R}_{nm}^2\rangle(1-\phi(t)^2)\right]^{-3/2}$$

$$\exp\left\{-\frac{3(\mathbf{R}_{nm}(t)-\phi(t)\mathbf{R}_{nm}(0))^2}{2\langle\mathbf{R}_{nm}^2\rangle(1-\phi(t)^2)}\right\}, \qquad (4.20)$$

where $\phi(t)$ is the normalized correlation function of the inter-fluorophore distance given in Eq. (4.62) of Appendix 4-B. Thus the average efficiency and the correlation function can be explicitly evaluated as

$$\langle E\rangle = \int d^3\mathbf{R}_{nm}E(R_{nm})P_{eq}(\mathbf{R}_{nm})$$

$$C_{nm}(t) = \int\int d^3\mathbf{R}_{nm}(t)d^3\mathbf{R}_{nm}(0)E(R_{nm}(t))E(R_{nm}(0))$$

$$G(\mathbf{R}_{nm}(t),t|\mathbf{R}_{nm}(0))P_{eq}(\mathbf{R}_{nm}) \qquad (4.21)$$

For small R_F, we can approximate the expression Eq. (4.18) as a delta-function and show that

$$\langle E\rangle \propto \left[\frac{\langle R_{nm}^2\rangle}{R_F^2}\right]^{-3/2}, \qquad (4.22)$$

$$C_{nm}(t) \sim [1-\phi^2(t)]^{-3/2}-1. \qquad (4.23)$$

In real experiments, the FRET efficiency measurement is mainly performed in the regime where $R_{nm} \leq R_F$ and the efficiency is sensitive to the inter-fluorophore distance only in the close vicinity of R_F. Although it is difficult to obtain the analytical expression of the FRET efficiency correlation function under such condition, a numerical example plotted in Fig. 4-3 still shows the close relation between $C_{nm}(t)$ and $\phi(t)$. We have plotted three different cases in Fig. 4-3, $\langle R_{nm}^2\rangle \ll R_F^2$ for a flexible chain, $\langle R_{nm}^2\rangle \sim R_F^2$ for a short stiff chain, and $\langle R_{nm}^2\rangle \gg R_F^2$ for a long stiff chain. In the short time limit, $C_{nm}(t)$ is a combination of all the relaxation modes, while in the long time limit, only the fundamental mode exists. As shown in Fig. 4-3, $C_{nm}(t)$
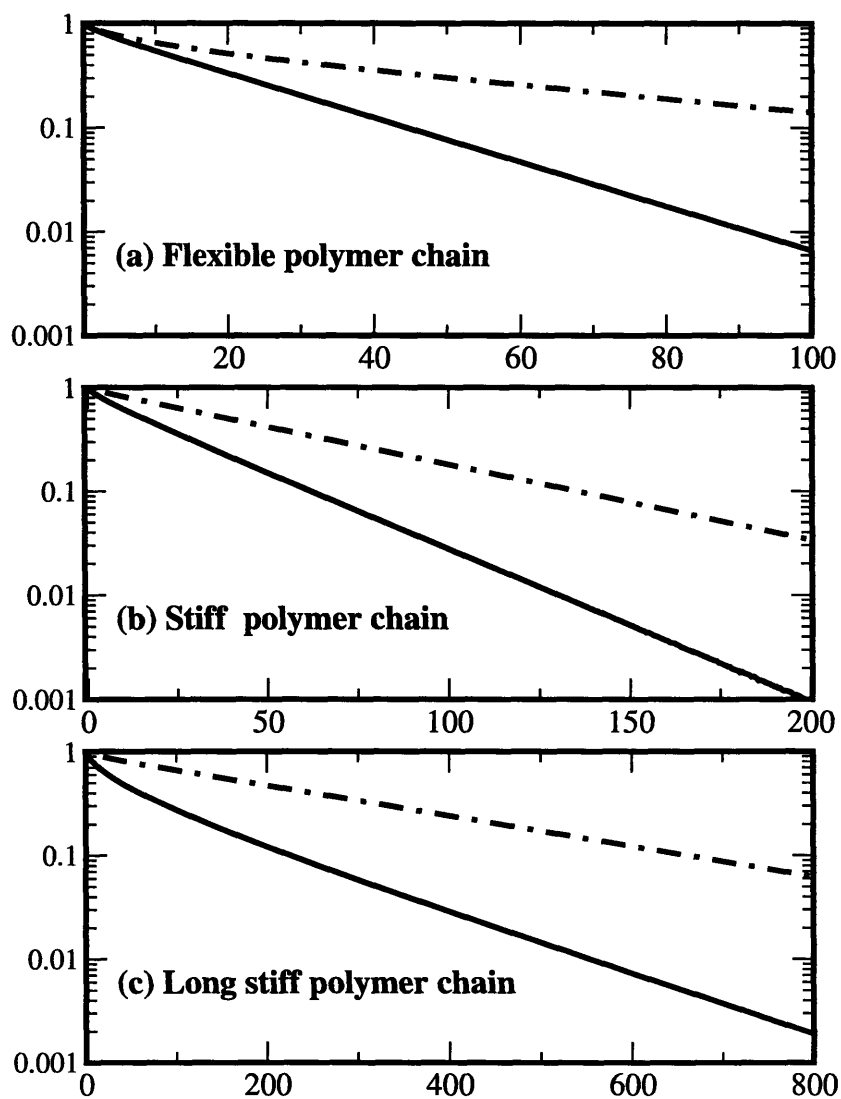
Figure 4-3: Comparison of the FRET efficiency correlation function $C_{nm}(t)$ for various $\langle R_{nm}^2 \rangle$. a_0 and $\zeta a_0^2/6k_BT$ are taken as the length unit and the time unit, respectively. The Förster radius R_F is taken to be 5. The solid lines are the efficiency correlation functions, and the dot-dashed lines are the corresponding distance-distance correlation function $\phi(t)$. (a) Flexible chains with $N = 10$, $L_p = 0.5$. (b) Stiff chains with $N = 10$, $L_p = 2.0$. (c) Long stiff chains with $N = 20$, $L_p = 2.0$.
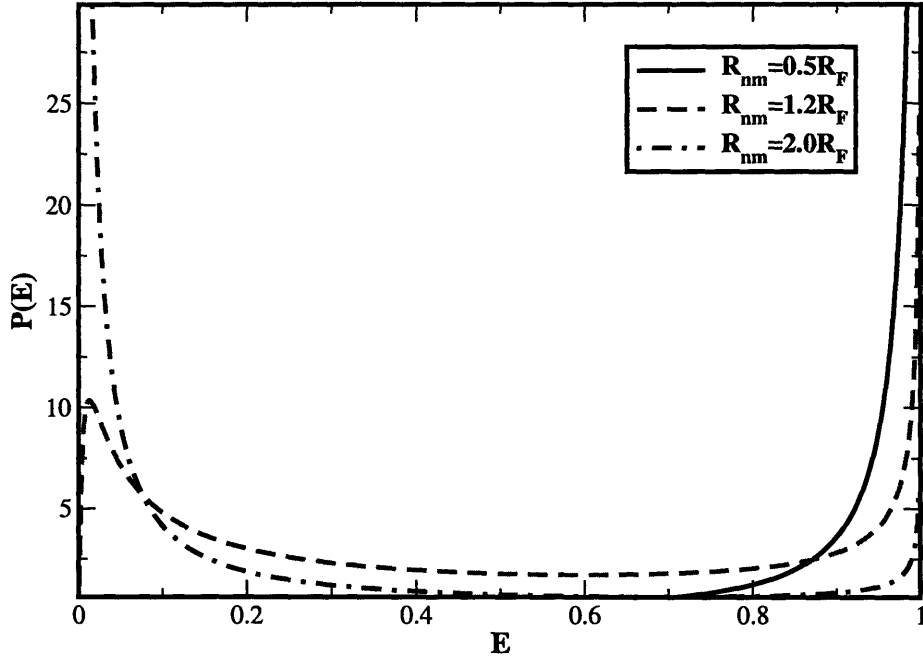
Figure 4-4: The distribution of the FRET efficiency with the Förster radius R_F as the length unit. $R_{nm} = |\mathbf{R}_{nm}|$ is the mean square root of the donor-acceptor distance. As R_{nm} increases from $0.5R_F$ to $2.0R_F$, the distribution shifts from the uni-modal distribution around $E = 1$, to the bi-modal distribution, and then to the uni-modal distribution around $E = 0$.

always decays on the same time scale as that of $\phi(t)$ for various stiffness and chain lengths, thus providing a good probe of the intra-chain dynamics.

Besides the FRET efficiency correlation function, the distribution function of the efficiency is also a good measure of the chain stiffness. In general, the efficiency distribution is obtained by transforming the equilibrium distribution of R_{nm} into the efficiency E of Eq. (4.18) as

$$P(E) = \sqrt{\frac{3}{2\pi}} \frac{R_F^3}{\langle \mathbf{R}_{nm}^2 \rangle^{3/2}} (1 - E)^{-1/2} E^{-3/2} \exp[-\frac{3R_F^2}{2\langle \mathbf{R}_{nm}^2 \rangle} (\frac{1 - E}{E})^{1/3}]. \quad (4.24)$$

As shown in Fig. 4-4, plots of the efficiency distribution with different mean square inter-fluorophore distance display different features. As the mean square inter-fluorophore distance increases, the FRET efficiency sharply shifts from the uni-modal peak at $E = 1$, to the bi-modal distribution, and then to the uni-modal peak at $E = 0$. These

features are explored numerically by Srinivas and Bagchi to distinguish the disordered and ordered conformations.[106] The complicate feature of the efficiency distribution implies that the average efficiency $\langle E \rangle$ does not provide enough information of the distribution.

In a recent experiment, Weiss and his coworkers investigated the single enzyme Staphylococcal nuclease with FRET. The instantaneous FRET efficiencies $E(t)$ and the correlation functions $C_{nm}(t)$ were evaluated for 100 labeled Staphylococcal nuclease molecules.[16] It was observed that the correlation functions had a wide distribution of time constants, which demonstrates the complexity of the intra-chain motion.

4.4.2 Correlation of FRET lifetime

Optical methods developed recently are capable of tracking single molecules under physiological conditions in real time. The environmental changes of individual molecules induce the conformational changes of molecular configurations on a much longer time scale than energy transfer. As a result, the dynamical tracking of lifetime information provides a measure of individual molecules in non-equilibrated and heterogeneous systems, and offers details of single molecule dynamics that are usually hidden in conventional ensemble measurements.

The decay of the fluorescence on the donor includes radiative decay and non-radiative energy transfer,

$$K = \frac{1}{\tau_D}[1 + (\frac{R_{nm}}{R_F})^{-6}], \tag{4.25}$$

where R_F is the Förster radius and τ_D is the fluorescence lifetime without acceptor. Since the intra-chain dynamics occurs on a much longer time scale than the FRET process, the polymer configuration remains the same when the FRET occurs, hence the lifetime is a "snap-shot" at the transient conformation,

$$\tau \approx \frac{1}{K} = \frac{\tau_D}{1 + (R_{nm}/R_F)^{-6}}. \tag{4.26}$$

Continuous "snap-shots" of transient configurations reveals the correlation between two configuration-controlled lifetimes, which reflects the slow intra-chain motion that modifies the donor-acceptor distance R_{nm}. The lifetime correlation function is defined as

$$C_{nm}(t) = \frac{\langle \tau(t)\tau(0) \rangle - \langle \tau \rangle^2}{\langle \tau^2 \rangle - \langle \tau \rangle^2}, \tag{4.27}$$

where $\langle \cdots \rangle$ is the average over various initial configurations of a given pair, and the configuration-controlled lifetime τ is related to the energy transfer efficiency E discussed in the previous section as $\tau = \tau_D(1 - E)$. Therefore, the lifetime correlation function is exactly the same as the efficiency correlation function in Eq. (4.17), which can be used to monitor the intra-chain dynamics at the single-molecule level.

The efficiency measurement discussed in the previous section and the lifetime measurement determine the similar quantities. Both measurements utilize the separation of the time scales for the reaction and the diffusion processes to detect the dynamical evolution of micro-environments at the single-molecule level. The lifetime method requires only one detection channel but with high time resolution usually in nanosecond scale, while the efficiency measurement requires simultaneously tracking donor and acceptor emissions but with relatively lower time resolution. Both methods are experimentally reliable for monitoring the intra-chain motion in real time.

4.4.3 Instantaneous diffusion coefficient

In FRET measurements, the experimental sample with the attached donor and acceptor dyes is either adsorbed to the glass surface or prepared in solution. Fluorescence images of the sample are detected by scanning the confocal volume, and photo-bleaching curves of donor and acceptor are simultaneously recorded with an integration time t_{bin}. As a result, the trajectories of the distance between two dyes are obtained. Each measurement of the inter-fluorophore distance R_{nm} can correspond to a large number of polymer configurations. To differentiate them, the variation of the distance with respect to time is examined in order to understand the dynamic

124

heterogeneity of structure. [82] The instantaneous diffusion coefficient measured in these experiments is defined as

$$\overline{D}(R_{nm}(0)) = \frac{1}{6t_{bin}}\langle(\mathbf{R}_{nm}(t_{bin}) - \mathbf{R}_{nm}(0))^2\rangle_G, \tag{4.28}$$

where t_{bin} is the experimental bin time due to the finite time resolution and $\langle\cdots\rangle_G$ stands for the integration over the Green's function for a fixed initial separation $R_{nm}(0)$. For the semi-flexible polymer chain, we are able to evaluate instantaneous diffusion coefficient directly with the Green's function in Appendix 4-B, giving

$$\overline{D}(R_{nm}(0)) = \langle\mathbf{R}_{nm}^2\rangle\frac{1 - \phi^2(t_{bin})}{6t_{bin}} + \mathbf{R}_{nm}^2(0)\frac{[1 - \phi(t_{bin})]^2}{6t_{bin}}. \tag{4.29}$$

This expression of $\overline{D}(R_{nm}(0))$ is a general result for any Gaussian process and implies:

1. As t_{bin} approaches 0, only the first term survives and the instantaneous diffusion coefficient reduces to $2D = 2k_BT/\zeta$, which describes the independent diffusive motions of the donor and acceptor sites and does not provide any information of the chain-configurations or the interactions.

2. As t_{bin} approaches ∞, averaging Eq. 4.29 over the initial position $\mathbf{R}_{nm}(0)$ yields the relation in the long time limit, $6\overline{D}t_{bin} = 2\langle\mathbf{R}_{nm}^2\rangle = \langle(\mathbf{R}_{nm}(t_{bin}) - \mathbf{R}_{nm}(0))^2\rangle$, where $\overline{D}$ is the diffusion coefficient of polymer beads.

3. The mean square distance in equilibrium $\langle\mathbf{R}_{nm}^2\rangle$,which is determined by the morphological structures of the polymer, relies on the condition of the solution. $\langle\mathbf{R}_{nm}^2\rangle$ in the collapsed state is smaller than that in the coiled state, and $\langle\mathbf{R}_{nm}^2\rangle$ in the coiled state is much smaller than that in the ordered state (rod, toroidal, etc.). As a result, $\overline{D}(R_{nm}(0))$ in collapsed structures is much smaller than that in coiled structures.

4. For a specific condition of solution when the mean square distance in equilibrium $\langle\mathbf{R}_{nm}^2\rangle$ is fixed, the variation of $\overline{D}(R_{nm}(0))$ has a quadratic dependence on the initial distance $R_{nm}(0) = |\mathbf{R}_{nm}(0)|$.

These conclusions are in qualitative agreement with recent experiments on PCN-4.[82] Instead of two fluorophores attached to the same chain, the donor and acceptor dye molecules in the reported experiment are attached to each end of a double helix DNA molecule, respectively. Therefore the quadratic dependence on $R_{nm}(0)$ is not exactly observed. It was observed that the instantaneous diffusion coefficient in the unfolded state is one order of magnitude greater than that in the folded condition, which means $\langle \mathbf{R}_{nm}^2 \rangle$ in the folded state is much smaller than that in the unfolded state.

4.5 The FRET lifetime distribution

In order to calculate the lifetime distribution, we consider a general scenario where the kinetics of the system described by

$$\dot{P}(t) = \mathcal{L}P(t) - KP(t), \tag{4.30}$$

where $P([\mathbf{r}], t)$ is the probability distribution function of the polymer chain and $\mathcal{L}$ is the propagation operator of the chain. As illustrated in Fig. 4-5, the depletion of the population is denoted by K and the intra-chain motion is governed by $\mathcal{L}$. At zero time, we pump the donor dye to an excited state, and then monitor the lifetime distribution. The Laplace transform of Eq. (4.30) yields

$$\hat{P}(z) = \frac{1}{z - \mathcal{L} + K}P_0, \tag{4.31}$$

where $\hat{P}(z)$ is the Laplace transform of $P(t)$ and P_0 is the initial population. To calculate the lifetime distribution function, we take the average of Eq. (4.31) over the equilibrium distribution P_{eq} and obtain the equation for the survival probability $\hat{N}(z) = \langle (z - \mathcal{L} + K)^{-1} \rangle$, where the bracket $\langle \cdots \rangle$ refers to the configurational average over the equilibrium distribution function P_{eq}, i.e., $\langle A \rangle = \int A P_{eq} d^N \mathbf{r}$. From $\hat{N}(z)$ we
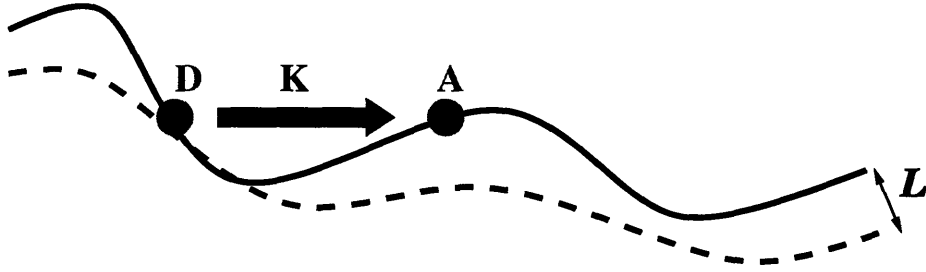
Figure 4-5: A sketch of intra-chain fluorescence resonant energy transfer process, with double arrow denoting the intra-chain dynamics $\mathcal{L}$, and with thick arrow denoting the population depletion from the donor.

calculate the Laplace transform of the ensemble lifetime distribution as

$$\hat{f}(z) = 1 - z\hat{N}(z) = \langle (K - \mathcal{L})(z - \mathcal{L} + K)^{-1} \rangle. \tag{4.32}$$

In the sluggish environment, $\mathcal{L} \ll K$, the relaxation of the reactive system is extremely slow so that the reaction rate depends only on the transient configuration, therefore, the lifetime is $\tau = \hat{P}(0) \approx K^{-1}$. The survival probability in Laplace space becomes $N(z) \approx \langle (z + K)^{-1} \rangle$, and the lifetime distribution function is the static average over the equilibrium configuration, i.e.,

$$f(t) = \int K e^{-Kt} P_{eq} d^N \mathbf{r}. \tag{4.33}$$

Under such conditions, the inter-fluorophore distance distribution as well as the transfer rate distribution can be obtained from single-molecule fluorescence lifetime measurements.[83] The ensemble averaged lifetime becomes the static average of the inhomogeneous lifetime τ, $\langle t \rangle \approx \langle K^{-1} \rangle$.[107]

However, natural functions of biological polymers are usually studied in solutions, where the static limit in Eq. (4.33) does not apply. Although the energy transfer reaction occurs on a faster time scale than the intra-chain relaxation, it is important to include the relaxation effects in the lifetime distribution function. To take into account of the polymer motion during the reaction, $\hat{P}(z)$ can be evaluated with inhomogeneous

127

cumulant expansion for a fixed initial configuration which has been used in studying spectral diffusion,[108] giving

$$P(\mathbf{R}_0, t) = \langle e^{-\int_0^t K(\tau)d\tau} \rangle_{\mathbf{R}_0}. \tag{4.34}$$

Here $\langle \cdots \rangle_{\mathbf{R}_0}$ stands for the homogeneous average for a fixed initial configuration and can be calculated with cumulant expansion, for example, to first order, as

$$P(\mathbf{R}_0, t) \approx \exp[-\int_0^t \langle K(\tau) \rangle_{\mathbf{R}_0} d\tau]. \tag{4.35}$$

For the semi-flexible chain model introduced in Section 4.2, the inhomogeneous average is performed over the Green's function in Eq. (4.64), giving

$$
\begin{aligned}
\langle K(\tau) \rangle_{\mathbf{R}_0} &= \int \frac{K(\tilde{\mathbf{R}} + \mathbf{R}_0\phi(t))}{[2\pi\langle \mathbf{R}_{nm}^2 \rangle(1 - \phi(t)^2)/3]^{3/2}} \exp[-\frac{3\tilde{\mathbf{R}}^2}{2\langle \mathbf{R}_{nm}^2 \rangle(1 - \phi(t)^2)}]d^3\tilde{\mathbf{R}} \\
&\approx K(\mathbf{R}_0) + 2Dt \sum_\mu \partial_\mu \partial_\mu K(\mathbf{R}_0),
\end{aligned} \tag{4.36}
$$

where we have applied the short time expansion of $K(\tilde{\mathbf{R}} + \mathbf{R}_0\phi(t)) \approx K(\mathbf{R}_0) + \sum_{\mu,\nu} \partial_\mu \partial_\nu K(\mathbf{R}_0)\tilde{R}_\mu \tilde{R}_\nu/2$ with μ, ν standing for x, y, z, $\langle \mathbf{R}_{nm}^2 \rangle(1 - \phi(t)^2) \approx 12Dt$, and $D = k_B T/\zeta$. Therefore Eq. (4.35) can be approximated as

$$
\begin{aligned}
P(\mathbf{R}_0, t) &\approx \exp[-K(\mathbf{R}_0)t - D\sum_\mu \partial_\mu \partial_\mu K(\mathbf{R}_0)t^2] \\
&\approx \exp[-K(\mathbf{R}_0)t - \frac{D\sum_\mu \partial_\mu \partial_\mu K(\mathbf{R}_0)}{K(\mathbf{R}_0)^2}],
\end{aligned} \tag{4.37}
$$

where in the second approximation t is replaced by the reaction time $1/K(\mathbf{R}_0)$ for a specific configuration in the fast reaction limit. Thus the lifetime

$$\tau \approx \frac{1}{K(\mathbf{R}_0)} \exp[-\frac{D\sum_\mu \partial_\mu \partial_\mu K(\mathbf{R}_0)}{K(\mathbf{R}_0)^2}] \tag{4.38}$$

becomes a weighted inhomogeneous reaction time. And the lifetime distribution be-

comes a weighted average over inhomogeneous configurations,

$$f(t) = \int K(\mathbf{R}_0) \exp[-\frac{D \sum_\mu \partial_\mu \partial_\mu K(\mathbf{R}_0)}{K(\mathbf{R}_0)^2}] P_{eq}(\mathbf{R}_0) d^3 R_0. \tag{4.39}$$

For the FRET rate described in Eq. (4.25), the weighting factor can be evaluated explicitly as

$$\exp[-\frac{D \sum_\mu \partial_\mu \partial_\mu K(\mathbf{R}_0)}{K(\mathbf{R}_0)^2}] = \exp\left\{-\frac{6D\tau_D}{R_0^2} \frac{5(R_0/R_F)^{-6}}{[1 + (R_0/R_F)^{-6}]^2}\right\}, \tag{4.40}$$

where τ_D is the fluorescence lifetime of the donor dye without acceptor. When the diffusion coefficient increases, small R_0 or large FRET rate will be favored, thus the lifetime distribution will be shifted toward small τ, hence the ensemble averaged lifetime decreases. Variational treatment by Portman and Wolynes has rigorously proved that the static and the dynamic averages are the upper and the lower bounds on the ensemble averaged survival probability for general diffusion-controlled reactions.[107] In the limit when $D \to 0$, the small FRET rate contribution will be maximized and the lifetime reduces to the reaction time for a static configuration, $\tau = K^{-1}$. Given the functional form of the energy transfer rate, each measurement of lifetime corresponds to a fixed donor-acceptor distance. Therefore, by measuring the FRET lifetime distribution, one can map out the distribution function of inter-fluorophore distance. This mapping however is modified according to Eq. (4.40) by taking into account the diffusion effect.

4.6 Intrinsic Viscosity

From standard viscoelasticity theory, the stress tensor is measured under the external shear flow $v_x = \alpha(t)y$ and is related to the desired time-dependent viscoelasticity $\eta(t)$ through $\sigma_{xy}(t) = \eta_s + \int_\infty^t \eta_p(t - t')\alpha(t')$ where $\eta_p(t)$ is the viscosity contribution from polymers. Given $\eta(t)$, the intrinsic viscosity is $[\eta] = \int_0^\infty \eta_p(\tau)d\tau/(\rho\eta_s)$ where ρ is the mass density of the polymer and η_s is the solvent viscosity. Similarly, we can determine the storage modulus $G'(\omega)$ and the loss modulus $G''(\omega)$ from the viscoelastic response

129

$\eta_p(t)$.

We derive the microscopic expression for the polymer viscosity $\eta_p(t)$. We begin with the definition of the intrinsic stress tensor

$$\langle \sigma_{p,xy}(t) \rangle = -\frac{c}{N} \sum_n \int F_{nx} r_{ny} P d^N \mathbf{r} \tag{4.41}$$

where P is the distribution function of the Gaussian chain at time t and c is the number concentration of the beads. In Eq. (4.41), the solvent contribution is not included in the stress and $\sigma_{p,xy}(t)$ is the contribution from single polymers. Under the shear flow, the distribution function of the polymer chain follows $\dot{P}(t) = \mathcal{L}P(t) - \sum_m \partial_{mx}[\alpha(t) r_{my} P(t)]$ where the operator $\mathcal{L}$ dictates the free propagation of the polymer and the second term is due to the external flow. To first order in perturbation, we have

$$P(t) = P_0 - \int_{-\infty}^t e^{\mathcal{L}(t-\tau)} \sum_m \frac{\partial}{\partial r_{mx}} \alpha(\tau) r_{my} P_0(\tau) d\tau \tag{4.42}$$

where $P_0 = P_{eq}$ is the equilibrium distribution. Substituting Eq. (4.42) into Eq. (4.41), we find

$$\eta_p(t) = \frac{c}{N} \beta \langle \sum_n F_{nx}(t) r_{ny}(t) \sum_n r_{mx}(0) F_{my}(0) \rangle \tag{4.43}$$

which is the linear response expression found in literature.[100, 102, 109, 110] Applying the Gaussian factorization to the above expression leads to

$$\begin{aligned}
\eta_p(t) &\approx \frac{c}{N} \beta \sum_{nm} \langle F_{nx}(t) r_{mx}(0) \rangle \langle F_{my}(0) r_{ny}(t) \rangle \\
&= \sum_{nm} \frac{c}{N} k_B T \langle \frac{\partial r_{mx}(t)}{\partial r_{nx}(0)} \rangle \langle \frac{\partial r_{ny}(t)}{\partial r_{my}(0)} \rangle
\end{aligned} \tag{4.44}$$

where we assume the motions along different Cartesian coordinates are decoupled. The Gaussian factorization and the decoupling assumption hold exactly for the Brownian motion of Gaussian chains.

The key result of this section is the last expression in Eq. (4.44), which relates single chain measurements to macroscopic viscoelastic responses. Here, the stability function $\partial \mathbf{r}_{mx}/\partial \mathbf{r}_{nx}$ measures the divergence of the trajectories with respect to initial conditions and cannot be obtained directly from bulk measurements. By virtue of this expression, we can evaluate the intrinsic viscoelasticity of a Gaussian chain by tracking bead motions along a polymer chain.

Accurate evaluation of the exact expression in Eq. (4.43) has been carried out by Pyun and Fixman, Bixon and Zwanzig, and etc. [99, 100, 101] We will calculate the viscosity within the semi-flexible Gaussian model. The viscoelasticity function in Eq. (4.44) can be transformed into normal modes as

$$\frac{\partial \mathbf{r}_{mx}(t)}{\partial \mathbf{r}_{nx}} = \sum_{p}^{N-1} \frac{\partial \mathbf{r}_{mx}(t)}{\partial \mathbf{x}_{px}(t)} \exp[-\frac{\lambda_p}{\zeta_p} t] \frac{\partial \mathbf{x}_{px}}{\partial \mathbf{r}_{nx}}, \tag{4.45}$$

where $\partial \mathbf{r}_{mx}/\partial \mathbf{x}_{px}$ is the unitary transform matrix element between the real coordinates and normal modes. For the semi-flexible Gaussian chain, $\eta_p(t)$ can be written as a sum over the exponentially decaying correlation functions of the normal modes

$$\eta_p(t) = k_B T \frac{c}{N} \sum_{p=1}^{N-1} \exp[-\frac{t}{\tau_p}], \tag{4.46}$$

where $\tau_p = \zeta_p/(2\lambda_p)$ is the decay time for each normal mode. In general, application of a shear flow does not invoke stretching modes, thus, only the bending motion of the polymer chain is considered in the expression for $\eta_p(t)$. Therefore the intrinsic storage modulus and the intrinsic loss modulus are $[G'(\omega)]_p = \int_0^\infty \omega \sin \omega t \sum_{p=1}^{N-1} \exp[-t/\tau_p] dt$ and $[G''(\omega)]_p = \int_0^\infty \omega \cos \omega t \sum_{p=1}^{N-1} \exp[-t/\tau_p]$. Given the expression for λ_p in Eq. (4.55) and $\zeta_p = 2N\zeta$, we have

$$\tau_p = \begin{cases} \frac{N^2 a_0^2 \zeta L_p}{3\pi^2 k_b T} p^{-2} = \tau_1 p^{-2} & L_p \ll N, \\ \frac{N^4 a_0^2 \zeta}{3\pi^4 k_B T L_p} p^{-4} = \tau_1' p^{-4} & L_p \geq N, \end{cases} \tag{4.47}$$

which describes both the flexible chain when $L_p \ll N$ and the stiff rod when $L_p \geq N$.

In the limit $L_p = 1/2$, the above expression recovers the time constants for p^{th} normal mode of the Rouse chain.[95] The expressions for $[G'(\omega)]_p$ and $[G''(\omega)]_p$ simplify in the following two cases.

1. In the low frequency limit, $\omega \tau_1 \ll 1$ and $\omega \tau_1' \ll 1$ $[G'(\omega)]_p$ and $[G''(\omega)]_p$ are approximated as

$$[G'(\omega)]_p \approx \begin{cases} (\omega\tau_1)^2 \sum_{p=1}^{\infty} p^{-4} = \pi^4 (\omega\tau_1)^2/90 & L_p \ll N \\ (\omega\tau_1')^2 \sum_{p=1}^{\infty} p^{-8} = \pi^8 (\omega\tau_1')^2/9450 & L_p \geq N, \end{cases} \quad (4.48)$$

and

$$[G''(\omega)]_p \approx \begin{cases} \omega\tau_1 \sum_{p=1}^{\infty} p^{-2} = \pi^2 \omega\tau_1/6 & L_p \ll N \\ \omega\tau_1' \sum_{p=1}^{\infty} p^{-4} = \pi^4 \omega\tau_1'/90 & L_p \geq N. \end{cases} \quad (4.49)$$

Therefore, $[G'(\omega)]_p$ and $[G''(\omega)]_p$ are proportional to ω^2 and ω, respectively, and reduce to the stiff rod limit when $L_p \geq N$.

2. In the high frequency limit, $\omega\tau_1 \gg 1$ and $\omega\tau_1' \gg 1$, the sum over p is approximated by an integral, so that

$$[G'(\omega)]_p \approx \begin{cases} (\omega\tau_1)^{1/2} \pi/[4\sin(\pi/4)] & L_p \ll N \\ (\omega\tau_1')^{1/4} \pi/[8\sin(\pi/8)] & L_p \geq N \end{cases} \quad (4.50)$$

and

$$[G''(\omega)]_p \approx \begin{cases} (\omega\tau_1)^{1/2} \pi/[4\cos(\pi/4)] & L_p \ll N \\ (\omega\tau_1')^{1/4} \pi/[8\cos(\pi/8)] & L_p \geq N \end{cases} \quad (4.51)$$

For the stiff chain, the bending motion has a $\omega^{1/4}$ dependence at high frequency, which implies $\eta_p(t) \propto t^{-1/4}$ when $t \ll \tau_1'$. This is consistent with the findings of the polymer bending motion in Refs. [111] and [112].

As shown in Figs. 4-6 and 4-7, numerical calculations of the intrinsic storage $G'(\omega)$ and loss moduli $G''(\omega)$ from the viscoelastic response function $\eta_p(t)$ in Eq. (4.46)
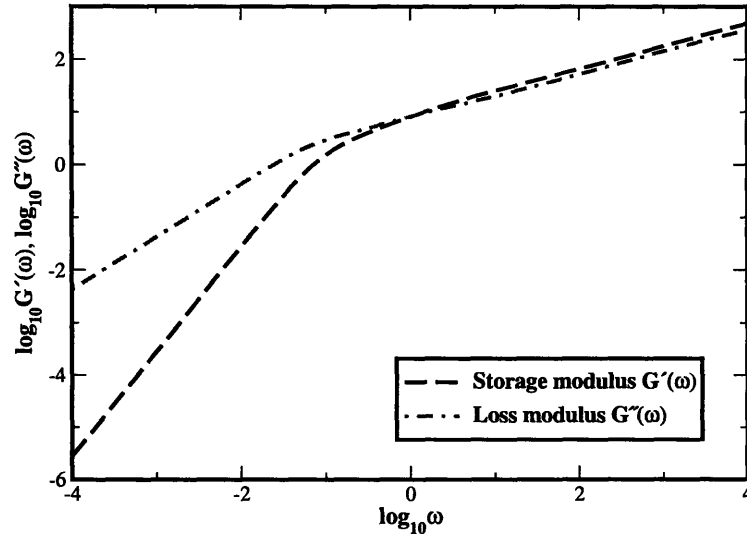
Figure 4-6: The intrinsic and loss storage modulus for a flexible chain with 5000 beads and the persistence length taken as 5. At low frequencies, $G'(\omega)$ scales as ω^2 and $G''(\omega)$ scales as ω. At high frequencies, both $G'(\omega)$ and $G''(\omega)$ scale as $\omega^{1/2}$.
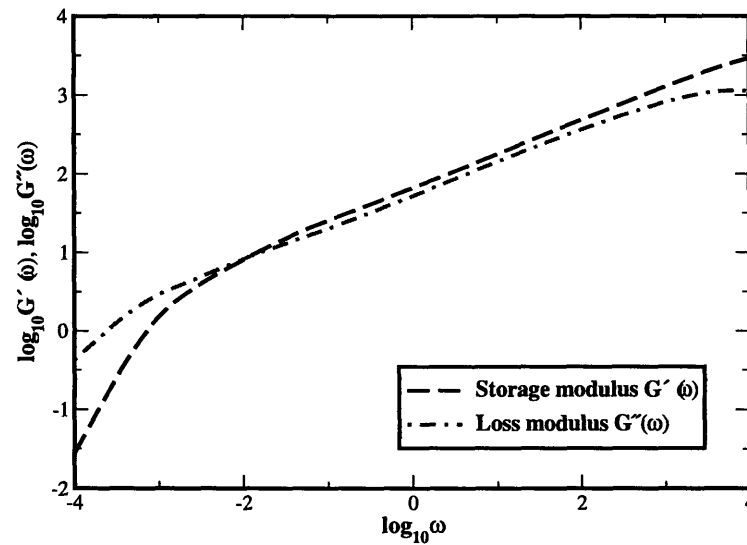
Figure 4-7: The intrinsic and loss storage modulus for a semi-flexible chain with 5000 beads and the persistence length taken as 500. At low frequencies, $G'(\omega)$ and $G''(\omega)$ scales as ω^2 and ω, respectively. At high frequencies, both $G'(\omega)$ and $G'''(\omega)$ scales as $\omega^{1/4}$.

confirm the two different scaling regions for both flexible and semi-flexible chains. In the numerical calculation, the number of beads on the polymer chain is taken as 5000, the persistence length L_p is 5 for the flexible chain and 500 for a semi-flexible chain.

In θ solvent, the intrinsic moduli for the semi-flexible chain can be calculated with τ_p obtained by the pre-averaging method in standard textbook,[95] as shown in Appendix 4-D.

1. In the low frequency limit, similar to the derivation above, $[G'(\omega)]_p$ and $[G''(\omega)]_p$ are still proportional to ω^2 and ω, respectively.

2. In the high frequency limit,

$$[G'(\omega)]_p \approx \begin{cases} (\omega\tau_1)^{2/3}\pi/[3\sin(\pi/3)] & L_p \ll N \\ (\omega\tau_1')^{2/7}\pi/[7\sin(\pi/7)] & L_p \geq N \end{cases} \tag{4.52}$$

and

$$[G''(\omega)]_p \approx \begin{cases} (\omega\tau_1)^{2/3}\pi/[3\cos(\pi/3)] & L_p \ll N \\ (\omega\tau_1')^{2/7}\pi/[7\cos(\pi/7)] & L_p \geq N \end{cases} \tag{4.53}$$

which are proportional to $\omega^{2/3}$ and $\omega^{2/7}$, respectively.

4.7 Concluding remarks

In Sec. 4.2 and 4.3, we have formulated the semi-flexible Gaussian chain with analogue to the Ornstein-Uhlenbeck random walk process and incorporated the persistent length into the Rouse model. The mean square bead-bead distance $\langle R_{nm}^2 \rangle$ is studied for different degrees of stiffness. For a flexible chain, the mean square distance exhibits the scaling relation for a random Gaussian coil $\langle R_{nm}^2 \rangle = 2L_p|n - m|a_0^2$; while for large persistence length, it scales as a rigid rod, $\langle R_{nm}^2 \rangle = |n-m|^2 a_0^2$. To study the intra-chain motion of semi-flexible chains, the evolution of R_{nm} is calculated based on the normal mode decomposition of the Langevin equation of a semi-flexible polymer chain. The resulting Green's function resembles a Gaussian process within a poten-

134

tial of mean force. The Brownian dynamics of the semi-flexible chain shows that the correlation function $\langle \mathbf{R}_{nm}(t) \cdot \mathbf{R}_{nm}(0) \rangle$ has a much longer time scale for a stiff chain than for a flexible polymer.

In Sec. 4.4, we have considered the fluorescence resonant energy transfer (FRET) process on a semi-flexible chain, where a donor-acceptor pair attached to the nth and the mth polymer beads are used to probe the conformational dynamics. The fluorescence lifetime correlation function and the FRET efficiency correlation function are closely related to the normalized distance correlation function $\phi(t)$. Thus both the lifetime correlation and the FRET efficiency correlation can be employed as possible measures of the intra-chain dynamics. Furthermore, the instantaneous diffusion coefficient due to finite time resolution t_{bin} has been calculated within the theoretical model. As $t_{bin} \to 0$, The instantaneous diffusion coefficient is obtained from the independent diffusive motion of the donor and acceptor sites. When measured with finite time resolution, the instantaneous diffusion coefficient $\overline{D}(R_{nm}^2) = \langle R_{nm}^2 \rangle [1 - \phi^2(t_{bin})]/t_{bin} + R_{nm}^2[1 - \phi(t_{bin})]^2/t_{bin}$ is much smaller in the collapsed structure than in the ordered structure, and the variation has a quadratic dependence on the donor-acceptor distance R_{nm}. Some of these predictions are in qualitative agreement with reported experiments. [82].

In FRET experiments, the intra-chain dynamics usually occurs on a much longer time scale than the energy transfer reaction. In Sec. 4.5, the FRET lifetime is discussed in the fast reaction limit. With inhomogeneous cumulant expansion, we have shown that the lifetime is a weighted reaction time for a given initial configuration, $\tau = K(\mathbf{R}_0)^{-1} \exp[-D \sum_\mu \partial_\mu \partial_\mu K(\mathbf{R}_0)/K(\mathbf{R}_0)^2]$. When the intra-chain relaxation process is extremely slow, $D \to 0$, this expression recovers the static limit, i.e., $\tau = K^{-1}$, and thus, the distribution function of the donor-acceptor distance can be mapped out from the single-molecule lifetime measurements. Furthermore, recent measurements of the viscosity-dependent intra-molecular quenching rate provide detailed information from the reaction-controlled limit to the diffusion-controlled limit.[42] Thus systematic studies and detailed analysis of the ensemble averaged lifetime is necessary to better understand the polymer dynamics.[78]

The macroscopic viscoelastic response of a polymer chain is related to the bead dynamics on a single polymer by Eq. (4.44), from which the intrinsic elastic moduli are derived. Explicit evaluations of the elastic storage modulus and the elastic loss modulus are performed with the consideration of the persistence length L_p. Our expressions exactly recover the results for the Rouse chain in the limit $L_p \to 1/2$, and predict the correct scaling over frequency for the bending motion of a stiff polymer in the stiff rod limit $L_p \geq N$.

Single-molecule FRET measurements of the semi-flexible chain yield rich information about intra-chain motion, for example, mean square distance, distance correlation function, instantaneous diffusion coefficient, and intrinsic viscosity. Further refinements of single-molecule spectroscopy will provide more accurate methods to examine the details of the intra-polymer interactions and lead to better understanding of the related issues such as protein folding and self-assembly of biological systems. Further consideration of hydrodynamic and excluded volume effects can be implemented in the theoretical model for a semi-flexible chain.

4.8 Appendix 4-A: approximate normal modes of semi-flexible chains

In a semi-flexible chain, the potential energy is

$$U = \frac{3k_BT}{8a_0^2} \sum_{n=1}^{N-2} [\frac{1+b}{1-b}(\mathbf{u}_{n+1} - \mathbf{u}_n)^2 + \frac{1-b}{1+b}(\mathbf{u}_{n+1} + \mathbf{u}_n)^2] + \frac{3k_BT}{4a_0^2}(\mathbf{u}_1^2 + \mathbf{u}_{N-1}^2), (4.54)$$

where $\mathbf{u}_n = \mathbf{R}_{n+1} - \mathbf{R}_n$ is the bond between the nth and the $n + 1^{th}$ beads. In the continuous limit, the potential energy reduces to Eq. (4.5) in section 4.2. Applying the transform of Eq. (4.7), we can decompose the potential energy into three parts

$U = T_1 + T_2 + T_3$, where

$$
\begin{aligned}
T_1 &= \frac{3k_BT}{8a_0^2}\frac{1+b}{1-b}\sum_{n=1}^{N-2}(\mathbf{u}_{n+1} - \mathbf{u}_n)^2 \\
&= \frac{12Nk_BT}{a_0^2}\sum_{p=1}^{N-1}\mathbf{x}_p^2\frac{1+b}{1-b}\sin^4\frac{p\pi}{2N} - \frac{1+b}{1-b}\cdot T_3, \\
T_2 &= \frac{3k_BT}{8a_0^2}\frac{1-b}{1+b}\sum_{n=1}^{N-2}(\mathbf{u}_{n+1} + \mathbf{u}_n)^2 \\
&= \frac{12Nk_BT}{a_0^2}\sum_{p=1}^{N-1}\mathbf{x}_p^2\frac{1-b}{1+b}\sin^2\frac{p\pi}{2N}\cos^2\frac{p\pi}{2N} - \frac{1-b}{1+b}\cdot T_3, \\
T_3 &= \frac{3k_BT}{4a_0^2}(\mathbf{u}_1^2 + \mathbf{u}_{N-1}^2) \\
&= \frac{24k_BT}{a_0^2}\sum_{p,q=1}^{N-1}\mathbf{x}_p\cdot\mathbf{x}_q\sin^2\frac{p\pi}{2N}\sin^2\frac{q\pi}{2N}[(-1)^{p+q} + 1]\cos\frac{p\pi}{2N}\cos\frac{q\pi}{2N},
\end{aligned}
$$

Therefore, in the large N limit, the off diagonal terms are N times smaller than the diagonal terms, and we approximately diagonalize the potential energy in normal modes, $U \approx \sum_{p=1}^{N-1}\lambda_p\mathbf{x}_p^2/2$ with

$$
\lambda_p = \frac{24Nk_BT}{a_0^2}\sin^2\frac{p\pi}{2N}(2L_p\sin^2\frac{p\pi}{2N} + \frac{1}{2L_p}\cos^2\frac{p\pi}{2N}) \tag{4.55}
$$

where $2L_p = (1+b)/(1-b)$ is the persistent length. In the limit of the flexible chain, the persistent length is relatively small compared to the contour length of the chain, the second term dominates and yields,

$$
\lambda_p \approx \frac{24Nk_BT}{a_0^2}\sin^2\frac{p\pi}{2N}\frac{1}{2L_p}\cos^2\frac{p\pi}{2N} \approx \frac{3\pi^2 k_BT}{Na_0^2 L_p}p^2. \tag{4.56}
$$

In the limit of $L_p \to 1/2$ or $b \to 0$, λ_p given in Eq. (4.55) is exactly the same as the result for Rouse chain. [95] In the strong persistence limit, the first term also contributes and may even dominates for large p, yielding the worm-like chain normal

modes,

$$\lambda_p \approx \frac{3\pi^2 k_B T p^2}{N a_0^2 L_p}(1 + \frac{\pi^2 L_p^2}{N^2}p^2) \approx \frac{3k_B T \pi^4 L_p}{N^3 a_0^2}p^4. \tag{4.57}$$

In this expression, all the normal modes will be suppressed for a rigid-rod like chain for $L_p \to \infty$ while keeping only the center of mass motion, which is a deficit of the approximate normal modes we obtained in this section. Full motion of the chain can be observed from numerical solutions of the original equation of motion in Eq. (4.6).

4.9 Appendix 4-B: Green's function for the semi-flexible Gaussian chain

As demonstrated in Appendix 4-A, the potential energy of a semi-flexible Gaussian chain is approximately diagonal and quadratic in normal coordinates $\mathbf{x}_p$ as shown in Appendix 4-A. The evolution of the normal modes follows the Smoluchowski equation,

$$\frac{\partial P}{\partial t} = \mathcal{L}P(t), \quad with \quad \mathcal{L} = \sum_{p=1}^{N-1} \frac{1}{\zeta_p}\frac{\partial}{\partial \mathbf{x}_p}(k_B T \frac{\partial}{\partial \mathbf{x}_p} + \lambda_p \mathbf{x}_p). \tag{4.58}$$

Solution of the above Fokker-Planck equation gives the Green's function

$$
\begin{aligned}
G(\mathbf{x}_p, t | \mathbf{x}_p(0)) &= \prod_{p=1}^{N-1}[\frac{2\pi k_B T}{\lambda_p}(1 - e^{-2\frac{\lambda_p}{\zeta_p}t})]^{-3/2} \cdot \\
&\exp\left\{-\frac{\sum_{p=1}^{N-1} \lambda_p[\mathbf{x}_p - \mathbf{x}_p(0)e^{-\frac{\lambda_p}{\zeta_p}t}]^2}{2k_B T(1 - e^{-2\frac{\lambda_p}{\zeta_p}t})}\right\},
\end{aligned}
\tag{4.59}
$$

and the equilibrium distribution of normal modes

$$P_{eq}(\mathbf{x}_p) = \prod_{p=1}^{N-1}(\frac{2\pi k_B T}{\lambda_p})^{-3/2}\exp\{-\frac{\sum_{p=1}^{N-1}\lambda_p \mathbf{x}_p^2}{2k_B T}\}. \tag{4.60}$$

The correlation function of the pth normal mode is calculated directly from above as $\langle \mathbf{x}_p(t) \cdot \mathbf{x}_p(0) \rangle = 3k_B T/\lambda_p \exp[-\lambda_p t/\zeta_p]$, and the equilibrium average of $\mathbf{R}_{nm}$ and the

138

correlation between $\mathbf{R}_{nm}(0)$ and $\mathbf{R}_{nm}(t)$ can be evaluated according to the decomposition in Eq. (4.12),

$$\langle \mathbf{R}_{nm}^2 \rangle \;=\; \sum_{p=1}^{N-1} (c_{nm}^p)^2 \frac{3k_B T}{\lambda_p} \tag{4.61}$$

$$\phi(t) = \frac{\langle \mathbf{R}_{nm}(t) \cdot \mathbf{R}_{nm}(0) \rangle}{\langle \mathbf{R}_{nm}^2 \rangle} \;=\; [\langle \mathbf{R}_{nm}^2 \rangle]^{-1} \sum_{p=1}^{N-1} (c_{nm}^p)^2 \frac{3k_B T}{\lambda_p} \exp[-\frac{\lambda_p}{\zeta_p} t]. \tag{4.62}$$

$\mathbf{R}_{nm}$ is a Gaussian variable because it is a linear combination of Gaussian normal mode The equilibrium distribution of $\mathbf{R}_{nm}$ is

$$P_{eq}(\mathbf{R}_{nm}) \;=\; \int d\mathbf{x}_p \delta(\mathbf{R}_{nm} - \sum_{p=1}^{N-1} c_{nm}^p \mathbf{x}_p) \, P_{eq}(\mathbf{x}_p)$$

$$= \; [\frac{2\pi}{3} \langle \mathbf{R}_{nm}^2 \rangle]^{-3/2} \exp\left\{ -\frac{3\mathbf{R}_{nm}^2}{2\langle \mathbf{R}_{nm}^2 \rangle} \right\}, \tag{4.63}$$

where cumulant expansion over the Gaussian normal modes and Eq. (4.61) are applied. In a similar fashion it can be shown that the joint distribution for $\mathbf{R}_{nm}(t)$ and $\mathbf{R}_{nm}(0)$ is

$$P(\mathbf{R}_{nm}(t), t, \mathbf{R}_{nm}(0)) = \left[\frac{4\pi^2}{9} \langle \mathbf{R}_{nm}^2 \rangle^2 (1 - \phi(t)^2) \right]^{-3/2} \cdot$$
$$\exp\left\{ -\frac{3[\mathbf{R}_{nm}^2(t) - 2\phi(t)\mathbf{R}_{nm}(t) \cdot \mathbf{R}_{nm}(0) + \mathbf{R}_{nm}^2(0)]}{2\langle \mathbf{R}_{nm}^2 \rangle (1 - \phi(t)^2)} \right\}, \tag{4.64}$$

and the evolution of $\mathbf{R}_{nm}$ is described by the corresponding Green's function,

$$G(\mathbf{R}_{nm}(t), t | \mathbf{R}_{nm}(0)) \;=\; \frac{P(\mathbf{R}_{nm}(t), t, \mathbf{R}_{nm}(0))}{P_{eq}(\mathbf{R}_{nm}(0))}$$

$$= \; \left[\frac{2\pi}{3} \langle \mathbf{R}_{nm}^2 \rangle (1 - \phi(t)^2) \right]^{-3/2} \cdot$$
$$\exp\left\{ -\frac{3(\mathbf{R}_{nm}(t) - \phi(t)\mathbf{R}_{nm}(0))^2}{2\langle \mathbf{R}_{nm}^2 \rangle (1 - \phi(t)^2)} \right\}. \tag{4.65}$$

4.10 Appendix 4-C: FRET rate distribution and correlation of semi-flexible Gaussian chain

The FRET rate depends on the distance R between the donor and the acceptor as, $K(R) = k_F (R_F/R)^6$, where R_F is the Förster radius at which the transfer efficiency is 50%, and k_F is the energy transfer rate at $R = R_F$. However, this rate expression diverges at $R \to 0$ where the transition dipole-dipole interaction no longer holds. To facilitate the calculation, we choose a slightly modified expression of $K(R)$ as

$$K(R) = \frac{k_F}{\epsilon + (R/R_F)^6} \tag{4.66}$$

where ϵ is a small quantity that denotes the break down of the weak dipole-dipole interaction when R is extremely small. It is shown later in this section that the average transfer rate $\langle K(R) \rangle$ is a large quantity because ϵ is usually small. The overall decay rate of the fluorescence on the donor molecule can be approximated by neglecting the radiative decay. The three-dimensional Fourier transform of the rate function $K(R)$ is

$$
\begin{aligned}
K(\mathbf{q}) &= \frac{2\pi^2 k_F R_F^2}{3q\epsilon^{2/3}} \{ \exp[-qR_F \epsilon^{1/6}] + \exp[-\frac{qR_F \epsilon^{1/6}}{2}] \cdot \\
&\quad [-\cos(\frac{\sqrt{3}}{2}qR_F \epsilon^{1/6}) + \sqrt{3}\sin(\frac{\sqrt{3}}{2}qR_F \epsilon^{1/6})] \}.
\end{aligned}
\tag{4.67}
$$

Considering ϵ is a small number and $qR_F \epsilon^{1/6} \ll 1$, the leading order of $K(\mathbf{q})$ is

$$K(\mathbf{q}) \approx \frac{2\pi^2 R_F^3 k_F}{3\sqrt{\epsilon}}, \tag{4.68}$$

which approximates energy transfer by a delta-function sink. Because $\mathbf{R}_{nm}$ is a Gaussian variable with distribution Eq. (4.63), the cumulant expansion yields $\langle \exp[i\mathbf{q} \cdot \mathbf{R}_{nm}] \rangle = \exp[-q^2 \langle \mathbf{R}_{nm}^2 \rangle/6]$, and the average over $K(\mathbf{R}_{nm})$ and the correlation of

$K(\mathbf{R}_{nm})$ are evaluated as

$$\langle K(\mathbf{R}_{nm})\rangle = \int_{\mathbf{q}} K(\mathbf{q})\exp[-q^2\langle\mathbf{R}_{nm}^2\rangle/6] = k_F\sqrt{\frac{3\pi}{2\epsilon}}\left(\frac{\langle\mathbf{R}_{nm}^2\rangle}{R_F^2}\right)^{-3/2} \quad (4.69)$$

$$\langle KG(t)K\rangle = \int_{\mathbf{q}}\int_{\mathbf{q}'} K(\mathbf{q})K(\mathbf{q}')\exp\left\{-\frac{\langle\mathbf{R}_{nm}^2\rangle}{6}[q^2 + q'^2 + 2\mathbf{q}\cdot\mathbf{q}'\phi(t)]\right\}$$

$$\approx k_F^2\frac{3\pi}{2\epsilon}\left(\frac{\langle\mathbf{R}_{nm}^2\rangle}{R_F^2}\right)^{-3}[1 - \phi^2(t)]^{-3/2}, \quad (4.70)$$

where $\int_{\mathbf{q}}$ stands for $\int d^3q/(2\pi)^3$ and $\phi(t) = \langle\mathbf{R}_{nm}(t)\cdot\mathbf{R}_{nm}(0)\rangle/\langle\mathbf{R}_{nm}^2\rangle$. Therefore the memory function $\chi(t)$ is directly related to the distance correlation function $\phi(t)$ as

$$\chi(t) = \frac{\langle K(\mathbf{R}_{nm}(t))G(t)K(\mathbf{R}_{nm}(0))\rangle}{\langle K(\mathbf{R}_{nm})\rangle^2} - 1$$

$$= [1 - \phi^2(t)]^{-3/2} - 1 = \sum_{l=1}^{\infty}(2l+1)!!/(2^l\, l!)\phi^{2l}(t) \quad (4.71)$$

where $(2l+1)!! = (2l+1)\cdot(2l-1)\cdots 3\cdot 1$. If we are able to calculate the correlation function $\phi(t)$, the corresponding correlation function for FRET rates is determined accordingly.

4.11   Appendix 4-D: Hydrodynamic interactions in semi-flexible Gaussian chains

In θ solvent, the hydrodynamic interactions among polymer beads must be considered. With the pre-averaging technique introduced in Zimm model,[95] we are able to evaluate the normal modes of semi-flexible chain approximately.

In the long chain limit when $L_p \ll N$, the persistent length introduces slight

deviations from the Zimm model in θ solvent, and we have

$$\zeta_p = (2L_p)^{1/2}\zeta_p^{ZM}, \tag{4.72}$$

$$\lambda_p = \frac{1}{2L_p}\lambda_p^{ZM}, \tag{4.73}$$

$$\tau_p = \frac{\zeta_p}{\lambda_p} = (2L_p)^{3/2}\tau_p^{ZM}, \tag{4.74}$$

where the superscript "ZM" means the corresponding quantities in Zimm model,

$$\zeta_P^{ZM} = \eta_s(12\pi^3 Na_0^2 p)^{1/2}, \tag{4.75}$$

$$\lambda_p^{ZM} = \frac{6\pi^2 k_B T}{Na_0^2}p^2, \tag{4.76}$$

$$\tau_p^{ZM} = \tau_1^{ZM}p^{-3/2}. \tag{4.77}$$

It is obvious that all the above relations reduce to the Rouse model when $L_p = 1/2$.

In the short chain limit when $L_p \gg N$, the corresponding quantities are

$$\zeta_p \approx (12\pi^3)^{1/2}\eta_s a_0 p^{1/2} N^{1/2}, \tag{4.78}$$

$$\lambda_p \approx \frac{3\pi^4 k_B T L_p}{N^3 a_0^2}p^4, \tag{4.79}$$

$$\tau_p = \tau_1 p^{-7/2}. \tag{4.80}$$

Chapter 5

Fluorescence lifetime measurement: Kinetic regimes and experimental time scales

5.1 Introduction

Reaction kinetics modulated by fluctuating environments has long been a theoretical and experimental interest.[9, 13, 23, 35, 36, 43, 44, 45, 46, 60, 81, 82, 107, 113, 114, 115] Examples of such processes include ligand binding in proteins, slow reactions in glasses, fluorescence resonance energy transfer (FRET), and intra-molecular fluorescence quenching on polymers. Recent advances in single-molecule techniques based on fluorescence spectroscopy provide powerful tools to measure the conformational structures and dynamics of synthetic and biological polymers. The FRET and intra-molecular fluorescence quenching rates depend strongly on donor-acceptor or fluorophore-quencher distance, and on conformational fluctuations of polymers or biomolecules. Hence it is of great importance to study the conformation-modulated reactions, yet a unified perspective of reaction kinetics modulated by fluctuating environments have not been fully investigated. A widely used approximation scheme to calculate intrachain reactions of polymers in dilute solutions was first presented by

Wilemski and Fixman,[44, 45] referred here as WF approximation. Szabo, Schulten and Schulten provided a first passage time approach to the diffusion equation with Smoluchowski boundary conditions, referred here as the SSS theory.[43] Weiss developed a systematic perturbation analysis for diffusion-controlled reactions, which recovers the WF approximation in the lowest order.[46] Recently, Portman and Wolynes applied a variational method and proved that the WF approximation is an upper bound for the survival probability.[107]

The experimentally observed fluorescence lifetime distribution is the result of the competition between the reaction from a distribution of conformations and the diffusion between different conformational states. In the homogeneous limit, reaction is extremely slow compared to relaxation, and the system can be well-approximated by equilibrium, yielding a homogeneous single-exponential decay. In the inhomogeneous limit, the survival probability is a static average over the initial configurations and has a highly non-exponential decay. Between the two limits, the relaxation process and the reaction kinetics are convoluted. The configuration-controlled regime is dominated by the reaction kinetics, and the diffusion-controlled regime is determined by the conformational relaxation process. Although complete analytic solutions are difficult, the first-order inhomogeneous cumulant expansion and the WF approximation provide exact lower and upper bounds to the real survival probability function, respectively. In the present work, we investigate these regimes for Markovian and non-Markovian fluctuations of reaction coordinates modulated by conformational fluctuations and account for the experimental time window used to monitor fluorescence. To address these two regimes and their asymptotic limits, we study a Markovian process in Sec. 5.2 and a semi-flexible chain as an example of non-Markovian processes in Sec. 5.3.

Reactions in biopolymers are often strongly coupled to internal relaxation processes, and the fluctuations of the reaction coordinate are generally non-Markovian. Reaction dynamics of biopolymers in solution can be directly probed in real time by fluorescence spectroscopy. [9, 13, 16, 23, 35, 81, 82, 83] One important technique is intra-molecular fluorescence quenching, which has been employed to measure contact

formation between two residues on an unfolded polypeptide chain by Eaton's group and other groups.[39, 40, 42] By varying solvent viscosity, Eaton and his group measure the full kinetics from the inhomogeneous limit to the homogeneous limit. In Sec. 5.3, we calculate the full kinetics of the fluorescence quenching in a semi-flexible Gaussian chain with a normal mode decomposition scheme.[116] Our calculations demonstrate that the first-order inhomogeneous cumulant expansion and the WF approximation provide lower and upper bounds for the real survival probability, respectively.

In Sec. 5.4, we discuss the effects of the experimental time scale on fluorescence lifetime measurements and the unified perspective it provides. The experimental time scale here refers to the time window to monitor fluorescence. Within a very short time window, transient configurations stay close to the static configurations, independent of the relaxation rate. Such experiments can be well described within the configuration-controlled regime. For long experimental time, the configuration-controlled picture breaks down even for the slow relaxing regions. The long time kinetics is dominated by the relaxation process and is described by the diffusion-controlled regime. By varying the length of the observation time, we can observe both kinetic regimes.

In Appendix 5-A, we generalize the WF approximation and show that the WF approximation is exact to the first order of $1/D$. In addition, we obtain the $1/D$ expansion of the average lifetime and recover the perturbation result by Weiss.[43, 46] A more detailed discussion of the generalized WF approximation and its applicability criteria are addressed in paper II of this series.[117] In Appendix 5-B, we discuss the relation between the experimental time scale and the apparent distribution of the measured quantity obtained by single-molecule experiments.

5.2 Markovian processes: Two regimes of lifetime distribution

Chemical reactions influenced by fluctuating environments can be described by the Smoluchowski equation coupled to a reactive sink,

$$\dot{P}(t) = \mathcal{L}P(t) - KP(t). \tag{5.1}$$

$\mathcal{L}$ characterizes the relaxation of the fluctuating environment, and K is the first-order reaction rate coefficient. Initially, the system is prepared in thermal equilibrium, i.e., $P(0) = P_0 = P_{eq}$. The overall population depletion is monitored over time. Exact solutions to this equation can be obtained for only a few specific forms of the reaction rate.[43, 46, 60, 113, 114, 115] Let us now discuss the calculation of the lifetime distribution function. we take the trace of the Laplace transform $\hat{P}(w)$ and write the survival probability as

$$\hat{S}(w) = \langle \frac{1}{w - \mathcal{L} + K} \rangle, \tag{5.2}$$

The brackets $\langle \cdots \rangle$ represent a spatial average over the equilibrium distribution. From $\hat{S}(w)$ the Laplace transform of the lifetime distribution is obtained : $\hat{f}(w) = 1 - w\hat{S}(w) = \langle (K - \mathcal{L})(w - \mathcal{L} + K)^{-1} \rangle$. The average lifetime, expressed as the first moment of the lifetime distribution function, is $\langle t \rangle = \int_0^\infty tf(t)dt = \hat{S}(0)$.

Fig. 5-1 illustrates the configuration-controlled regime, the diffusion-controlled regime, and their corresponding limits. In the static limit, the population is depleted independently at every configuration without relaxation. In the dynamic limit, the population is depleted with a homogeneous rate while the fast relaxation maintains the population shape. Between the two limits, the kinetics can be described by the reaction dominated configuration-controlled regime and the relaxation dominated diffusion-controlled regime. Increasing the diffusion coefficient, the overall kinetics traverses from the configuration-controlled regime to the diffusion-controlled regime.

146
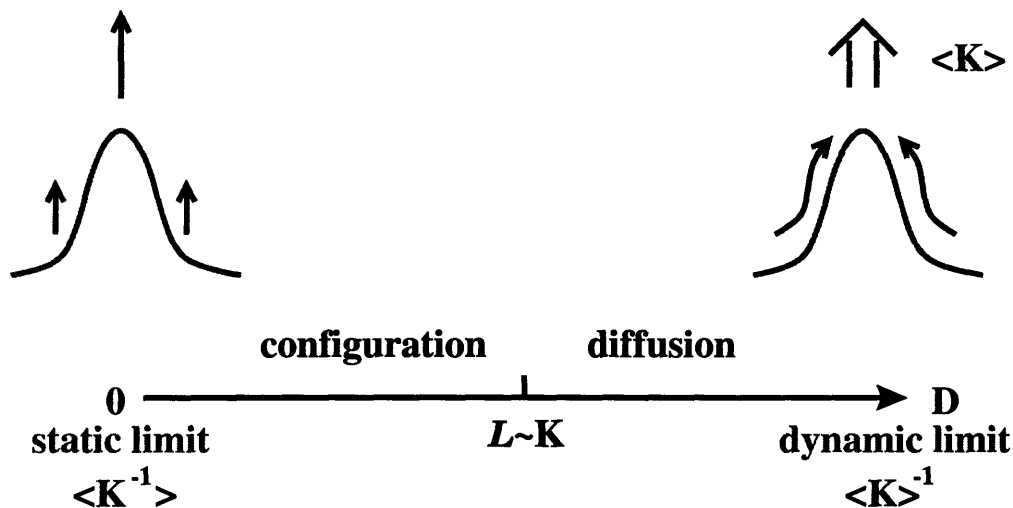
Figure 5-1: An illustration of the two kinetic regimes, the configuration-controlled regime and diffusion-controlled regime, and their corresponding limits.

Although these two regimes are not clearly separated, the boundary falls roughly into the region where the reaction and relaxation time scales become comparable.

Let us now study the Markovian fluctuations of the reaction coordinate. The reaction rate is given in quadratic form, $K(x) = \kappa x^2 + k_0$ with x the reaction coordinate. k_0, the nonzero decay rate at $x = 0$, is necessary to remove the divergence of the static average lifetime. The fluctuation of the reaction coordinate is controlled by a one-dimensional diffusive environment, $\mathcal{L} = D\partial_x[\partial_x + \partial_x(\beta U)]$. $D = \lambda\theta$ is the diffusion coefficient, $\beta U = x^2/(2\theta)$ is the potential of mean force, and θ is the variance of the fluctuations. The relaxation is an Ornstein-Uhlenbeck process with the survival probability given by[46, 60, 115, 118]

$$S(t) = \sqrt{\frac{4s}{(s+1)^2 - (s-1)^2 \exp[-2\lambda st]}} \exp\left\{-[\frac{\lambda}{2}(s-1) + k_0]t\right\}. \qquad (5.3)$$

$s = \sqrt{1 + 4\kappa\theta/\lambda}$ represents the coupling of the time scales associated with environmental relaxation and reaction kinetics. Next we expand the square root in Eq. (5.3) and express the survival probability as a combination of eigen modes. The average

147

lifetime, i. e. , the averaged sum of the eigen mode lifetimes, is

$$\langle t \rangle = \int_0^\infty S(t)dt = \sqrt{\frac{4s}{(s+1)^2}} \sum_{n=0}^\infty \frac{(2n-1)!!}{2^n n!} \left(\frac{s-1}{s+1}\right)^{2n} \frac{1}{\lambda(s-1)/2 + k_0 + 2n\lambda s} \quad (5.4)$$

The lowest eigen value $n = 0$ yields the long-time exponent. We discuss now the different dynamic scenarios:

5.2.1 Static limit: inhomogeneous average

The static limit case is displayed in Fig. 5-1. Sluggish environments such as glasses, $\mathcal{L} \ll K$, have slow relaxation rates that depend only on the initial configuration. The survival probability is the inhomogeneous average of the survival probabilities associated with each transient configuration, $S(t) = \langle \exp[-Kt] \rangle$. In this limit, the lifetime distribution function is $f(t) = \langle Ke^{-Kt} \rangle$, and the calculation of the average lifetime requires the inhomogeneous average of the time scale for each initial configuration, $\langle t \rangle = \langle K^{-1} \rangle$. Larger experimental time windows probe the configurations that relax gradually and essentially sample the configuration-controlled regime. The effects of the experimental time window in the dynamically regimes experienced by the chain conformation are elaborated in Sec. 5.4.

The static limit of the survival probability with a quadratic rate is obtained in the limit of $\lambda \to 0$ in Eqs. (5.3):

$$S(t) = \frac{1}{\sqrt{1 + 2\kappa\theta t}} \exp[-k_0 t]. \quad (5.5)$$

The averaged lifetime is:

$$\langle t \rangle = \sqrt{\frac{\pi}{2k_0\kappa\theta}} [1 - \text{Erf}(\sqrt{\frac{k_0}{2\kappa\theta}})] \exp[\frac{k_0}{2\kappa\theta}]. \quad (5.6)$$

For $k_0 \to 0$, the survival probability has a power-law decay $S(t) = 1/\sqrt{1 + 2\kappa\theta t}$ and a divergent average lifetime.

148

5.2.2 Configuration-controlled regime: inhomogeneous cumulant expansion

The configuration-controlled regime displayed in Fig. 5-1 is now addressed. Environmental fluctuations in viscous solvents are greatly reduced, but not negligible. The effects of the survival probability are evaluated with an inhomogeneous first-order cumulant expansion:[108]

$$S(t) = \langle \langle e^{-\int_0^t K(\tau)d\tau} \rangle_{\text{inhom}} \rangle \approx \langle \exp[-\int_0^t \langle K(\tau) \rangle_{\text{inhom}} d\tau] \rangle. \tag{5.7}$$

$\langle \cdots \rangle_{\text{inhom}}$ stands for the inhomogeneous average over trajectories at a given initial configuration.

In the short time limit, expansion of the configuration-controlled rate $\langle K(\tau) \rangle_{\text{inhom}}$ yields $S(t) \approx \langle \exp[-K(x_0)t - D\partial_x^2 K(x_0)t^2] \rangle$ and corresponds to a summation over the inhomogeneous Gaussian line shapes in spectroscopy.[56] The average lifetime, a weighted average over the inhomogeneous reaction times, is $\langle t \rangle \approx$ $\langle [K(x_0)]^{-1} \exp[-D\partial_x^2 K(x_0)/K(x_0)^2] \rangle$.[116]

The survival probability with a quadratic reaction rate is evaluated by a first-order cumulant expansion:

$$S(t) = \frac{1}{\sqrt{1 + 2\kappa\theta t e^{-2\lambda t}}} \exp\left\{ -[k_0 + \kappa\theta(1 - e^{-2\lambda t})]t \right\}. \tag{5.8}$$

The average lifetime $\langle t \rangle = \hat{S}(0)$, is displayed in Fig. 5-2. The plot shows that the first-order inhomogeneous cumulant expansion is the lower bound for the exact calculation and reduces to the static limit in the limit of $D = \lambda\theta \to 0$.

5.2.3 Diffusion-controlled reaction regime: the Wilemski-Fixman approximation

Let us now discuss the diffusion-controlled regime. Here, the relaxation time is shorter than the typical the reaction time. Expansion of $(w - \mathcal{L} + K)^{-1}$ followed by the
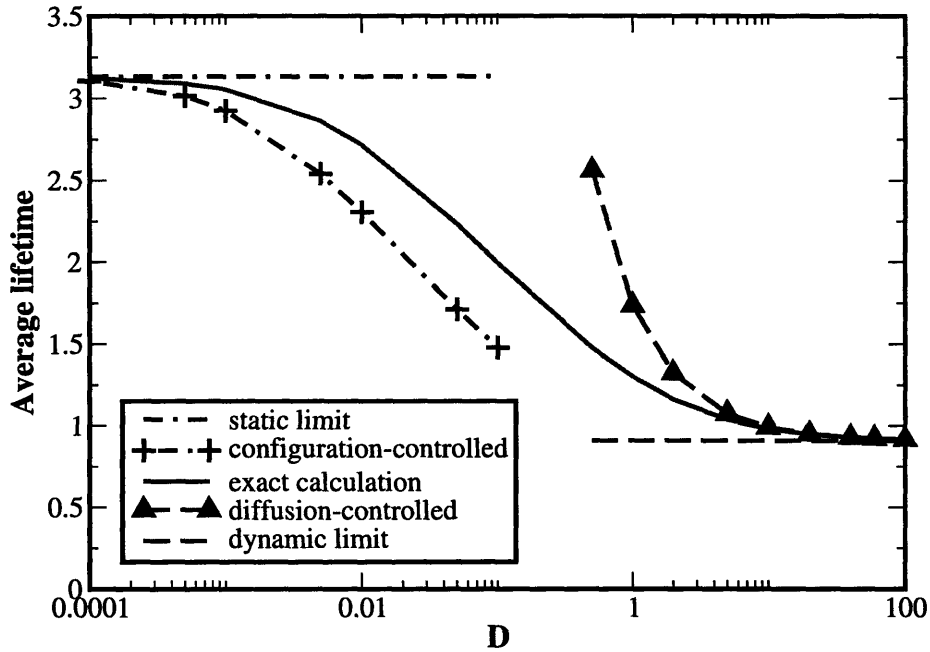
Figure 5-2: The average lifetime for the Markovian fluctuations of reaction coordinate studied in Sec. 5.2, where $\kappa = 1$, $k_0 = 0.1$ and $\theta = 1$. The diffusion coefficient D is equal to λ. The inhomogeneous cumulant expansion in configuration-controlled regime defines a lower bound for the survival probability and agrees well with the exact calculation as the reaction approaches the static limit. The WF approximation in the diffusion-controlled regime defines an upper bound and agrees with the exact calculation and the reaction approaches the dynamic limit.

ensemble average renders the survival probability:

$$\hat{S}(w) = \frac{1}{w} - \frac{1}{w^2}\langle K \rangle + \frac{1}{w^2}\langle K\hat{G}(w)K \rangle - \frac{1}{w^2}\langle KG(w)K\hat{G}(w)K \rangle + \cdots . \qquad (5.9)$$

$\langle \cdots \rangle$ represents the ensemble average and $\hat{G}(w) = 1/(w - \mathcal{L})$ is the Laplace transform of the Green's function $G(t)$ for the environmental relaxation. We now derive a closure for $\hat{S}(w)$. First let us separate out the asymptotic limit of $\hat{G}(w)$ as $\hat{G}(w) = \hat{G}'(w) + P_{eq}/w$ with $P_{eq}/w = \lim_{w\to 0}\hat{G}(w)$. The survival probability is approximated

as

$$\hat{S}(w) = \frac{1}{w} - \frac{1}{w^2}\langle K \rangle + \frac{1}{w^2}(\frac{\langle K \rangle^2}{w} + \langle K\hat{G}'K \rangle)$$

$$- \frac{1}{w^2}(\frac{\langle K \rangle^3}{w^2} + 2\langle K\hat{G}'K \rangle\frac{\langle K \rangle}{w} + \langle K\hat{G}'K\hat{G}'K \rangle) + \cdots$$

$$\approx \frac{1}{w} - \frac{k}{w^2} + \frac{k}{w^2}(\frac{k}{w} + k\hat{\chi}) - \frac{k}{w^2}(\frac{k}{w} + k\hat{\chi})^2 + \cdots$$

$$= \frac{1 + k\hat{\chi}(w)}{w[1 + k\hat{\chi}(w)] + k}. \tag{5.10}$$

$k = \langle K \rangle$ is the homogeneous average of the reaction rate and $\chi(t) = \langle KG'(t)K \rangle/k^2 = \langle KG(t)K \rangle/k^2 - 1$. $\chi(t)$, the memory function measures the relaxational effect of the reactive system. The Laplace transform of the lifetime distribution function is obtained from Eq. (5.10):

$$\hat{f}(w) = \frac{k}{w(1 + \hat{\chi}(w)k) + k} \tag{5.11}$$

with the average lifetime

$$\langle t \rangle = \hat{S}(w = 0) = \frac{1 + \hat{\chi}(0)k}{k}. \tag{5.12}$$

These results have been derived by Wilemski and Fixman using a different approach.[44, 45] Let us now make several observations:

1. $\langle KG'KG'K \rangle \approx k^3\hat{\chi}^2(w)$ applies at small reaction rates and fast relaxation times, i. e. , $\hat{\chi}(0)k \ll 1$. This is consistent with the stochastic rate model discussed in Ref. [118]. The survival probability was derived there from a second cumulant expansion of the stochastic rate,

$$S(t) = \langle e^{-\int K(t)dt} \rangle = \exp[-\langle K \rangle t + \frac{1}{2}\int \langle \delta K(t_1)\delta K(t_2) \rangle dt_1 dt_2 + \cdots]$$

$$\approx \exp[-kt + k^2\hat{\chi}(0)t]. \tag{5.13}$$

The average lifetime, $\langle t \rangle \approx k[1 - k\hat{\chi}(0)]^{-1} \approx 1/k + \hat{\chi}(0)$, recovers Eq. (5.12).

2. In the homogeneous limit, $\chi(z) \to 0$, $\hat{S}(w)$ from the WF theory is $\hat{S}(z) =$

151

$1/(z + k)$. Hence the survival probability decays exponentially and corresponds to a homogeneous Lorentzian line shape observed in optical spectroscopy. In the inhomogeneous limit, we have shown earlier in Sec. 5.2.2 that the survival probability is given by $S(t) = \langle \exp[-K(x_0)t - D\partial_x^2 K(x_0)t^2] \rangle$. This dependence corresponds to an inhomogeneous Gaussian line shapes.[56]

3. Evident from Eq. (5.10), the key approximation to the WF expression is $\langle KG'KG'K \rangle \approx k^3 \hat{\chi}^2(w)$.[44, 45] For localized reactions, $K = k(\mathbf{r}_0)\delta(\mathbf{r} - \mathbf{r}_0)$, the WF approximation and Eq. (5.10) are exact. This situation has been studied in the context of solvent-controlled electron transfer, where the non-adiabatic electron transfer occurs at the transition state. The diffusion-controlled electron transfer rate was first studied by Zusman and recently re-examined by Cao and Jung.[61, 65, 119, 120]

4. For moderate values of the diffusion coefficient, the long-time decay is still dominated by the fundamental relaxation mode and has a single-exponential decay. For finite D, the depletion rate at long time is generally different from the homogeneous average rate k, and is different from the WF approximation. A detailed discussion of the long time decay rate is given in Sec. 5.4.

5. The WF approximation in the diffusion-controlled regime provides an upper bound for the survival probability(see Ref. [107] by Portman and Wolynes). Quantitatively, the WF approximation is exact to the first order in $1/D$ for both Markovian and non-Markovian processes. A mathematical proof is given in Appendix 5-A for an arbitrary reaction rate using the generalized WF approximation. The $1/D$ expansion of the average lifetime obtained is in agreement with Weiss's work.[43, 46] A more detailed discussion of the WF approximation and its validity regime are presented in paper II of this series.[117]

The WF approximation for the quadratic reaction-rate process considered in Eq. (5.3) yields:

$$\langle t \rangle = \frac{1}{k} + \hat{\chi}(0) \approx \frac{1}{k} + \frac{1}{\lambda} \frac{\kappa^2 \theta^2}{k^2}. \tag{5.14}$$

The homogeneous average rate is $k = \kappa\theta + k_0$. As shown in Fig. 5-2, the WF approximation approaches the exact average lifetime for large λ. Direct expansion of the exact average lifetime in Eq. (5.4) for large λ yields:

$$\langle t \rangle = \frac{1}{k} + \frac{1}{\lambda}\frac{\kappa^2\theta^2}{k^2} - \frac{1}{\lambda^2}\frac{\kappa^2\theta^2}{2k^3}(3\kappa^2\theta^2 + 6\kappa\theta k_0 + k_0^2) + O(\frac{1}{\lambda^3}). \qquad (5.15)$$

Eq. (14) reduces to the WF approximation of the average lifetime up to the first order in $1/\lambda$. The negative sign in front of the $1/\lambda^2$ term supports the fact that the WF approximation always gives the upper bound to the survival probability. This is confirmed for a non-Markovian fluctuations of the reaction coordinate by a numerical calculation in Sec. 5.3.

5.2.4 Dynamical limit: homogeneous average

Let us now discuss the case where the relaxation time is much shorter than the reaction time. This kinetic scenario corresponds to a phenomenological Poisson process with a homogeneous reaction rate $k = \langle K \rangle$. In this limit, the average lifetime is $1/k$, and the survival probability reduces to $\exp(-kt)$. The average lifetime approaches the dynamic limit from above as D increases, and the homogeneous average is a lower bound for the system. This limit illustrated in Fig. 5-2 is obtained naturally from the diffusion-controlled reaction regime discussed in the previous sub-section. In the limit $\lambda \to \infty$ for the Markovian process considered in Eq. (5.3), the survival probability reduces to $S(t) = \exp(-kt)$, yielding the homogeneous decay.

5.3 Non-Markovian processes: Intra-molecular fluorescence quenching on a semi-flexible Gaussian chain

Formation of a specific contact between two residues on a polypeptide chain is a fundamental process in protein folding. Fluorescence quenching has recently been

employed to study the intra-molecular contact in polymer chains by measuring the average lifetime of fluorescence.[39, 40, 42] In the diffusion-controlled regime, the internal relaxation of the polymer chain is controlled by solvent viscosity, and it provides an effective way to decouple the relaxation process from the quenching process.

Without explicit considerations of the excluded volume effect and geometrical constraints, ideal polymers are flexible at all length scales and are described by Gaussian statistics. However, most single molecule experiments on bio-molecules are performed at length scales where the polymer exhibits some rigidity, and semi-flexibility is key to understand the measurements of single polymer dynamics. In Ref. [116], we extended the Gaussian chain model to include the chain stiffness and studied the Brownian dynamics of the semi-flexible chain with a normal mode decomposition of the Langevin equation. The equilibrium properties of semi-flexible chains were studied by Kratky and Porod, Harris and Hearst, Freed, Fixman and Kovac, Ha and Thirumalai, and many others.[85, 86, 87, 90, 92, 93] The non-Markovian features of the internal relaxation make it hard to solve the full kinetic equation analytically. Here we decompose non-Markovian fluctuations of the reaction coordinate into a sum of Markovian processes and investigate the coupled reaction and relaxation using path integral methods.

Eaton and coworkers measured the quenching rate for tryptophan-cysteine pairs using $K(R) = q_0 \exp[-\gamma(R - a_0)]$ with $\gamma = a_0^{-1}$. a_0 is the contact radius, q_0 is the quenching rate at contact, and R is the reaction coordinate described by the fluorophore-quencher distance. $K(R)$ falls off exponentially as a function of the reaction coordinate. For a tryptophan-cysteine pair, $q_0 = 4.2$ ns^{-1} and $a_0 = 0.4$ nm.[42, 41] For a Gaussian chain, with two amino acids, tryptophan and cysteine attached at the end points, the equilibrium distribution of the end-to-end distance is

$$P_{eq}(R) = [\frac{2\pi\langle R^2 \rangle}{3}]^{-3/2} 4\pi R^2 \exp\left[-\frac{3R^2}{2\langle R^2 \rangle}\right],$$
(5.16)

with $\langle R^2 \rangle$ the mean square fluorophore-quencher distance. The normal mode repre-

sentation of the end-to-end distance vector is

$$\mathbf{R} = \sum_{p=1}^{N-1} c_p \mathbf{x}_p \qquad (5.17)$$

with $c_p = -[(-1)^p - 1]/2 \cos(p\pi/2N)$. The normal mode representation of the internal relaxation Smoluchowski operator $\mathcal{L}$ is:

$$\mathcal{L} = \sum_{p=1}^{N-1} \frac{1}{\zeta_p} \frac{\partial}{\partial \mathbf{x}_p} \left(k_B T \frac{\partial}{\partial \mathbf{x}_p} + \lambda_p \mathbf{x}_p \right). \qquad (5.18)$$

$\mathcal{L}$ determines the Green's function and equilibrium distribution of each normal coordinate. A detailed derivation is given in Ref. [116]. The equilibrium distribution and the Green's function of the normal coordinates are

$$P_{eq}(\mathbf{x}_p) = \prod_{p=1}^{N-1} (\frac{2\pi k_B T}{\lambda_p})^{-3/2} \exp\{-\frac{\sum_{p=1}^{N-1} \lambda_p \mathbf{x}_p^2}{2k_B T}\}, \qquad (5.19)$$

and

$$G(\mathbf{x}_p, t | \mathbf{x}_p, t') = \prod_{p=1}^{N-1} \left[\frac{2\pi k_B T}{\lambda_p} (1 - e^{-2\frac{\lambda_p}{\zeta_p}(t-t')}) \right]^{-3/2} \cdot$$
$$\exp \left\{ -\frac{\sum_{p=1}^{N-1} \lambda_p [\mathbf{x}_p - \mathbf{x}_p(0) e^{-\frac{\lambda_p}{\zeta_p}(t-t')}]^2}{2k_B T [1 - e^{-2\frac{\lambda_p}{\zeta_p}(t-t')}]} \right\}, \qquad (5.20)$$

respectively. So all the normal coordinates are Markovian with different relaxation times. On the other hand, the reaction coordinate is a combination of these normal coordinates is generally non-Markovian. In this work, we carry out path integral simulations of the fluorescence quenching process on a semi-flexible chain.[74, 119, 121] The total time is discretized into slices $M\Delta = t$. In our simulation, initial configurations of the normal coordinates are generated according to the equilibrium distribution in Eq. (5.19) and propagated within each time slice according to the Green's function in Eq. (5.20). For each time step, we determine the end-to-end distance vector with Eq. (5.17) and the quenching rate accordingly. Formally, the
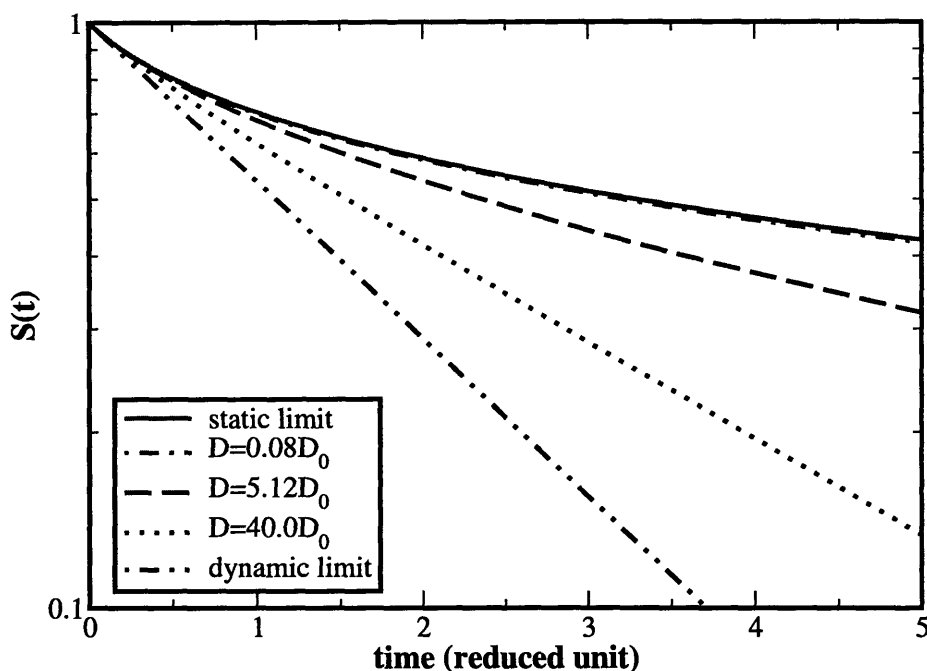
Figure 5-3: Path integral simulations of the survival probability $S(t)$ for the intramolecular fluorescence quenching experiments. $a_0^2/6D_0$ is the time unit. The persistence length $L_p = 2$, chain length $N = 10$ and the quenching rate at contact is estimated from Eaton et al's experiments to be $q_0 = 5.6$. All the survival probability functions for various solvent viscosities reduce to homogeneous single-exponential decay for large observation time.

survival probability is:

$$S(t) = \lim_{M\to\infty} \int d\mathbf{X}_{M-1} \cdots \int d\mathbf{X}_0 e^{-K(\mathbf{X}_{M-1})\Delta} G(\mathbf{X}_{M-1}, (M-1)\Delta; \mathbf{X}_{M-2}, (M-2)\Delta)$$
$$\cdots e^{-K(\mathbf{X}_1)\Delta} G(\mathbf{X}_1, \Delta; \mathbf{X}_0, 0) P_{eq}(\mathbf{X}_0) \tag{5.21}$$

with $\mathbf{X}$ a short notation of the normal coordinates $\{x_p\}$.

In experiments, the survival probability $S(t)$ or quantum yield is monitored over a wide range of experimental time scales, and the average lifetime is obtained by integration of $S(t)$ up to the experimental time,

$$\langle t \rangle = \int_0^{t_{exp}} S(t)dt. \tag{5.22}$$

156
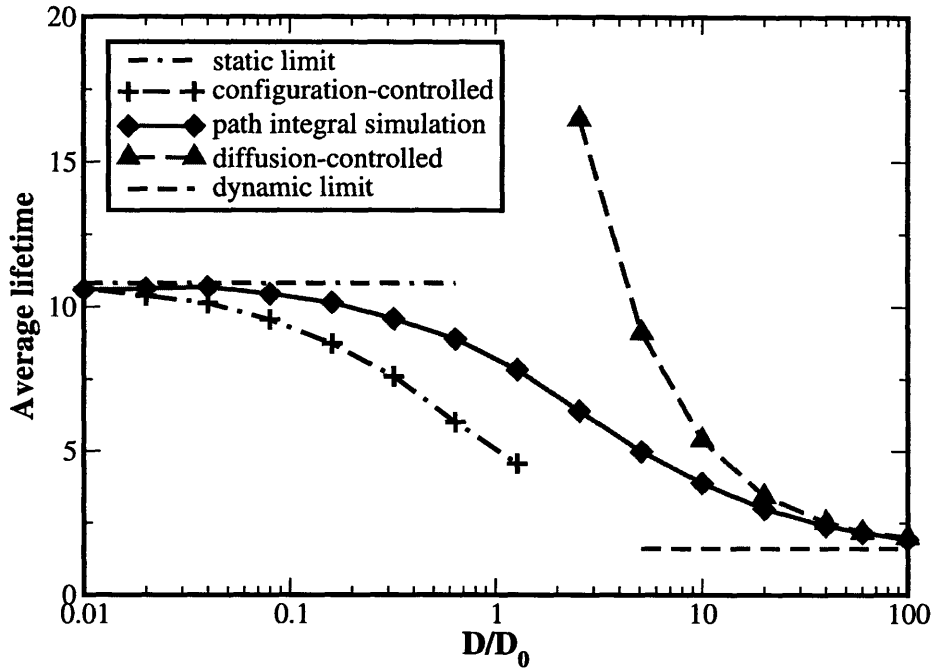
Figure 5-4: The average lifetime $\langle t \rangle$ calculated by path integral simulations for a fixed experimental time $t_{exp} = 40$ in the reduced time unit. Other parameters are the same as in Fig. 5-3. The WF approximation holds for fast intra-chain relaxation while the inhomogeneous cumulant expansion holds for slow intra-chain relaxation. The long time kinetics is always described by the WF approximation for the diffusion-controlled regime.

Eq. (5.22) reduces to $\hat{S}(w = 0)$ as t_{exp} approaches infinity. The configuration-controlled regime and the diffusion-controlled regime are explained in detail. We calculate survival probabilities and their corresponding average lifetimes for various solvent viscosities. The survival probability functions are shown in the master plot of Fig. 5-3, and the average lifetime for the full range from the static limit to the dynamic limit are plotted in Fig. 5-4. In both plots, a specific solvent at a viscosity of 10 cp and 293 K is taken as a reference state, $a_0 = 0.4$nm is the natural length unit, and $a_0^2/6D_0 \approx 25$ nanosecond is the corresponding time unit. In the reference state, the quenching rate at the contact is $q_0 = 5.6$. These numbers are used to match experimental values from Eaton's studies.[42]

The average lifetime from Eq. (5.22) is evaluated in a time window of $t_{exp} = 40$ and

plotted in Fig. 5-4. The average lifetime falls below the static limit is a clear indication of the reaction slow-down in absence of sufficient relaxation. This feature is more evident in Fig. 5-3: The survival probability in the static limit is the upper bound for the survival probability with nonzero diffusion coefficients, and inhomogeneous effects are significant for short observation times. In the long time limit, the kinetics is dominated by homogeneous decay.

In the configuration-controlled regime, an inhomogeneous cumulant expansion of Eq. (5.7) yields:

$$
\begin{aligned}
\langle K(\tau)\rangle_{\text{inhom}} &= \frac{q_0}{2}\exp[(\frac{\alpha}{2}-1)\gamma R_0\phi(t) + \gamma a_0]\cdot\Big\{1 + e^{2\gamma R_0\phi(t)} + \alpha(e^{2\gamma R_0\phi(t)} - 1) \\
&\quad + |1-\alpha|\operatorname{Erf}(\left|\frac{(1-\alpha)\sqrt{\gamma R_0\phi(t)}}{\sqrt{2\alpha}}\right|) \\
&\quad - e^{2\gamma R_0\phi(t)}|1+\alpha|\operatorname{Erf}(\left|\frac{(1+\alpha)\sqrt{\gamma R_0\phi(t)}}{\sqrt{2\alpha}}\right|)\Big\}
\end{aligned}
$$

$$
\text{with}\quad \alpha = \frac{\gamma\langle R^2\rangle(1-\phi^2(t))}{3R_0\phi(t)} \tag{5.23}
$$

$\phi(t) = \langle \mathbf{R}(t)\mathbf{R}(0)\rangle/\langle \mathbf{R}^2\rangle$ is the distance-distance correlation function given in Ref. [116]. Fig. 5-5 compares inhomogeneous cumulant expansion of the survival probability and the path integral calculation. The configuration-controlled reaction provides a better approximation as lower solvent diffusion coefficients. The exact survival probability is bounded from below by inhomogeneous averaging. At larger observation time, the exact survival probability yields a homogeneous decay, consistent with our observations in Fig. 5-3. A more detailed discussion of the experimental time scale will be addressed in Sec. 5.4.

In the diffusion-controlled regime, the memory function $\chi(t)$ is obtained directly from path integral simulations and the average lifetime is evaluated with Eq. (5.12). Fig. 5-4 shows that the WF approximation, $\langle t\rangle = 1/k + \hat\chi(0)$, is an upper bound for the average lifetime. The exact result is approached from above as the relaxation rate increases. For fast diffusion, $\langle t\rangle = 1/k + \hat\chi(0)$ converges to the dynamic limit with the order of $1/D$. The scaling of the average lifetime is demonstrated in the inset of
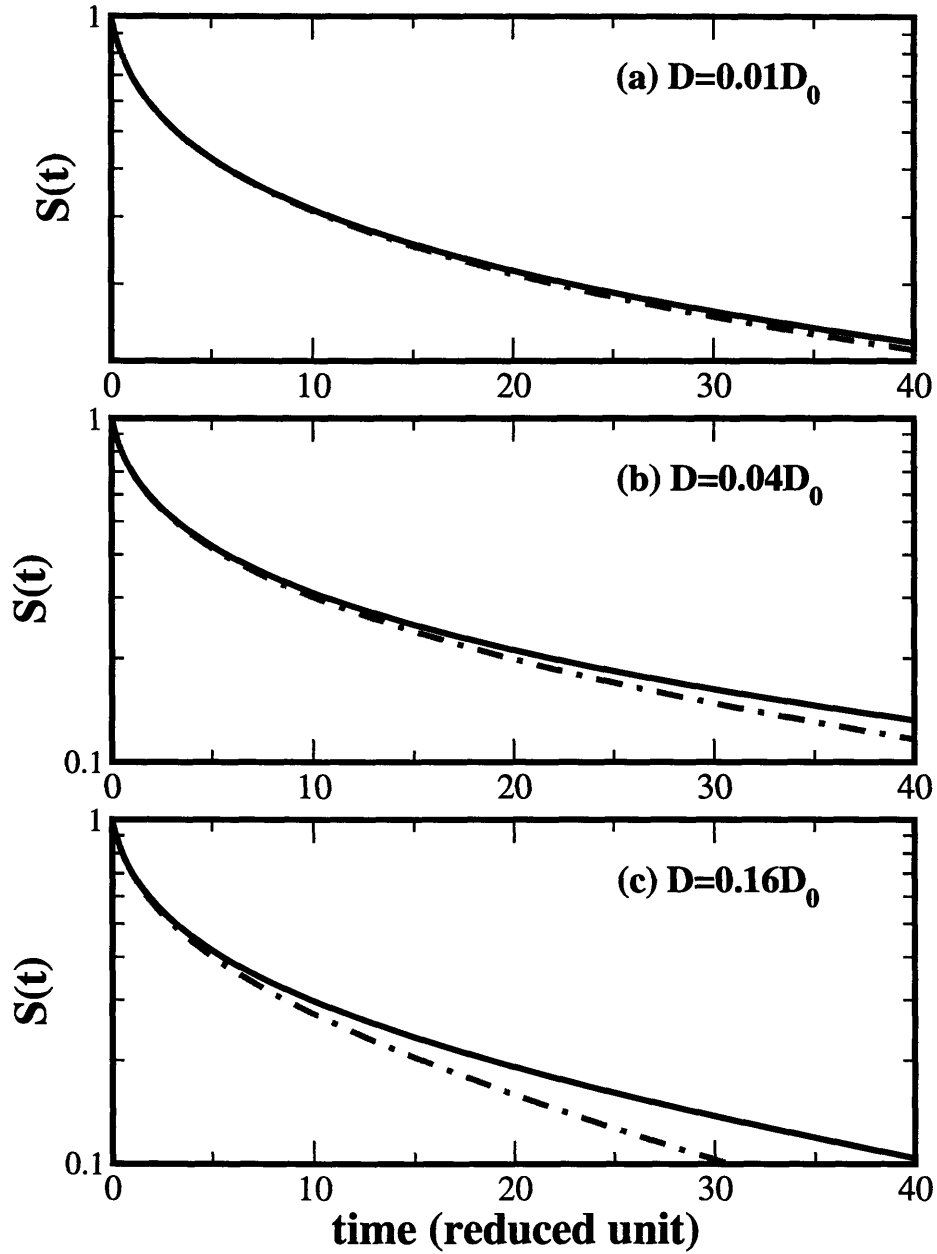
Figure 5-5: Comparison of the survival probability functions calculated by path integral simulation and first-order inhomogeneous cumulant expansion. As the intra-chain relaxation becomes slow, and $t \to 0$, the inhomogeneous cumulant expansion better approximates the real survival probability. As the observation time increases, the overall kinetics is dominated by the homogeneous decay.
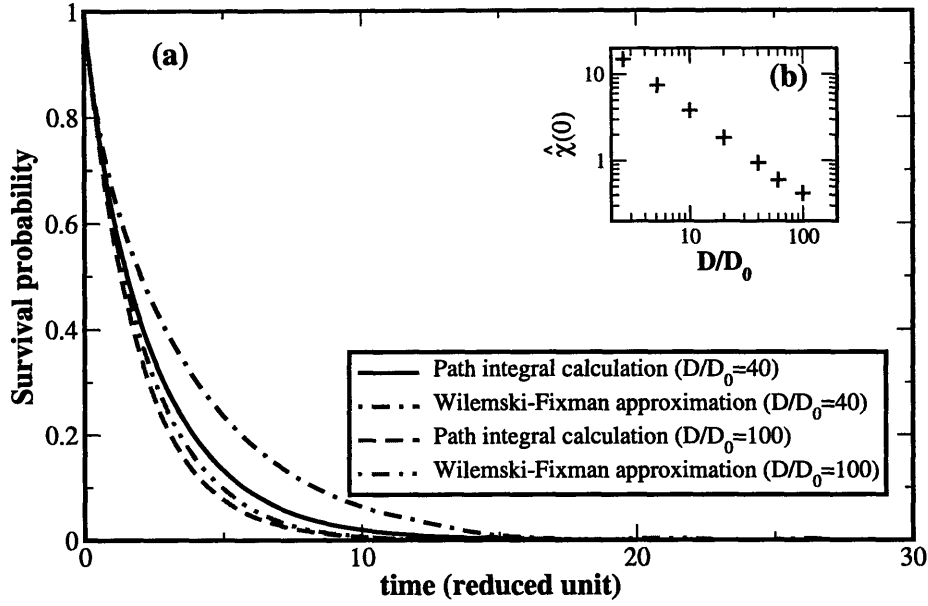
Figure 5-6: (a) The survival probability functions calculated and compared for path integral simulation and WF expansion. In the long time, the WF approximation always predicts a single-exponential decay, yet with a smaller decay rate than the actual survival probability obtained from the path integral simulation. The difference in rate decreases with the diffusion coefficient. (b) A log-log plot of the contact formation time $\hat{\chi}(0) = \int_0^\infty \chi(t)dt$ versus the diffusion coefficient. $\hat{\chi}(0)$ scales as $1/D$ in the diffusion-controlled regime.

Fig. 5-6. The log-log plot of $\hat{\chi}(0)$ precisely follows the $1/D$ scaling. In Fig. 5-6, we use the memory function $\chi(t)$ from the simulation to calculate the survival probability with the WF approximation. The numerical implementation is as follows. First, we rewrite Eq. (5.10) as

$$\hat{S}(w) = \frac{1}{w+k} + k[\frac{1}{z+k}\hat{\chi}(z) - \hat{S}(z)\hat{\chi}(z)] + k^2\frac{1}{z+k}\hat{\chi}(z)\hat{S}(z). \qquad (5.24)$$

Then, we invoke the inverse Laplace transform and obtain the iteration scheme,

$$
\begin{aligned}
S(t) &= e^{-kt} + k\int_0^t dt_1 \int_0^{t_1} dt_2 [e^{-k(t_1-t_2)}\chi(t_2) - S(t_1 - t_2)\chi(t_2)] \\
&\quad + k^2 \int_0^t dt_1 \int_0^{t_1} dt_2 \int_0^{t_2} dt_3 [e^{-k(t_1-t_2)}\chi(t_2 - t_3)S(t_3)].
\end{aligned} \qquad (5.25)
$$

160
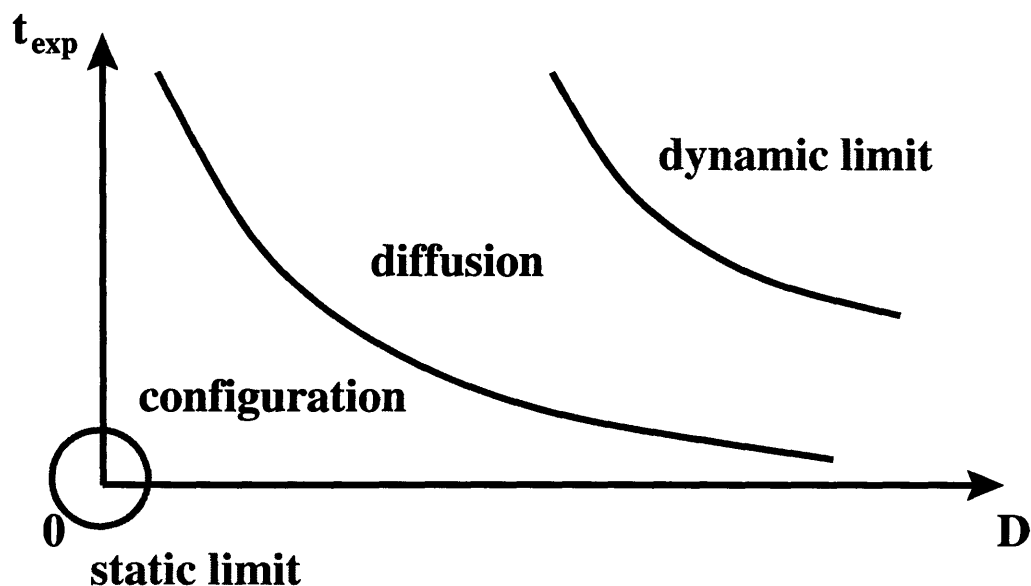
Figure 5-7: An illustrative sketch of the experimental time scale effects. The boundaries drawn in the plot are only for the purpose of explanation.

Fig. 5-6 shows that the survival probability calculated using the WF approximation approaches the exact results at larger diffusion coefficients.

5.4 Experimental time scale: a unified perspective

In the previous two sections, we explored the relation between the relaxation and the reaction time scales. In reality, finite experimental time windows play an important role in the kinetic interpretations. For example, in fluorescence quenching experiments we monitor the time range of population decay to obtain the average lifetime. In FRET experiments, an appropriate observation window is used to monitor the quantum yield and determine the donor-acceptor distance.[16, 35]

The mechanism of population depletion from its dependence on D and t_{exp} is illustrated in Fig. 5-7. At small time windows, only transient configurations can be probed no matter how fast the relaxation is and the static limit is retrieved. At larger experimental times, transient configurations are no longer frozen, yet the

relaxation perturbs slightly the transient configuration and the kinetics is typically in the configuration-controlled regime. The inhomogeneous cumulant expansion gives here the correction to the inhomogeneous limit. As illustrated in Fig. 5-7, the effective range of the configuration-controlled regime depends inversely on the relaxation rate. In the slow relaxation region, static configurations dominate the kinetics for a wide range of time. In the fast relaxation region, the static configurations relax quickly into other configurations. This behavior is clearly demonstrated in our numerical calculation for fluorescence quenching processes. The survival probabilities from the inhomogeneous cumulant expansion agree well with the exact results for small D and at short times, but the expansion fails to describe the long-time decay. That is seen clearly in Fig. 5-5.

Now we expand Eq. (5.7) to the second inhomogeneous cumulant:

$$S(t) \approx \langle \exp\left[-\int_0^t \langle K(\tau)\rangle_{\text{inhom}} d\tau + \int_0^t (t-\tau)\langle \delta K(\tau)\delta K(0)\rangle_{\text{inhom}} d\tau \right]\rangle. \qquad (5.26)$$

For the expansion to be valid, the second cumulant has to be smaller than the first cumulant for every initial position. Such criteria can not be satisfied in the long time limit. Generally speaking, in the $K \to 0$ limit, the slow-reacting population is first diffused to the fast-reacting region and then depleted at longer times. Hence the long time decay is always dominated by the diffusion process. At small fluctuations, we evaluate the survival probability using a full cumulant expansion instead of the inhomogeneous cumulant expansion. This scenario is similar to the Gaussian stochastic rate model discussed in Ref. [118]. The average lifetime is obtained from the second cumulant expansion, $\langle t \rangle = k[1 - k\hat{\chi}(0)]^{-1} \approx 1/k + \hat{\chi}(0)$, which reduces to the WF results for diffusion-controlled reactions. The second cumulant expansion over the equilibrium distribution in Eq. (5.26) generates the same result. The transition from the short-time to the long-time behavior was discussed by Pechukas and Ankerhold in the context of Agmon-Hopfield kinetics.[8] For an ergodic system, the average of lifetime over an extreme large experimental time generates the homogeneous limit. This has been demonstrated in the numerical calculation of fluorescence quenching pro-
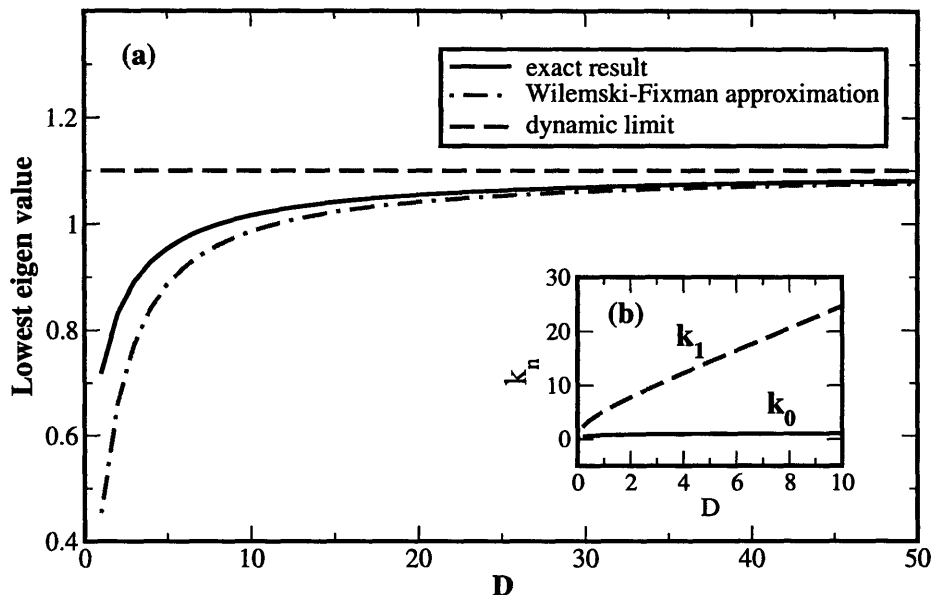
Figure 5-8: (a) The asymptotic decay rate for long experimental time. The exact lowest eigenvalue and the WF approximation are calculated for the Markovian fluctuations of the reaction coordinate defined in Sec. 5.2 with parameters same as those in Fig. 5-2. (b) The lowest two eigenvalues. The gap of them increases almost linearly with D for large diffusion coefficients.

cesses. Figs. 5-3, 5-5, and 5-6 show that the long time kinetics is always homogeneous regardless of the magnitude of the diffusion coefficient, yielding a single-exponential decay.

In that case, the long time decay of the population is determined by the lowest eigenvalue of the full kinetic equation in Eq. (5.1). [119] Let us now define $\mathcal{L} = D\partial_x[\partial_x + \partial_x(\beta U)]$ and a corresponding Hermitian operator $\mathcal{H} = e^{\beta U/2}\mathcal{L}e^{-\beta U/2}$. $\mathcal{H}$ transforms the original kinetic equation into a Schrödinger-like equation,

$$\partial_t(e^{\beta U(x)/2}P) = -K(e^{\beta U(x)/2}P) + \mathcal{H}(e^{\beta U(x)/2}P). \tag{5.27}$$

The lowest eigenvalue of $K - \mathcal{H}$ is k_f and the lowest eigenstate is $\psi_f(x)$. The long

163

time decay of the population is given by

$$\lim_{t \to 0} P(x,t) \propto \exp[-k_f t] e^{-\beta U(x)/2} \psi_f(x). \tag{5.28}$$

The overall population is proportional to $e^{-\beta U(x)/2} \psi_f(x)$ and decays in the long time limit with a homogeneous rate. The dominance of the lowest eigenvalue requires a large gap between the lowest two eigenvalues $t\Delta k \gg 1$. This indicates a lower bound on the experimental time. For the Markovian case of the reaction coordinate defined in Sec. 5.2, the eigenvalues are determined exactly as $k_n = \lambda(s-1)/2 + k_0 + 2n\lambda s$. The gap between the lowest two eigenvalues is $2\lambda s$ and is a convolution of the reaction time scale and the diffusion time scale. In the long time when $2\lambda s t \gg 1$, the population depletion is dominated by the lowest eigenvalue $k_f = \lambda(s-1)/2 + k_0$. As shown in Fig. 5-8, the dominant eigenvalue from the WF approximation approaches k_f from below as D increases. Both decay rates converge to $k = \langle K \rangle$ in the fast diffusion limit. The lowest two eigenvalues are plotted in the inset of Fig. 5-8, where the gap $k_1 - k_0 = 2\lambda s$ grows almost linearly with the diffusion coefficient at large D's.

5.5   Concluding remarks

Reaction kinetics modulated by environmental fluctuations are bounded by two different regimes. In the configuration-controlled regime, the reaction process dominates, and the average lifetime becomes a weighted average over the inhomogeneous reaction time. The asymptotic limit of this regime is the static limit where the average lifetime $\langle t \rangle = \langle K^{-1} \rangle$ is an inhomogeneous average over the equilibrium distribution. In the diffusion-controlled regime, the diffusion process dominates, and in the WF approximation, $\langle t \rangle = 1/k + \hat{\chi}(0)$, is the sum of the reaction time and the diffusion time. In the dynamic limit for fast diffusion, $\langle t \rangle = 1/\langle K \rangle$ becomes the reciprocal of the homogeneous rate. The exact survival probability is bounded from below by the first-order inhomogeneous cumulant expansion and from above by the WF approximation. For comparable reaction and relaxation times, in the long time limit

the convolution of reaction kinetics and the internal relaxation process eventually reaches a fixed distribution shape and the overall reaction is characterized by a single exponential.

Variation of the experimental time of the fluorescence measurements allows people to explore various kinetic regimes from the inhomogeneous limit across the homogeneous limit. At small time windows, only static configurations are probed. At larger time windows, the relaxation process modifies the transient configurations to a configuration-controlled regime. Further increase in the measurement time probes the diffusion-controlled regime where long time kinetics is dominated by relaxation. For ergodic systems, the long time average yields the homogeneous limit.

In Appendix 5-A, we generalize the WF approach to address the average lifetime. A perturbation expansion over $1/D$ of our equations reduces to the WF approximation to the first order of $1/D$. In addition, we recover the $1/D$ expansion of the average lifetime derived by Weiss.[46] In Appendix 5-B, we discuss the relation between the experimental time scale and the apparent distribution of the measured quantities such as lifetime distribution obtained in single molecule experiments.

Fluorescence quenching and fluorescence resonance energy transfer (FRET), can probe the details of the motions of synthetic and biological polymers. Semi-flexibility, hydrodynamic interactions, excluded volume effects, and experimental time scales greatly affect their equilibrium and non-equilibrium properties. In paper II of this series,[117] we address the contour-length dependence of the average lifetime due to semi-flexibility. Theoretical studies of these effects improve our understanding of the important issues related to biological functions of DNA and proteins.

5.6 Appendix 5-A: Generalized WF approximation and the Weiss expansion

A widely used approximation to calculate the average lifetime in the diffusion-controlled limit was first presented by Wilemski and Fixman.[44, 45] As demonstrated in Secs. 5.2

and 5.3, the WF approximation is only accurate to the first order in $1/D$, hence is useful for large diffusion coefficients. In 1980, Szabo, Schulten and Schulten presented an integral expression for the first passage time.[43] Later, Weiss obtained a $1/D$ expansion of the average lifetime based on a systematic perturbation analysis.[46] Here we generalize the WF approximation based on a perturbative expansion scheme. In paper II of this series, we discuss the relation of this generalization with single-molecule measurements and the validity region of the WF approximation.[117]

To proceed, we consider a generic scenario described by the diffusion equation, $\partial_t P = \mathcal{L}P - KP$, where K is the reaction rate and $\mathcal{L}$ is the relaxation operator proportional to the diffusion coefficient D. We write the operator $\mathcal{L}$ as $D\mathcal{L}_0$, where $\mathcal{L}_0 = \partial_x[\partial_x + \partial_x(\beta U)]$ is the relaxation operator for unit diffusion coefficient. For simplicity, we only consider the one dimensional case; the formalism is fully applicable to higher dimensions.

Next we employ the adjoint operator $\mathcal{L}^+$ definition which was used by Szabo, Schulten and Schulten in their solution to diffusion with Smoluchowski boundary conditions.[43] And we obtain the passage time for any given initial position x_0:

$$\mathcal{L}^+\tau(x_0) - K(x_0)\tau(x_0) = -1. \tag{5.29}$$

The average lifetime is the spatial average of $\tau(x_0)$ over the equilibrium distribution,

$$\langle t \rangle = \int dx_0 P_{eq}(x_0)\tau(x_0). \tag{5.30}$$

$P_{eq} = \mathcal{N}\exp[-\beta U]$ and $\mathcal{N}$ is the normalization constant. $\mathcal{L}_0$ is not a Hermitian operator. We define a corresponding Hermitian operator: $H = \exp[\beta U/2]\mathcal{L}_0\exp[-\beta U/2]$.[119] The adjoint operator is $\mathcal{L}^+ = \exp[\beta U/2]DH\exp[-\beta U/2]$. We define a functional space: $X = \left\{\phi(x)|\int \phi^2(x)dx = 1\right\}$ with inner product $(f,g) = \int f(x)g(x)dx$. Apparently $\phi_0(x) = \sqrt{\mathcal{N}}\exp[-\beta U/2] \in X$, and $H\phi_0 = 0$. The average lifetime defined in Eq. (5.30) is equivalent to $\langle t \rangle = (\phi_0, (K - DH)^{-1}\phi_0)$ and the homogeneous average rate is $k = (\phi_0, K\phi_0)$. The survival probability in Laplace space is obtained as $\hat{S}(z) = (\phi_0, (z + K - DH)^{-1}\phi_0)$ in the same fashion.

We now derive the generalized WF approximation. Assuming $\{\phi_0, \phi_1, \phi_2, \ldots \ldots\}$ is an orthogonal basis of X, we can express the operators K and H as block matrices,

$$K = \begin{bmatrix} K_{00} & K_{01} \\ K_{10} & K_{11} \end{bmatrix}, \quad H = \begin{bmatrix} 0 & 0 \\ 0 & H_{11} \end{bmatrix}. \tag{5.31}$$

K_{00} is the homogeneous average rate k. The survival probability is:

$$\hat{S}(z) = [z + k - K_{01}(z + K_{11} - DH_{11})^{-1}K_{10}]^{-1} = \frac{1 + \hat{\Omega}(z)}{k + z[1 + \hat{\Omega}(z)]}, \tag{5.32}$$

where $\hat{\Omega}(z) = k^{-1}\sum_{n=0}^{\infty}(-1)^n D^{-(n+1)}\hat{Y}_n(z/D)$ with

$$\hat{Y}_n(z) = K_{01}[(z - H_{11})^{-1}(K_{11} - K_{10}k^{-1}K_{01})]^n(z - H_{11})^{-1}K_{10}. \tag{5.33}$$

The average lifetime is

$$\langle t \rangle = \hat{S}(0) = k^{-1} + k^{-1}\hat{\Omega}(0) = \frac{1}{k} + \frac{1}{k^2}\sum_{n=0}^{\infty}\frac{(-1)^n}{D^{n+1}}\hat{Y}_n(0). \tag{5.34}$$

The first moment $\hat{Y}_0(0)$ is identical to $k^2\hat{\chi}(0)$ in the WF approximation. To show this, we write the Green's function in the Laplace domain as $(w - \mathcal{L}_0)^{-1} = \exp[-\beta U/2](w - H)^{-1}\exp[\beta U/2]$. Using the block matrix representation in Eq. (5.31), we evaluate $\hat{\chi}(w)$ as

$$\begin{aligned} \hat{\chi}(w) &= \frac{1}{k^2}\langle K\frac{1}{w - \mathcal{L}}K\rangle - \frac{1}{w} = \frac{1}{k^2}(\phi_0, K\frac{1}{w - DH}K\phi_0) - \frac{1}{w} \\ &= \frac{1}{Dk^2}K_{01}\frac{1}{w/D - H_{11}}K_{10}. \end{aligned} \tag{5.35}$$

$\hat{\chi}(z) = (Dk^2)^{-1}\hat{Y}_0(w/D)$ reduces to $\hat{Y}_0(0)/Dk^2$ in the limit of $w \to 0$. It is ready to show that

$$\begin{aligned} (D^2k^3)^{-1}\hat{Y}_1(w/D) &= k^{-3}\langle K[(w - \mathcal{L})^{-1} - z^{-1}P_{eq}]K[(w - \mathcal{L})^{-1} - z^{-1}P_{eq}]K\rangle \\ &\quad - \hat{\chi}^2(w) \end{aligned} \tag{5.36}$$

A similar expansion was obtained by Weiss using a perturbative correction to the WF approximation.[46]

5.7 Appendix 5-B: experimental time scale and single-molecule measurements

In this appendix we discuss the effects of experimental time window on fluorescence lifetime measurements. we consider single-molecule quantities monitored over a fixed time window t_{exp}. A general definition of the average value within this time window is given by Gopich and Szabo as,[122]

$$\bar{a} = \frac{1}{t_{exp}} \int_0^{t_{exp}} a[x(t)]|_{x_0} dt, \tag{5.37}$$

where $x(0) = x_0$ is the initial condition. In principle, $a[x(t)]$ can be any experimentally measured quantity, for example, the FRET rate[83] or the quantum yield in FRET experiments.[16] A similar scenario is discussed for two-state dynamics of single biomolecules by Geva and Skinner.[24] Based on Hochstrasser's experiments.[83] the distribution of the measured quantity $\bar{a}$ is related to the underlying equilibrium distribution $P_{eq}(x_0)$ as

$$
\begin{aligned}
P(\bar{a}|t_{exp}) &= \int P_{eq}(x_0) dx_0 \langle \delta \left(\bar{a} - \frac{1}{t_{exp}} \int_0^{t_{exp}} a[x(t)]|_{x_0} dt \right) \rangle_{\text{inhom}} \\
&= \int \frac{d\omega}{2\pi} e^{i\omega\bar{a}} \langle\langle \exp[-\frac{i\omega}{t_{exp}} \int_0^{t_{exp}} a[x(t)]|_{x_0} dt] \rangle_{\text{inhom}} \rangle, \tag{5.38}
\end{aligned}
$$

where the inner brackets $\langle \cdots \rangle_{\text{inhom}}$ stand for the inhomogeneous average over trajectories with fixed initial configuration and the outer brackets $\langle \cdots \rangle$ denote the average over $P_{eq}(x_0)$.

In the static limit, $t_{exp} \to 0$, $P(\bar{a}|0) = [P_{eq}(x_0)|\partial_{x_0} a(x_0)|^{-1}]_{x_0=x_0^*}$ with $a(x_0^*) = \bar{a}$. For small t_{exp}, the relaxation perturbs slightly the transient configuration, giving the configuration-controlled regime. As shown in Sec. 5.2, we perform a first-order

cumulant expansion over $a[x(t)]|_{x_0}$, yielding

$$P(\bar{a}|t_{exp}) \approx \left\langle \delta \left(\bar{a} - \frac{1}{t_{exp}} \int_0^{t_{exp}} \langle a[x(t)]|_{x_0} \rangle_{\text{inhom}} \right) \right\rangle. \tag{5.39}$$

For large t_{exp}, the inhomogeneous cumulant expansion breaks down. We invoke the full cumulant expansion over $a[x(t)]|_{x_0}$ in Eq. (5.38):

$$\lim_{t_{exp} \to \infty} P(\bar{a}|t_{exp}) = [2\pi\sigma^2(t_{exp})]^{-1/2} \exp[-\frac{(\bar{a} - \langle a \rangle)^2}{2\sigma^2(t_{exp})}]. \tag{5.40}$$

$\langle a \rangle$ and $\sigma^2(t_{exp}) = 2/t_{exp}^2 \int_0^{t_{exp}} (t_{exp} - t) \langle \delta a[x(t)] \delta a[x(0)] \rangle dt$ are the mean and the variance of the distribution, respectively. The same expression was obtained by Gopich and Szabo from the central limit theorem.[122] For large t_{exp}, the integral in $\sigma^2(t_{exp})$ reduces to $2\int_0^\infty \langle \delta a[x(t)] \delta a[x(0)] \rangle dt/t_{exp}$, which is proportional to the ratio of the relaxational time scale and the experimental time scale. If $a = K(x)$ and $\sigma^2(t_{exp}) \approx 2\langle K \rangle^2 \hat{\chi}(0)/t_{exp}$, the homogeneous decay rate $\langle K \rangle$ is observed in the dynamic limit, $t_{exp} \gg \hat{\chi}(0)$.

The above discussion agrees well with our picture illustrated in Fig. 5-7, where the overall kinetics is described by the diffusion-controlled regime for large experimental time window. Furthermore, the intermediate region between the static limit and the diffusion-controlled regime is described well by the configuration-controlled regime. Thus the inhomogeneous cumulant expansion is a natural bridge to link static limit and the dynamic limit.

The FRET rate and the quantum yield depend on the donor-acceptor distance and are affected by internal relaxation dynamics. The quantum yield can be directly measured, yet the FRET rate has to be determined indirectly from lifetime measurements. The lifetime distribution is related to the FRET rate:

$$f(t) \approx \int P(\bar{k}|t_{exp}) \bar{k} e^{-\bar{k}t}. \tag{5.41}$$

$f(t)$ in Eq. (5.41) is an approximation valid for small experimental observation times. This condition limits the use of FRET rate as a measure of lifetime distribution.

169

Chapter 6

Fluorescence lifetime measurement: Contour length dependence of single polymers

6.1 Introduction

Fluorescence quenching on a polymer chain has been of theoretical and experimental interest for a long time.[39, 40, 41, 42] The strong dependence of quenching rate on the fluorophore-quencher distance makes fluorescence quenching a sensitive probe of the loop formation dynamics in polypeptides and DNAs. Recent developments in time-resolved single-molecule fluorescence spectroscopy provide new tools to understand conformational dynamics on the molecular level.[9, 23, 81, 82, 123] The internal relaxation of the polymer makes the quenching reaction a complicated example of diffusion-controlled reactions. Over several decades, there have been extensive discussions of diffusion-controlled reactions.[43, 44, 45, 46, 47, 60, 113, 114, 115] A widely used approximation scheme to calculate intrachain reactions in dilute solutions was first presented by Wilemski and Fixman,[44, 45] which is referred here as the WF approximation. The main focus of this chapter is to quantify the reliability of the WF approximation for a Gaussian chain, validate the criteria with computer simulations,

and predict the contour length dependence of the average fluorescence lifetime.

In previous chapter, we studied two different regimes of the reaction kinetics modulated by conformational fluctuations and accounted for the effects of the experimental observation window in fluorescence measurements.[124] The stationary reaction process dominates in the configuration-controlled regime while the diffusion process dominates in the diffusion-controlled regime. A path integral simulation was used to model fluorescence quenching processes on a semi-flexible chain. We demonstrated that the first order inhomogeneous cumulant expansion in the configuration-controlled regime defines a lower bound for the survival probability, while the WF approximation in the diffusion-controlled regime defines an upper bound and approaches the exact result at large diffusion coefficients. In the present chapter, we derive the applicability criteria of the WF approximation by a memory function expansion combined with scaling arguments, and establish its relation to chain length, contact radius and quenching rate. Within the region of validity for the WF approximation, we investigate the chain length dependence of the fluorescence lifetime measurement of a single Gaussian chain.

Although the relaxation of each normal mode of a polymer chain is Gaussian and Markovian, the end-to-end distance motion is generally non-Markovian. The quenching rate probed by fluorescence experiments is a function of the end-to-end distance and is in general not localized. If the quenching rate is infinitely fast and localized at the contact radius, the fluorescence is quenched upon first contact and the fluorescence lifetime becomes the first contact time or the first passage time. Yet this equivalence does not hold for a general quenching rate. Several simplified approaches have been proposed to address the fluorescence quenching problem in a polymer chain. The Szabo-Schulten-Schulten theory in Ref. [43] considers the effective diffusion of the end-to-end distance. A similar approach has been adopted to study the semiflexible polymers where a potential of mean force is mapped out from the equilibrium distribution of the end-to-end distance.[125] These reduced approaches neglect the non-Markovian nature of the end-to-end distance motion and do not necessarily describe the complete range of scaling relations between the first

passage time and the contour length even for a simple Rouse chain. The WF approximation, although derived from a Markovian approximation for the quenching rate, works surprisingly well for a Gaussian chain and has been validated in a set of experiments and simulations.[40] For a diffusion process with a delta-function reaction rate, the quenching rate degree of freedom is Markovian and the WF approximation becomes exact. In Appendix 6-A, we demonstrate this special case and the equivalence of the delta-function sink and the radiative boundary condition. In general, the applicability of WF approximation to a polymer system depends strongly on the contour length, the experimental quenching rate, the contact radius, the solvent viscosity, etc. In Sec. 6.2, we discuss a generalized expansion of the WF approximation and a quantitative criteria for its reliability for a Gaussian chain.

For real polymers such as polypeptide chains, fluorescence lifetime measurements provide a quantitative tool to investigate the effects of chain contour length and stiffness. In a series of fluorescence quenching experiments, Eaton *et al* studied these effects in the diffusion-controlled regime by varying intervening residues on a polypeptide chain. In their experiments, a fluorophore-quencher pair, for example, tryptophan and cysteine, are attached to the ends of a polypeptide chain. On optical excitation, the fluorophore is excited to a state with long lifetime, and is quenched efficiently upon contact with the quencher. The average quenching lifetime $\langle t \rangle$ clearly indicates the loop formation. Their experiments show that the effective quenching rate $k_{eff} = 1/\langle t \rangle$ exhibits an $N^{-3/2}$ dependence for long chains and has a non-monotonic N dependence for short chains due to chain stiffness. In Sec. 6.3.3, a theoretical calculation is carried out to investigate this observation. Fluorescence resonance energy transfer (FRET) is another promising tool to probe polymer dynamics on short time and length scales. In FRET experiments donor and acceptor dye molecules are attached at two different points of one polymer or two different polymers. Upon excitation, non-radiative energy transfer from donor to acceptor may occur. The energy transfer rate has an inverse power-law dependence on the donor-acceptor distance. According to Förster theory, $K(R) = k_F(R/R_F)^{-6}$, with R_F the Förster radius at 50% transfer efficiency. A recent Brownian dynamics simulation by Srinivas and Bagchi showed a power-law

dependence of the average lifetime on the chain length with an exponent of 2.6.[126] A power-law dependence with a smaller exponent was observed earlier by Pastor, Zwanzig, and Szabo in a simulation of the first passage time in a Rouse chain.[47] The larger exponent observed in the FRET simulation may arise from the $1/R^6$ dependence, or an enhancement of the effective persistence length from the excluded volume effects. In Sec. 6.3 we analyze the contour length dependence based on the semi-flexible Gaussian chain model for polymers.[116]

6.2 Measurements and calculations of average fluorescence lifetime

Let us consider a general scenario where a fluorophore is attached to one end of a chain polymer and a quencher is attached to the other end. The fluorescence quenching process determined by the rate K is coupled to the internal relaxation of the polymer described by the relaxation operation $\mathcal{L}$. The survival probability of the fluorescence evolves as

$$\dot{P}(t) = \mathcal{L}P(t) - KP(t), \tag{6.1}$$

where the operator $\mathcal{L}$ represents the internal relaxation of the polymer and reduces to the Smoluchowski operator for simple diffusion, and $K = K(R)$ is the first order reaction rate coefficient which depends on the fluorophore-quencher distance R. In bulk measurements, we optically excite the fluorophores attached to polymers in solution to their excited states at zero time and then monitor the total fluorescence intensity. The average fluorescence lifetime is obtained by integrating the decay profile of fluorescence intensity. In single-molecule experiments, short laser pulses are constantly applied to the single polymer at high frequency so that the fluorophore is quickly pumped back to its excited state once the fluorescence is quenched by the quencher. As a result, fluorescence trajectories are registered with instantaneous interruptions of quenching events. With these sequences of events, we can determine

174
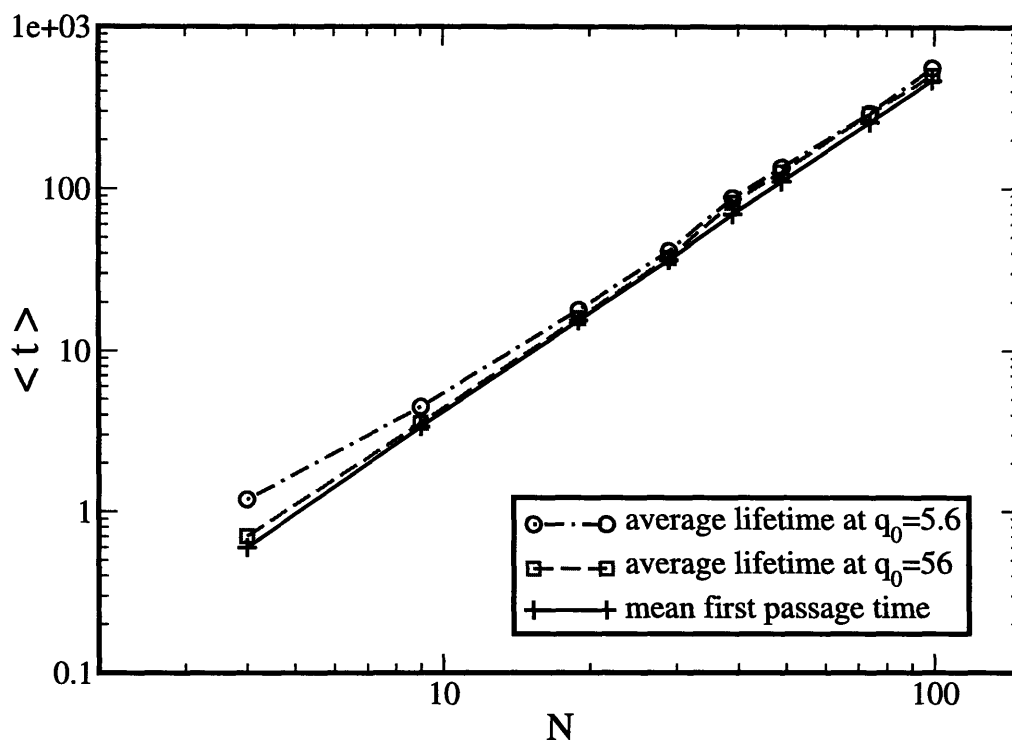
Figure 6-1: The difference between the mean first passage time and the average fluorescence lifetime. The delta-function quenching rate $K(R) = q_0\delta(R - a)$ is approximated by a narrow Gaussian in the simulation. The mean first passage time is obtained by assuming a Smoluchowski boundary condition.

the fluorescence lifetime distribution function and other single-molecule quantities, such as the multiple-event density and high order memory functions discussed later in this section. In comparison to bulk measurements, these single-molecule trajectories provide detailed information of the polymer dynamics without inhomogeneous averages, which is a powerful tool to probe conformational dynamics on the molecular level.

6.2.1 First Passage time and fluorescence lifetime

When the quenching process is localized, e. g., $K(R) = q_0\delta(R - a)$, the fluorescence quenching event is a clear indication of the formation of a physical contact. For

$q_0 \to \infty$, the fluorescence is quenched upon first contact and the quenching reaction reduces to the Smoluchowski boundary condition. In this limit the quenching time or the fluorescence lifetime becomes the first passage time or the first contact time. In reality, the fluorescence is not quenched completely upon contact. As a result, the fluorescence lifetime includes contributions from the second contact, the third contact, and so forth. These additional contributions distinguish the fluorescence lifetime from the first passage time.

In Fig. 6-1, we plot the simulation results of a Rouse chain. The simulation details are elaborated in Sec. 6.2.4. The delta-function quenching rate $K(R) = q_0 \delta(R - a)$ is approximated by a narrow Gaussian and the contact radius is identical to the bond length. The mean first passage time is obtained from simulation assuming the same Smoluchowski boundary condition as in Ref. [47]. At large q_0's , the average fluorescence lifetime approaches the mean first passage time. This result demonstrates the difference between the fluorescence lifetime and the first passage time, and this difference approaches zero in the limit $q_0 \to \infty$.

In Appendix 6-A, we discuss the equivalence of radiative boundary condition and delta-function sink. For the reaction rate given by $K(r) = k_0 \delta(r - a)$ and r governed by the diffusion operator $\mathcal{L}$, the WF approximation becomes exact and $\hat{\chi}_1(0)$ is the first contact time. In the limit $k_0 \to \infty$, the average fluorescence lifetime is equivalent to the first passage time. In general, this equivalence does not hold when K is not infinitely fast and localized, or when $\mathcal{L}$ is not a diffusion operator.

6.2.2 Generalized Wilemski-Fixman expansion and single-molecule measurements

In the time domain, the quenching time distribution is the time derivative of the survival probability $F(t) = -dS(t)/dt$, which in Laplace space is

$$\hat{F}(z) = 1 - z\hat{S}(z). \tag{6.2}$$

176

For the diffusion-controlled reaction, the survival probability is $\hat{S}(z) = \langle(z+K-\mathcal{L})^{-1}\rangle$, where $\langle\cdots\rangle$ represents the ensemble average over the initial equilibrium configuration. As such, the mean quenching time $\langle t\rangle = -\hat{F}'(z=0)$ is equivalent to the average lifetime $\hat{S}(0)$. We can also demonstrate this relation within the modulated reaction model discussed in literature.[27, 78, 118] The probability density for a quenching event at time t is the cumulative probability to have the previous quenching event occurring at least t time before, giving

$$F(t) = \langle \int_t^\infty Ke^{-(K-\mathcal{L})\tau}Kd\tau\rangle. \tag{6.3}$$

The Laplace transform of the quenching time distribution is $\hat{F}(z) = z^{-1}\langle K[(K - \mathcal{L})^{-1} - (z+K-\mathcal{L})^{-1}]K\rangle$, which is equivalent to Eq. (6.2). This interpretation relates the quenching time distribution function to the single event distribution function, $\langle Ke^{-(K-\mathcal{L})\tau}K\rangle$, discussed in Ref. [27] and [118], which provides a unique way to determine the lifetime distribution function in single-molecule measurements.

To calculate the average fluorescence lifetime, we derive a rigorous expression of $\hat{S}(0)$. First we expand the survival probability as

$$
\begin{aligned}
\hat{S}(z) &= \langle\frac{1}{z + K - \mathcal{L}}\rangle = \frac{1}{z} - \frac{1}{z^2}\langle K\rangle + \frac{1}{z^2}\langle K\hat{G}(z)K\rangle - \frac{1}{z^2}\langle K\hat{G}(z)K\hat{G}(z)K\rangle + \cdots \\
&= \frac{1}{z} - \frac{1}{z^2}\langle K\rangle + \frac{1}{z^2}(\frac{\langle K\rangle^2}{z} + \langle K\hat{G}'K\rangle) \\
&\quad - \frac{1}{z^2}(\frac{\langle K\rangle^3}{z^2} + 2\langle K\hat{G}'K\rangle\frac{\langle K\rangle}{z} + \langle K\hat{G}'K\hat{G}'K\rangle) + \cdots
\end{aligned}
\tag{6.4}
$$

where $\hat{G}(z) = 1/(z - \mathcal{L})$ is the Laplace transform of the Green's function $G(t)$ for internal relaxation, and $\hat{G}'(z) = \hat{G}(z) - P_{eq}/z$ is obtained by subtracting the asymptotic limit P_{eq}/z from $\hat{G}(z)$. This expansion is identical to Eq. (10) in paper I of this series,[124] and is cited here for completeness. Then we re-sum the expansion, leading to

$$\hat{S}(z) = \frac{1 + \Omega(z)}{k + z[1 + \Omega(z)]}. \tag{6.5}$$

$k = \langle K \rangle$ is the homogeneous average of the reaction rate and $\Omega(z) = k^{-1} \sum_{n=0}^{\infty} (-1)^n \hat{Y}_n(z)$. Given the definition of the n-th order memory function $\hat{\chi}_n(z) = k^{-(n+1)} \langle K \hat{G}' K \cdots \hat{G}' K \rangle$, we obtain the relation between $\hat{Y}_n(z)$ and the memory functions:

$$
\begin{aligned}
k^{-2} \hat{Y}_0(z) &= \hat{\chi}_1(z) \\
k^{-3} \hat{Y}_1(z) &= \hat{\chi}_2(z) - \hat{\chi}_1^2(z) \\
k^{-4} \hat{Y}_2(z) &= \hat{\chi}_3(z) - 2\hat{\chi}_1(z)\hat{\chi}_2(z) + \hat{\chi}_1^3(z) \\
k^{-(n+1)} \hat{Y}_{n-1}(z) &= \hat{\chi}_n(z) - \sum_{j=1}^{n-1} \hat{\chi}_j(z) k^{-(n-j+1)} \hat{Y}_{n-j-1}(z).
\end{aligned}
\tag{6.6}
$$

The re-summation result for the special case with $\mathcal{L}$ being the diffusion operator is derived in Ref. [124]. Under the Markovian assumption of the quenching rate, $\hat{\chi}_n(z) = \hat{\chi}_1^n(z)$, we have $Y_{n \geq 1} = 0$, and the expansion in Eq. (6.5) reduces to the well-known WF approximation,

$$
\hat{S}(z) = \frac{1 + k\hat{\chi}_1(z)}{k + z[1 + k\hat{\chi}_1(z)]}.
\tag{6.7}
$$

In fact, the n-th order memory function can be measured directly from single-molecule experiments. In these experiments, a high frequency laser source is constantly applied so that the fluorophore is re-excited once the fluorescence is quenched. Consequently, temporal trajectories of quenching events in a single polymer are recorded. The $n + 1$-event density $\hat{N}_{n+1} = k^{-1} \langle K \hat{G}(z) K \cdots K \hat{G}(z) K \rangle$ can be collected from these single-molecule trajectories and provides a comprehensive probe of the n-th order memory function.[27, 118]

$$
\hat{\chi}_n(z) = k^{-n}[\hat{N}_{n+1}(z) - z^{-1} \sum_{j=0}^{n-1} k^{j+1} \hat{\chi}_j(z) \hat{N}_{n-j}(z)]
\tag{6.8}
$$

with $\hat{N}_1 = 1$ and $\hat{\chi}_0(z) = 1$. Eq. (6.5) and Eq. (6.8) provide a link between the ensemble-averaged fluorescence intensity measurements and the single-molecule multi-event measurements.

6.2.3 Criteria for applying WF approximation

The average fluorescence lifetime is obtained easily from the expansion

$$\langle t \rangle = \hat{S}(0) = k^{-1} + k^{-2} \sum_{n=0}^{\infty} (-1)^n \hat{Y}_n(0), \qquad (6.9)$$

which reduces to the WF approximation $\langle t \rangle = 1/\langle K \rangle + \hat{\chi}_1(0)$ if truncated at the first order. The accuracy of the WF approximation is determined by the contribution from higher order terms in the expansion. Although a rigorous proof of the convergence criteria for the alternating series expansion is not available, we can estimate the higher order contributions for a Gaussian chain. From previous discussion, we know that all the nonzero contributions of the higher order terms arise from the non-Markovian nature of the quenching rate. Rescaling the time by the slowest relaxation time τ_R, we estimate $\hat{Y}_n(0) \propto k^{n+2} \tau_R^{n+1}$, which leads to the sufficient criteria for the applicability of the WF expression

$$k\tau_R < 1. \qquad (6.10)$$

This criteria involves two time scales of the reaction dynamics: the homogeneous average reaction time $1/k$ and the slowest relaxation time τ_R. Eq. (6.10) requires the relaxation time scale to be smaller than the reaction time scale, which is consistent with the local equilibrium approximation.[47, 127]

For a quenching reaction with a delta-function sink $K(R) = q_0\delta(R-a)$ on a Rouse chain, the homogeneous average rate is $k \sim q_0 a^2 / N^{3/2} b^3$, given that the contact radius a is normally much smaller than the equilibrium end-to-end distance. The slowest relaxation time is $\tau_R \sim N^2 b^2 / D_0$ where b is the equilibrium bond length. Combination of k and τ_R yields an explicit expression of the criteria in Eq. (6.10)

$$k\tau_R \sim q_0 b \, \frac{N^{1/2} b^2}{D} (\frac{a}{b})^2. \qquad (6.11)$$

Therefore, for a Gaussian chain of fixed bond length the WF approximation is accurate

for short contour length N, small contact radius a, small quenching rate q_0, or large diffusion coefficient D_0.

6.2.4 Simulation of a Rouse chain

To examine the accuracy of the criteria in Sec. 6.2.3, we perform computer simulations to compute the average fluorescence lifetime in a Rouse chain. In our simulation, we consider a Rouse chain with a fluorophore attached to one end and a quencher attached to the other end. The potential energy of the chain is

$$\beta U = \frac{3}{2b^2} \sum_{n=1}^{N-1} (\mathbf{r}_n - \mathbf{r}_{n+1})^2, \qquad (6.12)$$

where b is the equilibrium bond length and $\mathbf{r}_n$ is the position of the n-th bead. The quenching time is averaged over many trajectories. For each trajectory, the initial configuration is generated from the equilibrium distribution $P_{eq} = \mathcal{N} \exp[-\beta U]$, and $\mathcal{N}$ is the normalization factor. Here we adopt the Ermak-McCammon algorithm to generate dynamic trajectories of Rouse chain.[47, 128] The evolution of the n-th bead's position is

$$\mathbf{r}_n(t + \Delta) = \mathbf{r}_n(t) - D_0 \nabla_n \beta U \Delta + \mathbf{x}_n, \qquad (6.13)$$

where Δ is the time step and $\mathbf{x}_n$ is a random displacement from a normal distribution with zero mean and variance $2D_0\Delta$. The quenching probability for each time step is $1 - \exp[-K(R)\Delta]$ and R is the end-to-end distance at time t. Upon detection of a quenching event in our simulation, we record the quenching time and restart the simulation with a new initial configuration. In our simulation we take $b = 1$, $D_0 = 1$ and use a specific functional form of quenching rate.[41, 42] $K(R) = q_0 \exp[-\gamma(R-a)]$ with $\gamma = a^{-1}$.

The results for the average fluorescence lifetime are displayed in Fig. 6-2. The criteria in Eq. (6.11), although obtained from simple scaling arguments, is surprisingly reliable. At $a = 0.1, q_0 = 5.6$, the WF expression reproduces all the simulation results
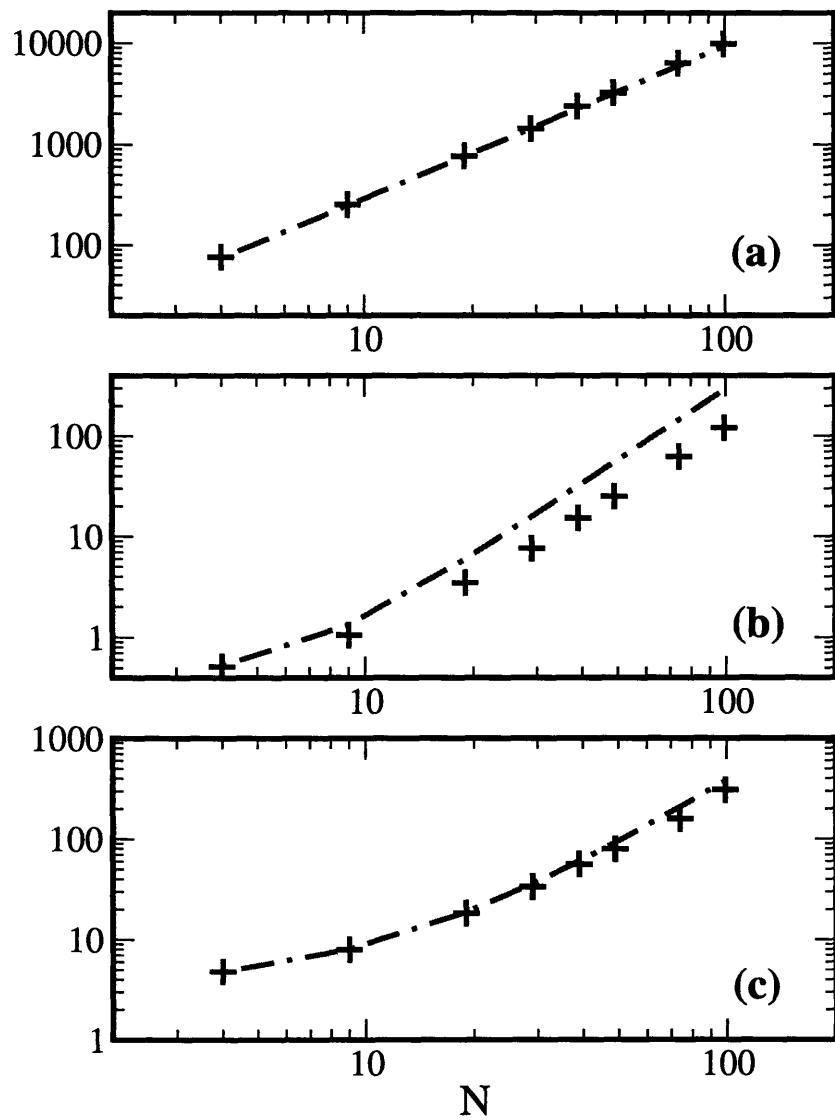
Figure 6-2: The average fluorescence lifetime from the WF approximation compared to the simulation: (a) $a = 0.1$, $q_0 = 5.6$; (b) $a = 1.0$, $q_0 = 5.6$; (a) $a = 1.0$, $q_0 = 0.56$. The simulation results are shown as plus symbols and the WF approximation $\langle t \rangle = 1/\langle K \rangle + \hat{\chi}_1(0)$ is shown as dot-dashed lines. As a, q_0 or N decreases, the WF approximation approaches the simulation results.

181

for the contour lengths up to $N = 100$. At a larger contact radius $a = 1$ with q_0 fixed, the WF approximation deviates from the simulation result, and the deviation becomes more prominent at larger contour lengths. At lower quenching rates q_0, the WF approximation shows excellent agreement with simulation. In all three sub-plots, the agreements are generally better for shorter Rouse chains. As predicted by Eq. (6.11), for short contour lengths, small contact radii or small q_0, the relaxation time scale is much smaller than the reaction time scale. In this limit, the Markovian assumption of the quenching rate or the local equilibrium approximation becomes valid, so the WF approximation is accurate.

It can be seen from Fig. 6-2 that the WF results have different slopes in the log-log plot at different contact radii. As demonstrated in Sec. 6.2.3, the WF approximation includes two contributions, the homogeneous average rate $1/\langle K \rangle$ and the average relaxation time $\hat{\chi}_1(0)$. To examine the details of the length dependences, we plot these two contributions separately in Fig. 6-3. The scalings of both quantities with contour length show strong dependencies on the contact radius. $1/\langle K \rangle$ scales as $N^{3/2}$ at $a = 0.1$ and has a smaller scaling exponent at a larger contact radius $a = 1$. The scaling exponent of $\hat{\chi}_1(0)$ decreases with the contact radius. Different contour length dependences are also observed for different contact radii with Smoluchowski boundary conditions, as shown by Pastor and Szabo's simulations, which corresponds to a delta-function sink in the limit $q_0 \to \infty$ (see Sec. II). Based on our calculation and their simulation, different scaling relations for different radii arise naturally from $\hat{\chi}_1(0)$. We investigate the contour length dependence in the following section and discuss Fig. 6-3 further.

6.3 Contour length dependence and semi-flexibility

For synthetic and biological polymers, fluorescence lifetime measurements provide a quantitative tool to investigate the dependence of fluorescence lifetime on contour length. Real polymers have excluded volume, hydrodynamic, and monomer-specific interactions, resulting in variations in chain stiffness over a wide range of length scales.
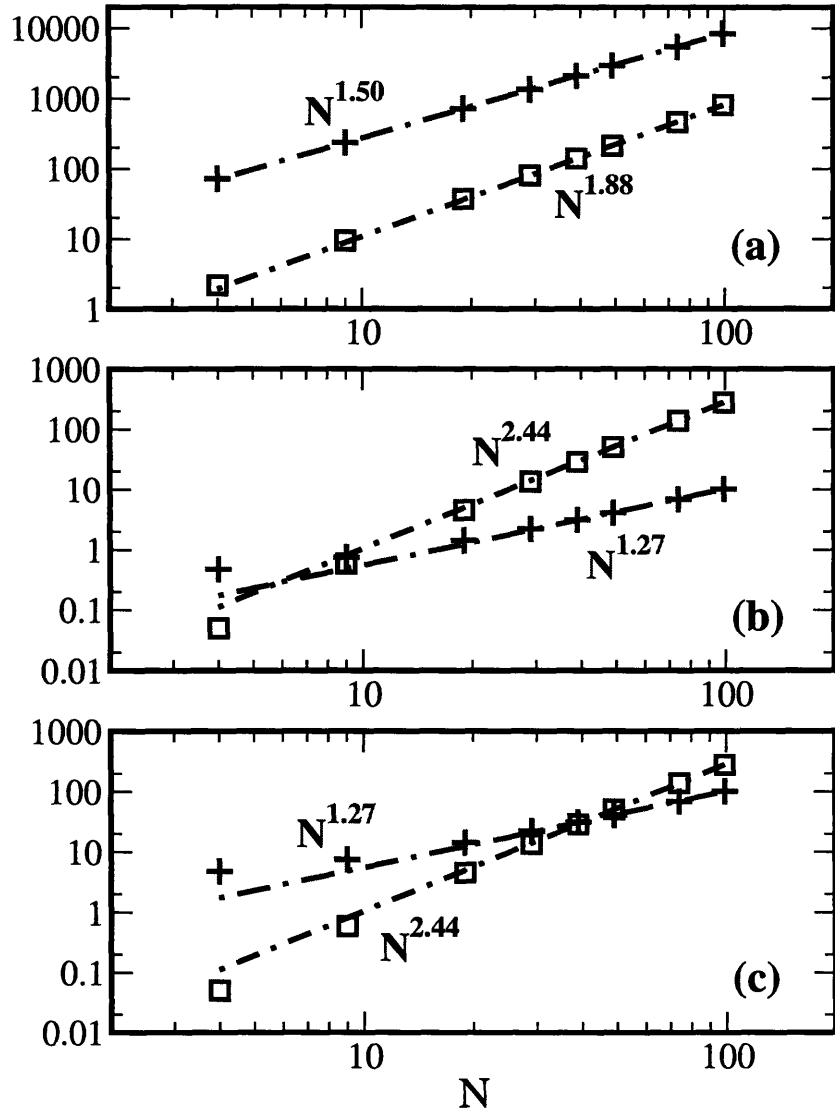
Figure 6-3: Scaling of $1/\langle K \rangle$ and $\hat{\chi}_1(0)$: (a) $a = 0.1$, $q_0 = 5.6$; (b) $a = 1.0$, $q_0 = 5.6$; (a) $a = 1.0$, $q_0 = 0.56$. $1/\langle K \rangle$ is shown as plus symbols and $\hat{\chi}_1(0)$ is shown as square symbols. The scaling relations are shown in dot-dashed lines.

In this section we study the effects of semi-flexibility and contour length dependence on conformational dynamics of single macromolecules. We limit our discussion to fluorescence quenching and fluorescence resonance energy transfer(FRET). The major difference between them is the distance dependence of $K(R)$: the fluorescence quenching rate falls off exponentially, $K(R) = q_0 \exp[-\gamma(R-a)]$, and the FRET rate has an inverse power-law dependence, $K(R) = k_F(R/R_F)^{-6}$.

For a Gaussian chain, the equilibrium distribution of the end-to-end distance is

$$P_{eq}(R) = 4\pi R^2 [2\pi \langle R^2 \rangle / 3]^{-3/2} \exp[-3R^2/2\langle R^2 \rangle], \qquad (6.14)$$

where $\langle R^2 \rangle$ is the mean square end-to-end distance. The Green's function of the end-to-end distance is:

$$
\begin{aligned}
G(R,t|R_0) &= \sqrt{\frac{2}{\pi}} \frac{\sqrt{3}R}{\sqrt{\langle R^2 \rangle} R_0 \phi(t) \sqrt{1 - \phi^2(t)}} \\
&\quad \exp\left[-\frac{3(R^2 + \phi^2(t)R_0^2)}{2\langle R^2 \rangle(1 - \phi^2(t))}\right] \sinh\left(\frac{3RR_0\phi(t)}{\langle R^2 \rangle(1 - \phi^2(t))}\right), \quad (6.15)
\end{aligned}
$$

where $\phi(t)$ is the normalized distance correlation function defined in the literature.[78] For a Rouse chain, the explicit form of $\phi(t)$ is given by Szabo and others.[47, 127]

In paper I,[124] we demonstrate that either the reaction or the relaxation time scale can dominate chain conformational kinetics depending on the experimental scenarios. The present discussion centers on the diffusion-controlled regime, which has been measured experimentally and studied numerically.[40, 42, 47] The WF theory defines two fundamental quantities, the homogeneous average rate $k = \langle K \rangle$ and the memory function $\chi_1(t)$. Both are sensitive to the functional form of the reaction rate. In Secs. 6.3.1 and 6.3.2, we assume a delta-function reaction sink $K(R) = q_0\delta(R-a)$ and analyze the dependence of k and $\hat{\chi}_1(0)$ on the persistence length and chain length. Here, a is the contact radius for fluorescence quenching processes and the Förster radius R_F for FRET processes. In Sec. 6.3.3, we use an exponential quenching rate and compare our predictions with the fluorescence quenching experiment by Eaton and his co-workers. In Sec. 6.3.4, we discuss the lifetime and yield measurements in
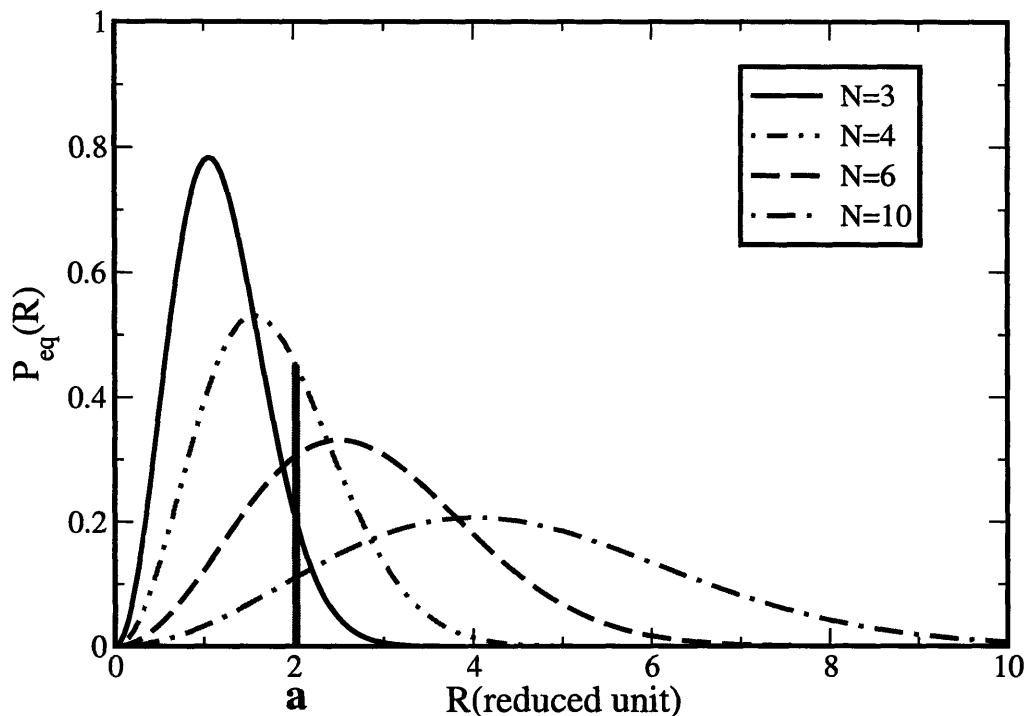
Figure 6-4: Equilibrium distribution of the end-to-end distance for the semi-flexible Gaussian chain with the persistence length $L_p = 2$. The length unit is the equilibrium bond length b. The delta-function sink is represented as a solid bar at $R = a$. The N dependence of the homogeneous average rate k is illustrated by the crossing points of the delta-function sink and the equilibrium distributions.

FRET experiments.

6.3.1 The homogeneous average rate k

Given the equilibrium distribution in Eq. (6.14) and the delta-function sink, we have

$$k \propto \frac{a^2}{\langle R^2 \rangle^{3/2}} \exp\left[-\frac{3a^2}{2\langle R^2 \rangle}\right], \qquad (6.16)$$

where the mean square end-to-end distance $\langle R^2 \rangle$ is a function of N. As illustrated in Fig. 6-4, at extremely small N, $a^2 > \langle R^2 \rangle$, the homogeneous average rate k is a probe of the right edge of the distribution and is dominated by the exponential factor $\exp[-3a^2/2\langle R^2 \rangle]$. For a^2 smaller than $\langle R^2 \rangle$, the probe falls on the left edge of the distribution and k has a complicated dependence on N for small N. In the

Table 6.1: Summary of the scaling exponents of $1/k$ and $\hat{\chi}_1(0)$ with the contour length in the large N limit where $a^2 \ll \langle R^2 \rangle$.

| | $1/k$ | $\hat{\chi}_1(0)$ without HI | | $\hat{\chi}_1(0)$ with HI | |
		small a	large a	small a	large a
flexible chain $L_p \ll N$	3/2	3/2	2	3/2	3/2
stiff chain $L_p \geq N$	3	3	4	3	7/2

Depending on the persistence length L_p, this regime is separated into two regions corresponding to $L_p \ll N$ and $L_p \geq N$, respectively. Small a represents the limit $b/a \gg \sqrt{N}$ while large a represents the opposite limit. HI refers to hydrodynamic interactions incorporated in the Zimm model.

limit of large N, and the homogeneous average rate k is dominated by the prefactor $a^2/\langle R^2 \rangle^{3/2}$. The scaling exponents of k with contour length in this regime, $a^2 \ll \langle R^2 \rangle$, is summarized in Table 6.1: For a flexible chain with persistence length $L_p \ll N$, the mean square end-to-end distance is $\langle R^2 \rangle = 2Nb^2 L_p$ and k scales as $N^{-3/2}$; while for a stiff chain with persistence length $L_p \geq N$, $\langle R^2 \rangle = N^2 b^2$ and k scales as N^{-3}.

6.3.2 The memory function $\hat{\chi}_1(0)$

The memory function $\chi_1(t)$ for a delta-function sink is rigorously obtained as

$$
\begin{aligned}
\chi_1(t) &= \frac{\langle KG(t)K \rangle}{k^2} - 1 \\
&= \frac{1}{2x_0\phi(t)\sqrt{1-\phi^2(t)}} \sinh\left(\frac{2x_0\phi(t)}{1-\phi^2(t)}\right) \exp\left[-\frac{2x_0\phi^2(t)}{1-\phi^2(t)}\right] - 1, \quad (6.17)
\end{aligned}
$$

where $x_0 = 3a^2/2\langle R^2 \rangle$ and $\phi(t)$ is the normalized distance correlation function. To estimate the contour length dependence, we expand $\chi_1(t)$ at small $2x_0\phi(t)/[1-\phi^2(t)]$, giving

$$
\chi_1(t) \approx [1-\phi^2(t)]^{-3/2} - 1 - 2x_0\phi^2(t)[1-\phi^2(t)]^{-5/2} + \cdots . \quad (6.18)
$$

At short times, both ends move independently, giving $\phi(t) \approx 1 - 6D_0/\langle R^2 \rangle t$.[116] In this time region, $\phi(t)$ is close to 1 and the expansion is no longer valid. We can estimate the invalid region of the expansion as $2x_0\phi(t)/[1-\phi^2] > 1$, giving $\phi(t) > 1-x_0$ or equivalently $t < \langle R^2 \rangle x_0/6D_0 = a^2/4D_0$. Accordingly, we break the full integration into two parts $\hat{\chi}_1(0) = I_1 + I_2$ with

$$I_1 = \int_0^T \chi_1(t)dt, \ and \ I_2 = \int_T^\infty \chi_1(t)dt, \tag{6.19}$$

where $T = a^2/4D_0$. Within $[0, T]$, $\chi_1(t) \approx 1/4\sqrt{2}x_0^{3/2}$, yielding an estimation of the first term

$$I_1 \sim T/4\sqrt{2}x_0^{3/2} = \langle R^2 \rangle^{3/2}/24\sqrt{3}D_0a. \tag{6.20}$$

Compared to the first passage time $\sqrt{2\pi}N^{3/2}b^3/12\sqrt{2}D_0a$ in the SSS theory where only the diffusion of the end-to-end distance is considered,[47] I_1 is off by a factor of $2\sqrt{2\pi}$. The second term I_2 is essentially dominated by the slowest relaxation time τ_R, yielding a different scaling

$$I_2 \sim \tau_R. \tag{6.21}$$

It is clear that two competing processes contribute differently to $\hat{\chi}_1(0)$. The diffusive motion of end-to-end vector dominates at short time, while the collective relaxation of the polymer dominates at long time. The relative weights of these two contributions are determined by the contact radius a. $\hat{\chi}_1(0)$ is dominated by I_1 at small a and by I_2 at large a, and the crossover falls roughly into the region where these two integrals are comparable. The length dependence of $\hat{\chi}(0)$ is determined by both I_1 and I_2. For the dependence on semi-flexibility and contact radius, we make several observations:

1. For a flexible chain when $L_p \ll N$, the mean square end-to-end distance is $\langle R^2 \rangle = 2Nb^2L_p$ and the slowest relaxation time is $\tau_R \sim N^2L_pb^2/D_0$. Hence, $I_1 \sim N^{3/2}$ dominates at small a while $I_2 \sim N^2$ dominates at large a, and the

187
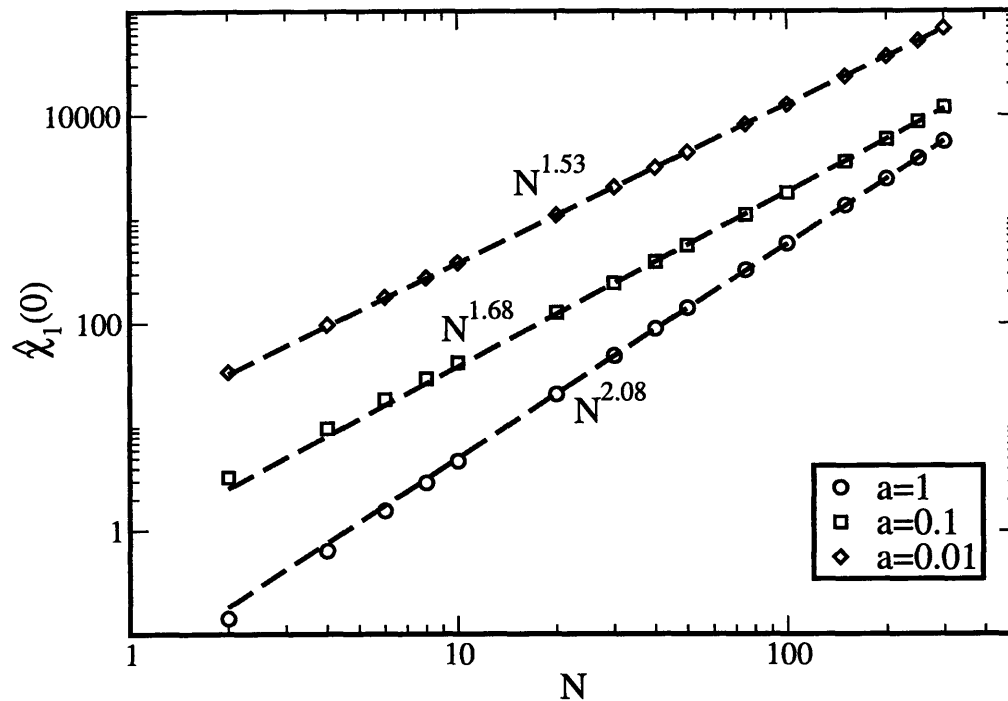
Figure 6-5: The contour length dependence of $\hat{\chi}_1(0) = \int_0^\infty \chi_1(t)dt$ for a delta-function sink. $\hat{\chi}_1(0)$ scales as $N^{2.08}$ at $a = 1$, $N^{1.68}$ at $a = 0.1$, and $N^{1.53}$ at $a = 0.01$. Exact calculations are plotted with symbols and the scaling relations are shown in dashed lines.

crossover occurs around $b/a \sim \sqrt{N}$. Our numerical calculation of $\hat{\chi}_1(0)$ for a Rouse chain ($L_p = 1/2$) with a delta-function sink corroborates this result. As shown in Fig. 6-5, $\hat{\chi}_1(0)$ scales as $N^{2.08}$ for $a = 1$, $N^{1.68}$ for $a = 0.1$, and $N^{1.53}$ for $a = 0.01$, respectively. The calculation strongly confirms the two competing contributions and that $I_1 \sim N^{3/2}$ dominates over $I_2 \sim N^2$ as the contact radius decreases. The decreasing scaling exponents with the contact radii are also observed for an exponential quenching rate in Fig. 6-3, where $\hat{\chi}_1(0)$ scales as $N^{2.44}$ at $a = 1.0$ and $N^{1.88}$ at $a = 0.1$. Although the contour lengths are not large enough to show the asymptotic scalings, we are still able to distinguish the leading contributions at different radii, which is a generic effect of the two competing processes.

2. For a stiff chain when $L_p \geq N$, the mean square end-to-end distance is $\langle R^2 \rangle = N^2 b^2$ and the slowest relaxation time is $\tau_R \sim N^4 b^2 / L_p D_0$. Consequently, I_1 scales with the contour length as N^3 and I_2 scales as N^4. Srinivas and Bagchi's simulations[126] for a semi-flexible chain with L_p comparable to the contour length and excluded volume effects reported an exponent of 2.6. This result lies between the flexible chain limit and the stiff chain limit.

3. In the presence of hydrodynamic interactions, the normal modes of a semi-flexible chain are approximated using the pre-averaged approximation for the hydrodynamics tensors introduced by Zimm.[94, 95] Details can be found in our previous work.[116] The scaling relations are summarized as:

$$\begin{cases} \text{When } L_p \ll N, & I_1 \sim N^{3/2}, & I_2 \sim N^{3/2}; \\ \text{When } L_p \geq N, & I_1 \sim N^3, & I_2 \sim N^{7/2}. \end{cases} \tag{6.22}$$

Consequently, $\hat{\chi}_1(0)$ scale with N and has a smaller exponent in presence of hydrodynamic effects.

In short summary, both $1/k$ and $\hat{\chi}_1(0)$ scale with the contour length for long polymer chains. The scaling exponents are listed in Table. 6.1. At small contact radius, $\hat{\chi}_1(0)$ is dominated by the integral I_1, which depends only on the equilibrium end-to-end distance. I_1 has the same scaling exponents with and without hydrodynamic interactions. While at large contact radius, $\hat{\chi}_1(0)$ is dominated by the integral I_2, which depends on the slowest relaxation time and has different scaling exponents with and without hydrodynamic interactions.

6.3.3 Intra-molecular fluorescence quenching: Comparison with Eaton's experiments

Quenching of the long-lived triplet state of tryptophan by cysteine provides an accurate way to measure the rate of loop formation in polymer chains. With tryptophan at one end of a semi-flexible peptide and cysteine at the other, Eaton *et al* were able

to obtain the diffusion-limited rate of contact formation. They measured the length dependence and the viscosity dependence of the effective quenching rate by varying the number of intervening Ala-Gly-Gln sequences. The effective quenching rate is defined as the inverse of average lifetime, $k_{eff} = 1/\langle t \rangle \approx k/[1 + k\hat{\chi}_1(0)]$. In this section, we mainly address two important experimental findings by the Eaton group:

1. The scaling of the effective quenching rate approaches $N^{-3/2}$ for chain length $N \sim 15$ but depends less on N for shorter peptides.[40]

2. The diffusion coefficient required to fit the diffusion-influenced rate is about 10 times smaller than the value expected for free diffusion of the contacting residues.[42]

From the Gaussian distribution in Eq. (6.14) and the exponential quenching rate $K(R) = q_0 \exp[-\gamma(R - a)]$, the homogeneous average quenching rate is obtained as

$$
\begin{aligned}
k = \langle K \rangle &= \int_a^\infty q_0 e^{\gamma(R-a)} P_{eq}(R) dR = \frac{1}{\sqrt{2\pi\zeta}} \exp\left[-\frac{1}{2\zeta}\right] \cdot \\
&\left(2 - 2\zeta + \sqrt{2\pi\zeta}(1 + \zeta) \exp\left[\frac{(1+\zeta)^2}{2\zeta}\right] \mathrm{erfc}\left[\frac{1+\zeta}{\sqrt{2\zeta}}\right]\right)
\end{aligned}
\tag{6.23}
$$

with $\zeta = \gamma^2 \langle R^2 \rangle / 3$. Given that $\langle R^2 \rangle = 2NL_p b^2$ for a flexible chain and $\gamma = a^{-1}$, ζ is a large number for small a and large N. In the asymptotic limit $\zeta \to \infty$, $\langle K \rangle$ reduces to $q_0 \sqrt{8/\pi} \zeta^{-3/2}$ and scales as $N^{-3/2}$. For the case where the contact radius is about the bond length, the asymptotic scaling is approached for large contour lengths. Furthermore, $1/\langle K \rangle$ does not exhibit a monotonic dependence on the contour length for short polypeptide chains due to the chain stiffness.

In Fig. 6-6, the effective quenching rate is calculated numerically with and without hydrodynamic interactions. The contour length dependence of the effective quenching rate is close to the experimental observation.[40] For short peptide chains, $k\hat{\chi}_1(0) \ll 1$, the overall quenching rate is dominated by the k given in Eq. (6.23). At large N, the probe radius a falls on the left edge of the equilibrium distribution and k decreases with increasing N, which agrees favorably with Eaton et al's calculation.[42] Our calculations predict a weaker dependence on N around $N = 3$ due to the chain
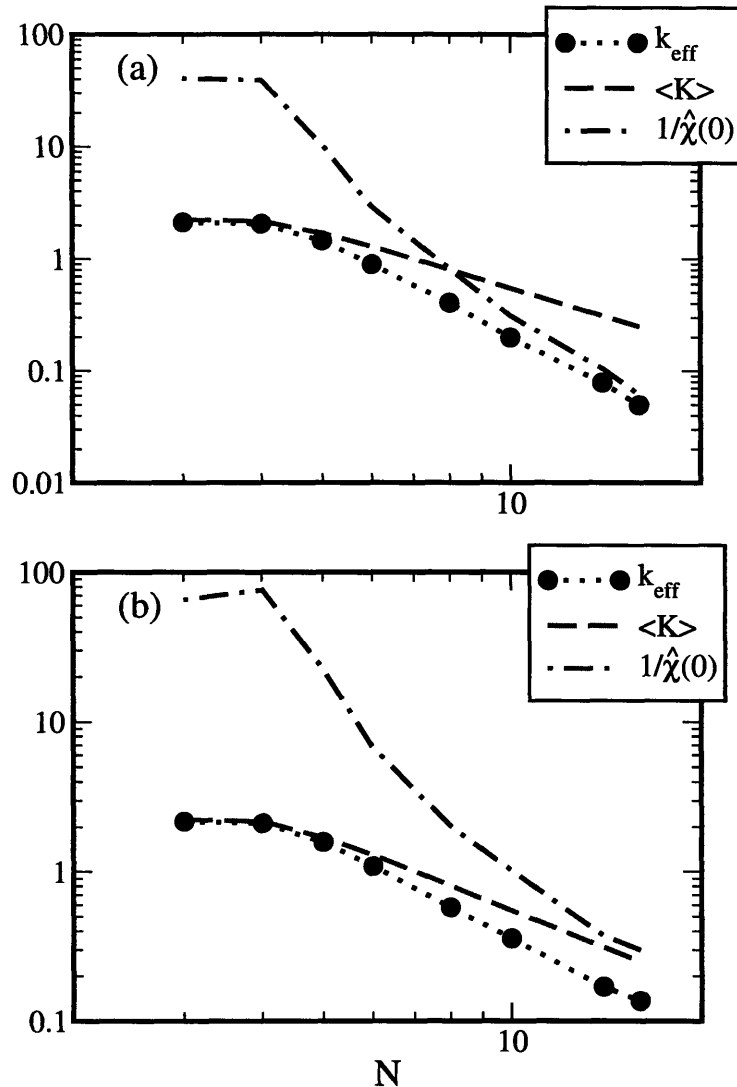
Figure 6-6: Dependence of the effective quenching rate $k_{eff} = 1/\langle t \rangle$ on the chain length (a) without hydrodynamic interactions and (b) with hydrodynamic interactions. The time unit is $b^2/6D_0$. The persistence length is $L_p = 2$, and the quenching rate at contact is estimated from experimental data to be $q_0 = 5.6$. Due to the chain stiffness, k_{eff} does not have a monotonic scaling for very short chains. For a relatively long chain, the effective rate is dominated by $1/\hat{\chi}_1(0)$, yielding N^{-2} scaling without hydrodynamic interactions and $N^{-3/2}$ scaling with hydrodynamic interactions, respectively. The $N^{-3/2}$ scaling was observed by Eaton et al for $N \sim 15$.

stiffness. The probe position a for a short peptide chain with $N = 3$ occurs at the right edge of the distribution, as illustrated in Fig. 6-4, and produces the small decline of the curve. In our simulation, the effective quenching rate for long peptide chains is dominated by $1/\hat{\chi}_1(0)$. In the absence of hydrodynamic interactions, $1/\hat{\chi}_1(0)$ scales with the contour length as N^{-2} where the contact radius is comparable to the bond length. While in the presence of hydrodynamic interactions, $1/\hat{\chi}_1(0)$ scales with the contour length as $N^{-3/2}$, which was also observed by Eaton $et\ al$ for $N \sim 15$.

To better approximate the exponential quenching rate with the delta-function sink, the effective probe radius should be greater than the contact radius a. Real polymers are closer to the worm-like chain model than the semi-flexible Gaussian chain model. The semi-flexible Gaussian chain model normally gives smooth equilibrium distribution $P_{eq}(R)$, as shown in Fig. 6-4, while the worm-like chain model predicts much sharper decay at right edges of the distribution.[42, 129] Therefore, the worm-like chain model predicts sharper decay of k as a falls at the right edge of the distribution. As a combination of these two effects, the homogeneous average quenching rate $k = \langle K(R) \rangle$ should decline faster at small contour lengths, as demonstrated in Eaton's experiments.[42]

In general, the effective diffusion process of the end-to-end distance R is non-Markovian. A natural way to introduce an effective diffusion coefficient is

$$D_{eff} = \frac{\langle R^2 \rangle}{6 \int_0^\infty \phi(t)dt}. \tag{6.24}$$

This definition differs from $D_0 = 2k_B T/\zeta$ used in Pastor, Zwanzig and Szabo's work [47] and reflects the independent motion of the polymer beads at both ends while containing no information on the collective motion of the whole polymer chain. A simple calculation shows that D_{eff} given by Eq. (6.24) is about 7 times smaller than $2k_B T/\zeta$ for chains of length $N = 10$ at 1 cp and 293 K, in agreement with the experimental findings of Eaton $et\ al.$[40, 42]

192

6.3.4 Fluorescence resonance energy transfer: Lifetime and quantum yield

Another laser-induced fluorescence spectroscopy technique that provides complementary information on the internal relaxation of biopolymers is fluorescence resonance energy transfer (FRET). This technique has been extensively used in single-molecule studies of conformational dynamics of proteins, DNAs, RNAs and other biomolecules.[81, 82, 123] The inverse power-law transfer rate diverges at $R \to 0$ where the transition dipole-dipole interaction no longer holds. To facilitate the calculation, we use a modified expression for $K(R)$

$$K(R) = \frac{k_F}{\epsilon + (R/R_F)^6} , \qquad (6.25)$$

where ϵ is a small quantity that represents the breakdown of the weak dipole-dipole interaction for small R. This expression reduces to the quantum yield for FRET processes when $\epsilon = 1$. Thus the discussion applies to quantum yield measurements as well. The Fourier transform of the FRET rate is

$$K(\mathbf{q}) = \frac{2\pi^2 k_F R_F^2}{3q\epsilon^{2/3}} \{ \exp[-qR_F\epsilon^{1/6}] +$$
$$\exp[-\frac{qR_F\epsilon^{1/6}}{2}] \cdot [-\cos(\frac{\sqrt{3}}{2}qR_F\epsilon^{1/6}) + \sqrt{3}\sin(\frac{\sqrt{3}}{2}qR_F\epsilon^{1/6})]\}, \quad (6.26)$$

which reduces to $2\pi^2 R_F^3 k_F/3\sqrt{\epsilon}$ when $qR_F\epsilon^{1/6} \ll 1$. Considering that ϵ is a small number, the FRET rate is well-approximated by a delta-function sink $K(R) = k_0\delta(R-R_F)$ with $k_0 = \pi R_F k_F/(6\sqrt{\epsilon})$.[116] The contour length dependence roughly follows Table 6.1.

6.4 Conclusion and discussions

Here we summarize our findings. For the fluorescence quenching process in a polymer chain, the fluorescence lifetime is not equivalent to the first passage time unless the quenching rate is infinitely fast and localized at the contact radius. Based on a gen-

eralized Wilemski-Fixman formalism, the fluorescence lifetime distribution function can be decomposed into memory functions that are measurable in single-molecule experiments. A sufficient criteria, $k\tau_R < 1$, for the validity of the WF approximation is obtained from the expansion for a Gaussian process. This criteria for a Gaussian chain predicts that $\langle t \rangle = 1/k + \hat{\chi}_1(0)$ is a reliable approximation for small contact radii, slow quenching rates or short contour lengths. The theoretical prediction is corroborated by computer simulations of quenching processes in a Rouse chain.

The dependence of physical properties, such as average fluorescence lifetime, on the chain length is crucial for characterizing polymers and can be used to quantitatively determine the chain stiffness. For reaction kinetics in the diffusion-controlled regime, the average fluorescence lifetime is well approximated by $\langle t \rangle = 1/k + \hat{\chi}_1(0)$. For localized reaction rate $K(R) = q_0 \delta(R - a)$, where a is the contact radius for fluorescence quenching or the Förster radius for FRET, $1/k$ scales as $N^{3/2}$ for flexible chains and N^3 for stiff chains. The scaling of the $\hat{\chi}_1(0)$ with the contour length N is characterized by two competing processes, the independent motion of the end-to-end vector and the slowest relaxation of polymer. The former dominates at a small contact radius and the latter dominates at a large contact radius. For flexible chains, $\hat{\chi}_1(0)$ scales as N^2 at a large contact radius and $N^{3/2}$ at a small contact radius, while for stiff chains, $\hat{\chi}_1(0)$ scales as N^3 at a large contact radius and N^4 at a small contact radius. The scaling relation for a flexible chain agrees well with Szabo's simulation.[47] Srinivas and Bagchi's simulations of a semi-flexible chain with L_p comparable to contour length gives an exponent of 2.6 for $\langle t \rangle$, which lies between the flexible and the stiff limits.[126] In the presence of hydrodynamic interactions, $\hat{\chi}_1(0)$ has a smaller scaling exponent, which scales as $N^{3/2}$ for a flexible chain, and as N^3 at a small contact radius and $N^{7/2}$ at a large contact radius for a stiff chain.

An application of the scaling relations to the fluorescence quenching experiments by Eaton and his group clarifies two findings:

1. For intra-molecular fluorescence quenching processes, the effective quenching rate is given by $k_{eff} = 1/\langle t \rangle$. For long polymer chains, the effective quenching rate is dominated by $\hat{\chi}_1(0)$ and exhibits $N^{-3/2}$ scaling. For short polymer chains,

194

the effective quenching rate is determined by k, the homogeneous average rate. k decreases as N increases when the contact radius falls on the left edge of the equilibrium distribution $P_{eq}(R)$, and increases with N when the contact radius falls on the right edge of the equilibrium distribution. Our calculations agree quantitatively with Eaton *et al*'s experimental data,[42] where the effective quenching rate k_{eff} approaches the $N^{-3/2}$ scaling for long polymer chains and depends less on N for short chains.

2. Through normal mode decomposition, non-Markovian relaxation of the end-to-end distance for a semi-flexible chain is composed of a number of Markovian processes. The end-to-end distance undergoes an effective diffusion on the potential of mean force. Phenomenologically, the effective diffusion coefficient is related to the distance correlation function by $6D_{eff}\int_0^\infty \phi(t)dt = \langle R^2 \rangle$. Numerical calculations demonstrate that D_{eff} for $N = 10$ is about 7 times smaller than the bead diffusion coefficient $D_0 = 2k_BT/\zeta$ at 1 cp and 293 K. This theoretical prediction agrees with recent experimental findings by Eaton and his coworkers. The effective diffusion constant required to fit the diffusion-influenced rates in their experiments is about ten times smaller compared to the free diffusion of the residues.[40, 42]

6.5 Appendix 6-A: Equivalence of boundary condition and delta-function sink

For a one-dimensional delta-function sink, $K(x) = k_0\delta(x - a)$, The homogeneous average rate is $k = k_0P_{eq}(a)$. Let us now obtain $\hat{\chi}_1(0)$ from the rate-rate correlation function

$$k^2\hat{\chi}_1(0) = \int \eta(x)P_{eq}(x)(K(x) - k)dx. \tag{6.27}$$

With the adjoint operator $\mathcal{L}^+$ definition which was used by Szabo-Schulten-Schulten in their solution to diffusion with an absorbing boundary, $\eta(x)$ satisfies

$$\mathcal{L}^+\eta(x) = -(K(x) - k). \tag{6.28}$$

The adjoint operator $\mathcal{L}^+ = e^{\beta U}\partial_x(D(x)e^{-\beta U}\partial_x)$ depends on the general position dependent diffusion coefficient $D(x)$. Consider now the boundary conditions $\eta(x \to \pm\infty) = 0$, we have

$$\eta(x) = \int_{-\infty}^{x} \frac{e^{\beta U(y)}}{D(y)}dy \int_{y}^{\infty} (K(\xi) - k)e^{-\beta U(\xi)}d\xi. \tag{6.29}$$

Substituting this equation into Eq. (6.27) and averaging over the equilibrium distribution $P_{eq}(x) = (\int_{-\infty}^{\infty} e^{-\beta U(y)}dy)^{-1}e^{-\beta U(x)}$, we obtain ,

$$k^2\hat{\chi}_1(0) = (\int_{-\infty}^{\infty} e^{-\beta U(y)}dy)^{-1} \int_{-\infty}^{\infty} \frac{e^{\beta U(x)}}{D(x)}dx \left[\int_{x}^{\infty} e^{-\beta U(y)}(K(y) - k)dy\right]^2. \tag{6.30}$$

Therefore, $\hat{\chi}_1(0)$ is given by

$$\begin{aligned}
\hat{\chi}_1(0) &= (\int_{-\infty}^{\infty} e^{-\beta U(y)}dy)^{-1} \int_{-\infty}^{a} \frac{e^{\beta U(x)}}{D(x)}dx \left[\int_{-\infty}^{x} e^{-\beta U(y)}dy\right]^2 \\
&+ (\int_{-\infty}^{\infty} e^{-\beta U(y)}dy)^{-1} \int_{a}^{\infty} \frac{e^{\beta U(x)}}{D(x)}dx \left[\int_{x}^{\infty} e^{-\beta U(y)}dy\right]^2.
\end{aligned} \tag{6.31}$$

And the average lifetime is

$$\begin{aligned}
\langle t \rangle &= \frac{1}{k} + (\int_{-\infty}^{\infty} e^{-\beta U(y)}dy)^{-1} \int_{-\infty}^{a} \frac{e^{\beta U(x)}}{D(x)}dx \left[\int_{-\infty}^{x} e^{-\beta U(y)}dy\right]^2 \\
&+ (\int_{-\infty}^{\infty} e^{-\beta U(y)}dy)^{-1} \int_{a}^{\infty} \frac{e^{\beta U(x)}}{D(x)}dx \left[\int_{x}^{\infty} e^{-\beta U(y)}dy\right]^2.
\end{aligned} \tag{6.32}$$

Eq. (6.32) is exactly a sum of contributions from the left and the right regions of the boundary with proper weight. It is the same result as the SSS theory with radiation boundary conditions. It proves the equivalence of delta-function sink and radiation boundary conditions. In the limit $k_0 \to \infty$, the radiative boundary becomes the

196

absorbing or Smoluchowski boundary and the fluorescence lifetime becomes $\hat{\chi}_1(0)$ in Eq. (6.31). This is the same as the first passage time given by the Szabo-Schulten-Schulten theory.[43]

In higher dimensions, the real reactive sink is defined as a hyper-plane in a multi-dimensional space. For example, $K(r) = k_0\delta(r - a)$ is actually a reactive spherical surface in a 3-D space. Under such conditions, the whole space can be separated into two regions, inside and outside the reactive surface. This separation scheme given in Eq. (6.32) still holds for such cases. With a reactive surface, the Wilemski-Fixman approximation is only exact when the reaction coordinate r is Markovian, for example, $\mathcal{L} = D\nabla \cdot [\nabla + \nabla\beta U(r)]$. For this special case, we can prove that the reaction rate degree of freedom $k(r)$ is precisely Markovian. Hence the average lifetime is

$$\langle t \rangle = \frac{1}{k} + \frac{1}{D}[\int_0^\infty r^2 e^{\beta U(r)} dr]^{-1} \left\{ \int_0^a e^{\beta U(r)} r^{-2} dr [\int_0^r e^{-\beta U(\rho)} \rho^2 d\rho]^2 + \int_a^\infty e^{\beta U(r)} r^{-2} dr [\int_r^\infty e^{-\beta U(\rho)} \rho^2 d\rho]^2 \right\}. \tag{6.33}$$

For non-Markovian reaction coordinate, the reaction rate degree of freedom is not Markovian even when the reaction rate is localized. Therefore the Wilemski-Fixman approximation is no longer exact.

Chapter 7

DNA stretching under hydrodynamic flows

7.1 Introduction

The mechanical properties of polymer systems are important in many applications, including lubricants and plastics. The bulk visco-elastic properties of these systems result from the microscopic deformation of the polymer chains when they are subject to external forces. This microscopic-macroscopic correspondence has generated interest in studying polymeric solutions at the microscopic level, including experiments at the single molecule level. Many single molecule experiments examine the behavior of single polymers, like DNA, subject to various stresses, including tensile stress and hydrodynamic flow [48, 49, 50, 51, 52, 53, 54, 130, 131, 132, 133]. One set of experiments by Chu's group monitor fluorescence labeled DNA subject to the stresses discussed above. The experiment monitors the entire contour in real time and gives a complete picture of the polymer dynamics [49, 50, 51, 52, 53, 54, 133, 134, 135, 136, 137]. In this chapter, we model DNA as a worm-like chain (WLC) with parameters previously determined in force-extension experiments and then use this model to examine the experimental results of Chu for the steady state configurations of DNA subject to constant plug, elongational, and shear flows [48, 49, 50, 51, 52, 53, 54, 133]. The ability to use parameters from one experiment to model different experiments confirms

the validity of the WLC model for DNA.

This DNA system has also been the subject of many Brownian dynamics simulations [138, 139, 140, 141, 142, 143]. Predicting the properties of a complete contour, requires a large number of long simulations performed on a large number of beads. With carefully chosen parameters, reasonable agreement between the experiments and these simulations exists, but these calculations are phenomenological and computationally intensive [139]. We propose a less computationally intensive first-principles path integral Monte Carlo algorithm based on equilibrium theory to study DNA subject to various hydrodynamic flows. If the relaxation of the polymer is fast, the experimentally observed configurations correspond to a generalized equilibrium distribution, which has an associated potential. With a reasonable formulation of the potential, we evaluate time averaged ensemble quantities with Monte Carlo techniques. Although this approach will not describe dynamics, it is computationally more efficient than Brownian dynamics and allows the prediction of important time averaged quantities, like the mean extension of the polymer that we examine in this letter. Previously, Larson and Chu, as well as others, used similar Monte Carlo techniques on bead and spring models to describe time averaged properties of DNA polymers subject to constant plug flow [144].

DNA is a difficult polymer to model because it is semi-flexible with a large persistence length of 53 nm, compared to a typical length studied in experiments of 50 μm, and its contour length only extends under strong forces [139, 144]. Bead and spring simulations require a large number of beads to account for bending energy and constrained dynamics to maintain the contour length. We adopt a more natural model for DNA, the WLC model of Kratky and Porod [95]. The WLC replaces the Rouse-like bead and spring model with a continuous contour of fixed length and includes an energy associated with bending the polymer. The bending energy is experimentally measurable, which removes a fitting parameter. The first analytic treatment of the WLC model appear in a 1973 paper by Fixman and Kovac [92]. Later work by Marko and Siggia with improvements by Bouchiat demonstrate that the WLC model predictions agree extremely well with the force extension experiments on DNA by

Bustamante's group [145]. The agreement suggests that the WLC captures the fundamental thermodynamics of DNA [130, 133, 146]. The WLC is also the basis for the force extension relations used in simulations by Doyle and in the analytic theory by Zimm [139, 147]. Doyle neglects hydrodynamic interactions while Zimm incorporates the interactions with a length dependent rescaling of the flow field determined by the Kirkwood approximation.

In the absence of an external field, the energy of the WLC is a simple contour integral, $\beta E = \int_0^L \frac{A}{2}|\partial_s \hat{\mathbf{t}}|^2 ds$, where L is the polymer's length [92]. The inverse temperature, β makes all quantities unitless and the tangent vector $\hat{\mathbf{t}}$ of the contour $\mathbf{R}(s)$ is normalized to fix the contour length, $|\hat{\mathbf{t}}| = 1$. An external potential, $\beta U(\mathbf{R}(s))$ modifies the energy resulting in a path integral partition function,

$$Z = \int D\mathbf{R}(s) \exp\left(-\int_0^L \left\{\frac{A}{2}|\partial_s \hat{\mathbf{t}}|^2 + \beta U(\mathbf{R}(s))\right\} ds\right). \tag{7.1}$$

We can derive the form of $\beta U(\mathbf{R}(s))$ for many experiments. For example, in the experiments of Smith, Finzi and Bustamante, one end of the DNA strand is attached to a glass surface and magnetic tweezers stretch the other end of the DNA [133]. The external potential is $U(\mathbf{R}(s)) = -f|R_z(0) - R_z(L)| = -f|\int_0^L \hat{t}_z ds|$, where f is the force applied to the two ends and $\hat{t}_z$ is the component of the tangent vector in the direction of the force. The solution maps into the trajectory of a quantum rigid-rotor and has good agreement with experiment [92, 130, 146]. We parameterize the bending energy of the WLC model with the persistence length determined by these references, $A = 53nm$, to remove fitting parameters and validate the consistency of the WLC description of DNA in various experiments. We neglect the persistence length's dependence on various experimental conditions, such as buffer concentrations and the dye used in imaging.

The potential is not easily defined for hydrodynamic flows because hydrodynamic flows are dynamic phenomenon, but the flow still performs work on each monomer. If we ignore the intrachain hydrodynamic interactions of a polymer in a potential flow, like constant plug flow or elongational flow, the work is proportional to differences in

the potential. For a free-draining polymer, we add the potential of all of the monomer units, which becomes an integral over the contour. A simple double integral over the contour can incorporate the two body potential, but this is not done here. Removal of the free draining approximation is more difficult, but previous studies show that hydrodynamic interactions lead to only modest corrections to many time averaged quantities [143, 144].

7.2   Constant Plug Flow

The constant plug flow potential is $V = -F \cdot z$, where F is the flow rate, and the polymer's potential is $-F\xi \int_0^L z(s)ds$, where ξ is the friction per unit length. Based on the findings of Larson *et al.*, we assume the friction does not vary with the flow rate or over the polymer, but we do not know the friction constant explicitly [144]. Most experiments report the viscosity of the polymer in the solution, whose relation to friction has a non-trivial geometric dependence. The friction is the only fitting parameter, but it is comparable in all simulations and simply scales the flow rates. The Kirkwood approximation in Zimm's calculation for constant plug flow replaces the bare uniform force on each segment from the flow field with a dressed force that is also uniform and justifies a rescaled friction constant [147].

Perkins *et al.* performed the constant flow experiment with optical tweezers [51]. Fluid passes over the polymer creating a force along the entire polymer. Integration by parts gives an insightful formula for the potential, $-F \cdot \xi \int_0^L (L - s)\hat{t}_z ds$. The energy of the potential comes from a tension that scales linearly along the chain. The tension is the greatest at the end tethered to the bead because the whole chain pulls on this end, and it lessens further down the chain until it becomes zero at the free end. For a strong flow, the polymer is almost completely extended in the z-direction, and the components in the x and y directions are small perturbations of the linear configuration. The energy of the WLC is approximately

$$\beta E \approx \int_0^L \left[A/2|\partial_s \hat{t}_\perp|^2 + \frac{F\xi}{2}(L - s)|\hat{t}_\perp|^2 \right] - \frac{F\xi}{2}L^2, \qquad (7.2)$$

where $\hat{t}_\perp$ is the transverse components of the tangent vector, the x and y directions, and the component in the z direction is approximately $t_z = 1 - \frac{1}{2}|\hat{t}_\perp|^2$ [146]. The action corresponds to a quantum harmonic oscillator with a linearly ramped spring constant. The x and y components act independently and the partition function for each component is Gaussian,

$$
\int \mathcal{D}(\hat{t}_\perp^{(x,y)}(s)) \exp \left(-\frac{A}{2} \hat{t}_\perp^{(x,y)}(s) \frac{d\hat{t}_\perp^{(x,y)}(s)}{ds} \Bigg|_0^L \right.
$$
$$
\left. + \int_0^L \int_0^L ds ds' \delta(s-s') \left\{ \frac{A}{2} \hat{t}_\perp^{(x,y)}(s') \frac{d^2\hat{t}_\perp^{(x,y)}(s)}{ds^2} - \hat{t}_\perp^{(x,y)}(s') \frac{F\xi}{2}(L-s)\hat{t}_\perp^{(x,y)}(s)) \right\} \right).
$$

Since the operator in the exponential is Hermitian, the Green's function for the average square of the transverse component, $u(s, s') = \langle \hat{t}_\perp^{(x,y)}(s)\hat{t}_\perp^{(x,y)}(s')\rangle$, is a weighted sum of eigenfunctions, $G(s, s') = \sum_n |u_n(s)\rangle \lambda_n^{-1} \langle u_n(s')|$, that satisfy the differential equation

$$
-A\frac{d^2 u_n(s)}{ds^2} + F\xi(L-s)u_n(s) = \lambda_n u_n(s) \tag{7.3}
$$

with the boundary conditions $u_n'(0) = u_n'(L) = 0$. The analytic solutions to the equation are sums of Bessel functions. The rms of the traverse displacement is $\sqrt{\sum_n \lambda_n^{-1}|\int_0^L u_n(s)ds|^2}$, which is shown in Fig. 7-1. Since $\langle t_z \rangle \approx 1 - \frac{1}{2}(\langle (\hat{t}_\perp^{(x)}(s))^2 \rangle + \langle (\hat{t}_\perp^{(y)}(s))^2 \rangle) = 1 - \sum \lambda_n^{-1} u_n^2(s)$, the average extension in the z-direction is approximately $L - \sum \lambda_n^{-1} \int_0^L ds u_n^2(s) = L - \sum \lambda_n^{-1}$. Since the eigenvalues change slowly with the flow rate in the high stretching regime, the width and extension also change slowly. The rms displacement displays a trumpet shape that is qualitatively similar to the shapes observed in experiments, simulations, and other theories [51, 144, 148, 149].

Without the the large flow rate approximation, the action of the tangent vector corresponds to the imaginary time Schrödinger equation for a rigid-rotor in a time dependent potential,

$$
\frac{\partial \Psi(s)}{\partial s} = \left[\frac{\hat{L}^2}{2A} + F\xi(L-s)\cos(\theta) \right] \Psi(s). \tag{7.4}
$$
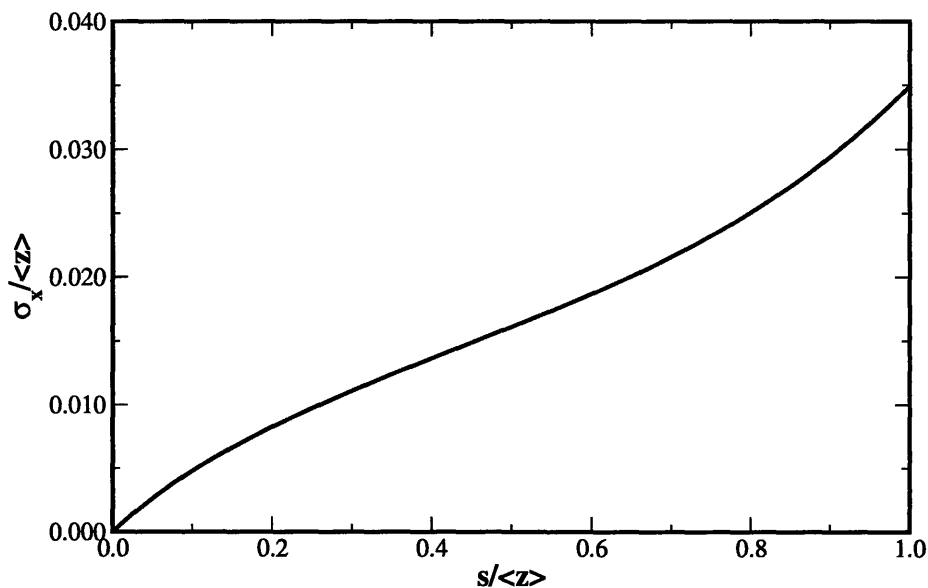
Figure 7-1: The root mean square displacement of the traverse component of the polymer in a strong constant plug flow. The displacement is plotted as a function of distance along the flow field. Note the resemblance to the trumpet shape observed in experiment and simulation.

In this equation, $\hat{L}$ is the angular momentum operator, and $\cos(\theta)$ is the projection of the tangent vector onto the direction of the flow field. This equation resembles the constant force calculations with a simple time dependence $(L-s)$ [146]. This equation can be solved by using a spherical harmonic basis set and numerically propagating the resulting matrix [146, 130]. The only difficulty is the initial condition of the wave-function, for which we use results that are consistent with the high stretching calculation above, $t_z(0) = 1$ and $t_z(0) = t_y(0) = 0$.

Fig. 7-2 compares the predictions of mean fractional extension versus flow rate for the rotor Hamiltonian, the Monte Carlo simulation discussed below, the experimental results of Perkins et al., and the Brownian dynamic simulations of Doyle [51, 139]. Since the experiment cannot determine the end-to-end distance, the fractional extension is the maximum distance between any points on the polymer contour compared against the contour length. The flow rate is in a dimensionless form, $Wi = \tau_F/\tau_p$, where τ_F is the characteristic time of the flow and τ_p is the longest relaxation rate of the free polymer, which is determined by equations in the references [139, 140, 141].

204
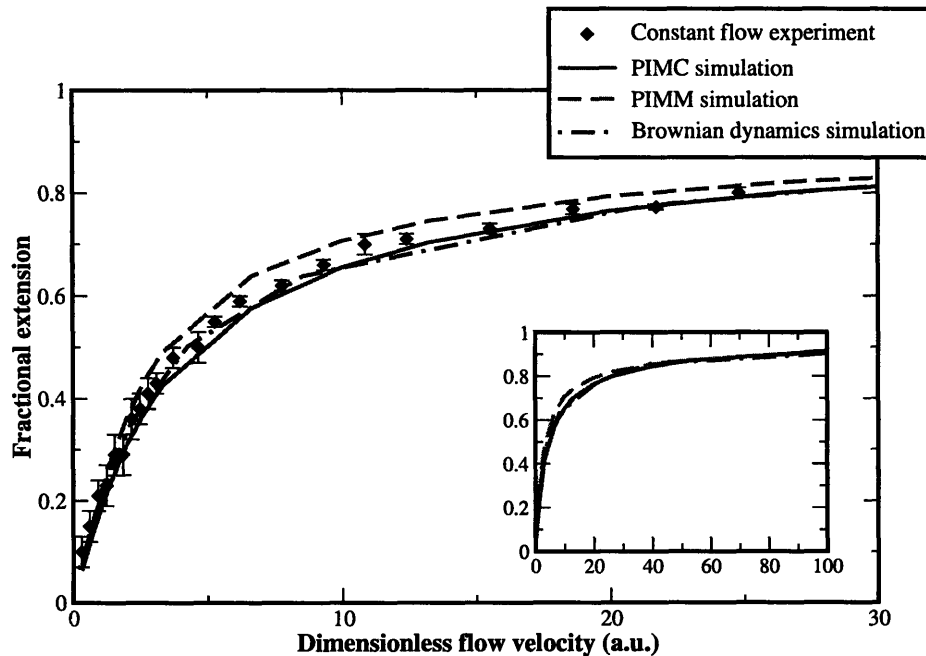
Figure 7-2: Comparison of the constant plug flow experiment in Ref. 51, the path-integral Monte Carlo simulation, the path-integral matrix multiplication method, and the Brownian dynamics simulation reported in Ref. 139. Inset compares asymptotic behavior of the simulations for large flow rates.

For elongational and shear flows, the dimensionless form corresponds to Weissenberg numbers. Both simulations compare well with experiment. The mean extension initially increases rapidly with the flow rate. At about 60% of full extension, the rate of increase in the extension slows to an asymptotic approach to full extension in the large flow rate limit.

A slight discrepancy for moderate flow rates results from the initial condition, which is correct in the strong stretching limit and is not important for weak flows. Monte Carlo techniques correct the discrepancy, as would different initial conditions, which are not done here to avoid additional fitting parameters. Although we do not present these results since they appear elsewhere, the matrix multiplication method exactly reproduces the constant force results of Bouchiat, which agrees with the experiments of Bustamante, since no ambiguity about the initial conditions exists, and the rigid rotor equation is the same [130, 133, 145, 146].

205

7.3 Elongational Flow

The quantum rigid-rotor analogy extends to the elongational flow by changing the form of the external potential to $-F\xi \int_0^L ds(z^2(s) - 1/2(x^2(s) + y^2(s)))$, where F is the flow rate over length. The potential depends on the position instead of the tangent vector. Unless we know the starting position, which depends on the steady-state distribution, we do not know $\mathbf{R}(s)$ and cannot predict the s dependence of the field. To overcome the difficulties presented by this potential, we evaluate the path integral using Monte Carlo techniques.

As a calibration, we analyze the constant plug flow experiment with Monte Carlo and compare these results with our previous results. We discretized the polymer into 844 segments, two segments per persistence length for a DNA chain that is 22.4 μm in length. The discretization captures the rigidity of the polymer without incorporating phenomenological bending springs. The segments are fixed in length and only the angles are varied. We fix one end of the polymer at the origin and perform $12 \cdot 10^6$ Monte Carlo steps with the potential energy defined above. The Monte Carlo algorithm fits the experiment and Brownian dynamic simulation results better than the matrix multiplication method, as shown in Fig. 7-2. These results give us confidence in using this algorithm to evaluate more complicated flows.

Elongational flow corresponds to the experiments of Smith and Chu and of Perkins, Smith, and Chu [50, 53]. In these experiments, the DNA is freely flowing with the fluid. Since the forces caused by this flow are linear, we decompose the motion of the polymer into center of mass and relative motion of the polymer segments. The Monte Carlo procedure is the same as for the constant plug flow, except that the energy is determined in the relative coordinate frame. Fig. 7-3 shows the fractional extension results compared against the experimental results of Chu and the Brownian dynamic simulations of Doyle [139].

Even for this more complicated flow, the fractional extensions predicted by both of the simulations agree extremely well with the experimental results. The fractional extension as a function of flow rate rises quickly to about 80% before a slow asymp-
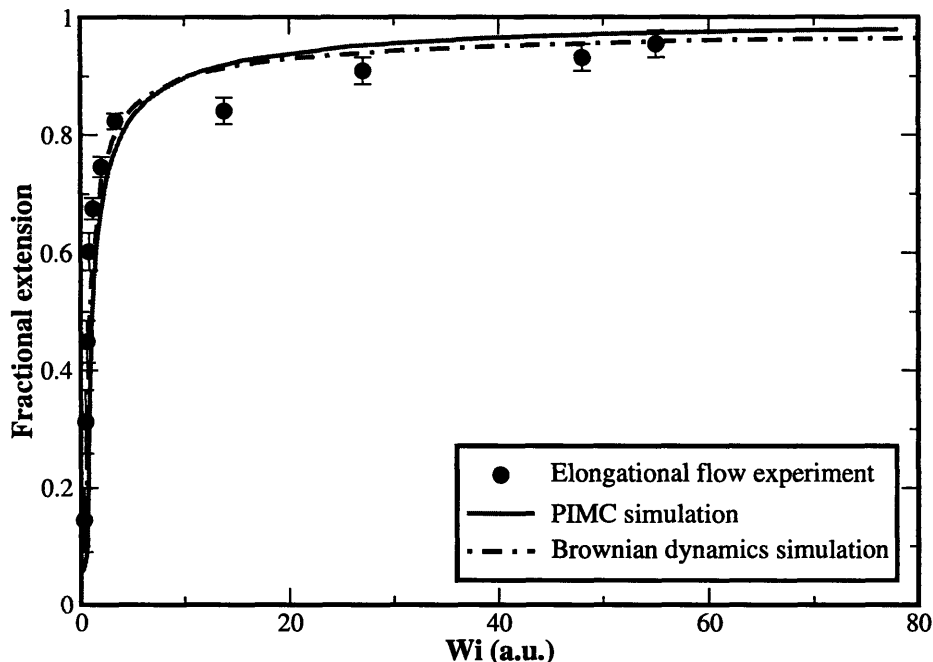
Figure 7-3: Comparison of the elongational flow experiment in Ref. 53, the path-integral Monte Carlo simulation, and the Brownian dynamics simulation reported in Ref. 139.

totic approach to full extension. In the strong flow limit, the Monte Carlo simulation slightly overestimates the extension, as compared to the experiment and Brownian dynamics simulation, but all three results agree extremely well for weak and moderate flows. The agreement between the simulations and experiments for the constant plug and elongational flows demonstrates that the Monte Carlo technique successfully reproduces the results for potential flows and that the WLC model is a good description of DNA and possibly other semi-flexible biological polymers in potential flows.

7.4 Shear Flow

Encouraged by the success of the path integral Monte Carlo method on potential flows, we investigate the application of these methods to non-conservative flow fields like shear flow. The simple shear flow also has an analogous rigid-rotor Hamiltonian with an electrostatic potential $U \propto -x \cdot z$ and a non-conservative B-field, $\hat{r} \times \hat{y}$, where

207

$\hat{r}$ is the position vector and $\hat{y}$ is the unit vector in the y direction. Similar to the elongational flow, we avoid the difficulty of the position dependence by evaluating the action with Monte Carlo.

The shear flow experiment that we analyze is similar to the elongational flow experiment [54, 139]. The DNA freely flows with the fluid, and we calculate the forces in the center of mass frame using the simple shear relations, $F_z = F\xi x$ and $F_x = F_y = 0$, where F is flow rate over length. Although shear flow is not a potential flow, the fluid still performs work on the system, which allows us to define a local energy change by integrating the force along the linear path connecting two configurations. The probability of a transition occurring is proportional to the energy difference in the local frame. Several authors used this approach to describe other polymer systems in shear flows [150, 151, 152, 153]. Since the potential changes as the polymer moves, detailed balance does not hold and the polymer rotates through space, but this simulation can be viewed as a Glauber dynamics [154]. The Monte Carlo algorithm for the shear flow follows the same steps as the constant plug flow and elongational flow with the potential defined locally. A trajectory dependence exists, which may require a larger number of simulation steps than the potential flows, but we still only use $12 \cdot 10^6$ Monte Carlo steps.

The force extension relations for shear flow are plotted in Fig. 7-4. As with the potential flows, the path integral Monte Carlo method agrees extremely well with both experiment and the Brownian dynamics simulation. Because we only used $12 \cdot 10^6$ Monte Carlo steps, some scatter in the data exists. We added a trend line in Fig. 7-4 to help the eye follow the data. For weak shear rates there is a fast initial rise in the mean extension. After the initial rise, the data quickly asymptotes to about 40% extension. The small asymptotic value can be understood by examining the decomposition of the shear flow field into an elongational part and a rotational part. At an angle of about $\pi/4$ in the xz plane, the polymer gets stretched, but at $-\pi/4$ the polymer gets compressed [54, 139, 155]. The rotational part moves the polymer between these angles resulting in an averaging over these angles and a decreased total extension. This cycling from the extended to the compressed states has been observed in the
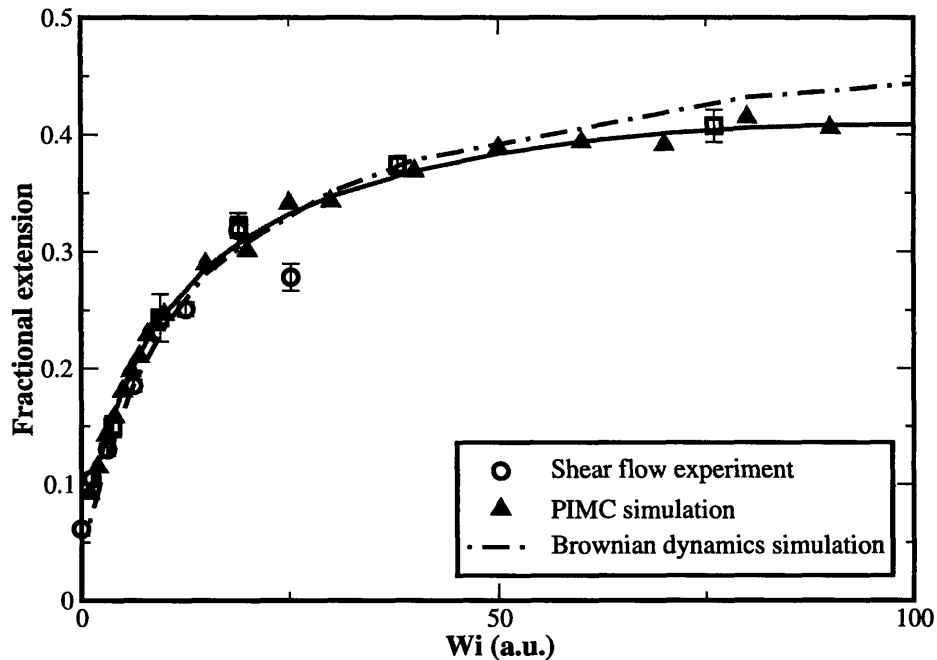
Figure 7-4: Comparison of the shear flow experiment in Ref. 54, the path-integral Monte Carlo simulation, and the Brownian dynamics simulation reported in Ref. 139. To aid the eye, the solid curve follows the trend of the Monte Carlo data.

experiment, the Brownian dynamics simulations, and our Monte Carlo simulations. The correspondence shows that the Glauber dynamics of a Monte Carlo simulation does capture some of the real dynamics of the system.

7.5 Summary and Conclusion

As demonstrated in this chapter, the WLC is a good model for DNA and possibly other semi-flexible biopolymers. With a single fitting parameter, the friction constant, which linearly scales the flow rate, the solution to the path integral quantitatively agrees with experimental results for DNA subject to constant plug, elongational, and shear flows. The model is based on physical principles without phenomenological force extension relations. Although hydrodynamics are strictly dynamic phenomenon, time averaged quantities are quasi-equilibrium phenomenon in an effective potential. This description is possible because relaxation to the steady state distribution is fast and

contributions from intra-chain hydrodynamics can often be neglected. The equilibrium partition function corresponds to an ensemble average, which demonstrates the correspondence between time-averages of single molecule trajectories and ensemble averages for ergodic systems. These techniques are computationally inexpensive since we do not have to run many trajectories to average over initial distributions. This path integral approach is applicable to other semi-flexible biopolymer systems.

Chapter 8

Non-perturbative vibrational energy relaxation effects on vibrational line shapes

8.1 introduction

Vibrational phase and energy relaxation of molecules in solution plays an essential role in chemical and biological processes. The energy transfer in and out of vibrational modes is closely related to reaction dynamics in condensed phases. To probe the solute-solvent interactions, extensive experimental studies have been carried out using time resolved laser spectroscopy, in particular ultrafast laser spectroscopy.[156, 157, 158, 159, 160, 161, 162, 163, 164, 165, 166, 167] Here we consider a simple model of vibrational relaxation of a dilute diatomic solute in a solvent. For this system, the Hamiltonian can be separated into solute, solvent, and solute-solvent interaction contributions. The standard approach to vibrational phase and energy relaxation is based on perturbation theory and the Fermi's golden rule. [168] In this approach, the vibrational energy relaxation (VER) rate constant between a pair of system eigenstates is proportional to the Fourier transform of the quantum force-force correlation function calculated at the corresponding energy gap. In reality,

the classical force correlation function from conventional MD simulations is often used.[169, 170, 171, 172, 173, 174, 175, 176, 177, 178] This approach does not yield quantitative agreement with experimental results although semi-empirical quantum correction factors can significantly improve the agreement.[171, 173, 179] Another standard approach uses a classical description of the solute oscillator and a generalized Langevin equation to describe the coupling of the vibration to the bath.[180, 181] This approach is valid at high temperatures or at low frequencies. In the limit of strong solute-solvent interactions, the contribution of the higher order perturbations is crucial and these approaches break down.

Optical line shapes in condensed phases have been the subject of extensive experimental and theoretical studies. Kubo, Anderson and many others introduced the stochastic line shape theory to study two-level electronic transitions.[182, 183, 184] Modern femtosecond laser techniques can probe the intermolecular and intramolecular vibrations directly. Spectral line shapes from nonlinear spectroscopy, such as hole burning, photon-echo, pump-probe, provide important information of dynamical processes in condensed phases. Mukamel and his coworkers introduced the Brownian oscillator model to describe the coupling between a two-level system and a stochastic bath. The theoretical formulation they developed have been applied to interpret a wide range of spectroscopic experiments.[159, 160, 185, 186, 187, 188, 189] Recently, Cho, Sung and Silbey have extended the Brownian oscillator model to a multi-level system coupled to a bath with arbitrary time scales.[190, 191] Continuous efforts by Hynes, Skinner, Stratt, and many others have been devoted to calculate the line shape function using liquid theory and simulations.[170, 171, 172, 173, 175, 176, 177, 178] Yet, these theoretical models consider pure dephasing without a full account of VER contributions. Some recent studies include VER effects in the Markovian limit.

It is crucial to establish a reliable method that can accurately calculate vibrational line shapes, and precisely predict the VER effects without the Gaussian Markovian assumptions underlying the master equation approach.[192, 193] To address solute-solvent interactions and maintain a quantum description, the vibrational degree of freedom has to be treated exactly. In this chapter, we propose a non-perturbative

approach based on the Feynman's path integral,[121] and systematically investigate the VER effects in vibrational line shapes. In the non-perturbative approach, the wavefunctions are propagated through the solute eigen-state space under the influence of the solvent. The wavefunction is then projected to the specified state using the dipole operator, and computed signals of spectroscopic measurements are averaged over all possible trajectories of bath fluctuations. For the dissipative harmonic oscillator, the non-perturbative approach gives analytical expressions and quantifies the errors introduced by different approximation schemes of VER. For the dissipative Morse potential, the non-perturbative approach demonstrates the VER effects as a function of anharmonicity. The strength of dissipation and the anharmonicity induced dephasing rate are derived in Appendix 8-A. In the present analysis, we only consider the fundamental transition between the ground and the first excited states. A different paper will discuss spectra of overtones and combinations in ABA molecules.[194]

The non-perturbative formulation of quantum dynamics we propose makes a few predictions relevant to experiments: (1) The non-Markovian effects of VER generate asymmetric envelops in the temporal absorption profile, which are also manifested as side bands in the absorption spectrum. (2) Non-perturbative calculations yield non-Lorentzian peaks in absorption spectrum. The peaks are rationalized in terms of the couplings of population relaxations from different vibrational states and provide an alternative explanation of non-Lorentzian line shapes.[195] (3) Non-perturbative VER effects lead to non-Lorentzian broadening along the diagonal direction in the frequency domain photon echo spectra. This phenomenon is different from the pure dephasing induced line broadening discussed in the literature. (4) Quantum baths generate more coherence in the long time profile but have less effects on the short-time profile. (5) For anharmonic oscillators, the absorption spectrum has asymmetric central peaks, and the asymmetry increases with anharmonicity. (6) For O-H stretch in D_2O environments, non-Markovian VER effects generate a small recurrence in the three-pulse photon echo peak shift (3PEPS).

The rest of the chapter is organized as follows. In Sec. 8.2, we discuss the non-

perturbative and perturbative calculations of vibrational line shapes, including vibrational absorption, population relaxation, and photon echo. Using a perturbative expansion, the solute-solvent interaction is decomposed into the diagonal and off-diagonal components in the solute eigen-state space, which are responsible for phase relaxation and population relaxation, respectively. In the limit of weak solute-solvent interaction, the temporal absorption profile can be approximately factorized into the population relaxation profile in pump-probe experiments and the pure dephasing profile. The well-known relation for the dephasing rate, the population relaxation rate and the pure dephasing rate is recovered under the Markovian approximation. In Sec. 8.3, we apply both the perturbative and non-perturbative methods to a harmonic oscillator linearly coupled to a Gaussian bath in the absence of pure dephasing. The errors introduced by different approximation schemes are examined both analytically and numerically. Non-Markovian VER effects generate asymmetric envelops in the time domain absorption signal which are manifested as side bands in the frequency domain spectrum. These side bands are solvent-induced multiple-photon transitions and only present in the non-Markovian treatment. The non-perturbative VER effects result in non-Lorentzian central peaks. In Sec. 8.4, we numerically investigate the anharmonic effects in a dissipative Morse oscillator spectra, which display as asymmetric line shapes. The perturbation schemes neglect the cross terms of population relaxation and pure dephasing, and therefore deviate significantly from the exact results at large anharmonicities. In Sec. 8.5, we examine the VER effects on three-pulse photon echo peak shift (3PEPS) experiments in a hydrogen-bonded system. The nonlinear 3PEPS measurement is a sensitive probe of the non-Markovian VER effects. Numerical calculations reveal a small recurrence at 200 fs, which cannot be reproduced by the Markovian VER rate. Section 8.6 concludes our analysis.

8.2   General formalism

For chemical reactions occurring in solutions, solvent molecules play an essential role in the dynamics of the solute. In the present chapter, we consider a solute molecule

with one vibrational degree of freedom embedded in an environment of solvent atoms or molecules. The complete Hamiltonian is

$$H = H_s + H_b + V_{sb}, \tag{8.1}$$

where the vibrational mode is referred to as the system H_s, all the remaining degrees of freedom are considered as the bath H_b, and the coupling between them is the solute-solvent interaction V_{sb}. The system Hamiltonian is diagonalized by a set of eigenstates $|n\rangle$ with eigen-energies E_n. In the interaction picture, the solute-solvent interaction becomes a time-dependent operator $V(t) = e^{i(H_s+H_b)t}V_{sb}e^{-i(H_s+H_b)t}$. The central quantity in calculating vibrational spectra is the propagator given in the interaction picture

$$\langle n|G(t)|n\rangle = \langle n|e^{-iHt}|n\rangle = e^{-iE_nt}e^{-iH_bt}\langle \mathcal{T}e^{-i\int_0^t V(\tau)d\tau}\rangle_n, \tag{8.2}$$

where $\mathcal{T}$ is the chronological ordering operator, and $\langle \cdots \rangle_n = \langle n|\cdots|n\rangle$ stands for the expectation value of the nth vibrational state. Unless specified, $\hbar$ is unity implicitly. In the non-perturbative approach, the time-dependent solute-solvent interaction $V(\tau)$ is evaluated explicitly at every time step during the course of wave function propagation. Here $|n\rangle$ stands for the unperturbed system basis set while in real systems the basis set is mixed with system-bath couplings. This mixing of wavefunctions is inconsequential for the standard VER rate treatment, but has substantial effects on non-perturbative VER treatment. In gas phase, only $\Delta\nu = 1$ transition is allowed for linear dipole operator if the system is initially in ground state. However, the system-bath coupling modifies the dipole interaction operator in the system basis set and induces multiple-photon transitions. As a result, the central peak in the absorption line shape is non-Lorentzian, and there are also solvent-induced side bands corresponding to $\Delta\nu = 0,\ 2,\ \cdots$.

8.2.1 Formal definitions of vibrational line shapes

The propagator in Eq. (8.2) is used to derive expressions of vibrational spectroscopic measurements, in particular, absorption spectrum, pump-probe signals, and photon echo. These expressions not only are useful for present analysis, but also provide the basis for more reliable numerical simulations. We will demonstrate the latter aspect in future publications. Here we assume that each application of the laser field results in one vibrational transition, so that the excitation pathway can be established unambiguously.

Absorption spectrum

Among vibrational spectroscopic measurements, absorption is one of the most important probes of relaxation. The time-domain absorption amplitude is defined as

$$A_{abs}(t) = \sum_n \langle \langle n+1|G(t)|n+1\rangle \rho_n \langle n|G(t)|n\rangle^\dagger \rangle_b = \sum_n \rho_n A_{n,n+1,abs}(t), \qquad (8.3)$$

where $\langle \cdots \rangle_b$ represents the thermal average over the bath degrees of freedom and $\sum_n$ is the sum over the solute vibrational degree of freedom. Initially the bath is in thermal equilibrium. The real part of the absorption amplitude is related to the free-induction decay (FID) signal, and the Fourier transform of absorption amplitude yields the absorption spectrum,

$$A_{abs}(\omega) = \mathrm{Re} \int_0^\infty A_{abs}(t)e^{i\omega t}dt, \qquad (8.4)$$

which can be measured by the Fourier transformed IR spectroscopy (FT-IR).

Pump-probe signal

In a pump-probe experiment, one molecule is excited vibrationally and the subsequent vibrational relaxation transfers vibrational energy to other degrees of freedom of the original excited molecule and its neighboring molecules. Here we treat the population

transfer from the nth to n+1th vibrational states. The pump-probe signal is given as

$$I_{pp} = \sum_n \rho_n \langle |\langle n+1|G(t)|n+1\rangle|^2 \rangle_b. \tag{8.5}$$

For later applications, we also write the pump-probe signal as $I_{pp}(t) = \sum_n \rho_n I_{n+1,pop}(t)$, with $I_{n,pop}$ the population relaxation profile defined as

$$I_{n,pop}(t) = \langle |\langle n|G(t)|n\rangle|^2 \rangle_b. \tag{8.6}$$

The Infrared-Raman technique developed by Laubereau and Kaiser,[156] which uses resonant vibrational pumping by a tunable mid-IR pulse and a subsequent probe by an incoherent anti-Stokes Raman, provides a powerful tool to study VER. Recently advances in ultrafast laser technology allows the IR technique to reach its full potential. Yet, it is important to note that the anti-Stokes Raman spectra also include other excitations generated by vibration-rotation couplings not included in our model.

Photon echo

The photon echo measurement is a sensitive probe of homogeneous dephasing and an important example of nonlinear spectroscopy. In two-pulse photon echo (2PE) experiments, two coherent laser pulses interact with a sample at a well-controlled time separation. The first pulse creates a coherent ensemble of atomic or molecular polarization, which dephases during the waiting time interval. The second pulse partially rephases the lost coherence and creates an echo signal. The simple version of a photon-echo experiment is a resonant third-order process with zero intermediate waiting time. The three pulse photon echo (3PE) measurement with a finite waiting time is discussed later in Sec. 8.5. Let us assume that the spectral resolution is sufficiently high to resolve all the possible excitation pathways in a molecular system. For the purpose of demonstration, we consider a simple excitation pathway, $\rho_{nn} \rightarrow$

$\rho_{n+1,n} \rightarrow \rho_{n,n+1} \rightarrow \rho_{nn}$, which is described by

$$A_{echo}(t_1, t_2) = \langle\langle n|e^{-iHt_2}|n\rangle\langle n+1|e^{-iHt_1}|n+1\rangle\langle n|e^{-iHt_1}|n\rangle^\dagger\langle n+1|e^{-iHt_2}|n+1\rangle^\dagger\rangle_b. \quad (8.7)$$

By carrying out a series of detection experiments, one can obtain the real part, the imaginary part, or the amplitude of $A_{echo}(t_1, t_2)$ in Eq. (8.7), respectively.

Path integral evaluation

The expressions of the vibrational spectroscopic measurements provide the basis for numerical evaluations. In these calculations, we generate time trajectories of system-bath interaction $V(t)$, and evaluate the propagator $G(t)$ along each trajectory. Then, we calculate the spectroscopic signals and average over all the trajectories. For a classical bath, one can exactly simulate the bath degree of freedom using conventional molecule dynamics techniques, generate a time-dependent force through the system-bath coupling, and propagate the quantum vibrational degree of freedom exactly. Due to the intrinsic complexity of quantum baths, an exact simulation of the bath modes is not yet available.[196] But for vibrational line shapes, as shown later, a quantum representation of bath degrees of freedom is not necessary at room temperatures. Hence, we can propagate quantum vibrational degree of freedom under classical force of the bath. Another technique, the surface hopping method, is used widely to treat a classical anharmonic bath coupled to a quantum system.[197, 198, 199, 200, 201] In the present chapter we focus on a Gaussian bath linearly coupled to the system. Linearized dissipative models have been applied extensively to study dynamic processes in condensed phases, including activated dynamics, electron and proton transfer, diffusion, and vibrational energy relaxation. For a Gaussian bath, several numerical techniques can be applied:

1. For a Uhlenbeck process, the force-force correlation function is exponential, i. e. , $C(t) = \langle\delta f^2\rangle_b e^{-\gamma t}$. The propagation of random force is a Markovian process satisfying $G_f(f,t|f',t') = \int_{-\infty}^{\infty} G_f(f,t|f'',t'')G_f(f'',t''|f',t')df''$, where

the Green's function of random force is a Gaussian distribution,

$$G_f(f, t|f', t') = [2\pi\langle\delta f^2\rangle_b(1 - e^{-2\gamma(t-t')})]^{-1/2} \exp\left[-\frac{(f - f'e^{-\gamma(t-t')})^2}{2\langle\delta f^2\rangle_b(1 - e^{-2\gamma(t-t')})}\right] \quad (8.8)$$

The equilibrium distribution of the random force is $P_{eq}(f) = [2\pi\langle\delta f^2\rangle_b]^{-1/2} \cdot$ $\exp[-f^2/2\langle\delta f^2\rangle_b]$, assuming that the random force has a zero mean. With the Markovian property, one can generate a number of random force trajectories by first generating $f(t_0)$ from the equilibrium distribution and then using Eq. (8.8) to generate the random forces at subsequent time steps. The quantum system of vibrational degrees of freedom is propagated along each trajectory, and vibrational line shapes are calculated exactly. The bath average is obtained through an average over all the trajectories.

2. For a set of linearly coupled harmonic oscillators, one can always identify the normal coordinates of the bath through an orthogonal transform, and each normal mode is a Uhlenbeck process. For example, we use bi-exponential friction kernel in the O-H relaxation. Hence, one can first generate the normal coordinates using the method in (1) and then generate the bath modes using the orthogonal transform.

3. For a quantum Gaussian bath, integration of the bath modes leads to influence functionals which couples the system variables at different times. As a numerical technique, the influence functional formalism[202] becomes tedious when multiple excitations are involved. As an alternative, the method proposed by Cao, Ungar, and Voth[203] samples the Gaussian random force directly without introducing the influence functional formalism, and propagates the system under the influence of quantum forces. This method is particularly adequate for complicated multiple-time propagation of a vibrational system.

8.2.2 Perturbative expressions: Factorization and cumulant expansion

Factorization

In the perturbative approach, we decompose the system-bath coupling $V(t)$ into the diagonal and the off-diagonal operators in the vibrational eigen space, giving

$$V_D(t) = \sum_n \langle V(t) \rangle_n |n\rangle\langle n| \quad \text{and} \quad V_{OD}(t) = V(t) - V_D(t). \tag{8.9}$$

The corresponding propagator can be written as

$$
\begin{aligned}
\langle n|G(t)|n\rangle &\approx e^{-iE_n t}e^{-iH_b t}\langle n|\mathcal{T}e^{-i\int_0^t V_D(\tau)d\tau}\;\mathcal{T}e^{-i\int_0^t V_{OD}(\tau)d\tau}|n\rangle \\
&= e^{-iE_n t}e^{-iH_b t}\mathcal{T}e^{-i\int_0^t \langle V_D(\tau)\rangle_n d\tau}\;\left\langle \mathcal{T}e^{-i\int_0^t V_{OD}(\tau)d\tau}\right\rangle_n.
\end{aligned}
\tag{8.10}
$$

In Eq. (8.10), we decompose the exponential function of two time-dependent operators into the product of the two corresponding exponentials, which is valid only if $V_D(t)$ and $V_{OD}(t)$ commute. The approximation neglects the contribution from $[V_D(t), V_{OD}(t)]$, which is generally nonzero for anharmonic potentials. In Sec. 8.4 we demonstrate quantitatively that $[V_D(t), V_{OD}(t)]$ increases with anharmonicity and results in large deviations between the perturbative and the exact results.

We now apply the decomposition in Eq. (8.10) to the vibrational line shapes in Sec. 8.2.1 and derive the perturbative expressions for the temporal absorption profile, population relaxation profile and photon echo. The absorption amplitude in Eq. (8.3) can be rewritten as

$$
\begin{aligned}
A_{n,n+1,abs}(t) &\approx e^{-i\Omega_{n,n+1}t}\left\langle \mathcal{T}e^{-i\int_0^t \omega_{n,n+1}(\tau)d\tau}\left\langle \mathcal{T}e^{-i\int_0^t V_{OD}(\tau)d\tau}\right\rangle_{n+1}\left\langle \mathcal{T}e^{-i\int_0^t V_{OD}(\tau)d\tau}\right\rangle_n^\dagger\right\rangle_b \\
&\approx e^{-i\Omega_{n,n+1}t}\left\langle \mathcal{T}e^{-i\int_0^t \omega_{n,n+1}(\tau)d\tau}\right\rangle_b\left\langle\left\langle \mathcal{T}e^{-i\int_0^t V_{OD}(\tau)d\tau}\right\rangle_{n+1}\right\rangle_b \\
&\quad\left\langle\left\langle \mathcal{T}e^{-i\int_0^t V_{OD}(\tau)d\tau}\right\rangle_n\right\rangle_b^\dagger,
\end{aligned}
\tag{8.11}
$$

where $\Omega_{n,n+1} = E_{n+1} - E_n$ is the frequency gap and $\omega_{n,n+1}(t) = \langle V_D(t)\rangle_{n+1} - \langle V_D(t)\rangle_n^*$

is the diagonal frequency difference induced by the solute-solvent interaction. In Eq. (8.11), we first decouple the bath averages of the diagonal and the off-diagonal parts, then perform the bath average on each propagator separately. As discussed in Eq. (8.10), the first approximation neglects the commutator between $V_D(t)$ and $V_{OD}(t')$. The second approximation neglects the cross terms between the propagators, and is correct only for weak solute-solvent interactions.

With the propagator in Eq. (8.10), the population relaxation profile in Eq. (8.6) reduces to

$$
\begin{aligned}
I_{n,pop}(t) &\approx \left\langle \left| \langle n | \mathcal{T} e^{-i \int_0^t V_{OD}(\tau) d\tau} | n \rangle \right|^2 \right\rangle_b \approx \langle \langle n | e^{-i \int_0^t V_{OD}(\tau) d\tau} | n \rangle \rangle_b \langle \langle n | e^{-i \int_0^t V_{OD}(\tau) d\tau} | n \rangle^\dagger \rangle_b \\
&= \left| \langle n | \langle e^{-i \int_0^t V_{OD}(\tau) d\tau} \rangle_b | n \rangle \right|^2 .
\end{aligned}
\tag{8.12}
$$

Comparing the above equation with Eq. (8.11), we realize that

$$
A_{n,n+1,abs}(t) \approx e^{i\Omega_{n,n+1} t} \sqrt{I_{n,pop}(t) I_{n+1,pop}(t)} A_{n,n+1,dep}(t),
\tag{8.13}
$$

where $A_{n,n+1,dep}(t) = \langle \exp[-i \int_0^t \omega_{n,n+1}(\tau) d\tau] \rangle_b$ is the contribution from pure dephasing. Eq. (8.13) demonstrates that temporal absorption profile can be approximately factorized into the population relaxation profile and the pure dephasing profile. As a result, the off-diagonal part of the interaction, $V_{OD}(t)$, contributes to population relaxation, and the diagonal part of the interaction, $V_D(t)$, contributes to pure dephasing.

Inserting Eq. (8.10) into the photon echo expression defined in Eq. (8.7) and following the same factorization scheme as Eq. (8.11), we arrive at

$$
\begin{aligned}
A_{echo}(t_1, t_2) &\approx e^{i\Omega_{n,n+1}(t_2-t_1)} \Big\langle \Big[e^{i \int_{t_1}^{t_1+t_2} \omega_{n,n+1}^*(\tau) d\tau - i \int_0^{t_1} \omega_{n,n+1}(\tau) d\tau} \langle \mathcal{T} e^{-i \int_{t_1}^{t_1+t_2} V_{OD}(\tau) d\tau} \rangle_n \\
&\quad \langle \mathcal{T} e^{-i \int_0^{t_1} V_{OD}(\tau) d\tau} \rangle_{n+1} \langle \mathcal{T} e^{-i \int_0^{t_1} V_{OD}(\tau) d\tau} \rangle_n^\dagger \langle \mathcal{T} e^{-i \int_{t_1}^{t_1+t_2} V_{OD}(\tau) d\tau} \rangle_{n+1}^\dagger \Big] \Big\rangle_b \\
&\approx e^{i\Omega_{n,n+1}(t_2-t_1)} \langle e^{i \int_{t_1}^{t_1+t_2} \omega_{n,n+1}(\tau) d\tau - i \int_0^{t_1} \omega_{n,n+1}(\tau) d\tau} \rangle_b \\
&\quad \langle \langle \mathcal{T} e^{-i \int_{t_1}^{t_1+t_2} V_{OD}(\tau) d\tau} \rangle_n \rangle_b \langle \langle \mathcal{T} e^{-i \int_0^{t_1} V_{OD}(\tau) d\tau} \rangle_{n+1} \rangle_b \\
&\quad \langle \langle \mathcal{T} e^{-i \int_0^{t_1} V_{OD}(\tau) d\tau} \rangle_n \rangle_b^\dagger \langle \langle \mathcal{T} e^{-i \int_{t_1}^{t_1+t_2} V_{OD}(\tau) d\tau} \rangle_{n+1} \rangle_b^\dagger,
\end{aligned}
\tag{8.14}
$$

where the photon echo signal is also decomposed into the population relaxation contribution from the off-diagonal interaction and the pure dephasing contribution from the diagonal interaction.

second-order cumulant expansion

To further simplify the analysis, we truncate the solute-solvent interaction to second order of bath fluctuation, which is valid for weak solute-solvent interactions or fast bath relaxations. First, the temporal profile for population relaxation from the nth vibrational state is approximated by taking the bath average $\langle \cdots \rangle_b$ for each propagator in Eq. (8.12) separately, giving

$$
I_{n,pop}(t) \approx \left| \langle n | \langle e^{-i \int_0^t V_{OD}(\tau) d\tau} \rangle_b | n \rangle \right|^2 \approx |\exp[-h_n(t)]|^2 , \tag{8.15}
$$

where $h_n(t) = \int_0^t \int_0^\tau \langle n | \langle V_{OD}(t_1) V_{OD}(t_2) \rangle_b | n \rangle dt_1 dt_2$ characterizes the population relaxation from the nth vibrational state. The last approximation switches the exponential function and quantum expectation value after invoking the cumulant expansion, and assumes a diagonal form of $\langle V_{OD}(t_1) V_{OD}(t_2) \rangle_b$ while neglecting its off-diagonal elements.

Similarly, application of the second order cumulant expansion to the pure dephasing profile leads to

$$
A_{n,n+1,dep}(t) = \langle \exp[-i \int_0^t \omega_{n,n+1}(\tau) d\tau] \rangle_b \approx \exp[-i \langle \omega_{n,n+1} \rangle_b t - g(t)] \tag{8.16}
$$

where $g(t) = \int_0^t \int_0^\tau \langle \delta \omega_{n,n+1}(t_1) \delta \omega_{n,n+1}(t_2) \rangle_b dt_1 dt_2$ is the line shape function, and $\langle \omega_{n,n+1} \rangle_b$ is the Stokes shift. Combining the population relaxation profile and the pure dephasing signal, the absorption amplitude in Eq. (8.11) reduces to

$$
A_{n,n+1,abs}(t) \approx e^{-i\Omega_{n,n+1}t} \exp[-i \langle \omega_{n,n+1} \rangle_b t - g(t) - h_n^*(t) - h_{n+1}(t)]. \tag{8.17}
$$

The 2PE signal in Eq. (8.14) after the second-order cumulant expansion becomes

$$A_{echo}(t_1, t_2) \approx e^{i\Omega_{n,n+1}(t_2-t_1)} \exp[i\langle\omega_{n,n+1}\rangle_b(t_2 - t_1)]$$

$$\times \exp[-2g^*(t_1) - g(t_2) - g^*(t_2) + g^*(t_1 + t_2)]$$

$$\times \exp[-h_{n+1}(t_1) - h_n(t_2) - h_n^*(t_1) - h_{n+1}^*(t_2)]. \qquad (8.18)$$

In the limit $h_n(t) \to 0$, equation (8.18) reduces to the well-known 2PE expression for a two-level system.[159] A generalization of Eq. (8.18) to an arbitrary number of vibrational states in the limit of $h_n(t) \to 0$ was recently proposed by Sung and Silbey.[191] Their treatment includes diagonal matrix elements only while VER effects are absent.

In many cases, composite approximation schemes are adopted to explain the vibrational measurements. The decomposition relation in Eq. (8.13) and the second order cumulant expansion yield,

$$A_{n,n+1,abs}(t) \approx (I_{n,pop}(t)I_{n+1,pop}(t))^{1/2} \exp[-i\Omega_{n,n+1}t - i\langle\omega_{n,n+1}\rangle_b t - g(t)]. \qquad (8.19)$$

The advantage of this decomposition is that the population relaxation profile is measured from pump-probe experiments and contains non-perturbative information of VER. As we will demonstrate later that the decomposition yields results close to non-perturbative calculations, accurately reproducing the short time oscillations. But this approximation neglects the cross terms between the population relaxations from the nth and the n+1th states and the coupling between population relaxation and pure dephasing, and does not contain any phase information of VER. Because of these approximations, equation (8.19) cannot reproduce asymmetric absorption spectra for anharmonic systems.

8.2.3   Markovian approximation

The essence of Markovian approximation is that the relaxation of the vibrational degree of freedom is much slower than the relaxation of bath modes. Under the

Markovian limit, the line shape function and the population relaxation exponent are linearly increasing with time, i. e. ,

$$g(t) \approx \Gamma'_{n,n+1}t, \quad \text{and} \quad h_n(t) \approx \frac{\Gamma_n}{2}t \tag{8.20}$$

where $\Gamma'_{n,n+1} = \int_0^\infty \langle \delta\omega_{n,n+1}(t)\delta\omega_{n,n+1}(0)\rangle_b dt$ and $\Gamma_n = 2\int_0^\infty \langle n|\langle V_{OD}(\tau)V_{OD}(0)\rangle_b|n\rangle d\tau$ are usually complex, with the real part being the population relaxation rate and the imaginary part being the frequency shift. Consequently, the population relaxation profile is approximated by an exponential function $I_{n,pop}(t) \approx \exp[-\Re(\Gamma_n)t]$, and the pure dephasing profile becomes $A_{n,n+1,dep}(t) \approx \exp[-\Gamma'_{n,n+1}t - i\langle\omega_{n,n+1}\rangle_b t]$. In Eq. (8.17), the absorption profile is approximated by $A_{n,n+1,abs}(t) \approx \exp[-i\Omega_{n,n+1} - i\langle\omega_{n,n+1}\rangle_b t - \Gamma_{n,n+1}t]$ with $\Gamma_{n,n+1} = (\Gamma_n^* + \Gamma_{n+1})/2 + \Gamma'_{n,n+1}$. Thus, the time dependent expression of Eq. (8.13) recovers the well-known relation,

$$k_{n,n+1} = \frac{k_n + k_{n+1}}{2} + k'_{n,n+1}, \tag{8.21}$$

$k_n = \Re(\Gamma_n)$ is the population relaxation rate, $k'_{n,n+1} = \Re(\Gamma'_{n,n+1})$ is the pure dephasing rate, and $k_{n,n+1} = \Re(\Gamma_{n,n+1})$ is the dephasing rate. Under the Markovian approximation, the photon echo signal is readily simplified as

$$\begin{aligned}
A_{echo}(t_1, t_2) &\approx e^{i\Omega_{n,n+1}(t_2-t_1)} \exp\left[-i\langle\omega_{n,n+1}\rangle_b(t_2 - t_1) - \Gamma'_{n,n+1}t_2 - \Gamma'^*_{n,n+1}t_1\right] \\
&\times \exp\left[-\frac{\Gamma_{n+1} + \Gamma_n^*}{2}t_1 - \frac{\Gamma_n + \Gamma_{n+1}^*}{2}t_2\right].
\end{aligned} \tag{8.22}$$

Considering that pure dephasing in anharmonic potentials is much faster than population relaxation, we can approximate the population relaxation with the Markovian rate and the pure dephasing signal with second-order cumulant expansion,

$$A_{n,n+1,abs}(t) \approx e^{-i\Omega_{n,n+1}t}\exp[-i\langle\omega_{n,n+1}\rangle_b t - g(t) - \frac{\Gamma_n^*}{2}t - \frac{\Gamma_{n+1}}{2}t]. \tag{8.23}$$

For the dissipative harmonic oscillator discussed later in Sec. 8.4, the diagonal couplings are zero and $A_{n,n+1,dep}(t) = 1$, and equation (8.23) becomes identical to the

Markovian approximation. For a dissipative Morse potential in Sec. 8.5, the deviations of Eqs. (8.19) and (8.23) from the non-perturbative results increase with anharmonicity.

8.2.4 Inconsistency of the Markovian rate approximation of VER

Let us now discuss the physical meaning of $h_n(t)$. Usually the solvent relaxation rate γ, the VER rate, pure dephasing rate, and the vibrational frequency satisfy $\Omega_{n,n+1} > k'_{n,n+1} > k_n > \gamma$. The population relaxation process occurs through the resonance between the vibrational frequency and the bath spectrum while the dephasing rate corresponds to the bath spectrum at zero frequency. Given the fact that $\gamma \ll \Omega_{n,n+1}$, vibrational relaxation is much slower than pure dephasing, hence $k'_{n,n+1} \gg k_n$ and the line shapes are usually dominated by pure dephasing. In this case, vibrational relaxation is either ignored or approximated with a Markovian rate. However, this argument is not self-consistent because the Markovian rate approximation is only valid at sufficient long time while the vibrational line shape generally depends on the full time history of the off-diagonal contribution.

To illustrate this point, we consider a linear system-bath coupling, $f(t)q$, which will be further investigated in later sections. The second order cumulant expansion gives

$$h_n(t) = \sum_{m \neq n} \frac{\langle \delta f^2 \rangle_b q_{nm}^2}{\hbar^2} \int_0^t (t - \tau) e^{-\gamma t} \cos \Omega_{mn} \tau \, d\tau \qquad (8.24)$$

In the limit of a fast bath, $h_n(t) \approx \gamma t (\sum_{m \neq n} \langle \delta f^2 \rangle_b q_{nm}^2 / \hbar^2 \Omega_{mn}^2)$ and yields a Markovian rate. In the limit of a frozen bath $\gamma \to 0$, $h_n(t) \approx \sum_{m \neq n} \langle \delta f^2 \rangle_b q_{nm}^2 (1 - \cos \Omega_{mn} t)/\hbar^2 \Omega_{mn}^2$, which leads to side bands with $\Delta \omega = \Omega_{mn}$ around the central peak in the vibrational line shapes. As we mentioned in Sec. 8.2, the side bands are induced by the system-bath coupling. Apparently $h_n(t)$ is intrinsically oscillatory over the complete time domain while the Markovian approximation implies $h_n(t) \to 0$ and

$k_n \to 0$, which is obviously inadequate to describe the VER contribution. The slow bath assumption renders the Markovian description of the VER effects inadequate.

8.3 Analytical solutions of dissipative harmonic oscillator

For the purpose of illustration, we first model the vibrational degree of freedom as a harmonic oscillator linearly coupled to a classical bath. The classical bath assumption is often adopted because one can always separate the degrees of freedom into those with low frequencies $\hbar\omega \leq k_B T$, which may be treated classically as the bath, and those with high frequencies $\hbar\omega > k_B T$, which must be treated quantum mechanically as the system. The Hamiltonian is thus given by

$$H = \frac{p^2}{2\mu} + \frac{1}{2}\omega_0^2 q^2 + f(t)q, \qquad (8.25)$$

where $f(t)$ is a Gaussian random force resulting from the bath degree of freedom. The bath relaxation is described by the friction kernel $C_{cl}(t) = \langle \delta f(t) \delta f(0) \rangle_b$, where the subscript represents a classical bath. Quantum effects of the Gaussian bath are discussed in Sec. 8.3.5. In numerical calculations, we assume an exponentially decaying friction kernel, $C_{cl}(t) = \langle \delta f^2 \rangle_b \exp[-\gamma t]$. $\langle \delta f^2 \rangle_b$ is the mean square fluctuation of the random force and is a probe of the average strength of the solute-solvent interaction. The linear solute-solvent coupling here has no diagonal contribution; thus, there is no pure dephasing contribution and all the vibrational line shapes are generated by VER. The analytical solutions offer us a good benchmark of the accuracies of various approximations.

226

8.3.1 Exact path integral calculation

Now we discuss the exact calculations of the vibrational line shapes defined in Sec. 8.2. The propagator of the forced harmonic oscillator is[121]

$$
\begin{aligned}
G(q_2, t; q_1, 0) &= \sqrt{\tfrac{\mu\,\omega_0}{2\pi i\hbar\sin\omega_0 t}} \exp\left\{ \tfrac{i\mu\,\omega_0}{2\hbar\sin\omega_0 t}[(q_2^2 + q_1^2)\cos\omega_0 t - 2q_1 q_2] \right\} \\
&\quad \exp\left\{ -\tfrac{i\mu\omega_0}{2\hbar\sin\omega_0 t}\left[\tfrac{2q_1}{\mu\omega_0}\int_0^t f(\tau)\sin\omega_0(t-\tau)d\tau + \tfrac{2q_2}{\mu\omega_0}\int_0^t f(\tau)\sin\omega_0\tau d\tau\right] \right\} \\
&\quad \exp\left\{ -\tfrac{i\mu\,\omega_0}{2\hbar\sin\omega_0 t}\left[\tfrac{2}{\mu^2\omega_0^2}\int_0^t\int_0^t f(\tau)f(\tau')\sin\omega_0(t-\tau)\ \sin\omega_0\tau' d\tau d\tau'\right] \right\}. \quad (8.26)
\end{aligned}
$$

The transition moments between a pair of vibrational eigenstates are given by

$$
\begin{aligned}
G_{mn}(t) &= e^{\frac{i}{\hbar}E_m t}\int_{-\infty}^{\infty}\int_{-\infty}^{\infty}\phi_m(q_2)G(q_2, t; q_1, 0)\phi_n(q_1)dq_1 dq_2 \\
&= \frac{G_{00}(t)}{\sqrt{m!n!}}\sum_{r=0}^{l}\frac{(-1)^{m+n}m!n!}{(m-r)!(n-r)!}(i\zeta)^{n-r}(i\zeta')^{m-r},\ \ \text{with } l = \max\{m, n\}, \\
\zeta(t) &= \frac{1}{\sqrt{2\mu\omega_0\hbar}}\int_0^t f(\tau)\exp[-i\omega_0\tau]d\tau, \\
\zeta'(t) &= \frac{1}{\sqrt{2\mu\omega_0\hbar}}\int_0^t f(\tau)\exp[i\omega_0\tau]d\tau. \quad (8.27)
\end{aligned}
$$

In Eq. (8.27), $\phi_n(q)$ is the nth eigenfunction and ζ, ζ' are incomplete Fourier transforms of the random force at the fundamental frequency. The diagonal transition moment $G_{00}(t)$ for the ground state is given by $G_{00}(t) = \exp[-\zeta(t)\zeta'(t)]$. For the rest of this chapter, we only consider the fundamental transition between the ground state $|g\rangle = |0\rangle$ and the first excited state $|e\rangle = |1\rangle$ unless specified otherwise. A different paper will discuss spectra of overtones and combinations in ABA molecules.[194] The absorption amplitude for $|g\rangle \rightarrow |e\rangle$ is thus $A_{ge,abs}(t) = \langle\langle e|e^{-iHt}|e\rangle\langle g|e^{-iHt}|g\rangle^\dagger\rangle_b$. We apply Eq. (8.27) twice for $m = n = 0$ and $m = n = 1$, respectively, and obtain the absorption amplitude $A_{ge,abs}(t) = e^{-i\omega_0 t}(1 + \partial_z)|_{z=1}\langle\exp[-z\zeta(t)\zeta'(t)]\rangle_b$. For a Gaussian bath, the average can be directly calculated with the cumulant expansion, giving

$$
\begin{aligned}
A_{ge,abs}(t) &= e^{-i\omega_0 t}\left[1 + 2(\alpha_{11} + \alpha_{22}) + 4(\alpha_{11}\alpha_{22} - \alpha_{12}^2)\right]^{-3/2}(1 + \alpha_{11} + \alpha_{22}) \\
\text{where}\ \ \alpha_{ij}(t) &= \frac{1}{\mu\omega_0\hbar}\int_0^t\int_0^\tau \langle f(\tau)f(\tau')\rangle_b\psi_i(\tau)\psi_j(\tau')d\tau d\tau',\ \ i, j \in \{1, 2\}. \quad (8.28)
\end{aligned}
$$

$\psi_1(\tau)$ and $\psi_2(\tau)$ are short-hand notations for $\cos\omega_0\tau$ and $\sin\omega_0\tau$, respectively. Given the exponential friction kernel, $\alpha_{ij}(t)$ can be evaluated explicitly. We find that the envelop of $A_{ge,abs}(t)$ exhibits a power-law decay in the long time limit, i. e. , $A_{ge,abs}(t) \approx e^{-i\omega_0 t}(1 + \Gamma_{ge}t/2)^{-2}$., with Γ_{ge} equal to the dephasing rate defined later in the Markovian limit (see Sec. 8.3.3).

We use the transition amplitudes in Eq. (8.27) to evaluate the population relaxation signal in pump-probe experiments $I_{n,pop}(t)$ analytically. For instance, the population relaxation profiles for the ground and the first excited states are:

$$I_{g,pop}(t) = [1 + 2(\alpha_{11} + \alpha_{22}) + 4(\alpha_{11}\alpha_{22} - \alpha_{12}^2)]^{-1/2}$$

$$\text{and } I_{e,pop}(t) = [1 + 2(\alpha_{11} + \alpha_{22}) + 4(\alpha_{11}\alpha_{22} - \alpha_{12}^2)]^{-5/2} \cdot$$
$$[1 + 2(\alpha_{11} + \alpha_{22}) + 3(\alpha_{11} + \alpha_{22})^2 - 4(\alpha_{11}\alpha_{22} - \alpha_{12}^2)$$
$$+8(\alpha_{11} + \alpha_{22})(\alpha_{11}\alpha_{22} - \alpha_{12}^2) + 16(\alpha_{11}\alpha_{22} - \alpha_{12}^2)^2]. \quad (8.29)$$

In the long time limit, it is straightforward to show that both $I_{g,pop}$ and $I_{e,pop}$ decays as t^{-1}.

In the absence of pure dephasing, the decomposition relation Eq. (8.13) becomes $|A_{n,n+1,abs}(t)|^2 \approx I_{n,pop}(t)I_{n+1,pop}(t)$, which is obtained under the weak coupling assumption. To explicitly check its validity, we compare the decomposition relation with the exact results from the path integral calculations. To be specific, we expand Eqs. (8.28) and (8.29) in orders of $\langle \delta f^2 \rangle_b$,

$$|A_{ge,abs}(t)|^2 \approx 1 - 4(\alpha_{11} + \alpha_{22}) + 13(\alpha_{11} + \alpha_{22})^2$$
$$-12(\alpha_{11}\alpha_{22} - \alpha_{12}^2) + O(\langle \delta f^6 \rangle_b),$$
$$I_{g,pop}(t)I_{e,pop}(t) \approx 1 - 4(\alpha_{11} + \alpha_{22}) + 15(\alpha_{11} + \alpha_{22})^2$$
$$-16(\alpha_{11}\alpha_{22} - \alpha_{12}^2) + O(\langle \delta f^6 \rangle_b). \quad (8.30)$$

These two quantities are equal only up to first order in $\langle \delta f^2 \rangle_b$. For a harmonic oscillator linearly coupled to a classical bath, the diagonal coupling $V_D(t)$ is zero; hence, the only approximation introduced in Eq. (8.11) is the independent bath average for

each propagator. The difference $2(\alpha_{11}^2 + \alpha_{22}^2 + 2\alpha_{12}^2)$ between the two expressions in Eq. (8.30) is a quantitative measure of this assumption. The positive definite difference indicates that the decomposition relation over-estimates the absorption profile in the second order of $\langle \delta f^2 \rangle_b$.

The transition moments in Eq. (8.27) allow us to calculate the exact two-pulse photon echo (2PE) signal in Eq. (8.7) as

$$A_{echo}(t_1, t_2) = e^{i\omega_0(t_2-t_1)}(1 + \partial_{z_1})|_{z_1=1}(1 + \partial_{z_2})|_{z_2=1}[\det M(z_1, z_2)]^{-1/2} \qquad (8.31)$$

where the matrix $M(z_1, z_2)$ is

$$\begin{bmatrix} 1 + 2z_1\alpha_{11}(t_1, t_1) & 2z_1\alpha_{12}(t_1, t_1) & 2\sqrt{z_1 z_2}\alpha_{11}(t_1, t_2) & 2\sqrt{z_1 z_2}\alpha_{12}(t_1, t_2) \\ 2z_1\alpha_{12}(t_1, t_1) & 1 + 2z_1\alpha_{22}(t_1, t_1) & 2\sqrt{z_1 z_2}\alpha_{12}(t_2, t_1) & 2\sqrt{z_1 z_2}\alpha_{22}(t_1, t_2) \\ 2\sqrt{z_1 z_2}\alpha_{11}(t_1, t_2) & 2\sqrt{z_1 z_2}\alpha_{12}(t_2, t_1) & 1 + 2z_2\alpha_{11}(t_2, t_2) & 2z_2\alpha_{12}(t_2, t_2) \\ 2\sqrt{z_1 z_2}\alpha_{12}(t_1, t_2) & 2\sqrt{z_1 z_2}\alpha_{22}(t_1, t_2) & 2z_2\alpha_{12}(t_2, t_2) & 1 + 2z_2\alpha_{22}(t_2, t_2) \end{bmatrix}, \qquad (8.32)$$

with $\alpha_{ij}(t_1, t_2) = [2\mu\omega_0\hbar]^{-1} \int_0^{t_1} \int_0^{t_2} \langle f(\tau)f(\tau') \rangle_b \psi_i(\tau)\psi_j(\tau') d\tau d\tau'$ is defined similarly as in Eq. (8.28).

8.3.2 Perturbation

We now investigate the perturbation method. The diagonal matrix element of the propagator is given by

$$\langle n|e^{-iHt}|n\rangle = e^{-i\omega_n t}\langle n|\mathcal{T} \exp[-i\int_0^t f(\tau)q(\tau)d\tau]|n\rangle, \qquad (8.33)$$

where $q(t)$ is the time-dependent position operator in the interaction picture. We note that, because of $V_D(t) = 0$, the factorization in Eq. (8.10) becomes exact. We first neglect the cross terms between propagators and perform the bath average over each propagator separately, giving

$$A_{n,n+1,abs}(t) \approx e^{-i\omega_0 t}\langle\langle n+1|\mathcal{T}e^{-i\int_0^t f(\tau)q(\tau)d\tau}|n+1\rangle\rangle_b\langle\langle n|\mathcal{T}e^{-i\int_0^t f(\tau)q(\tau)d\tau}|n\rangle\rangle_b^\dagger. \ (8.34)$$

Next, we exchange the order of the bath average and the expectation value over vibrational states, and perform the second order cumulant expansion for the Gaussian bath,

$$
\begin{aligned}
A_{n,n+1,abs}(t) &\approx e^{-i\omega_0 t}\langle n+1| \exp\left[-\int_0^t \int_0^\tau q(\tau)q(\tau')\langle f(\tau)f(\tau')\rangle_b d\tau d\tau'\right]|n+1\rangle \\
&\quad \times \langle n| \exp\left[-\int_0^t \int_0^\tau q(\tau)q(\tau')\langle f(\tau)f(\tau')\rangle_b d\tau d\tau'\right]|n\rangle.
\end{aligned}
\tag{8.35}
$$

Finally, we take the expectation value of the exponent, which is only accurate when the exponent is diagonal, giving

$$
A_{n,n+1,abs}(t) \approx e^{-i\omega_0 t} \exp[-h_{n+1}(t) - h_n^*(t)],
\tag{8.36}
$$

where $h_n(t) = \frac{1}{\hbar^2}\int_0^t \int_0^\tau \langle f(\tau)f(\tau')\rangle_b \langle n|q(\tau)q(\tau')|n\rangle$ characterizes the population relaxation process from the nth vibrational state. For a harmonic oscillator, $h_n(t)$ can be evaluated explicitly to be $\mu\hbar\omega_0 h_n(t) = 2(n+1/2)\int_0^t d\tau \int_0^\tau d\tau' \langle f(\tau)f(\tau')\rangle_b \cos\omega_0(\tau - \tau')$. Particularly by setting $n = 0$ in this expression, we obtain the second order cumulant expansion result for $A_{ge,abs}(t)$,

$$
A_{ge,abs}(t) \approx e^{-i\omega_0 t} \exp[-2(\alpha_{11}(t) + \alpha_{22}(t))],
\tag{8.37}
$$

where $\alpha_{11}(t)$ and $\alpha_{22}(t)$ are defined in Eq. (8.28).

Compared to the exact path integral expression, the second order cumulant expansion is accurate up to first order in the bath fluctuation $\langle \delta f^2 \rangle_b$. The essential difference is the absence of the cross term α_{12} in the second order cumulant expression result. To facilitate the comparison with the exact expression, we expand the square of Eq. (8.37) to second order, giving

$$
|A_{ge,abs}|^2 = 1 - 4(\alpha_{11} + \alpha_{22}) + 8(\alpha_{11} + \alpha_{22})^2 + O(\langle \delta f^6 \rangle_b).
\tag{8.38}
$$

The overall deviation from the exact result is $5(\alpha_{11} + \alpha_{22})^2 - 12(\alpha_{11}\alpha_{22} - \alpha_{12}^2)$, which is a combination of all the approximations in Eqs. (8.34–8.36). It is readily shown

that this difference is positive definite, indicating that the second order cumulant expansion always under-estimates the absorption profile.

Applying the approximations in Eqs. (8.34–8.36) to Eq. (8.6), the population relaxation profile discussed in Sec. 8.2.1 is $I_{n,pop}(t) \approx |\exp[-h_n(t)]|^2$. Setting $n = 0$ and $n = 1$, we obtain the second order cumulant expansion of the population relaxation at the ground and the first excited states, respectively,

$$I_{g,pop}(t) \approx \exp[-(\alpha_{11}(t) + \alpha_{22}(t))] \quad \text{and} \quad I_{e,pop}(t) \approx \exp[-3(\alpha_{11}(t) + \alpha_{22}(t))]. \tag{8.39}$$

Combination of these two expressions leads to Eq. (8.37). These perturbative expressions, which neglect the cross terms among propagators and invoke separate bath averages of propagators, differ from the exact results in Eq. (8.29).

Similarly, the photon echo signal from the second order cumulant expansion can be derived as

$$A_{echo}(t_1, t_2) \approx e^{i\omega_0(t_2 - t_1)} \exp[-2(\alpha_{11}(t_1) + \alpha_{22}(t_1) + \alpha_{11}(t_2) + \alpha_{22}(t_2))], \tag{8.40}$$

where there is no contribution from pure dephasing. Again, this expression gives the correct expansion up to first order in bath fluctuations, thus is only applicable to weak solute-solvent interactions.

8.3.3 Markovian approximation

Under the Markovian approximation, the population relaxation profiles are given by $I_{n,pop}(t) \approx \exp[-\Re(\Gamma_n)t]$. For the dissipative harmonic oscillator, Γ_n is given as

$$\begin{aligned}
\Gamma_n &= 2 \int_0^\infty \langle n|\langle V_{OD}(t) V_{OD}(0)\rangle_b|n\rangle dt \\
&= 2 \int_0^\infty \langle f(t)f(0)\rangle_b (e^{-i\omega_0 t} q_{n,n+1}^2 + e^{i\omega_0 t} q_{n,n-1}^2) dt, \tag{8.41}
\end{aligned}$$

where $q_{n,n+1} = q_{n+1,n} = \sqrt{(n+1)\hbar/2\mu\omega_0}$ is the off-diagonal element of the position operator. In this limit, we readily work out the two population relaxation rates from

the ground state and the first excited state, respectively, yielding

$$\Gamma_g = k_g = \frac{\gamma}{\omega_0^2 + \gamma^2} \frac{\langle \delta f^2 \rangle_b}{\mu \hbar \omega_0}, \qquad \Gamma_e = k_e = \frac{\gamma}{\omega_0^2 + \gamma^2} \frac{3 \langle \delta f^2 \rangle_b}{\mu \hbar \omega_0}. \qquad (8.42)$$

Then, the average population relaxation rate is $k_{ge} = (k_g + k_e)/2$. It is straightforward to obtain the absorption profile and the echo signal at the Markovian limit

$$
\begin{aligned}
A_{ge,abs}(t) &\approx e^{-i\omega_0 t} \exp[-\frac{\Gamma_g + \Gamma_e}{2} t] \\
A_{echo}(t_1, t_2) &\approx e^{i\omega_0(t_2 - t_1)} \exp\left[-\frac{\langle \delta f^2 \rangle_b}{\mu \hbar \omega_0} \frac{\gamma(t_1 + t_2)}{\omega_0^2 + \gamma^2} \right].
\end{aligned} \qquad (8.43)
$$

8.3.4 Numerical results and discussions

To demonstrate the differences between the non-perturbative and perturbative approaches, we calculate the vibrational line shapes for a dissipative harmonic oscillator described by the Hamiltonian in Eq. (8.25). The results are plotted in Fig. 8-1, 8-2 and 8-3. To facilitate the comparison with the Morse potential discussed in Sec. 8.4, we take the same frequency in reduced unit, $\omega_0 = 120$, and the same effective mass in reduced unit, $\mu = 0.5$, which were used in simulations by Tuckerman, Bader and Berne.[180, 181] The effective $\hbar$ is 0.029534. The friction kernel of the bath fluctuation is assumed to be single exponential, i. e. , $\langle \delta f(t) \delta f(0) \rangle = \langle \delta f^2 \rangle_b \exp[-\gamma|t|]$, which is a simplified description of environmental fluctuations. The decay rate $\gamma = 10$ is 1/12 of the reduced frequency and the mean square fluctuation of the random force is $\langle \delta f^2 \rangle = 0.3 \mu \hbar \omega_0^3$.

Non-Markovian effects of VER

In Fig. 8-1, we illustrate the absorption profile $A_{ge,abs}(t)$ and its Fourier transforms $A_{ge,abs}(\omega) = \text{Re} \int_0^\infty e^{i\omega t} A_{ge,abs}(t) dt$ from the path integral method in Eq. (8.28), the second order cumulant expansion in Eq. (8.37), and the Markovian approximation in Eq. (8.43). As indicated in Sec. 8.3.2, the perturbative and the exact results are identical up to first order in the bath fluctuation $\langle \delta f^2 \rangle_b$. The perturbative approach
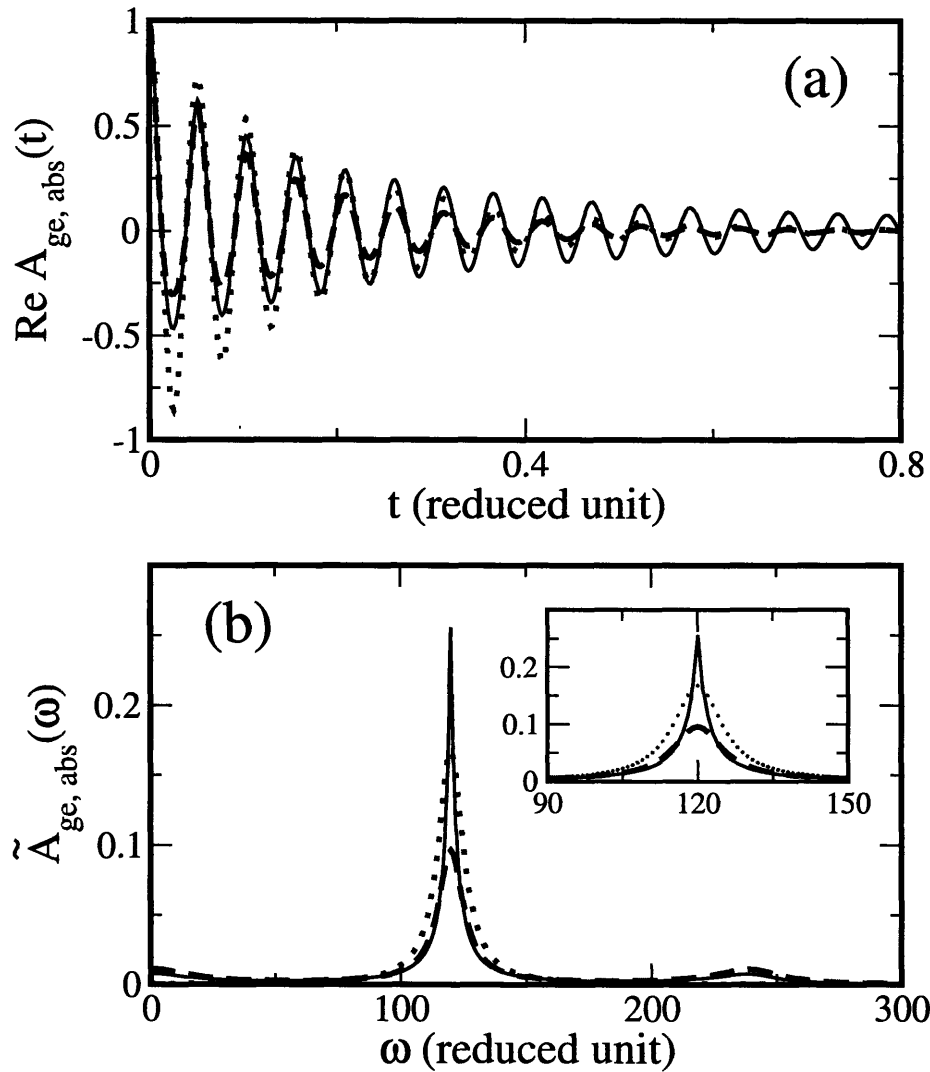
Figure 8-1: Comparison of the temporal absorption profile of the dissipative harmonic oscillator calculated with the exact path integral expression in Eq. (8.28) (solid line), the second order cumulant expansion in Eq. (8.37) (dashed line), and the Markovian approximation in Eq. (8.43) (dotted line). The corresponding frequency domain line shapes are given in the lower panel (b) with the details of the central peak in the inset. The parameters are $\omega_0 = 120$, $\gamma = 10$, and $\langle \delta f^2 \rangle_b = 0.3\mu\hbar\omega_0^3$.
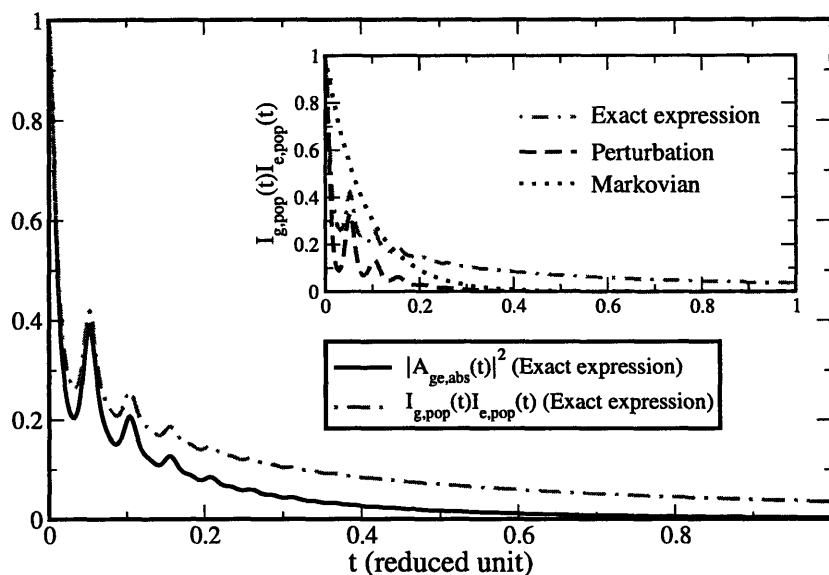
Figure 8-2: Examination of the decomposition relation given by Eq. (8.13) for the dissipative harmonic oscillator. The exact results, the cumulant expansion, and the Markovian approximation of the VER signal $I_{g,pop}I_{e,pop}$ are shown in the inset. The parameters are the same as in Fig. 8-1. For a linearly coupled harmonic oscillator , there is no pure dephasing, $|A_{ge,dep}(t)|^2 = 1$.

only provides qualitative agreements and does not reproduce the line shape quantitatively. The Markovian approximation only captures the overall decay of the absorption profile. In the long time limit, both perturbation and Markovian approximation yield exponential decaying envelops for the absorption amplitude with the decay rate $k_{ge} = (k_g + k_e)/2$, whereas the exact result gives a power-law decaying envelop of t^{-2} (see Sec. 8.3.1). Hence, the exact result is more coherent than the perturbative and the Markovian approximations. This difference becomes more prominent for stronger solute-solvent interactions.

As shown in Fig. 8-1, both the non-perturbative and the second order cumulant expansion results have asymmetric envelops while the Markovian result is symmetric. This non-Markovian effect is an important feature of VER effects. To illustrate this point, we examine the seconder order cumulant expansion expression for the population relaxation in Eq. (8.39). The exponent of the population relaxation profile

is an incomplete Fourier transform of the friction kernel at the fundamental frequency, giving

$$2(\alpha_{11}(t) + \alpha_{22}(t)) \;=\; \frac{\langle \delta f^2 \rangle_b}{2\mu\omega_0\hbar} \left[\frac{\omega_0^2 - \gamma^2}{(\omega_0^2 + \gamma^2)^2} + \frac{\gamma t}{\omega_0^2 + \gamma^2} \right.$$
$$\left. - \frac{(\omega_0^2 - \gamma^2)\cos\omega_0 t - 2\omega_0\gamma\sin\omega_0 t}{(\omega_0^2 + \gamma^2)^2} e^{-\gamma t} \right] . \qquad (8.44)$$

Equation (8.44) is intrinsically oscillatory with the fundamental frequency ω_0. As a result, the absorption amplitude is smaller on the negative side than on the positive side, generating an asymmetric temporal profile. Under the Markovian approximation, the exponent is simplified to be linear in time. Then, the oscillatory feature is completely removed, yielding a symmetric profile. Apparently the exponent is proportional to the mean square fluctuation of the bath, $\langle \delta f^2 \rangle_b$, and the asymmetry is more prominent for stronger solute-solvent interactions.

The asymmetric feature is also demonstrated in the Fourier spectrum. The exact and the second order cumulant expansion results show small side bands at zero frequency and the second harmonic frequency while the Markovian approximation is a perfect Lorentzian. These side bands are generated by the oscillations in the exponent. To illustrate this point, we further expand the perturbative expression of Eq. (8.37), yielding

$$A_{ge,abs}(t) \;\approx\; e^{-i\omega_0 t} \exp\left[-\frac{2\langle \delta f^2 \rangle_b(\omega_0^2 - \gamma^2)}{\mu\omega_0\hbar(\omega_0^2 + \gamma^2)^2} - \frac{\Gamma_g + \Gamma_e}{2}t \right] \sum_{n=0}^{\infty} \frac{(-1)^n}{n!}$$
$$\left(\frac{\langle \delta f^2 \rangle_b}{\mu\omega_0\hbar(\omega_0^2 + \gamma^2)^2} e^{-\gamma t}[(-\omega_0^2 + \gamma^2)\cos\omega_0 t - 2\gamma\omega_0\sin\omega_0 t] \right)^n . \quad (8.45)$$

After collecting the Fourier components at zero, the first and the second harmonic frequencies, we identify several features in the absorption line shape:

1. The central peak at ω_0 is a Lorentzian with width equal to the dephasing rate k_{ge}.

2. The peaks at $\omega = 0$ and $2\omega_0$ are slightly asymmetric with width $k_{ge} + \gamma$.

235

3. In the limit $\omega_0 \gg \gamma$, the ratio of the peak at $2\omega_0$ (or zero frequency) to the major peak at ω_0 is directly proportional to the dimensionless bath fluctuations,

$$\frac{\tilde{A}(2\omega_0)}{\tilde{A}(\omega_0)} = \frac{\tilde{A}(0)}{\tilde{A}(\omega_0)} \approx \frac{\langle \delta f^2 \rangle_b}{\mu \hbar \omega_0^3} \frac{k_{ge}}{k_{ge} + \gamma}. \tag{8.46}$$

The Markovian approximation neglects the constant term $-2\langle \delta f^2 \rangle_b (\omega_0^2 - \gamma^2)/\mu\omega_0\hbar(\omega_0^2 + \gamma^2)^2$ in the exponent and generates a higher peak at $\omega = \omega_0$ than the second order cumulant expansion. The quantitative relations in (1) and (2) provide a possible way to measure the two parameters, $\langle \delta f^2 \rangle$ and γ, of the bath fluctuations.

Non-Lorentzian line shapes

Compared to the exact result of non-perturbative calculations, the absorption spectrum from the second order cumulant expansion reproduces the line shapes at $\omega = 0$, ω_0 and $2\omega_0$. Yet, the central peak of the exact spectrum at ω_0 is substantially different from a Lorentzian. Given the long time power-law decay profile of the exact absorption profile, $A_{ge,abs}(t) \approx e^{-i\omega_0 t}(1 + \Gamma_{ge}t/2)^{-2}$ with $\Gamma_{ge} = k_{ge}$, the central peak is a Meijer G-function and has a height of $2/k_{ge}$ and a width of $k_{ge}/2$. The non-Lorentzian absorption spectrum was also obtained by Kosloff and Rice from dynamical semigroup techniques that go beyond the weak coupling limit.[195] In their analysis, the non-Lorentzian peak is attributed to double quantum transition resulting from the quadratic system-bath coupling where both population and pure dephasing are present. Apparently, the dissipative harmonic oscillator discussed in the present chapter is linearly coupled to the bath without pure dephasing contribution; hence, the non-Lorentzian shape we obtained results from couplings of population relaxations. This is a new interpretation of the absorption line shape.

The non-Lorentzian line shapes are also obtained in the photon echo profile. Fig. 8-3 is a comparison of the time domain echo signals and their frequency domain line shapes. The two time domain echo signals in the left column are obtained from the non-perturbative path integral method and the second order cumulant expansion, respectively. The line shapes in the right column are the corresponding absolute
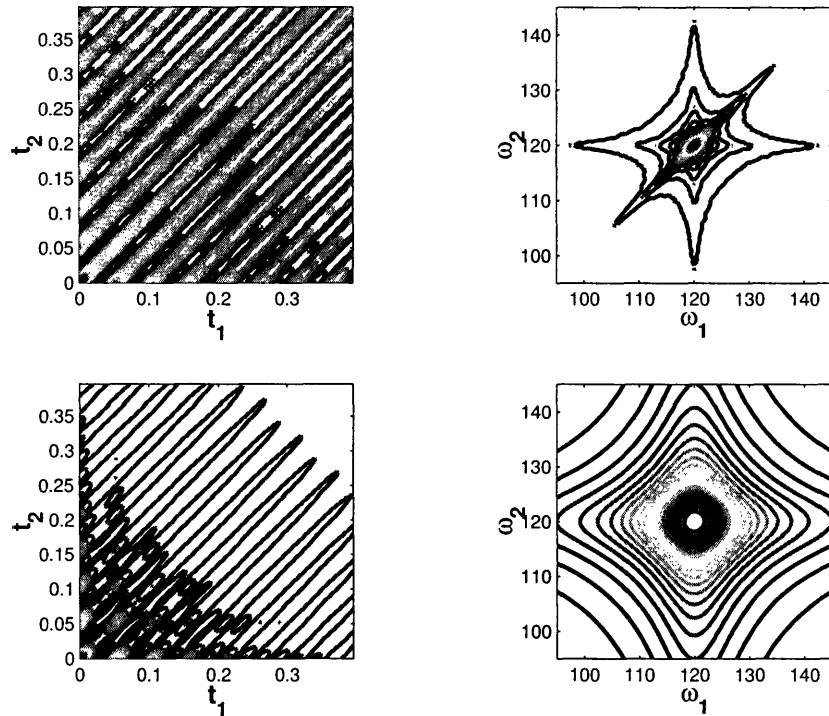
Figure 8-3: The time domain echo signals (in the left column) and their frequency domain contours (in the right column) for the dissipative harmonic oscillator. From top to bottom, the plots are the non-perturbative calculation and the second order cumulant expansion, respectively. The parameters used in the calculations are the same as in Fig. 8-1.

value spectra obtained from[189]

$$|A_{echo}(\omega_1, \omega_2)| = \left| \int_0^\infty \int_0^\infty e^{i\omega_1 t_1 - i\omega_2 t_2} A_{echo}(t_1, t_2) dt_1 dt_2 \right|. \tag{8.47}$$

The second cumulant expansion has a symmetric 2D Lorentzian line shape and is almost identical to the Markovian line shape (not shown in Fig. 8-3). The close resemblance in the 2D Fourier spectra indicates the same long time behavior for both approximations. The exact result, as shown in the absorption profile, decays in a power-law form of t^{-2} at long times. The Fourier spectrum shows a much wider distribution along the diagonal direction than the anti-diagonal direction. In the dissipative harmonic oscillator we discussed here, the pure dephasing rate is zero, hence the elongated line shape along the diagonal direction can only result from population

relaxation, which is different from the pure-dephasing induced broadening discussed in the literature.[159] Compared to linear absorption spectrum, the nonlinear photon echo is much more sensitive to the non-perturbative effects.

Decomposition relation: Comparison of different approximations for VER

In Fig. 8-2, the decomposition relation in Eq. (8.13) is examined for the same parameter as those in Fig. 8-1. As we discussed in Sec. 8.3.1, the decomposition expression, obtained with the factorization approximation, is only accurate up to first order in $\langle \delta f^2 \rangle_b$ and over-estimates the absorption intensity. This is clearly indicated by the deviation of $I_{n,pop}(t)I_{n+1,pop}(t)$ from $|A_{n,n+1,abs}(t)|^2$. Compared to the exact result, the factorization approximation reproduces the short-time oscillations correctly and exhibits a slower decay profile in the long time. Hence, the composite approximation scheme of Eq. (8.19) in Sec. 8.2.2 over-estimates the absorption profile. The second-order cumulant expansion of the VER contribution derive in Eq. (8.39) clearly under-estimates the absorption profile and decays faster than the exact result. The Markovian approximation is appropriate only for an estimation of the decay rate. Consequently, the composite approximation scheme of Eq. (8.23) reduces to the Markovian approximation in the absence of pure dephasing, and fails to capture any non-Markovian features of VER. For the case of anharmonic potentials investigated later in Sec. 8.4, the pure dephasing profile imposes a monotonic decaying envelop, where Eq. (8.19) agrees better with the exact result.

These calculations clearly demonstrate the limitations of the perturbative approach and the Markovian approximation. The perturbative expressions, which are obtained under the assumption of weak solute-solvent interactions, can provide a qualitative description of vibrational line shapes, but can not accurately reproduce the details. The Markovian approximation over-simplifies the time-dependence with simple relaxation rates, and fails to capture the VER effects. That is why a more rigorous non-perturbative approach is important and necessary for studying vibrational line shapes in condensed phases.
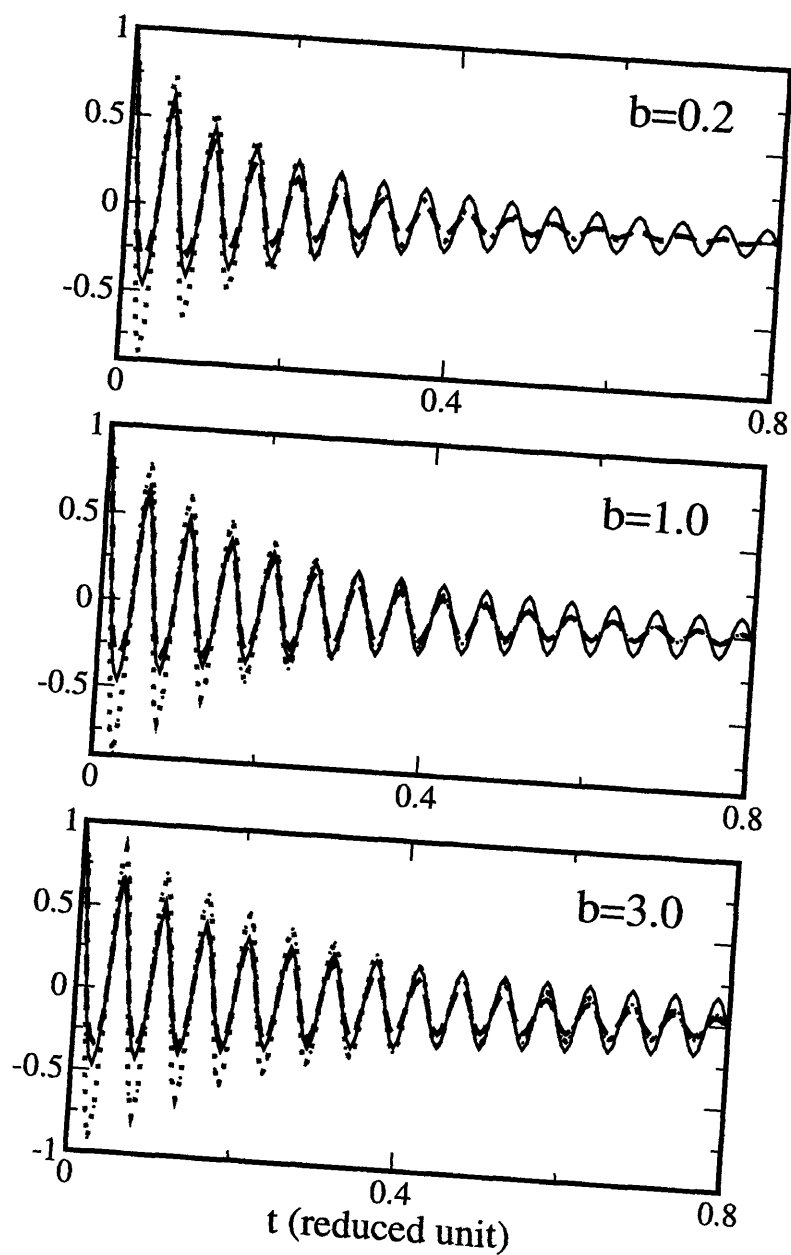
Figure 8-4: Comparison of $\mathrm{Re}A_{ge,abs}(t)$ calculated with the exact path integral expression (solid line), the second order cumulant expansion (dashed line), and Markovian approximation (dotted line) for the dissipative harmonic oscillator coupled to a quantum Gaussian bath. $b = \beta\hbar\omega_0$ is the temperature parameter. The real part of the quantum force-force correlation is the same as in Fig. 8-1, and the imaginary part is given by $-i\tilde{C}_2(\omega) = \tanh(\beta\hbar\omega_0/2)\tilde{C}_1(\omega)$. The high temperature limit $\beta\hbar\omega_0 \to 0$ is Fig. 8-1a.

239

8.3.5 Quantum bath

To demonstrate the quantum effects, we plot several absorption profiles in Fig. 8-4 and compare with the classical results. The details of the derivation are elaborated in Appendix 8-B. Here we set the real part of the quantum force-force correlation equal to the classical force-force correlation function used in Fig. 8-1, i. e. , $C_1(t) = \langle \delta f^2 \rangle_b \exp[-\gamma|t|]$, and assume the same parameters therein. The Fourier transform of $C_1(t)$ is $\tilde{C}_1(\omega) = 2\gamma \langle \delta f^2 \rangle_b / (\omega_0^2 + \gamma^2)$, and the imaginary part of the quantum force-force correlation function is determined from Eq. (8.69),

$$C_2(t) = \frac{1}{\pi} \int_0^\infty \tanh \frac{\beta \hbar \omega_0}{2} \tilde{C}_1(\omega) \sin \omega t d\omega. \tag{8.48}$$

As shown in Fig. 8-4, the quantum absorption profiles are generally more coherent than the classical ones in the long time limit and have weaker effects on the short time profile. The perturbative approach yields closer resemblance to the exact result at lower temperatures. The asymmetry in the absorption profile from the vibrational energy relaxation remains prominent for quantum baths.

8.4 Dissipative Morse oscillator: a numerical example

Let us now consider a numerical example of anharmonic potentials and investigate the vibrational line shapes for a Morse oscillator linearly coupled to a Gaussian bath. The full Hamiltonian is given by

$$H = \frac{p^2}{2\mu} + D_e(1 - e^{-\beta q})^2 + f(t)q, \tag{8.49}$$

where D_e is the dissociation energy. Again the classical bath is represented by a Gaussian random force $f(t)$ and the bath relaxation is characterized by the friction kernel $C_{cl}(t) = \langle f(t)f(0) \rangle_b$. For simplicity, we study the transition between the ground and first excited states. To facilitate the comparison with early studies in

literature,[181] the Lennard-Jones fluid of Argon are used as the reference units with parameters $\epsilon/k_B = 120K$, $m = 6.632 \times 10^{-26}Kg$ and $\sigma = 3.41\text{Å}$. In these units, the dissociation energy is $D_e = 207.36\epsilon = 2.15$ eV. The diatomic molecule consists of two atoms with the same mass as Argon coupled by a Morse potential, giving the effective mass $\mu = 0.5m = 20.0$ amu. $\beta = 4.167\sigma^{-1} = 1.22$ Å^{-1}, and the fundamental frequency $\omega_0 = \sqrt{2D_e\beta^2/\mu} = 120\sqrt{\epsilon/m\sigma^2} = 296$ cm^{-1}. $\hbar$ in the reduced unit is $\hbar^* = \hbar(m\sigma^2\epsilon)^{-1/2} = 0.029534$. To compare the non-perturbative and perturbative approaches, we calculate the vibrational line shapes for a solute-solvent interaction of $\langle \delta f^2 \rangle_b = 0.3\mu\hbar\omega_0^3$. The bath relaxation is an exponential $C_{cl}(t) = \langle \delta f^2 \rangle_b e^{-\gamma t}$ with $\gamma = 10$.

The perturbative absorption profile with second order cumulant expansion is given in Eq. (8.17), and the pure dephasing and population relaxation cumulants are

$$
\begin{aligned}
g(t) &= \frac{1}{\hbar^2} \int_0^t \int_0^\tau \langle \delta f(\tau) \delta f(\tau') \rangle_b (\langle q \rangle_{n+1} - \langle q \rangle_n)^2 d\tau d\tau', \\
h_n(t) &= \frac{1}{\hbar^2} \int_0^t \int_0^\tau \langle \delta f(\tau) \delta f(\tau') \rangle_b \sum_{m\neq n} q_{nm}^2 e^{i\Omega_{mn}(\tau-\tau')} d\tau d\tau',
\end{aligned}
\tag{8.50}
$$

where q_{nm} is the matrix element of q. In the Markovian limit, Eq. (8.17) reduces to $A_{n,n+1,abs}(t) \approx e^{-i\Omega_{n,n+1}t} \exp[-\Gamma'_{n,n+1}t - \frac{1}{2}(\Gamma_n + \Gamma_{n+1})t]$, where $\Gamma'_{n,n+1}$ and Γ_n are the pure dephasing rate and the population relaxation rate given by

$$
\begin{aligned}
\Gamma'_{n,n+1} &= \frac{(\langle q \rangle_{n+1} - \langle q \rangle_n)^2}{\hbar^2} \int_0^\infty \langle \delta f(\tau) \delta f(0) \rangle_b d\tau \\
\Gamma_n &= \sum_{m\neq n} \frac{2q_{nm}^2}{\hbar^2} \int_0^\infty \langle \delta f(\tau) \delta f(0) \rangle_b e^{i\Omega_{mn}\tau} d\tau.
\end{aligned}
\tag{8.51}
$$

8.4.1 Asymmetric envelops in the temporal absorption profile

As shown in Fig. 8-5a, the second order cumulant expansion illustrates the presence of asymmetric signals at short times but fails to reproduce the long time decaying envelop. Similar to the dissipative harmonic oscillator studied in Sec. 8.3, the ap-
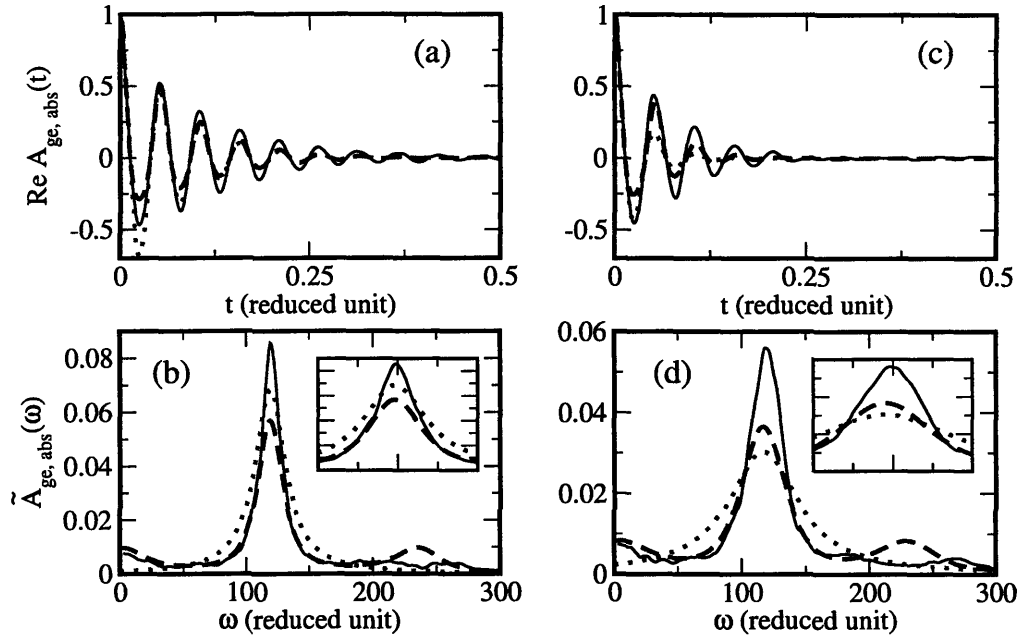
Figure 8-5: Absorption line shapes of the dissipative Morse oscillator calculated with the non-perturbative method (solid line), the second order cumulant expansion (dashed line), and the Markovian approximation (dotted line). The solvent relaxation rate is assumed to be $\gamma = 10$. The solute-solvent interaction is $\langle \delta f^2 \rangle_b = 0.3 \mu \hbar \omega_0^3$. At anharmonicity $\chi_e = 0.00427$ in (a) and (b), the dissociation threshold is $D_e = 58.5 \omega_0$ and the fundamental frequency $\omega_0 = 120$. At anharmonicity $3\chi_e$ in (c) and (d), the dissociation energy is $D_e/3$ but μ and ω_0 remain the same.

pearance of asymmetry in the absorption profile clearly demonstrates the VER effects from the off-diagonal elements of the solute-solvent interaction. For the exponential frictional kernel, $g(t)$ and $h_n(t)$ are evaluated explicitly as

$$
g(t) = \frac{\langle \delta f^2 \rangle_b}{\hbar^2} (q_{n+1,n+1} - q_{nn})^2 \frac{\gamma t - 1 + e^{-\gamma t}}{\gamma^2}
$$

$$
h_n(t) = \frac{\langle \delta f^2 \rangle_b}{\hbar^2} \sum_{m \neq n} q_{nm}^2 \left[\frac{\Omega_{mn}^2 - \gamma^2}{(\Omega_{mn}^2 + \gamma^2)^2} + \frac{\gamma t}{\Omega_{mn}^2 + \gamma^2} \right.
$$
$$
\left. - \frac{(\Omega_{mn}^2 - \gamma^2) \cos \Omega_{mn} t - 2 \Omega_{mn} \gamma \sin \Omega_{mn} t}{(\Omega_{mn}^2 + \gamma^2)^2} e^{-\gamma t} \right] . \tag{8.52}
$$

242

According to Eq. (8.52), the pure dephasing profile decays monotonically while the VER profile is an oscillatory function. The bath relaxation rate is significantly smaller than the energy gap, i. e., $\gamma \ll \omega_0$, and the vibrational energy gap falls far into the tail of the spectral density of bath relaxation. The pure dephasing rate is equivalent to a Fourier transform with zero frequency, and is located at the center of the spectral density of bath relaxation. Consequently, the pure dephasing rate is much larger than the population relaxation rate in the long time limit. At short times, $h_n(t)+h_{n+1}(t) \gg g(t)$; hence, the VER dominates at short times and the asymmetric envelop becomes more prominent. The Markovian approximation employs simple rate approximation and completely removes the oscillatory feature in population relaxation and produces a symmetric profile over the complete time range.

The absorption spectrum of the Markovian approximation illustrated in Fig. 8-5b, has a symmetric Lorentzian line shape from the simple rate approximation. The perturbation renders side bands at zero and the second harmonic frequencies in addition to the central peak. This is a direct result of the asymmetric VER signal at short times. The side bands are solvent-induced multiple-photon transitions which are absent in the Markovian VER treatment. Apparently, the exact result has a non-Lorentzian central peak, differing from the Markovian approximation. Yet, the non-Lorentzian central peak is not as sharp as that of a dissipative harmonic oscillator in Fig. 8-1. This difference results from the dominant contribution of pure dephasing, which is absent in a harmonic oscillator. Pure dephasing profile, when superimposed onto population relaxation profile, generates an exponentially decaying envelop in the long time and results in a less sharp non-Lorentzian peak.

8.4.2 Asymmetric central peak in absorption spectrum

In addition to the non-Lorentzian peak and side bands, the non-perturbative calculation demonstrates an asymmetric central peak in frequency domain. Absence of these features from the perturbative and Markovian approximations indicates that they arise from neglected term in the factorization of perturbative approach. Careful investigation of the approximations in Sec. 8.2.2 reveals that the source of this asymmetry is
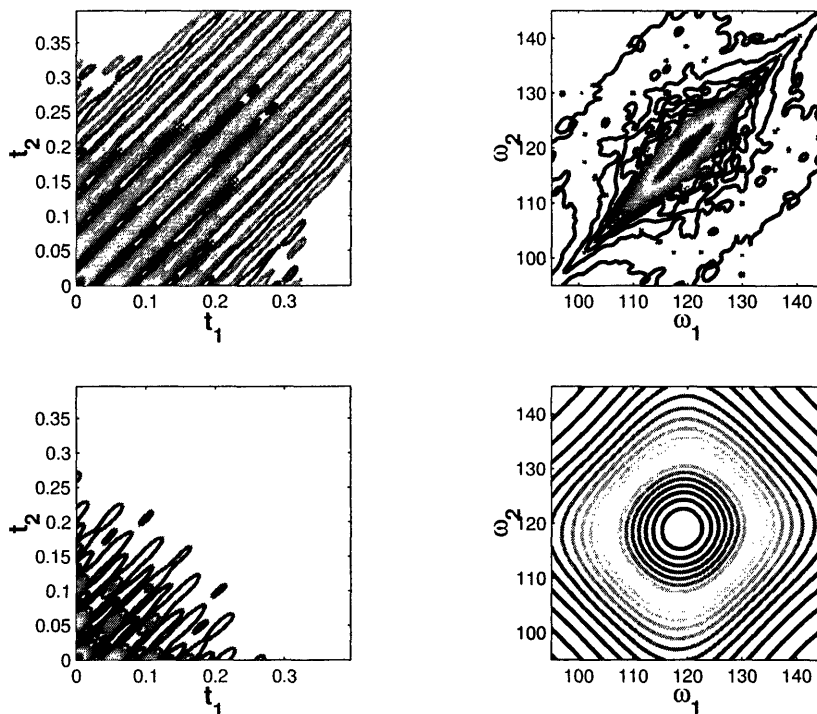
Figure 8-6: The time domain echo signals (in the left column) and their frequency domain contours (in the right column) for the dissipative Morse oscillator. From top to bottom, the plots are the non-perturbative calculation and the second order cumulant expansion, respectively. The parameters used in the calculations are the same as in Fig. 8-5a and Fig. 8-5b.

the cross products of the off-diagonal coupling, $\langle\langle V_{OD}(t_1)V_{OD}(t_2)\rangle_n\langle V_{OD}(t_1)V_{OD}(t_2)\rangle_{n+1}\rangle_b$. For an anharmonic potential, the frequency gaps Ω_{mn} are not identical, the frequency mismatch generates a complex envelop function, while the negligence of cross products in the perturbative and the Markovian approximations only yields a real envelop. The presence of the imaginary part of the envelop function creates interferences of difference frequency components, giving an asymmetric profile. As anharmonicity increases, the frequency mismatch becomes larger and thus the interference becomes stronger, yielding more asymmetric central peaks, as shown in Fig. 8-5d. Apparently, the cross product of the off-diagonal coupling is proportional to $\langle\delta f^2\rangle_b^2$ and depends strongly on the strength of bath fluctuations. In Sec. 8.5, the O-H stretch has a much
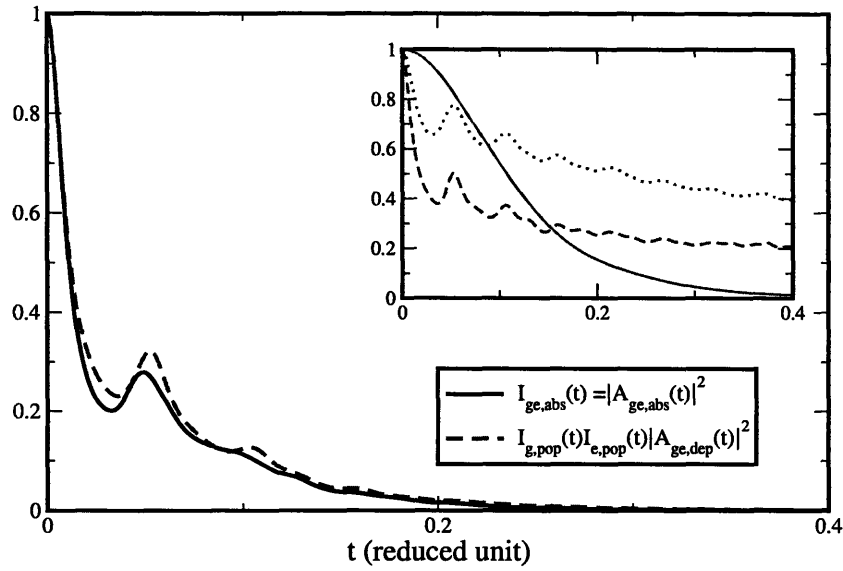
Figure 8-7: Examination of the decomposition relation in Eq. (8.13) for the dissipative Morse potential. Inset: The decomposed signals $I_{g,pop}(t)$ (dotted line) $I_{e,pop}(t)$ (dashed line) and $|A_{ge,dep}(t)|^2$ (solid line). $A_{ge,abs}(t)$, $I_{g,pop}(t)$ and $I_{e,pop}(t)$ are the exact results calculated numerically with the same parameters as those in Fig. 8-5a and Fig. 8-5b.

weaker coupling to the bath than the Morse oscillator calculated in this section, and demonstrates a less prominent asymmetric absorption spectrum.

The asymmetric and non-Lorentzian line shape is better manifested in the nonlinear two-pulse photon echo (2PE) profile. As shown in Fig. 8-6, the exact result shows a strong asymmetric elongation along the diagonal, and is significantly different from the Lorentzian line shape predicted by the second order cumulant expansion and the Markovian approximations. The Markovian approximation has identical line shapes as the second order cumulant expansion and is not included here to avoid redundancy. Small irregular structures in the exact line shape is due to insufficient averaging in Monte Carlo simulation.

245

8.4.3 Decomposition relation: Anharmonic effects

To check the decomposition relation, we calculate $I_{ge,abs}(t) = |A_{ge,abs}(t)|^2$ and compare it with the product of $I_{g,abs}(t)$, $I_{e,abs}(t)$ and $|A_{ge,dep}(t)|^2$. Due to the presence of anharmonicity, the absorption profile is dominated by pure dephasing in the long time limit, so that the factorization result yields close resemblance to the non-perturbative absorption profile, displayed in Fig. 8-7. The initial decay, the major oscillation at $t \approx 0.05$, and the long time relaxation are closely predicted by the factorization scheme. The similarity between the absorption intensity and the decomposed signal indicates the applicability of the approximation scheme of Eq. (8.19) introduced in Sec. 8.2.4, which directly superimposes the population relaxation profile measured from pump-probe experiments onto the pure dephasing profile. This approach is different from the cumulant approximation where both the population relaxation and the pure dephasing are truncated at the second-order cumulant. Consequently, the absorption spectrum is no longer a Lorentzian shape. As we discussed earlier in Sec. 8.2.4, due to the omission of imaginary part of the population relaxation signal, the composite approximation scheme can not reproduce the asymmetric central peak of the absorption spectrum.

To investigate the anharmonic effects, we compare the absorption intensity and the pure dephasing signal at $\chi_e = \hbar\omega_0/4D_e$, $2\chi_e$ and $3\chi_e$ in Fig. 8-8 with ω_0 and μ fixed. The position operator q of a Morse oscillator is[204, 205]

$$q \approx -\frac{1}{\beta}\ln[1 - \sqrt{\chi_e}(b + b^\dagger)] \approx \frac{\hbar}{2\mu\omega_0}\left[(b + b^\dagger) + \sqrt{\chi_e}(b + b^\dagger)^2\right], \qquad (8.53)$$

where b and $b^\dagger$ are the creation and annihilation operators of the Morse oscillator, respectively, and $\chi_e = [8D_e\mu/(\hbar^2\beta^2)]^{-1/2}$ is the anharmonicity parameter. The spectrum of the Morse oscillator is $E_n = \hbar\omega_0[(n + 1/2) - \chi_e(n + 1/2)^2]$, with $1/(2\chi_e)$ the number of bounded states in the potential well. For the Morse oscillator discussed here, $\chi_e \approx 0.00427$. The population relaxation rate is much smaller than the pure dephasing rate due to the large difference between the frequency gap and the bath relaxation rate. Furthermore, the ratio between V_D and V_{OD} is proportional to
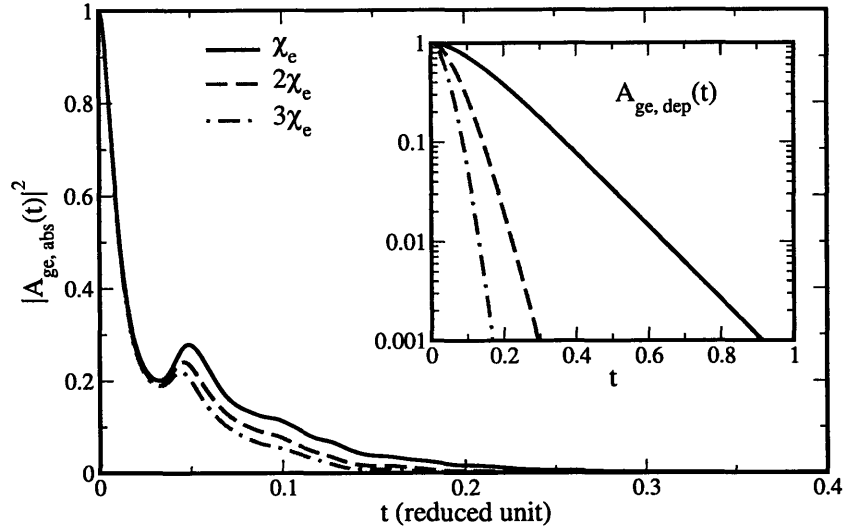
Figure 8-8: The non-perturbative absorption amplitude $|A_{ge,abs}(t)|^2$ and the pure dephasing profile $A_{ge,dep}(t)$ for different anharmonicities of a dissipative Morse potential. Other parameters such as ω_0, μ, γ and $\langle \delta f^2 \rangle_b$ remain the same as previous calculations.

$\sqrt{\chi_e}$. With increasing anharmonicity, the contribution from pure dephasing becomes dominant; hence, the short time oscillatory feature from the population relaxation is further suppressed and the absorption profile decays faster.

8.4.4 VER effects as a function of anharmonicity

We now examine the different perturbation schemes of VER and compare the absorption profiles at three different anharmonicities, χ_e, $2\chi_e$ and $3\chi_e$ in Fig. 8-9. The approximations employed in the second order cumulant expansion include decoupling of the diagonal V_D and the off-diagonal V_{OD}, independent bath averages of propagators, and cumulant expansion, which are discussed in detail in Sec. 8.2.2 and 8.3.2. The factorization propagator in Eq. (8.10) neglects the commutator between $V_D(t)$ and $V_{OD}(t)$. For the linear coupling, the commutator can be estimated explicitly as

$$[V_D(\tau), V_{OD}(\tau')] \propto f(\tau)f(\tau')\frac{\hbar}{2\mu\omega_0} \sqrt{\chi_e}. \tag{8.54}$$
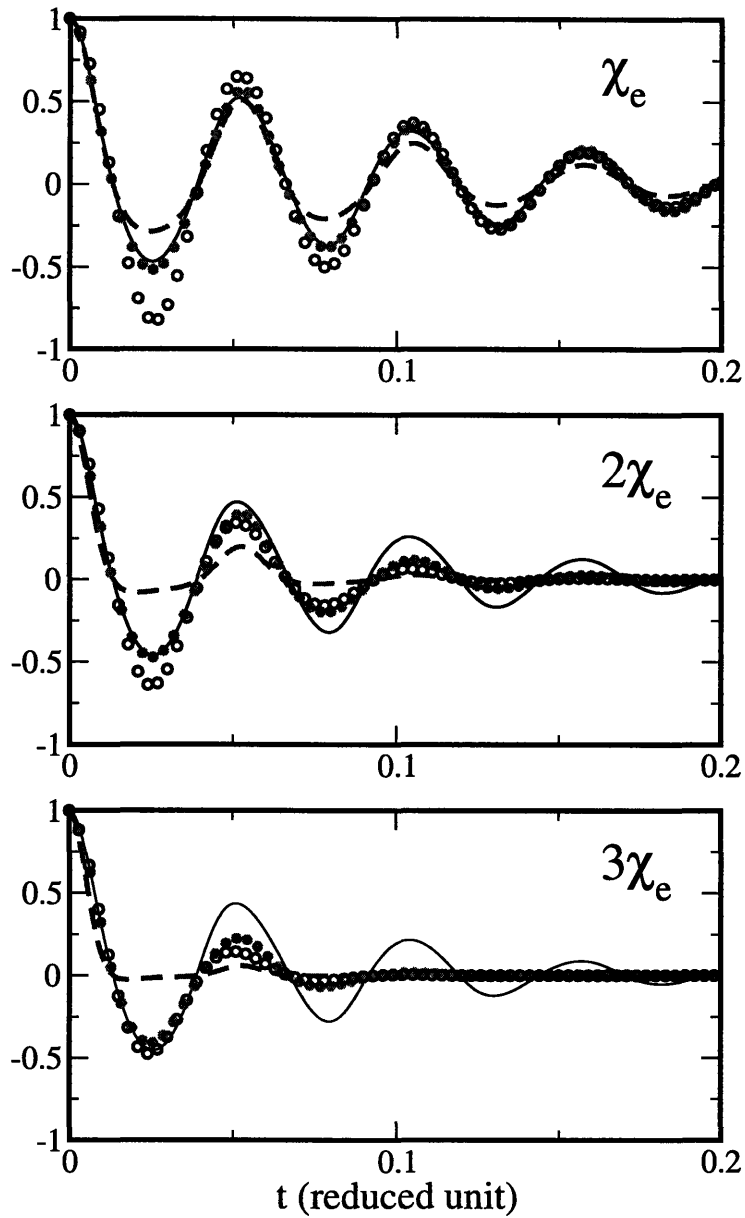
Figure 8-9: Comparison of the non-perturbative calculation in Eq. (8.3), the second order cumulant expansion in Eq. (8.17), and the two composite approximation schemes in Eq. (8.19) and Eq. (8.23) at different anharmonicities. Other parameters such as ω_0, μ, γ and $\langle \delta f^2 \rangle_b$ remain the same as previous calculations. The exact results of the non-perturbative calculation are plotted in solid lines, the second order cumulant expansion in dashed lines, Eq. (8.19) in solid circles, and Eq. (8.23) in open circles.

and is proportional to the square root of the anharmonicity. The negligence of this term significantly reduces the accuracy of the perturbative approximation at large anharmonicities. Furthermore, the commutator term includes the off-diagonal coupling, and is oscillatory. Similar to the population relaxation term, the commutator term contributes significantly at short times and the contribution increases with anharmonicity. The non-perturbative signal, which includes the commutator $[V_D(t), V_{OD}(t)]$ and cross terms between different propagators, is generally more coherent than the perturbative approximations. The difference between the non-perturbative and the perturbative results becomes more prominent at larger anharmonicities.

The composite approximation of Eq. (8.19) superimposes the population relaxation profile from pump-probe experiments onto the pure dephasing, and accurately reproduces the asymmetric temporal profile at small anharmonicities. With increasing anharmonicity, the cross products of the off-diagonal couplings and diagonal couplings neglected from the decomposition in Eq. (8.19) contribute substantially to absorption profile. Hence, the deviation from the exact result increases with anharmonicity. The composite approximation of Eq. (8.23) assumes a Markovian rate for VER and yields a symmetric absorption profile. For the anharmonicities we studied, Eq. (8.23) does not work as well as Eq. (8.19). The strong deviations of the approximation schemes from the exact result at large anharmonicities justify the need for the non-perturbative treatment of vibrational line shapes.

8.5   O-H stretch in D_2O environments

Now we demonstrate the importance of VER effects in a real system. The parameters of several VER systems are estimated and listed in Table 8.1. The dimensionless bath fluctuation is estimated from simulations and frequency gap fluctuations assuming a Morse potential and a linear system-bath coupling. Although real systems include vibration-rotation couplings, intermolecular couplings, and other effects, the linear coupling assumed in our model still serves as a quantitative estimation of the VER effects. To illustrate the detailed contributions from VER, we perform a series of

249

Table 8.1: Relevant parameters of several VER systems.

	$O-H^a$	$O-D^b$	$I_2{}^c$	$C-O$ stretch^d	$HbCO^e$	HgI^f
Ω_{01} (cm^{-1})	3400	2500	210.9	1714.4	1950	125
Ω_{12} (cm^{-1})	3150	2350	207.2	1706.3	1924	-
$\langle \delta f^2 \rangle_b/(\mu\hbar\omega_0^3)$	0.0162	0.0148	0.0313	0.064	0.029	0.068
γ_1^{-1} (fs)	~ 60	~ 30	~ 2500	3.4	500	65
γ_2^{-1} (fs)	~ 1200	~ 500	-	100	1200	-

^{a}O $-$ H stretch in liquid D$_2$O in Refs. [206] and [207]. $\langle \delta f^2 \rangle_b$ is extracted from frequency gap fluctuations.

^{b}O $-$ D stretch in liquid H$_2$O in Ref. [208]. $\langle \delta f^2 \rangle_b$ is extracted from force-force correlation function simulation.

^{c}I$_2$ in Xenon solvent at 313 K and 3.0 g/cm^3 in Ref. [171]. $\langle \delta f^2 \rangle_b$ is from force-force correlation function simulation.

^{d}CH$_3$CO$_2$H cyclic dimer in CCl$_4$ solvent from Ref. [209]. $\langle \delta f^2 \rangle_b$ is extracted from frequency gap fluctuation measurements.

^{e}Carbonmonoxide Hemoglobin in D$_2$O solvent from Ref. [210]. $\langle \delta f^2 \rangle_b$ is extracted from vibrational relaxation rate measurements.

^{f}HgI in ethanol from Ref. [211]. $\langle \delta f^2 \rangle_b$ is extracted from force-force correlation function simulation.

calculations for the O-H stretch in D$_2$O environment. The effective Hamiltonian is assumed to be the same as Eq. (8.49) and includes a Morse oscillator linearly coupled to a Gaussian classical bath. The electronic field experienced by the O-H stretch in the hydrogen bond network is found to follow under-damped motion by computer simulations,[175, 176, 177, 178] photon echo spectroscopy, [206] and other ultrafast infrared (IR) measurements. [207, 212, 213] It is shown in the literature[175, 176, 177, 178, 206, 207, 208, 212, 213, 214] that the relaxation time is about 30$\sim$170 fs in the short time profile while the characteristic time of the long time decay is roughly 0.5$\sim$2.0 ps. The two different time scales of the frictional kernel arise from a hydrogen-bond stretching at short times and a collective relaxation at long times. The ratio of the short-time relaxation rate to the O-H stretch frequency (~ 3430cm^{-1}) is roughly 0.01 $\sim$ 0.05. The dimensionless bath fluctuation amplitude estimated from simulations and experiments[175, 176, 177, 178, 207] is $\langle \delta f^2 \rangle_b/(\mu\hbar\omega_0^3) \approx 1.22 \times 10^{-2}$. For simplicity, we choose a bi-exponential friction kernel to reflect the two time scales, i. e. , $\langle \delta f(\tau)\delta f(0)\rangle_b = \langle \delta f^2 \rangle_b[pe^{-\gamma_1 t} + (1-p)e^{-\gamma_2 t}]$, where $\gamma_1^{-1} = 40$ fs and $\gamma_2^{-1} = 600$

Table 8.2: Parameters of O-H stretch.

D	8.84×10^{-12} erg
β	2.175×10^{8} cm^{-1}
μ	1.66^{-24} g
ω_0	7.2916×10^{14} s^{-1}
γ_1^{-1}	40 fs
γ_2^{-1}	600 fs
p	0.8
$\langle \delta f^2 \rangle_b / \mu \hbar \omega_0^3$	0.0122

The parameters of O-H stretch are taken from Ref. [215] and the D_2O environmental parameters γ_1, γ_2 and $\langle \delta f^2 \rangle_b$ are estimated from literature.[175, 176, 177, 178, 207].

fs. The dissociation energy D_e and β are obtained from the literature[215] and the parameter are summarized in Table 8.2. Given the Morse parameters, the number of the bounded states in O-H bond is estimated to be 22, and the anharmonicity parameter is $\chi_e \approx 0.0217$.

8.5.1 Solute-solvent coupling

The second order cumulant expansion yields almost identical temporal absorption profiles as the non-perturbative calculation due to the weak bath fluctuations and the asymmetric envelop from non-Markovian VER effects is rather weak. On the other hand, the Markovian approximation assumes fast relaxation of bath and is only applicable to the long time limit when $t \gg \gamma_1^{-1}, \gamma_2^{-1}$. The presence of the slow relaxation in the friction kernel violates this assumption; consequently, the Markovian approximation over-estimates the decay rate substantially and deviates significantly from both the non-perturbative and the perturbative calculations. These findings are illustrated in Fig. 8-10a. In Fourier space, the weakly asymmetric envelop of the absorption profile is reflected in the weak side bands of absorption spectrum. The side bands are generated by the solvent-induced multiple-photon transitions and non-Markovian VER treatment.

For the O-H bond, the anharmonicity parameter χ_e is as large as 0.0217. This is about 50 times larger than the Morse potential discussed in Sec. 8.4. The dimension-

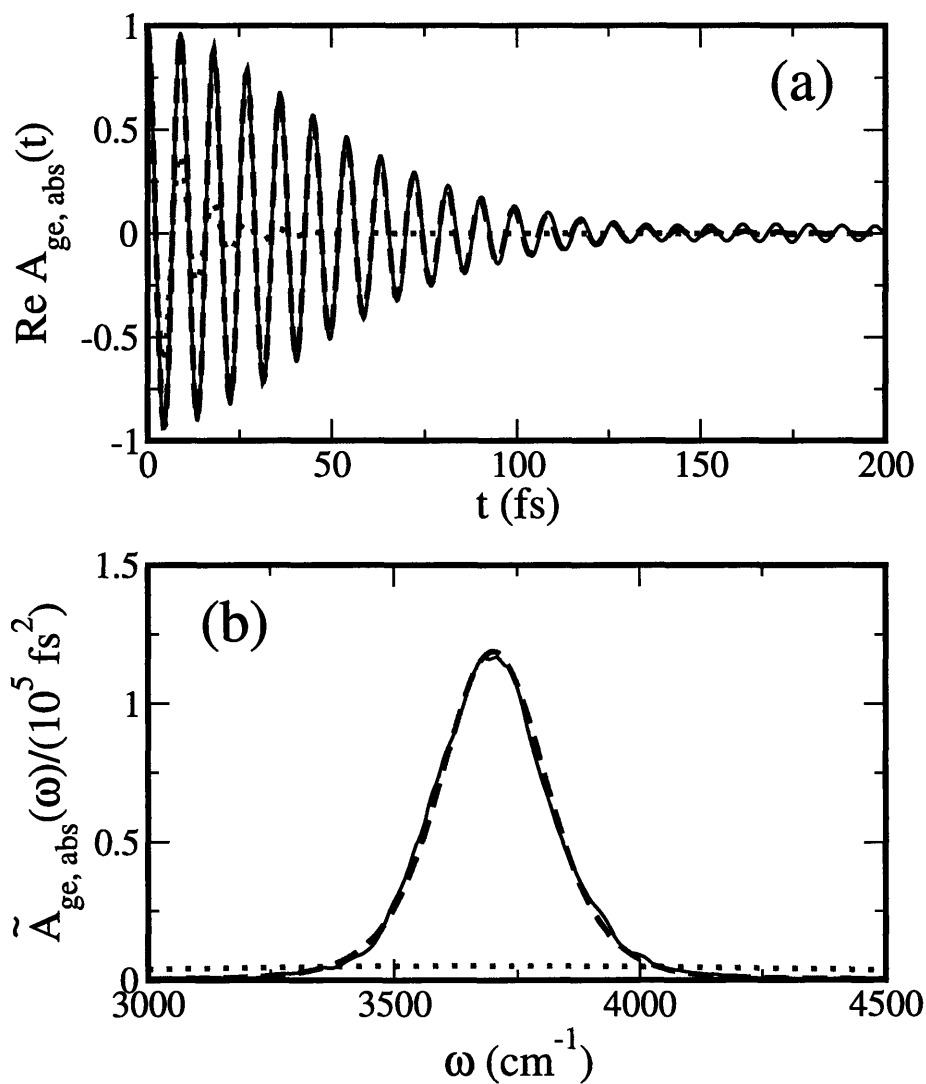Figure 8-10: Comparison of the non-perturbative calculation, the second cumulant expansion, and the Markovian approximations for the O-H stretch in D_2O network. The parameters are summarized in Table 8.2. The exact results of the non-perturbative calculation are plotted in solid lines, the second order cumulant expansion results in dashed lines and the Markovian approximation in dotted lines.

less bath fluctuation is about 25 times smaller than that in Sec. 8.4. Due to these two effects, a weakly asymmetric central peak of the absorption spectrum compared to Fig. 8-5 is observed and the perturbation result reproduces the absorption spectrum quite accurately.

8.5.2 VER effects in 3PEPS measurements

In the three pulse photon echo peak shift (3PEPS) experiment, the integrated photon echo signal is collected and the photon echo peak shift is determined as a function of the intermediate waiting time t_w.[159, 162, 163, 207] For the purpose of illustration, we consider the same excitation path way discussed in Sec. 8.2.1. Assuming delta-function pulses, we derive the three pulse photon echo (3PE) amplitude as

$$
\begin{aligned}
A_{echo}(t_1, t_w, t_2) \quad &= \langle\langle e^{-iH(t_w+t_2)}\rangle_{n+1}\langle e^{-iHt_1}\rangle_n\langle e^{-iHt_2}\rangle_n^\dagger\langle e^{-iH(t_1+t_w)}\rangle_{n+1}^\dagger\rangle_b + \\
&\quad \langle\langle e^{-iHt_2}\rangle_{n+1}\langle e^{-iH(t_1+t_w)}\rangle_n\langle e^{-iH(t_w+t_2)}\rangle_n^\dagger\langle e^{-iHt_1}\rangle_{n+1}^\dagger\rangle_b. \quad (8.55)
\end{aligned}
$$

The integrated photon echo signal is $I_{echo}(t_1, t_w) = \int_0^\infty |A_{echo}(t_1, t_w, t_2)|^2\, dt_2$. t_1 is the dephasing time between the first pulse and the second pulse, t_w is the waiting time between the second and the third pulses, and t_2 is the rephasing time between the third and the probe pulses. Following the same perturbation scheme discussed in Sec. 8.3.2, we separate pure dephasing from the diagonal coupling and VER from the off-diagonal coupling. The echo signal $A_{echo}(t_1, t_w, t_2)$ is given by

$$
\begin{aligned}
A_{echo}(t_1, t_w, t_2) \quad &\approx \quad e^{-\Omega_{n,n+1}(t_2-t_1)} \exp[-g^*(t_1) + g(t_w) - g^*(t_2) \\
&\quad -g^*(t_1 + t_w) - g(t_w + t_2) + g^*(t_1 + t_w + t_2)] \cdot \\
&\quad \big(\exp[-h_{n+1}^*(t_1 + t_w) - h_n^*(t_2) - h_{n+1}(t_w + t_2) - h_n(t_1)]+ \\
&\quad \exp[-h_{n+1}^*(t_1) - h_n^*(t_w + t_2) - h_{n+1}(t_2) - h_n(t_1 + t_w)]\big) \quad (8.56)
\end{aligned}
$$

where $g(t)$ is the line shape function and $h_n(t)$ characterizes the population relaxation contribution from the n-th vibrational state. In the limit $t_w = 0$, Eq. (8.56) reduces to the 2PE expression in Eq. (8.18). If the off-diagonal solute-solvent interaction is

253

negligible compared to the pure dephasing, i. e. , $h_n(t) \approx 0$, equation (8.56) reduces to the well-know result of three-pulse photon echo response function for a two-level system.[159, 162]

In Fig. 8-11, we plot the integrated photon echo signal

$$I_{echo}(t_1, t_w) = \int_0^\infty |A_{echo}(t_1, t_w, t_2)|^2 \, dt_2 \qquad (8.57)$$

without VER, with the Markovian VER rate, and with the cumulant approximation of VER, respectively. Perturbative calculations are sufficiently accurate here due to weak bath fluctuations. In Eq. (8.56), the pure dephasing terms containing t_w cancel out at large t_w and $I_{echo}(t_1, t_w)$ reaches a stable nonzero function of t_1 without VER, as shown in Fig. 8-11a. VER essentially decreases the signal amplitude during the waiting time t_w. At short waiting times, the cumulant approximation of VER imposes small oscillation onto the integrated echo intensity, yet does not affect the overall shape of the integrated photon echo signal. The average population relaxation time is estimated to be $(k_g + k_e)^{-1} \approx 850 fs$. At large t_w, the echo intensity approaches zero with population relaxation, as shown in Fig. 8-11b and Fig. 8-11c, which is completely different from the case where VER is not accounted.

A nontrivial VER contribution is demonstrated in the peak shifts of integrated echo signal. Considering the experimental resolutions, we compute the integrated echo signal with a sliding window average of 10 fs and fit $I_{echo}(t_1, t_w)$ with a Gaussian function, as shown in Fig. 8-12b. It is clear in Fig. 8-12a that the peak shifts demonstrate different time scales, and the peak-shift amplitude decreases due to the VER effects. The perturbation calculation with second-order cumulant expansion yields small recurrence around 200 fs, which corresponds to the frequency difference of the fundamental and the overtone $\Omega_{12} - \Omega_{01} \sim 250$ cm^{-1}. The recurrence can not be reproduced with VER rates and therefore is a clear indication of non-Markovian VER effects. The experimentally observed recurrence at $150 \sim 170$ fs includes additional contributions from the the under-damped frictional kernel.[207] The small oscillation around 40 fs is attributed to insufficient average from the narrow sliding window of
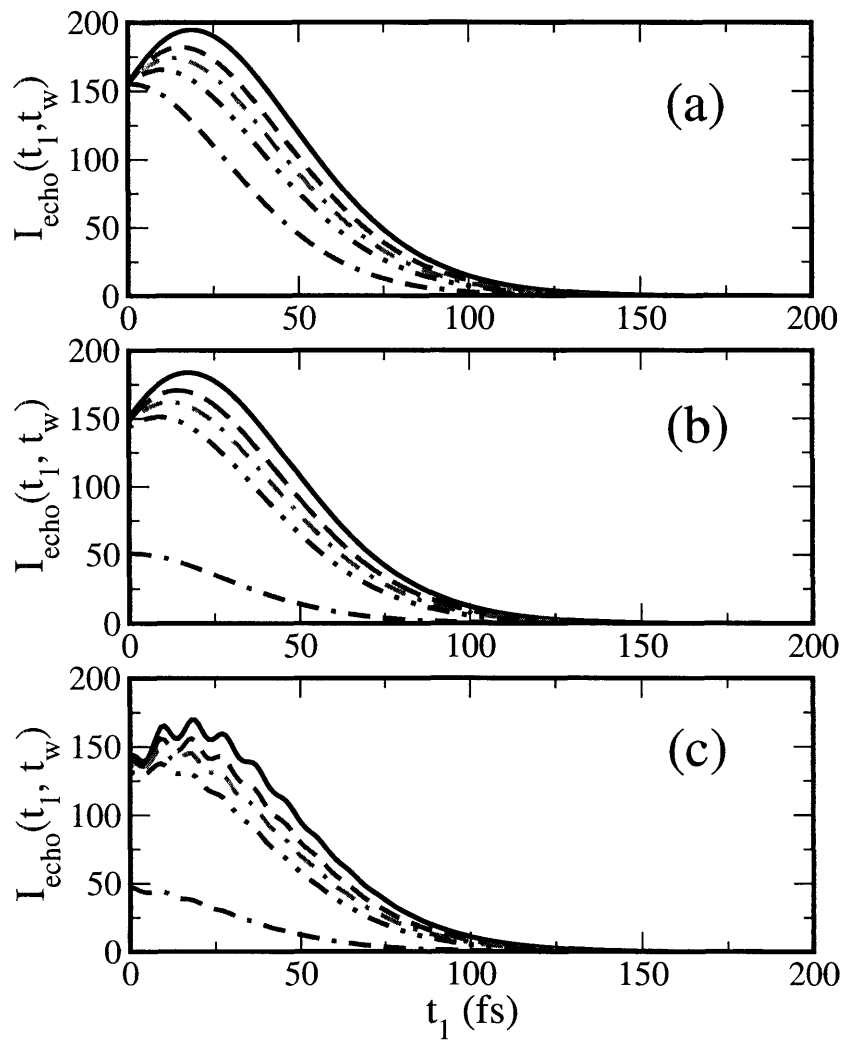
Figure 8-11: Comparison of the perturbative calculations of the echo intensity $I_{echo}(t_1, t_w)$ (a) without VER, (b) with Markovian VER, and (c) with cumulant approximation of VER. The waiting time t_w is varied, from top to bottom, $t_w = 0, 10, 20, 40, 1000$ fs. The unit of $I_{echo}(t_1, t_w)$ is fs.
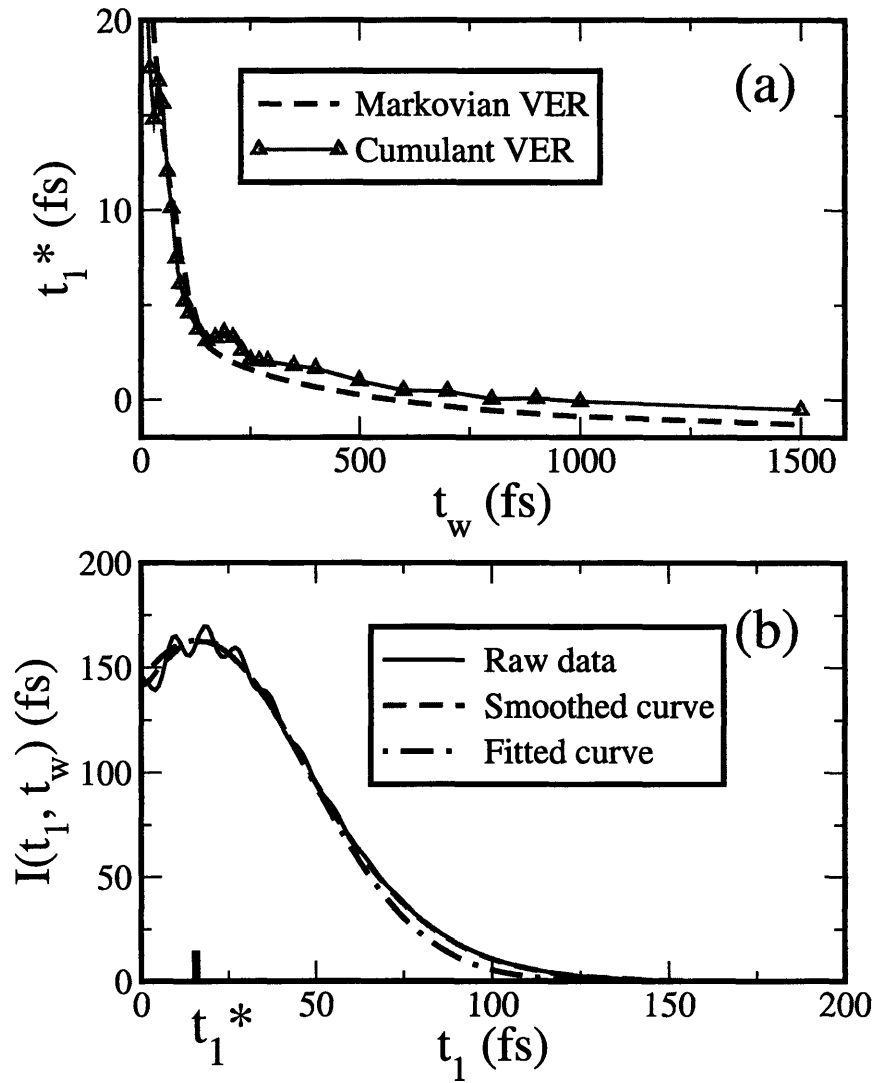
Figure 8-12: (a) Comparison of the echo shifts with Markovian VER and with cumulant VER (triangles). $I_{echo}(t_1, t_w)$ is first smoothed with a sliding window average of 10 fs, and the peak shifts are then determined with Gaussian fitting. (b) Determination of the peak shift t_1^*.

10 fs and Gaussian fitting errors. Compared to the linear absorption spectrum, the nonlinear 3PEPS is a more sensitive probe of the anharmonic effects.

8.6 Conclusions

Non-perturbative and perturbative approaches are applied to vibrational line shape calculations. The non-perturbative approach based on Feynman's path integral formalism directly evaluates the quantum propagator in the interaction picture. In the perturbative approach, the solute-solvent interaction is first decomposed into diagonal and off-diagonal elements and the absorption profile is factorized into two parts: the population relaxation profile related to the off-diagonal coupling and the pure dephasing profile related to the diagonal coupling. This factorization scheme neglects the commutator between the diagonal and the off-diagonal coupling, an important contribution which increases with anharmonicity. In the factorization scheme, we evaluate the bath average for each propagator separately, and obtain the decomposition relation, $A_{abs}(t) \approx e^{i\Omega_{n,n+1}t}\sqrt{I_{n,pop}(t)I_{n+1,pop}(t)}A_{n,n+1,dep}(t)$. Next, we apply the second-order cumulant expansion to the decomposition relation and derive the line shape function $g(t)$ and the population relaxation function $h_n(t)$. The approximation scheme of Eq. (8.19) directly superimposes the population relaxation profile from pump-probe experiments onto the pure dephasing profile and can reproduce the asymmetric absorption profile. The approximation scheme of Eq. (8.23) treats population relaxation with the corresponding Markovian limit while evaluating the pure dephasing at the second-order cumulant. Due to the Markovian approximation to VER, Eq. (8.23) gives a symmetric absorption profile without side bands in the absorption spectrum. In the VER rate description, the solvent relaxation is much slower than the vibrational frequency gap and the line shapes are dominated by pure dephasing. On the other hand, the Markovian treatment of the VER contribution to line shapes requires a fast bath relaxation which results in the inconsistency of the Markovian VER rate. Finally, in the Markovian limit, the decomposition relation recovers the well-known relation among the vibrational dephasing rate, the population

relaxation rate, and the pure dephasing rate.

Analytical solutions for a dissipative harmonic oscillator yield quantitative estimation of the errors for different approximation schemes. $I_{g,pop}(t)I_{e,pop}(t)$ differs from $|A_{ge,abs}(t)|^2$ at second order of bath fluctuations $\langle \delta f^2 \rangle_b/(\mu \hbar \omega_0^3)$. Consequently, the decomposition in Eq. (8.13) is valid for weak solute-solvent interactions, and becomes less accurate for strong solute-solvent interactions or for vibrational relaxation systems with small frequency gaps. We also show that the approximation scheme of Eq. (8.19) over-estimates while the second order cumulant expansion always under-estimates the effects of friction. For the dissipative harmonic potential, non-Markovian VER effects generate asymmetric envelops in the time domain absorption profile, and side bands in the frequency domain absorption spectrum. The side bands are solvent-induced multiple-photon transitions and are absent in the Markovian VER treatment. The non-Lorentzian peak in non-perturbative treatments of absorption spectrum arises from couplings of population relaxations from different vibrational states. The non-perturbative VER effects manifest as a non-Lorentzian broadening along the diagonal direction in the frequency domain photon echo spectra. Quantum baths have more coherence in the long time profile but show less effects on the short time profile and the coherence decreases with increasing temperature.

For the dissipative Morse potential, the interference of population relaxations from different vibrational states leads to an asymmetric central peak in the absorption spectrum with the asymmetry increasing with anharmonicity. The second order cumulant expansion and the Markovian approximation result in a symmetric Lorentzian spectrum but can not reproduce vibrational line shapes correctly. When the frequency gap is much larger than the bath relaxation rate, pure dephasing dominates over population relaxation. In addition, the ratio between the diagonal coupling and the off-diagonal coupling is proportional to the square root of anharmonicity; therefore, the contribution from pure dephasing becomes dominant at large anharmonicities. All the three approximation schemes, the second order cumulant expansion, the composite schemes of Eq. (8.19) and Eq. (8.23), neglect the cross terms of population relaxations from different vibrational states and the cross terms between V_D and

V_{OD}, and deviate significantly from exact results at large anharmonicities. Relatively speaking, Eq. (8.19) is better than Eq. (8.23) for all the anharmonicities we study.

For an O-H stretch in hydrogen-bond environments, the Markovian approximation substantially over-estimates the decay rate from slow bath relaxation, and results in significant deviation from both the non-perturbative and the perturbative calculations. Three pulse photon echo peak shift (3PEPS) measurement provides a more sensitive nonlinear probe of the VER effects. In these experiments, both the integrated 3PE signal amplitude and the echo peak shifts become smaller due to VER effects. More importantly, the non-Markovian VER effects generate a small recurrence around 200 fs. This recurrence corresponds to the frequency difference of the fundamental Ω_{01} and the overtone Ω_{12}, a result that can not be reproduced by the Markovian VER rate. In general, nonlinear spectroscopic measurements such as two-pulse and three-pulse IR photon echoes are more sensitive to the non-perturbative and non-Markovian VER effects than linear absorption.

The non-perturbative approach proposed in this chapter treats the solute-solvent interaction accurately. Combined with the explicit treatment of the solvent degree of freedom, the non-perturbative propagation method provides a numerical tool to calculate the vibrational spectrum in condensed phases. The various perturbation schemes allow us to analyze contributions from different relaxation mechanisms and compare information contents from different spectroscopic measurements. In particular, the second-order cumulant expressions with both the pure dephasing moment $g(t)$ and the VER moment $h_n(t)$ capture the essential features of vibrational line shapes for most realistic systems. The non-perturbative approach is essential for quantitative comparison with experimental measurements in systems with strong dissipative or non-Gaussian environments.

8.7 Appendix 8-A: Anharmonicity induced dephasing

We now explore the molecular origin of pure dephasing. Taylor expansion of the solute-solvent interaction leads to

$$V(q - x) = V(q) + (a + a^+)f(x) + \frac{1}{2}(aa^+ + a^+a)e(x) + \cdots . \tag{8.58}$$

a and a^+ are the annihilation and creation operators for the vibrational mode, $f(x)$ and $e(x)$ are functions of solvent coordinates. In the above equation, the first term is a constant, the second term is the off-diagonal linear coupling, and the third term is the diagonal quadratic coupling.

Harmonic oscillator

For a harmonic oscillator with $H_s = \omega_0(aa^+ + a^+a)/2$, we explicitly evaluate the temporal profile of vibrational relaxation and dephasing from second order cumulant expansion of the solute-solvent interaction. The linear coupling to the solvent in Eq. (8.58) yields the vibrational relaxation rate

$$
\begin{aligned}
k_n &= k(n \to n+1) + k(n \to n-1) \\
&= |\langle n|a^+|n+1\rangle|^2 2 \int_0^\infty e^{i\omega_{n,n+1}} \langle f(t)f(0)\rangle_b dt \\
&+ |\langle n|a^+|n-1\rangle|^2 2 \int_0^\infty e^{-i\omega_{n-1,n}} \langle f(0)f(t)\rangle_b dt,
\end{aligned} \tag{8.59}
$$

where $\omega_{n+1,n}$ is the energy gap. The depletion rate out of the n-th vibrational state can be separate into two parts: the rate for increasing one vibrational level $k(n \to n+1)$ and the rate for decreasing one vibrational level $k(n \to n-1)$. The two rate constants between a pair of adjacent levels satisfy the detailed balance relation.

For a linear harmonic oscillator, the frequency ω_0 is a constant independent of the quantum level, therefore $\omega_{n-1,n} = \omega_{n,n+1} = \omega_0$. We can write $k(n \to n+1) = (n+1)k_+$

and $k(n \rightarrow n - 1) = nk_-$. Hence, the master equation for population relaxation is

$$\dot{P}_n = (n+1)k_- P_{n+1} + nk_+ P_{n-1} - P_n[(n+1)k_+ + nk_-] \qquad (8.60)$$

which gives $\partial_t \bar{n} = -(k_- - k_+)\bar{n} + k_+$ with $\bar{n} = \sum nP_n$ the average excitation number. Thus, we recover the equilibrium average $\bar{n}_{eq} = k_+/(k_- - k_+)$ and the reactive rate $k = k_- - k_+ = \zeta(\omega_0)/\mu$, which is exactly the classical relaxation rate for the harmonic oscillator.

From the quadratic coupling, we can calculate the dephasing rate

$$k_{n,n+1} = \frac{1}{2}\{|\langle n+2|a^+|n+1\rangle|^2 - |\langle n|a^+|n-1\rangle|^2\} \int_0^\infty \langle \delta e(t)\delta e(0)\rangle dt \qquad (8.61)$$

where $\delta e(t) = \partial^2 V - \langle \partial^2 V \rangle_b$ is the fluctuation in the curvature of the solute-solvent interaction. For a harmonic oscillator, the prefactor is a constant and the dephasing rate is constant.

Higher-order terms in the Taylor expansion of the solute-solvent interaction potential yields off-diagonal terms such as aa, a^+aa, etc., which are responsible for multi-photon processes. They become less important as the resonant frequency is multiples of the single photon frequency and gives much weak resonance with the low frequency bath. The linear terms can be incorporated in the first order expression.

Anharmonic oscillator

For an harmonic oscillator, the energy gap decreases with the quantum number. The low frequency solvent has a stronger response at low frequency and the population relaxation rate increases with the quantum number. The dephasing rate is proportional to the zero frequency of the solvent spectrum and thus is dominated by the strength of the coupling matrix. At larger vibrational quantum numbers, the width of vibrational wave function broadens due to a stronger solute-solvent coupling. Thus, the pure dephasing rate increases at larger vibrational quantum numbers.

For a harmonic oscillator, the linear coupling to the solvent results in vibrational

relaxation, whereas the quadratic solute-solvent coupling results in vibrational dephasing. The situation is different for an anharmonic potential, for which the vibrational coordinate has both an off-diagonal part q_{OD}, giving rise to dissipation, and a diagonal part q_D, giving rise to pure dephasing. Formally, the solute coordinate operator can be expanded as

$$q = q_0 + q_1(a + a^+) + q_2(aa^+ + a^+a)/2 + q_2'(aa + a^+a^+)/2 + \cdots \qquad (8.62)$$

where q_0, q_1, q_2, q_2' are expansion coefficients. Combined with Eq. (8.58), the diagonal part of the solute-solvent interaction becomes

$$V_D = \frac{aa^+ + a^+a}{2}(-q_2\partial V + q_1\partial^2 V) + \cdots \qquad (8.63)$$

which defines the quadratic fluctuating force $e = (-q_2\partial V + q_1\partial^2 V)$. It is well-known that the pure dephasing has two mechanisms: the quadratic coupling to the solvent and the anharmonicity in the solute vibrational mode. Below we demonstrate that these two mechanisms are essentially equivalent.

We now derive the anharmonicity-induced dephasing rate for the Morse potential $V(q) = D_e(1 - e^{-\beta q})^2$, where D_e the dissociation energy and β the inverse length-scale. The fundamental frequency of the Morse oscillator is $\omega_0 = \sqrt{2D_e\beta^2/\mu}$ and the total number of the bound states is $N/2$ with $N + 1 = \sqrt{8D_e\mu/\beta^2} = \chi_e^{-1}$. We use the following relation from Refs. 49 and 50,

$$
\begin{aligned}
b + b^+ &\approx \frac{N+1}{\sqrt{N}}[1 - e^{-\beta q} - \frac{2}{\beta^2(N+1)^2}(e^{\beta q}p^2 + p^2 e^{\beta q})] \\
&\approx \chi_e^{-1/2}\beta q - \chi_e^{-1/2}[\frac{1}{2}\beta^2 q^2 + \frac{\beta^2 p^2}{\mu^2\omega_0^2}]
\end{aligned}
$$

$$(8.64)$$

where $N + 1 \approx N$ for large N. The second order contribution expressed with the

creation and annihilation operators yields

$$b + b^+ \approx q_1(a + a^+) + \beta q_1^2 [\frac{1}{2}(a + a^+)^2 - (a - a^+)^2], \tag{8.65}$$

which has the diagonal components with $q_2 = 3\beta q_1^2$. Based on the definition in Eq. (8.61), the pure dephasing rate is

$$k' = q_2^2 \int_0^\infty \Re\langle e(t)e(0)\rangle_b dt \approx (\frac{3\beta}{2\mu\omega_0})^2 k_B T \hat{\eta}(0), \tag{8.66}$$

where $\hat{\eta}(0) = \int_0^\infty \eta(t)dt$ is the integrated friction coefficient. The last expression is the classical limit of the dephasing rate first obtained by Oxtoby and later by many others.[216, 217] To see this, we expand the Morse potential $V(q) = D_e\beta^2 q^2 - D_e\beta^3 q^3 + \cdots$ and identify the cubic coefficient $f_c = 6D_e\beta^3$. Thus, the well-known result of $k' = f_c^2 k_B T \hat{\eta}(0)/4\mu^4\omega_0^6$ is recovered.[217]

It should be noted that the dephasing rate differ by a factor of 9 if the momentum term in Eq. (8.64) is neglected. Using the exact form for $a + a^+$ as the coupling to the solvent, it is possible to introduce linear dissipation without pure dephasing for an anharmonic oscillator. Such a coupling is not only a non-linear function of coordinate but also a function of momentum. We thus conclude that for realistic systems the anharmonicity in vibrational modes contributes significantly to pure dephasing.

8.8   Appendix 8-B: Dissipative harmonic oscillator coupled to a quantum bath

In this appendix, we extend the previous discussion in Sec. 8.3 to a quantum bath. For simplicity, we assume the same dissipative harmonic oscillator as in Eq. (8.25). In this case, the quantum force-force correlation function is a complex function, $C_{qm}(t) = \langle f(t)f(0)\rangle = C_1(t) - iC_2(t)$, where the real part $C_1(t)$ is an even function and the imaginary part $C_2(t)$ is an odd function. The Fourier transform of the force-force correlation function is $\tilde{C}_{qm}(\omega) = \int_{-\infty}^\infty e^{i\omega t}C_{qm}(t)dt = \tilde{C}_1(\omega) - i\tilde{C}_2(\omega)$. The fluctuation-

dissipation theorem requires

$$-i\tilde{C}_2(\omega) = \tanh\frac{\beta\hbar\omega}{2}\tilde{C}_1(\omega),\tag{8.67}$$

where $\tilde{C}_2(\omega)$ is purely imaginary since $C_2(t)$ is an odd function. In the high temperature limit, $\tilde{C}_1(\omega) \to \tilde{C}_{cl}(\omega)$ and $\tilde{C}_2(\omega) \to 0$.

Let us consider a quantum bath consisting of a number of harmonic oscillators $H_b = \sum_j(p_j^2/2m_j + m_j\omega_j^2x_j^2/2)$ and a bilinear system bath coupling $H_{sb} = -q\sum_j g_jx_j$. For the harmonic bath, the quantum force-force correlation function is explicitly given as

$$C_{qm}(t) = \sum_j \frac{\hbar}{2m_j\omega_j}c_j^2[\coth\frac{\beta\hbar\omega_j}{2}\cos\omega_jt - i\sin\omega_jt],\tag{8.68}$$

which reduces to the classical force-force correlation function in the high temperature limit. Completing the Fourier transforms, one can readily show that[181, 218]

$$\tilde{C}_1(\omega) = \frac{\beta\hbar\omega}{2}\coth\frac{\beta\hbar\omega}{2}\tilde{C}_{cl}(\omega) \text{ and } -i\tilde{C}_2(\omega) = \frac{\beta\hbar\omega}{2}\tilde{C}_{cl}(\omega).\tag{8.69}$$

It is straightforward to prove that the transition moments given in Eq. (8.27) are still valid[121] given that $f(\tau)$ is now a complex variable. Following the same procedure as in Sec. 8.3.1, we derive the exact expression of the absorption profile as

$$A_{ge,abs}(t) = e^{-i\omega_0t}\frac{1 + \alpha_{11} + \alpha_{22}}{[1 + 2(\alpha_{11} + \alpha_{22}) + 4(\alpha_{11}\alpha_{22} - \alpha_{12}\alpha_{12}^*)]^{3/2}}.\tag{8.70}$$

This expression is almost identical to Eq. (8.28) except that α_{12} is a complex function. With the quantum force-force correlation function, we obtain the explicit expression of α_{12} as

$$\alpha_{12} = \frac{1}{2\mu\omega_0\hbar}\int_0^t d\tau \int_0^t d\tau' [C_1(\tau - \tau')\sin\omega_0(\tau + \tau') + iC_2(\tau - \tau')\sin\omega_0(\tau - \tau')].\tag{8.71}$$

Equation (8.71) reduces to α_{12} in Eq. (8.28) in the classical limit when $C_2 = 0$.

In the perturbative approach, we follow the same procedure as in Sec. 8.3.2 and obtain

$$
\begin{aligned}
A_{ge,abs}(t) &\approx e^{-i\omega_0 t} \exp\left\{-\frac{1}{2}\int_0^t d\tau \int_0^t d\tau'[C_{qm}(\tau-\tau')\langle q(\tau)q(\tau')\rangle_e \right. \\
&\quad \left. +C_{qm}^\dagger(\tau-\tau')\langle q(\tau)q(\tau')\rangle_g^\dagger]\right\} \\
&\approx e^{-i\omega_0 t} \exp\left\{-\frac{1}{\mu\omega_0\hbar}\int_0^\tau d\tau \int_0^t d\tau'[2C_1(\tau-\tau')\cos\omega_0(\tau-\tau') \right. \\
&\quad \left. -C_2(\tau-\tau')\sin\omega_0(\tau-\tau')]\right\}.
\end{aligned}
\tag{8.72}
$$

The first term in the exponent equals $2(\alpha_{11}(t) + \alpha_{22}(t))$ is the classical perturbation result of Eq. (8.37) and the second term represents the quantum effects from the imaginary part of the force-force correlation function.

In the long time limit, we invoke the Markovian approximation in the perturbative expression of Eq. (8.72), and obtain $A_{n,n+1,abs}(t) \approx e^{-i\omega_0 t}\exp[-(\Gamma_{n+1} + \Gamma_n)t/2]$, where $\Gamma_n = \int_0^\infty [2(n+1/2)C_1(\tau)\cos\omega_0\tau - C_2(\tau)\sin\omega_0\tau]d\tau$ is the population relaxation rate from the vibrational state n. Hence, the presence of the imaginary part of the quantum correlation function reduces the decay rate of the envelop, creating more coherent oscillations in absorption profile.

Bibliography

[1] B. J. Berne, *Statistical Mechanics, Part B: Time-dependent Processes*, Plenum Press, New York, 1977.

[2] R. I. Cukier and J. M. Deutch, Phys. Rev. **177**, 240 (1969).

[3] N. Agmon and J. J. Hopfield, J. Chem. Phys. **79**, 2042 (1983).

[4] J. E. Straub, M. Borkovec, and B. J. Berne, J. Chem. Phys **84**, 1788 (1986).

[5] H. Tang, S. M. Jang, M. S. Zhao, and S. A. Rice, J. Chem. Phys. **101**, 8737 (1994).

[6] M. S. Zhao and S. A. Rice, Int. J. Quantum Chem. **58**, 593 (1996).

[7] E. J. Heller, J. Phys. Chem. **99**, 2625 (1995).

[8] P. Pechukas and J. Ankerhold, J. Chem. Phys. **107**, 2444 (1997).

[9] T. Basché, W. E. Moerner, M. Orrit, and U. P. Wild, *Single Molecule Optical Detection, Imaging and Spectroscopy*, VCH Publishers, New York, 1996.

[10] W. E. Moerner and M. Orrit, Science **283**, 1670 (1999).

[11] S. M. Nie and R. N. Zare, Annu. Rev. Phys. Chem **26**, 567 (1997).

[12] W. P. Ambrose, P. M. Goodwin, J. C. Martin, and R. A. Keller, Science **265**, 364 (1994).

[13] L. Edman, U. Mets, and R. Rigler, Proc. Natl. Acad. Sci. USA **93**, 6710 (1996).

[14] Y. Jia et al., Proc. Natl. Acad. Sci. USA **94**, 7932 (1997).

[15] H. P. Lu, L. Xun, and X. S. Xie, Science **282**, 1877 (1998).

[16] T. J. Ha et al., Chem. Phys. **247**, 107 (1999).

[17] C. G. Baumann et al., Biophys. J. **78**, 1965 (2000).

[18] W. E. Moerner, Science **265**, 46 (1994).

[19] J. L. Skinner and W. E. Moerner, J. Phys. Chem. **100**, 13251 (1996).

[20] P. D. Reilly and J. L. Skinner, Phys. Rev. Lett. **71**, 4257 (1993).

[21] F. L. H. Brown and R. J. Silbey, J. Chem. Phys. **108**, 7434 (1998).

[22] E. Barkai and R. Silbey, Chem. Phys. Lett. **310**, 287 (1999).

[23] X. S. Xie and J. K. Trautman, Annu. Rev. Phys. Chem. **49**, 441 (1998).

[24] E. Geva and J. L. Skinner, Chem. Phys. Lett. **288**, 225 (1998).

[25] A. M. Berezhkovskii, A. Szabo, and G. H. Weiss, J. Chem. Phys. **110**, 9145 (1999).

[26] G. K. Schenter, H. P. Lu, and X. S. Xie, J Phys Chem A **103**, 10477 (1999).

[27] J. S. Cao, Chem. Phys. Lett. **327**, 38 (2000).

[28] N. Agmon, J. Phys. Chem. B **104**, 7830 (2000).

[29] H. Frauenfelder and P. G. Wolynes, Science **229**, 337 (1985).

[30] K. D. Rector et al., J. Phys. Chem. A **103**, 2381 (1999).

[31] J. Wang and P. Wolynes, Phys. Rev. Lett. **74**, 4317 (1995).

[32] J. Onuchic, J. Wang, and P. Wolynes, Chem. Phys. **247**, 175 (1999).

[33] V. Chernyak, M. Schulz, and S. Mukamel, J. Chem. Phys. **111**, 7416 (1999).

[34] K. D. Weston, P. J. Carson, H. Metiu, and S. K. Buratto, J. Chem. Phys. **109**, 7474 (1998).

[35] S. Weiss, Science **283**, 1676 (1999).

[36] T. Ha et al., Proc. Natl. Acad. Sci. USA **96**, 893 (1999).

[37] L. Stryer, Annu. Rev. Biochem. **47**, 819 (1978).

[38] A. Hillisch, M. Lorenz, and S. Diekmann, Curr. Opin. Struc. Biol. **11**, 201 (2001).

[39] O. Bieri et al., Proc. Natl. Acad. Sci. USA **96**, 9597 (1999).

[40] L. Lapidus, W. Eaton, and J. Hofrichter, Proc. Natl. Acad. Sci. USA **97**, 7220 (2000).

[41] L. J. Lapidus, W. A. Eaton, and J. Hofrichter, Phys. Rev. Lett. **87**, art. no. 258101 (2001).

[42] L. Lapidus, P. Steinbach, W. Eaton, A. Szabo, and J. Hofrichter, J. Phys. Chem. B **106**, 11628 (2002).

[43] A. Szabo, K. Schulten, and Z. Schulten, J. Chem. Phys. **72**, 4350 (1980).

[44] G. Wimeski and M. Fixman, J. Chem. Phys. **60**, 866 (1974).

[45] G. Wilemski and M. Fixman, J. Chem. Phys. **60**, 878 (1974).

[46] G. H. Weiss, J. Chem. Phys. **80**, 2880 (1984).

[47] R. W. Pastor, R. Zwanzig, and A. Szabo, J. Chem. Phys **105**, 3878 (1996).

[48] H. Babcock, D. Smith, J. Hur, E. Shaqfeh, and S. Chu, Phys. Rev. Lett. **85**, 2018 (2000).

[49] T. T. Perkins, S. R. Quake, D. E. Smith, and S. Chu, Science **258**, 1122 (1992).

[50] T. Perkins, D. Smith, and S. Chu, Science **276**, 2016 (1997).

[51] T. Perkins, D. Smith, R. Larson, and S. Chu, Science **268**, 83 (1995).

[52] S. Quake, H. Babcock, and S. Chu, Nature **388**, 151 (1997).

[53] D. Smith and S. Chu, Science **281**, 1335 (1998).

[54] D. Smith, H. Babcock, and S. Chu, Science **283**, 1724 (1999).

[55] R. Kubo, N. Toda, and N. Hashitsume, *Statistical physics II*, Springer-Verlag, Berlin, Germany, 1985.

[56] S. Mukamel, *The Principles of Nonlinear Optical Spectroscopy*, Oxford University Press, New York, 1995.

[57] S. H. Northrup and J. T. Hynes, J. Chem. Phys. **73**, 2700 (1980).

[58] R. F. Grote and J. T. Hynes, J. Chem. Phys. **73**, 2715 (1980).

[59] D. Chandler, *Introduction to Modern Statistical Mechanics*, Oxford University Press, New York, 1987.

[60] R. Zwanzig, J. Chem. Phys. **97**, 3587 (1992).

[61] L. D. Zusman, Chem. Phys. **49**, 295 (1980).

[62] H. Sumi and R. A. Marcus, J. Chem. Phys. **84**, 4894 (1986).

[63] J. T. Hynes, J. Phys. Chem. **90**, 3701 (1986).

[64] D. Y. Yang and R. I. Cukier, J. Chem. Phys. **91**, 281 (1989).

[65] J. Cao and Y. Jung, J. Chem. Phys. **112**, 4716 (2000).

[66] N. G. van Kampen, *Stochastic Processes in Physics and Chemistry*, North-Holland Physics, Amersterdam, The Netherlands, 1992.

[67] J. Ross and M. O. Vlad, Annu. Rev. Phys. Chem. **50**, 51 (1999).

[68] A. Suárez and R. Silbey, Chem. Phys. **218**, 445 (1994).

[69] P. D. Reilly and J. L. Skinner, J. Chem. Phys. **102**, 1540 (1995).

[70] X. H. Xu and E. S. Yeung, Science **275**, 1106 (1997).

[71] G. J. Schutz, H. Schindler, and T. Schmidt, Biophys. J. **73**, 1073 (1997).

[72] J. S. Cao, Phys. Rev. E **63**, article No. 041101 (2001).

[73] J. S. Cao, J. Chem. Phys. **114**, 5137 (2001).

[74] H. Risken, *The Fokker-Planck Equation*, Springer-Verlag, Berlin, Germany, 1984.

[75] J. Wang and P. Wolynes, J. Phys. Chem. **100**, 1129 (1996).

[76] E. Barkai, Y. Jung, and R. Silbey, Phys. Rev. Lett. **8720** (2001).

[77] G. Weiss and J. Masoliver, Physica A **296**, 75 (2001).

[78] S. L. Yang and J. S. Cao, J. Chem. Phys. **117**, 10996 (2002).

[79] H. Yang and X. S. Xie, Chem. Phys. **284**, 423 (2002).

[80] R. Metzler, E. Barkai, and J. Klafter, Phys. Rev. Lett. **82**, 3563 (1999).

[81] A. A. Deniz et al., Proc. Natl. Acad. Sci. USA **97**, 5179 (2000).

[82] D. S. Talaga et al., Proc. Natl. Acad. Sci. USA **97**, 13021 (2000).

[83] M. Lee, J. Y. Tang, and R. M. Hochstrasser, Chem. Phys. Lett. **344**, 501 (2001).

[84] C. Eggeling, J. Widengren, R. Rigler, and C. A. M. Seidel, Anal. Chem **70**, 2651 (1998).

[85] O. Kratky and G. Porod, Recl. Trav. Chim. Pays-Bas. **68**, 1106 (1949).

[86] G. Porod, J. Polym. Sci. **10**, 153 (1953).

[87] R. A. Harris and J. E. Hearst, J. Chem. Phys. **44**, 2595 (1966).

[88] J. E. Hearst and R. A. Harris, J. Chem. Phys. **45**, 3106 (1966).

[89] J. E. Hearst, R. A. Harris, and E. Beals, J. Chem. Phys. **46**, 398 (1967).

[90] K. F. Freed, J. Chem. Phys. **54**, 1453 (1971).

[91] K. F. Freed, Adv. Chem. Phys. **22**, 1 (1972).

[92] M. Fixman and J. Kovac, J. Chem. Phys. **58**, 1564 (1973).

[93] B. Y. Ha and D. Thirumalai, J. Chem. Phys. **106**, 4243 (1997).

[94] B. H. Zimm, J. Chem. Phys. **24**, 269 (1956).

[95] M. Doi and S. F. Edwards, *The Theory of Polymer Dynamics*, Oxford University Press, New York, 1986.

[96] T. G. Mason and D. A. Weitz, Phys. Rev. Lett. **74**, 1250 (1995).

[97] J. C. Crocker et al., Phys. Rev. Lett. **85**, 888 (2000).

[98] J. G. Kirkwood, Recl. Trav. Chim. Pays-Bas. **68**, 649 (1949).

[99] C. W. Pyun and M. Fixman, J. Chem. Phys. **44**, 2107 (1966).

[100] M. Bixon and R. Zwanzig, J. Chem. Phys. **58**, 1459 (1973).

[101] M. Bixon and R. Zwanzig, J. Chem. Phys. **68**, 1890 (1978).

[102] B. U. Felderhof, J. M. Deutch, and U. M. Titulaer, J. Chem. Phys. **63**, 740 (1975).

[103] R. G. Winkler, P. Reineker, and L. Harnau, J. Chem. Phys. **101**, 8119 (1994).

[104] J. B. Lagowski, J. Noolandi, and B. Nickel, J. Chem. Phys. **95**, 1266 (1991).

[105] R. G. Winkler, Phys. Rev. Lett. **82**, 1843 (1999).

[106] G. Srinivas and B. Bagchi, J. Chem. Phys **116**, 837 (2002).

[107] J. J. Portman and P. G. Wolynes, J. Phys. Chem. A **103**, 10602 (1999).

[108] G. Diezemann, J. Chem. Phys. **116**, 1647 (2002).

[109] H. Yamakawa, G. Tanaka, and W. H. Stockmayer, J. Chem. Phys. **61**, 4535 (1974).

[110] W. H. Stockmayer, G. Wilemski, H. Yamakawa, and G. Tanaka, J. Chem. Phys. **63**, 1039 (1975).

[111] M. Pasquali, V. Shankar, and D. C. Morse, Phys. Rev. E **64**, article no. 020802 (2001).

[112] F. Gittes and F. C. Mackintosh, Phys. Rev. E **58**, 1241 (1998).

[113] N. Agmon and J. Hopfield, J. Chem. Phys. **78**, 6947 (1983).

[114] R. Zwanzig, Acc. Chem. Res. **23**, 148 (1990).

[115] Wang J. and P. Wolynes, Chem. Phys. Lett. **212**, 427 (1993).

[116] S. Yang, J. Witkoskie, and J. Cao, J. Chem. Phys. **117**, 11010 (2002).

[117] S. Yang and J. Cao, J. Chem. Phys. **121**, 572 (2004).

[118] S. Yang and J. Cao, J. Phys. Chem. B **105**, 6536 (2001).

[119] J. Cao, J. Phys. Chem. A **103**, 10571 (1999).

[120] Y. Jung and J. Cao, J. Chem. Phys. **117**, 3822 (2002).

[121] R. P. Feynman and A. R. Hibbs, *Quantum Mechanics and Path Integrals*, McGraw-Hill Book Co., New York, 1965.

[122] I. V. Gopich and A. Szabo, J. Chem. Phys. **107**, 5058 (2003).

[123] X. Zhuang et al., Science **296**, 1473 (2002).

[124] S. Yang and J. Cao, J. Chem. Phys. **121**, 562 (2004).

[125] S. Jun, J. Bechhoefer, and B. Ha, Europhys. Lett. **64**, 420 (2003).

[126] G. Srinivas and B. Bagchi, J. Phys. Chem. B **105**, 9370 (2001).

[127] J. Sung and S. Lee, J. Chem. Phys. **115**, 9050 (2001).

[128] D. Ermak and J. McCammon, J. Chem. Phys. **69**, 1352 (1978).

[129] Z. Wang and D. Makarov, J. Chem. Phys. **117**, 4591 (2002).

[130] C. Bouchiat et al., Biophys. J. **76**, 409 (1999).

[131] T. Strick, J. Allemand, D. Bensimon, A. Bensimon, and V. Croquette, Science **271**, 1835 (1996).

[132] P. Cluzel et al., Science **271**, 792 (1996).

[133] S. Smith, L. Finzi, and C. Bustamante, Science **258**, 1122 (1992).

[134] P. Thomen, U. Bockelmann, and F. Heslot, Phys. Rev. Lett. **88**, 8102 (2002).

[135] R. W. Hammond, X. L. Shi, and M. D. Morris, J. Microcolumn Separations **44**, 713 (2000).

[136] X. L. Shi, R. W. Hammond, and M. D. Morris, Polymer **42**, 8483 (2001).

[137] I. Auzanneau, C. Barreau, and L. Salome, Comptes Rendus Acad. Sci. Ser. III-Sci. Vie-Life Sci. **316**, 459 (1993).

[138] N. Andrews, A. McHugh, and J. Schieber, J. Rheol. **42**, 281 (1998).

[139] P. Doyle, B. Ladoux, and J. Viovy, Phys. Rev. Lett. **84**, 4769 (2000).

[140] P. Doyle, E. Shaqfeh, G. McKinley, and S. Spiegelberg, J. Non-Newton. Fluid Mech. **76**, 79 (1998).

[141] P. Doyle, E. Shaqfeh, and A. Gast, J. Fluid Mech. **334**, 251 (1997).

[142] J. Hur, E. Shaqfeh, and R. Larson, J. Rheol. **44**, 713 (2000).

[143] R. Jendrejack, J. de Pablo, and M. Graham, J. Chem. Phys. **116**, 7752 (2002).

[144] R. Larson, T. Perkins, D. Smith, and S. Chu, Phys. Rev. E **55**, 1794 (1997).

[145] C. Bustamante, J. Marko, E. Siggia, and S. Smith, Science **265**, 1599 (1994).

[146] J. Marko and E. Siggia, Macromolecules **28**, 8759 (1995).

[147] B. Zimm, Macromolecules **31**, 6089 (1998).

[148] P. DeGennes, J. Chem. Phys. **60**, 5030 (1974).

[149] F. Brochardwyart, Europhys. Lett. **30**, 387 (1995).

[150] P. Lai and K. Binder, J. Chem. Phys. **98**, 2366 (1993).

[151] S. Tan, Polymer **40**, 695 (1999).

[152] L. Miao, H. Guo, and M. Zuckermann, Macromolecules **29**, 2289 (1996).

[153] G. Xu, J. Ding, and Y. Yang, Rheol. Acta **40**, 60 (2001).

[154] J. DaSilva and E. Jage, Phys. Lett. A **135**, 17 (1989).

[155] B. Ladoux and P. Doyle, Europhys. Lett. **52**, 511 (2000).

[156] A. Laubereau and W. Kaiser, Rev. Mod. Phys. **50**, 607 (1978).

[157] T. Elsaesser and W. Kaiser, Annu. Rev. Phys. Chem. **42**, 83 (1991).

[158] D. W. Oxtoby, Adv. Chem. Phys. **47**, 487 (1981).

[159] S. Mukamel, *Principles of Nonlinear Optical Spectroscopy*, Oxford University Press, New York, 1995.

[160] S. Mukamel, Annu. Rev. Phys. Chem. **51**, 691 (2000).

[161] J. C. Owrutsky, D. Raftery, and R. M. Hochstrasser, Annu. Rev. Phys. Chem. **45**, 519 (1994).

[162] G. R. Fleming and M. Cho, Annu. Rev. Phys. Chem. **47**, 109 (1996).

[163] W. P. de Boeij, M. S. Pshenichnikov, and D. A. Wiersma, Annu. Rev. Phys. Chem. **49**, 99 (1998).

[164] A. Tokmakoff, B. Sauter, and M. D. Fayer, J. Chem. Phys. **100**, 9035 (1994).

[165] W. Zhao and J. C. Wright, Phys. Rev. Lett. **84**, 1411 (2000).

[166] T. S. Yang et al., J. Chem. Phys. **110**, 12070 (1999).

[167] Z. Bihary, R. B. Gerber, and V. A. Apkarian, J. Chem. Phys. **115**, 2695 (2001).

[168] B. J. Berne and R. Pecora, *Dynamic Light Scattering*, Wiley-Interscience, New York, 1976.

[169] Y. C. Sun, H. D. Gai, and G. A. Voth, J. Chem. Phys. **100**, 3247 (1994).

[170] B. M. Ladanyi and R. M. Stratt, J. Phys. Chem. A **102**, 1068 (1998).

[171] S. A. Egorov and J. L. Skinner, J. Chem. Phys. **105**, 7047 (1996).

[172] D. E. Sagnella, J. E. Straub, T. A. Jackson, M. Lim, and P. A. Anfinrud, Proc. Natl. Acad. Sci. USA **96**, 14324 (1999).

[173] K. F. Everitt, J. L. Skinner, and B. M. Ladanyi, J. Chem. Phys. **116**, 179 (2002).

[174] Q. Shi and E. Geva, J. Phys. Chem. A **107**, 9059 (2003).

[175] R. Rey and J. T. Hynes, J. Chem. Phys. **104**, 2356 (1996).

[176] E. L. S. III and R. Rey, J. Chem. Phys. **116**, 237 (2002).

[177] R. Rey and J. T. Hynes, J. Phys. Chem. A **106**, 11993 (2002).

[178] C. P. Lawrence and J. L. Skinner, J. Chem. Phys. **117**, 5827 (2002).

[179] S. A. Egorov, E. Rabani, and B. J. Berne, J. Phys. Chem. B **103**, 10978 (1999).

[180] M. Tuckerman and B. J. Berne, J. Chem. Phys. **98**, 7301 (1993).

[181] J. S. Bader, B. J. Berne, E. Pollak, and P. Hänggi, J. Chem. Phys. **104**, 1111 (1996).

[182] A. Nitzan, S. Mukamel, and J. Jortner, J. Chem. Phys. **60**, 3929 (1974).

[183] A. Nitzan and R. Silbey, J. Chem. Phys. **60**, 4070 (1974).

[184] S. H. Lin, J. Chem. Phys. **61**, 3810 (1974).

[185] Y. J. Yan and S. Mukamel, J. Chem. Phys. **94**, 179 (1991).

[186] R. F. Loring, Y. J. Yan, and S. Mukamel, J. Chem. Phys. **87**, 5840 (1987).

[187] Y. Tanimura and S. Mukamel, J. Chem. Phys. **99**, 9496 (1993).

[188] V. Chernyak and S. Mukamel, J. Chem. Phys. **114**, 10430 (2001).

[189] A. Tokmakoff, J. Phys. Chem. A **104**, 4247 (2000).

[190] J. Y. Sung and M. H. Cho, J. Chem. Phys. **113**, 7072 (2000).

[191] J. Y. Sung and R. J. Silbey, J. Chem. Phys. **115**, 9266 (2001).

[192] R. Karrlein and H. Grabert, J. Chem. Phys. **108**, 4972 (1998).

[193] T. Kato and Y. Tanimura, J. Chem. Phys. **117**, 6221 (2002).

[194] M. Kryvohuz and J. Cao, (2004), in preparation.

[195] R. Kosloff and S. A. Rice, J. Chem. Phys. **72**, 4591 (1980).

[196] S. Okazaki, Adv. Chem. Phys. **118**, 191 (2001).

[197] S. Hammes-Schiffer and J. C. Tully, J. Chem. Phys. **101**, 4657 (1994).

[198] S. A. Corcelli and J. C. Tully, J. Phys. Chem. A **106**, 10849 (2002).

[199] O. V. Prezhdo and P. J. Rossky, J. Chem. Phys. **107**, 825 (1997).

[200] R. Kapral and G. Ciccotti, J. Chem. Phys. **110**, 8919 (1999).

[201] D. F. Coker and L. Xiao, J. Chem. Phys. **102**, 496 (1995).

[202] N. Makri, J. Phys. Chem. B **103**, 2823 (1999).

[203] J. Cao, L. W. Ungar, and G. A. Voth, J. Chem. Phys. **104**, 4189 (1996).

[204] J. Wu and J. Cao, J. Chem. Phys. **115**, 5381 (2001).

[205] M. Kryvohuz and J. Cao, J. Chem. Phys. (2004), accepted.

[206] J. Stenger, D. Madsen, P. Hamm, E. T. J. Nibbering, and T. Elsaesser, Phys. Rev. Lett. **87**, 027401 (2001).

[207] C. J. Fecko, J. D. Eaves, J. J. Laparo, and A. Tokmakoff, Science **301**, 1698 (2003).

[208] J. B. Asbury et al., J. Phys. Chem. A **108**, 1107 (2004).

[209] M. Lim and R. M. Hochstrasser, J. Chem. Phys. **115**, 7629 (2001).

[210] M. Lim, P. Hamm, and R. M. Hochstrasser, Proc. Natl. Acad. Sci. USA **95**, 15315 (1998).

[211] G. Gnanakaran and R. M. Hochstrasser, J. Chem. Phys. **105**, 3486 (1996).

[212] S. Woutersen, U. Emmerichs, H. K. Nienhuys, and H. J. Bakker, Phys. Rev. Lett. **81**, 1106 (1998).

[213] A. Pakoulev, Z. H. Wang, Y. S. Pang, and D. D. Dlott, Chem. Phys. Lett. **380**, 404 (2003).

[214] S. Palese, S. Mukamel, R. J. D. Miller, and W. T. Lotshaw, J. Phys. Chem. **100**, 10380 (1996).

[215] E. L. S. III, W. P. Reinhardt, and J. T. Hynes, J. Chem. Phys. **77**, 3583 (1982).

[216] D. W. Oxtoby, Adv. Chem. Phys. **40**, 1 (1979).

[217] A. M. Levine, M. Shapiro, and E. Pollak, J. Chem. Phys. **88**, 1959 (1988).

[218] U. Weiss, *Quantum Dissipative Systems*, World Scientific, Singapore, 1999.